Anatoly M. Pravilov

Radiometry in Modern Scientific Experiments

SpringerWienNewYork

SpringerWienNewYork

A.M. Pravilov

Radiometry in Modern Scientific Experiments

SpringerWienNewYork

Dr. A. M. Pravilov
Fock Inst. of Physics
198504 St. Petersburg
Russia
pravilov@photonics.phys.spbu.ru

Printed in Germany

SpringerWienNewYork is a part of Springer Science+Business Media
springer.at

Cover design: WMXDesign GmbH, Heidelberg, Germany

Typesetting: SPi, Pondicherry, India

Printed on acid-free and chlorine-free bleached paper
SPIN: 12792443

Library of Congress Control Number: 2011931168

ISBN 978-3-7091-0103-2 e-ISBN 978-3-7091-0104-9
DOI 10.1007/978-3-7091-0104-9
SpringerWienNewYork

Preface

This book deals with the methods of calibration of light sources and photodetectors, as well as spectral responsivity of optical instruments and absolute measurements of spectral photon flux from photoprocesses under study in wide spectral range, from near infrared to vacuum ultraviolet, $\lambda \approx 1{,}200$–100 nm, and wide range of radiation intensities, up to several quanta per second in absolute and arbitrary units. It provides useful information about characteristics of physical and chemical detectors of radiation, which have not been described in the well-known literature. This book is directed to the readers who in the course of their work, in particular, experiments, have to measure luminescence spectra, spectral radiation intensities in wide, from infrared to vacuum ultraviolet, spectral range in wide light intensity range, to calibrate light sources and light detectors in these ranges, and to determine quantum yields of photoprocesses in absolute or arbitrary units. The book can be used as a textbook for students and postgraduate students who in the course of their future work will deal with the measurements mentioned above.

St. Petersburg, Russia A. M. Pravilov

Acknowledgments

I am very grateful to Springer-Verlag GmbH for its suggestion to publish my work.

Many experiments required for proving the methods and devices described in this book were carried out with the assistance of my colleagues. I very much appreciate their help and collaboration. Especially I am grateful to Igor Sidorov, Dr. Sergey Ryabov, Dr. Igor Shulpyakov, Dr. Sergey Lukashov, and Dr. Sergey Poretsky.

Dr. Oleg Marchenko translated the manuscript and drew figures; his work was indispensable for the completion of the book, and I would like to express my sincere gratitude for his assistance.

Finally, I wish to thank my wife Natalya for her selfless patience, kind understanding, and support throughout the entire period of my researches.

Contents

List of Abbreviations

BESSY II	Physikalisch-Technische Bundesanstalt (PTB) electron storage ring
CCD	Charge coupled device
CGPM	General Conference on Weights and Measures
CINAT	Collision-induced nonadiabatic transition
CIPM	International Committee for Weights and Measures
EIA	Electronic Industry Association
IEEE	Electrotechnical Commission
IR	Infrared spectral range
IUPAC	International Union of Pure and Applied Chemistry
MCP	Microchannel plates
MLS	PTB metrology light source
NEP	Noise equivalent power
NEP*	Noise equivalent power normalized to unit bandwidth of the detection system
NIST	National Institute of Standards and Technology (USA)
NPI	National Physical Laboratory (UK)
PMT	Photomultiplier tube
S/*N*	Signal-to-noise ratio
SR	Synchrotron radiation
UV	Ultraviolet spectral range
VUV	Vacuum ultraviolet spectral range

List of Symbols: Latin and List of Symbols: Greek should be the same

A	Square of the input opening of the photodetector
$[A]$	Concentration of the product used in actinometry
c	Light velocity in vacuum
c_1	The first radiation constant
c_2	The second radiation constant
D	Detectivity
D^*	Detectivity normalized to unit bandwidth of the detection system
$D(\lambda)$	Spectral detectivity
e	Electron (elementary) charge
eV	Energy of one electron accelerated over the potential 1 V
$E = hv$	Energy of a single photon in eV
$E = N_A hv$	Einstein
E_e	Irradiance
$E_e(\lambda)$	Spectral irradiance
E_{hv}	Photon irradiance
$E_{hv}(\lambda)$	Spectral photon irradiance
E_λ	Energy of a single photon in J
E_w	Work function for photocathode
$F(\lambda)$	Spectral transparency function of monochromator
$F_k(\tilde{v})$	The King correction factor
G	Total gain of photomultiplier dynode system
h	Planck's constant
H_e	Radiant exposure
H_v	Luminous exposure
I_{hv}	Intensity of optical radiation (radiation intensity)
$I_{hv}(\lambda_i–\lambda_j)$	Spectral radiation intensity in the $\lambda_i–\lambda_j$ spectral range
$I^{et}_{hv}(\lambda)$	Spectral radiation intensity of calibrated radiation source
$I^{u}_{hv}(\lambda)$	Uncorrected spectral radiation intensity
$I(\lambda)$	True spectrum
$I^*(\lambda)$	"Distorted" spectrum
I_{abs}/I_0	Radiation fraction absorbed by actinometer

$I_{\parallel}$	Horizontally polarized component of the Rayleigh scattered light
$I_{\perp}$	Vertically polarized component of the Rayleigh scattered light
J	Rotational quantum number
J_e	Radiant intensity
J_v	Luminous intensity
k	The Boltzmann constant
k_{ij}	Reaction rate constant
$k(\lambda)$	Absorption coefficient
K_{m}	Maximum spectral luminous efficiency
K_λ	Spectral sensitivity of the eye
l	Cell length
$L(\lambda)$	Spectral reflectivity
L_e	Radiance
$L_e(\lambda)$	Spectral radiance
$l_e(\lambda)$	Spectral radiance (arbitrary units)
$L_e^0(\lambda, T)$	Black body spectral radiance of nonpolarized radiation
L_{hv}	Photon radiance
$L_{hv}(\lambda)$	Spectral photon radiance
$l_{hv}(\lambda)$	Spectral photon radiance (arbitrary units)
L_v	Luminance
M_e	Radiant emittance
$M_e(\lambda)$	Spectral radiant emittance
$M_e^0(\lambda, T)$	Black body spectral radiant emittance of nonpolarized radiation
M_{hv}	Photon emittance
$M_{hv}(\lambda)$	Spectral photon emittance
M_v	Luminous emittance
n	Refraction factor
n	Number of pairs of charged carriers
$n_{hv}(\lambda)$	Volumetric density of absorbed radiation
N	Density of molecules in cm^{-3}
N_{A}	Avogadro constant
$N_{hv}(\lambda)$	Number of photons
p	Pressure
Q_v	Luminous energy
Q_e	Radiant energy
R	Distance
$R(\lambda)$	Specific spectral responsivity
S	Sensitivity (responsivity)
$S(\lambda)$	Spectral sensitivity (responsivity)
$s(\lambda)$	Spectral responsivity function (arbitrary units)
$S(\lambda_0)$	Responsivity at λ_0
S_e	Radiant responsivity
S_{hv}	Photon responsivity
$S_e(\lambda)$	Spectral radiant responsivity (function)

$s_e(\lambda)$	Spectral radiant responsivity (arbitrary units)
$S_{hv}(\lambda)$	Spectral photon responsivity (function)
$s_{hv}(\lambda)$	Spectral photon responsivity (arbitrary units)
S_v	Luminous responsivity
S_e^{pt}	Phototube sensitivity
t_{ph}	Photolysis time interval
T_{b}	Brightness temperature
T_{c}	Color temperature
v	Vibrational quantum number
V	Volume of the actinometer system
V_{eff}	The volume irradiating the photodetector
w	Photolysis producing rate
X	Photodetector input
$X(\lambda)$	Spectral input
$X(\lambda_0)$	Input at λ_0
$x(\lambda)$	Spectral input in arbitrary units
Y	Photodetector output
$Y(\lambda)$	Spectral output
$Y_{et}(\lambda)$	Spectral output caused by irradiation from the calibrated radiation source
$y_{et}(\lambda)$	Spectral output caused by irradiation from the calibrated radiation source (arbitrary units)

List of Symbols: Greek

α	Polarizability
α	Temperature coefficient for bolometers and thermistors
$\alpha(\lambda,T)$	Absorptivity (absorptance) of a body or surface
γ	Anisotropy
$\varepsilon(\lambda,T)$	Emissivity of a body or surface
$\eta(\lambda)$	Quantum efficiency
λ	Light (radiation) wavelength
λ_{max}	Wavelength cutoff dictated by the work function of the photocathode material
ν	Frequency of oscillation
$\tilde{\nu}$	Wavenumber
$\rho(\lambda)$	Spectral reflectivity
ρ_n	Depolarization ratio
σ_0	Absorption cross section
σ_i	Photoionization cross section
$\sigma(\tilde{\nu})$	Rayleigh scattering cross section of diatomic molecules

$\sigma_{\mathrm{r}}(\tilde{\nu})$	Integral cross section of Rayleigh scattering within the total solid angle
$\sigma_{\mathrm{ss}}(\tilde{\nu})$	Rayleigh scattering cross section of particles having spherically symmetry
τ	Lifetime
$\tau(\lambda)$	Spectral transmittance
$\varphi_{\mathrm{AB}}(\lambda)$	Integral absolute quantum yield of AB molecule photodecay
φ_i^{AB}	Integral absolute quantum yield for *i*-th process of AB molecule photodecay
$\varphi_i^{\mathrm{AB,c}}(\lambda_j - \lambda_k)$	Convolution quantum yield of *i*-th primary photoprocess within the band λ_j/λ_k
$\varphi_i^{\mathrm{AB}}(\lambda)$	Absolute quantum yield for *i*-th process of AB molecule photodecay
$\Phi_{\mathrm{A}}(\lambda)$	Quantum yield of the photoprocess utilized in actinometry
$\Phi_{\mathrm{B_i}}^{\mathrm{AB}}(\lambda)$	Absolute quantum yield of the product B_i of the AB photolysis
$\Phi_{\mathrm{lum}}(\lambda)$	Absolute luminescence quantum yield of AB or photodecay product AB – $\mathrm{B_i}$
$\Phi_{\mathrm{B_i}}^{\mathrm{AB}}$	Integral absolute quantum yield for formation of the product of AB photodecay $\mathrm{B_i}$
$\Phi_{\mathrm{B_i}}^{\mathrm{AB,c}}(\lambda_j - \lambda_k)$	Convolution quantum yield for formation of the $\mathrm{B_i}$ photoproduct within the band λ_j/λ_k
Φ_e	Radiant power (flux)
$\Phi_{\mathrm{B_i}}^{\mathrm{AB}}(\lambda)$	Absolute quantum yield of the product $\mathrm{B_i}$ of the AB photolysis
$\Phi_{\mathrm{lum}}(\lambda)$	Absolute luminescence quantum yield of AB or photodecay products AB – $\mathrm{B_i}$
$\Phi_{h\nu}$	Photon flux
Φ_v	Luminous flux
$\Phi_e(\lambda)$	Spectral radiant power
$\phi_e(\lambda)$	Spectral radiant power in arbitrary units
$\Phi_{h\nu}(\lambda)$	Spectral photon flux
$\Phi_{h\nu}^{et}(\lambda)$	Spectral photon flux of calibrated radiation source
$\phi_{h\nu}^{et}(\lambda)$	Spectral photon flux of calibrated radiation source (arbitrary units)
$\Phi_{h\nu}^{R}$	Rayleigh scattering photon flux from the unit volume

List of Symbols: Other Symbols

$\neq$	Rovibrational excitation
$\overset{*}{\neq}$	Rovibronic excitation

Chapter 1
Introduction

Abstract The chapter outlines the radiometry fields discussed in this book. Here are defined the basic quantities used for description of radiation features and of the units in the visible and other ranges of electromagnetic radiation related to radiometry. Relationships between the energetic, photometric, and photonic units are given. In the final sections, some principles are considered to be a basis for making radiometric measurements in scientific laboratory with guaranteeing the least uncertainties.

1.1 General

Radiometry is a field of physical science concerning with the study of measuring methods of electromagnetic radiation including measurements in the optical range. As anywhere in physics, the use of proper physical quantities and their units is emphasized to adequate and deeper understanding. Also some aspects of radiometry have been already discussed in monographs, e.g., *Optical Radiation Measurements* edited by F. Grum and C.J. Bartleson [1–3]. This book is aimed to give expanded discussion on such specific items as follows:

- The laboratory calibration methods for *light* (*radiation*) sources and photodetectors.
- The calibration methods in absolute and arbitrary units for the systems involving spectral device and photodetector.
- Light (radiation) intensity and probability measurements for photoprocesses under study.

Sources and detectors of electromagnetic radiation in spectral ranges specified from the *near infrared* radiation (*near IR*) to *vacuum ultraviolet* radiation (*vacuum UV*), where the wavelength runs from 1,200 to 100 nm, will be considered briefly in Chaps. 2 and 3, since these questions were discussed for last time in the books, which were published some decades ago, whereas the pace of development in each

A.M. Pravilov, *Radiometry in Modern Scientific Experiments*,
DOI 10.1007/978-3-7091-0104-9_1,

of these areas has been very rapid. In these chapters particular emphasis will be placed on metrological aspects, wherein the author will also treat his own practice on these fields. Herein one type of photodetectors, so-called *gas-phase actinometers*, as well as measuring methods realized by the author with such a detector over many years, will be discussed in detail. Nowadays some of the methods mentioned above are uncommon in experimental practice, although actinometry measurements provided with an *oxygen actinometer* may give very noticeable advantages with respect to the methods utilizing properties of usual commercial photodetectors exploited in the vacuum UV range.

There are frequently happened experimental situations which require the intensity measurements to be expressed in terms of absolute units, such as W/nm or photon/s nm. For example, there exist tasks, where we have to obtain the yield or probability for a process occurring with photon absorption, or where we need to estimate the radiation yield in accomplishing of interaction for the system under investigation. Such events occur under conditions of *chemiluminescence* or *chemiluminescence induced by absorption*. Also, there is no question that the *absolute quantum yield* is to be much more valuable than quantum yield measured in arbitrary units. Furthermore, it often makes measurements within a wide spectral range, where a distorted spectrum is recorded and the procedure of spectrum correction should be executed. There are true words with absolute certainty belonged to a greatest Russian scientist and founder of the periodic table and Russian metrology D.I. Mendeleev who wrote: "Science begins with starting measurements; and exact science is to be inconceivable without a measure." Methods of absolute calibration of photodetectors and light sources and absolute measurements of radiation intensities of processes under study are discussed in Chaps. 4 and 6.

A spectral device equipped with a dispersing unit such as monochromator, spectrograph, Fourier spectrometer, as well as a photodetector should always produce a *distorted* spectrum $I^*(\lambda)$, which differs from the *true* spectrum $I(\lambda)$. The distinction between the measured spectrum and the true one arises from that the intensity of radiation passing through the dispersing unit depends on wavelength λ, and also from that the function $F(\lambda)$ as a ratio of the intensity at the output of the dispersing device to the intensity at its input depends upon the spectral transparency function of the device. Moreover, the *sensitivity* (*responsivity*) of any photodetector is also a function, $S(\lambda)$, of the wavelength λ. Thus, for the given functions $F(\lambda)$ and $S(\lambda)$, one can find the original spectrum as follows: $I(\lambda) = I^*(\lambda)/[F(\lambda)S(\lambda)]$. In the other words, the measured spectrum should be corrected by means of the product of the functions $F(\lambda)$ and $S(\lambda)$ to find the original spectrum of the source. There is no question that the original spectrum is to be much more valuable than the distorted one. Methods of calibration of spectral instruments which give a possibility for correction distorted spectra are discussed in Chap. 5.

The methods for corrections of measured spectra as well as the methods for measurements of radiation intensity in absolute units, all have features within a particular spectral range, because of the absence of universal photodetector.

Further, the measuring methods for strong intensities differ dramatically from that applied for detecting weaker intensities.

The author never encountered monographs nor reviews wherein the measuring methods in absolute units and the methods of spectrum correction over all the spectral and intensity ranges mentioned above were discussed. Each method has many features, which should be well-known to the researcher who is going to apply it to practice.

1.2 Radiometric, Photometric, and Photonic Quantities and Units

Optical radiation is a kind of electromagnetic radiation of wavelength from 0.1 nm to 1 mm, although, there exist different viewpoints regarding this definition. Rather the range is named "optical" through habit and due to the methods applied to generate radiation of this kind, whereas distinctions between applications of these methods disappear today. As usual, electromagnetic radiation of wavelength range from 0.1 or 1 to 100 nm is the so-called far ultraviolet radiation. In its short wavelength range, far ultraviolet radiation is defined as soft X-rays, for example, the radiation can be generated by slowing down of a high-energy electron beam. Electromagnetic radiation of wavelength from 100 to about 190 nm is generally identified as *vacuum ultraviolet* due to that the radiation, as well as radiation of shorter wavelengths, is strong absorbed by air. Further, the range of wavelengths from 190 to 400 nm is associated with the so-called near ultraviolet, from 400 to 750 nm with radiation of the *visible region*, from 750 to 2,500 nm – with radiation of the *near infrared* range, from 2.5×10^3 to 2.5×10^4 nm – with *infrared radiation*, and from 2.5×10^4 nm to 1 mm – with radiation of the *far-infrared* range. It is assumed the lower limit of radiofrequency radiation to begin with radiation of wavelength 1 mm. It is obvious that boundaries between the regions defined above are conventional.

The wavelength λ of optical radiation can be expressed to be as follows:

$$\lambda = c/v, \tag{1.1}$$

where c is the light velocity in vacuum ($c = 2.9979 \times 10^8$ m/s), v is frequency of oscillations in hertz. Wavelength of optical radiation is usually expressed in nanometers (1 nm $= 10^{-9}$ m) or angström (1 Å $= 10^{-8}$ cm $= 10^{-10}$ m), the latter is an off-system unit. An off-system energetic unit is of frequent use to define the wavelength in the optical range, this is a so-called *electron volt* (1 eV $= 1.602 \times 10^{-19}$ J), which is equal to the energy of one electron accelerated over the potential 1 V. The relationship between the wavelength λ and the energy E is given by the *Planck's equation*:

$$E = hv = hc/\lambda = 1,239.8/\lambda \text{ eV}, \tag{1.2}$$

where $h = 6.626 \times 10^{-34}$ J s is the *Planck's constant*, λ is expressed in nanometers. The energy of a single photon can be also expressed in energy units:

$$E_\lambda = hc/\lambda = 2.000 \times 10^{-25}/\lambda \text{ J } (\lambda \text{ in meters}) \tag{1.3}$$

or

$$E_\lambda = 2.000 \times 10^{-16}/\lambda \text{ J } (\lambda \text{ in nanometers}). \tag{1.4}$$

For the given number of photons $N_{hv}(\lambda)$, each having the energy hv associated with the wavelength λ, the total photon energy is to be equal to the product of $N_{hv}(\lambda)$ by the quantity in the right-hand side of (1.3) or (1.4). In turn, for the given total energy of photons $E\lambda$, we can calculate the number of photons $N_{hv}(\lambda)$ to be as follows:

$$N_{hv}(\lambda) = E_\lambda \lambda/hc = E_\lambda \lambda/2.000 \times 10^{-25} (\text{with } E_\lambda \text{ in joules and } \lambda \text{ in meters}) \tag{1.5}$$

or

$$N_{hv}(\lambda) = E_\lambda \lambda/2.000 \times 10^{-16} (\text{within } E_\lambda \text{ in joules and } \lambda \text{ in nanometers}). \tag{1.6}$$

A so-called *wavenumber* is another off-system unit. To describe radiation properties wavenumber is often used in radiometry instead of wavelength. Its magnitude $\tilde{\nu}$ is numerically equal to the reciprocal value of the wavelength λ: $\tilde{\nu} = 1/\lambda$, i.e., it represents the number of wavelengths per length unit.

Another off-system unit used least often is the so-called *Einstein*, which is equal to the energy of photons associated with one mole of photons. In order to calculate the energy, we should multiply the photon energy given in (1.2) by the Avogadro constant:

$$E = N_A hv = N_A hc/\lambda. \tag{1.7}$$

Historically, it was the visible light range which was closely studied first. So-called *photometric* (*luminous*) *quantities and units* were introduced to describe energetic properties of *visible* light flows well before the modern theory of electromagnetic waves was established. The photometric quantities deal with *luminous flows*, i.e., those are concerned only with the visible light. The author would have to say about these units, because of their importance in technical documentations accompanying modern models of photodetectors. Their features are expressed in terms of photometric units so far today. However, common units of energy are often used to describe energetic properties of radiation in the other ranges of electromagnetic spectrum, these quantities and units are called *radiometric* in that case. Finally, there exist so-called *photonic quantities and units*, which may be more important quantities to chemists and physicists due to that these units can give a quantum yield of some process, instead of energetic ones. The quantum yield is an

important value associated with the probability of the process proceeding under photon absorption regardless the photon energy.

Some quantities treated in terms of radiometric, photometric, and photonic units are listed in Table 1.1.

Table 1.1 Radiometric, photometric, and photonic quantities and units

Quantity	Radiometry[a]	Photometry[a]	Photonic quantities[a]
Radiant energy (luminous energy)[b]	Q_e [J[c]]	Q_v [lm s[c,d]]	Photon number, N_{hv}
Radiant power or flux (luminous flux)	Φ_e [W]	Φ_v [lm][e,f]	Photon flux[g], Φ_{hv} [photon/s] or [s^{-1}]
Radiant power spectral density (spectral radiant power)	$\Phi_e(\lambda)$ [W/nm]		Photon flux spectral density (spectral photon flux[h]), $\Phi_{hv}(\lambda)$ [photon/(s nm)] or [s^{-1} nm^{-1}]
Radiant emittance (luminous emittance)	M_e [W/m^2]	M_v [lx][i]	Photon emittance, M_{hv} [photon/(s m^2)] or [s^{-1} m^{-2}]
Spectral radiant emittance	$M_e(\lambda)$ [W/(m^2 nm)]		Spectral photon emittance, $M_{hv}(\lambda)$ [photon/(s m^2 nm)] or [s^{-1} m^{-2} nm^{-1}]
Radiant intensity (luminous intensity)	J_e [W/sr]	J_v [cd][j]	Photon intensity, J_{hv} [photon/(s sr)] or [s^{-1} sr^{-1}]
Spectral radiant intensity	$J_e(\lambda)$ [W/sr nm]		Spectral photon intensity, $J_{hv}(\lambda)$ [photon/(s sr nm)] or [s^{-1} sr^{-1} nm^{-1}]
Radiance (luminance)	L_e [W/sr m^2]	L_v [cd/m^2]	Photon radiance, L_{hv} [photon/(s sr m^2)] or [s^{-1} sr^{-1} m^{-2}]
Spectral radiance	$L_e(\lambda)$ [W/(sr m^2 nm)]		Spectral photon radiance, $L_{hv}(\lambda)$ [photon/(s sr m^2 nm)] or [s^{-1} sr^{-1} m^{-2} nm^{-1}]
Irradiance (illuminance)	E_e [W/m^2]	E_v [lx]	Photon irradiance, E_{hv} [photon/(s m^2)] or [s^{-1} m^2]
Spectral irradiance	$E_e(\lambda)$ [W/(m^2 nm)]		Spectral photon irradiance, $E_{hv}(\lambda)$ [photon/(s m^2 nm)] or [s^{-1} m^{-2} nm^{-1}]
Radiant (luminous) exposure	H_e [J/m^2]	H_v [lm c/m^2] [lx s]	Photon exposure, H_{hv} [photon/m^2 or m^{-2}]

[a]Symbols and units are also given in *square brackets*
[b]Photometry quantities are given in *brackets* hereafter in this column
[c]Abbreviations of units are given in *brackets* hereafter in the second and third columns
[d]This unit is sometimes called *talbot*
[e][lm] = [candela sr]
[f]Luminous flux is also called luminous power
[g]This quantity is also called *intensity of optical radiation* or *radiation intensity*, I_{hv}
[h]This quantity is also called spectral intensity of optical radiation or spectral radiation intensity, $I_{hv}(\lambda)$
[i][lx] = [lm/m^2]
[j]SI base unit (see below)

Radiant energy Q_e is the energy transported by electromagnetic waves, where subscript e indicates the energetic nature of the quantity, and subscript v refers the quantity to visible light. C*andela* (cd) is a base unit of photometry, it will be treated below more precisely. Candela is used to form other units of photometry. For example, *lumen* is a measure of *luminous flux*, one lumen is equal to one candela multiplied by one second: 1 lm = 1 cd s.

Radiant power or *luminous flux*, or simply *flux* Φ, is the total radiant energy emitted by a source per unit time: $\Phi = \mathrm{d}Q(\lambda)/\mathrm{d}t$. It should be paid attention to the absence of any spectral functions on wavelength in photometry, because candela and its derived units are all associated with the spectral curve of human eye.

Radiant power spectral density $\Phi_e(\lambda)$ is the radiation flux expressed in wavelength unit $\Phi_e(\lambda) = \mathrm{d}\Phi_e/\mathrm{d}\lambda$.

Radiant emittance or *luminous emittance M* is the radiation flux emitted from source unit area: $M = \mathrm{d}\Phi/\mathrm{d}A$, where d$A$ is the area element.

Spectral radiant emittance $M_e(\lambda)$ is the radiant emittance M expressed in unit wavelength interval: $M_e(\lambda) = \mathrm{d}M_e/\mathrm{d}\lambda$.

Radiant intensity or *luminous intensity J* is the radiant power Φ per unit solid angle Ω of radiation propagation: $J_e = \mathrm{d}\Phi/\mathrm{d}\Omega$.

Spectral radiant intensity $J_e(\lambda)$ is the radiant intensity within unit wavelength interval: $J_e(\lambda) = \mathrm{d}J_e/\mathrm{d}\lambda$.

Of special note is the luminous power or luminous intensity, that is *candela*, which is a base unit in photometry. Candela, along with such units as meter, kilogram, second, mole, ampere, and others, is a base unit in the SI system. Since the 16th *General Conference on Weights and Measures* (*CGPM*) in 1979, candela has been defined as "The candela is the luminous intensity, in a given direction, of a source that emits monochromatic radiation of frequency 540×10^{12} Hz and that has a radiant intensity in that direction of 1/683 watts per steradian" [4]. Prior to 1948, various standards for luminous intensity were in use in a number of countries. These were typically based on the brightness of the flame from a *standard candle* of defined composition, or the brightness of an incandescent filament of specific design. One of the best known of these was the English standard of *candlepower*. One candlepower was the light produced by a pure spermaceti candle weighing one-sixth of a pound and burning at a rate of 120 grains per hour. Germany, Austria, and Scandinavia used the hefnerkerze, a unit based on the output of a Hefner lamp. International Commission on Illumination proposed a *new candle* based on the luminance of a *black body radiator* at the temperature of freezing platinum. The value of the new unit was chosen to make it similar to the earlier unit candlepower. The decision was promulgated by the *International Committee for Weights and Measures* (*CIPM*) in 1946. The value of the new candle is such that the brightness of the full radiator at the temperature of solidification of platinum is 60 new candles per square centimeter. It was then ratified in 1948 by the ninth CGPM which adopted a new name for this unit, the candela (see [4] and references therein).

Since 1934, at first in the USA and in time in others countries, new standards of candela were established. Figure 1.1 shows the arrangement for the candela standard set in the USSR in 1948 [5].

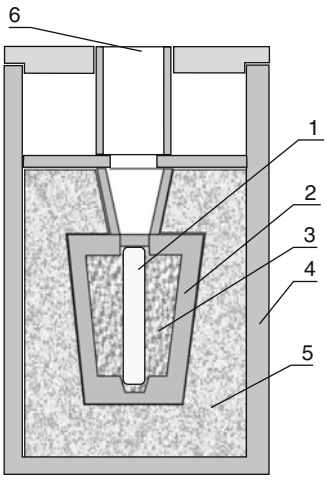

Fig. 1.1 The arrangement of candela standard. *1* – the pipe made of fused thorium oxide ThO_2, temperature of which is kept equal to that of solidification of platinum 2,043 K; *2* – the crucible made of fused thorium oxide ThO_2, which is filled up a pure platinum *3*; *4* – the quartz cell filled up thorium oxide ThO_2 *5*; *6* – the viewing window

The standard consists of the pipe fabricated of thorium oxide of inner diameter 2.5 mm, and length 45 mm; the pipe is submerged in a pure platinum and covered by the lid with the hole of diameter 1.5 mm. It is the hole that is the light source! Platinum can heat up to temperature just higher than its melting temperature, and it can then be cooled with a controlled rate. Such a light source being a black body, whose temperature is equal to the platinum melting point 2,043 K, has brightness 60 cd/cm^2. In some countries this kind of the candela standard was accepted as the *Primary Source State Standard*.

Up to the end of the twentieth century, a wide range of precision blackbody sources for radiometric applications covering the spectral range from UV to far IR and temperature range from 80 to 3,200 K was developed in Russia, Great Britain, USA, and Germany. Recent advances in high-temperature technology and a novel design made it possible to develop the Planck sources of temperatures as high as 3,200 K, with high uniformity and stable radiation characteristics. These large-area blackbodies allow the creation of a new generation of spectral irradiance standards with uncertainty of 0.1% (see [6–11] and references therein).

A *cryogenic blackbody* operating at temperatures from 100 to 450 K was developed to provide calibration of *IR radiometers* [6]. This type of light source has large-area aperture of 100-mm diameter. Light sources of this type are expensive and used only for metrological purposes.

There are available systems for reproducing, storing and transferring light and temperature facilities, which involve the *primary state standards* of light power and temperature, *secondary and industrial standards*, and *reference sources* and reference *tungsten ribbon filament strip lamps* (hereafter *strip lamps*) of the first and lower grades. The latter is provided with proper measurement facilities. Finally, the system also involves *light metering lamps* assigned to reproduce a designed flux, light power, and illuminance, as well as strip lamps assigned to be working standards for radiation spectra. There are about 20 samples available of each

standard grade, excepting the primary state standards, and reference lamps that allows the all standards to be verified. The lower grade lamps are calibrated and verified by means of the higher grade lamps. Appropriate state standards approve the system of the lamps, standard sources as well as calibration and verification techniques.

Radiance (*luminance*) L_e is the radiant intensity dJ_e emitted by element of radiant surface dA in the direction of sight: $L_e = dJ_e/dA$.

Spectral radiance $L_e(\lambda)$ is the radiance per wavelength unit: $L_e(\lambda) = dL_e/d\lambda$.

Irradiance or *illuminance* E_e is the ratio of the radiant power falling on the radiant surface element to the value of the element: $E_e = d\Phi_e/dS$.

Spectral irradiance $E_e(\lambda)$ is the irradiance per wavelength unit: $E_e(\lambda) = dE_e/d\lambda$.

Radiant or *luminous exposure* H is the ratio of the radiant energy dQ falling on the surface element dS: $H = dQ/dS$.

The photometric quantities can be used to treat features of radiation sources and to describe properties of studied photoprocesses. Features of photodetectors will be discussed in Chap. 3.

1.3 Relationship Between Radiometric, Photometric, and Photonic Units

It is clear that the relationship between the energetic light units and photonic ones follows from (1.2). Below a few useful formulae are as follows:

$$\Phi_{hv} = 6.29 \times 10^{18}\ \Phi_e/hv\ \text{photon/s}, \tag{1.8}$$

where hv in electron volts, Φ_e in watts.

$$1\ \text{eV} = 8,065.5447\ \text{cm}^{-1}, \tag{1.9}$$

$$v = 2.418 \times 10^{14}\ hv\,\text{Hz}, \tag{1.10}$$

where hv in electron volts.

The relationship between candela and joule (J) can be found experimentally only, because candela as the basic unit was chosen arbitrary. The photometric units, such as candela and its derivations, are genetically concerned with the curve of spectral sensitivity of the eye $K\lambda$ (Fig. 1.2).

By this is meant that the definition of candela in terms of joule is true only for a given wavelength, namely, for the radiation of wavelength $\lambda = 555$ nm the following relationship is taken place:

$$1\ \text{W} = 683\ \text{lm}. \tag{1.11}$$

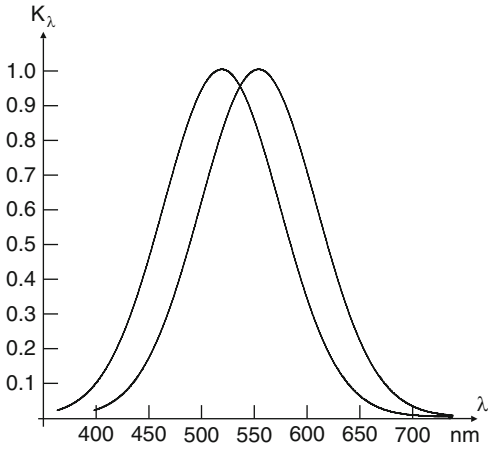

Fig. 1.2 The relative spectral sensitivity curve of the average human eye; for bright light (the right-hand side) and for feeble light (the left-hand side)

Generally, for the given emission spectrum of a source, expressed in the absolute units Φ_e W/nm or $\Phi_{h\nu}$ photon/(c nm), the photometric units of the spectrum can be found by exploiting the luminous efficiency function (see Fig. 1.2) as follows:

$$\Phi_v = K_m \int K_\lambda \Phi_e(\lambda) d\lambda, \tag{1.12}$$

where Φ_e is expressed in lumens; $K_m = \Phi_v/\Phi = 683$ lm/W is found to be the maximum spectral luminous efficiency, i.e., the spectral efficiency at the wavelength $\lambda = 555$ nm. The integral is taken over all visible range.

1.4 The Essential Features Required of Metrological Assurance for Radiometric Measurements

The basic principles of the radiometric measurements are common for each kind of measurements:

- Only verified measurement devices should be used.
- To be consistent with the measuring technique and neatly calculate measurement errors with taking into account the *Student coefficients* (see Appendix A).

The secondary standards maintenance is often beyond the capabilities of available apparatus of any laboratory due to a very high cost of verification procedures for all available measuring devices, such as light sources and detectors, so often as it is a need to provide regular measurements. Furthermore, each radiometric measuring procedure has its feature associated with particular experimental environments. It should be adhered to some regulations as listed below in order to avoid uncontrolled errors and take into account only inherent ones.

1. Provide a sufficient number of measurements, where possible, that enables to exploit the Student's coefficients method.
2. Use a few detectors and light sources having overlapping spectral regions. In general, both the detector and spectral lamp can fulfill the function of working or standard device (see Sect. 1.1). For example, in case of the standard detector, the light source is the *comparator* device, and vice versa. Whenever possible, work with a few detectors and light source to provide calibration. In the event of unpremeditated changes in radiating intensity of a source or incidental changes in sensitivity of a detector there is chance to compare obtained data by means of the other devices. Perform calibration procedure routinely, whenever possible.
3. Wherever possible, apply a few calibration methods, each being based on different effects, with scrupulous attention to the field of application of every method. Verify the linearity property of the measuring devices.
4. When performing calibration or measuring procedure, be consistent with identity of measuring conditions, particularly, with identity of layout of such a procedure.

References

1. Walsh, J.W.T.: Photometry. Constable and Company, London (1953)
2. Grum, G., Becherer, R.J.: Radiometry. In: Grum, F. (ed.) Optical Radiation Measurements, A Treatise, vol. 4. Academic, New York (1979)
3. Budde, W.: Physical detectors of optical radiation. In: Grum, F., Bartleson, C.J. (eds.) Optical Radiation Measurements, A Treatise, vol. 1. Academic, New York (1983)
4. Candela: http://en.wikipedia.org/wiki/Candela
5. Epshtein, M.I.: Izmereniya Opticheskogo Izlucheniya v Elektronike (Measurements of Optical Radiations in Electronics). Energiya, Moscow (1975)
6. Sapritsky, V.I., Khlevnoy, B.B., Khromchenko, V.B., Lisiansky, B.E., Mekhontsev, S.N., Melenevsky, U.A., Morozova, S.P., Prokhorov, A.V., Samoilov, L.N., Shapoval, V.I., Sudarev, K.A., Zelener, M.F.: Precision blackbody sources for radiometric standards. Appl. Opt. **36**, 5403–5408 (1997)
7. Sapritsky, V.I.: A new standard for the candela in the USSR. Metrologia **24**, 53–59 (1987)
8. Sapritsky, V.I.: National primary radiometric standards of the USSR. Metrologia **27**, 53–60 (1990)
9. White, M., Fox, N.P., Ralph, V.E., Harrison, N.J.: The characterisation of a high temperature blackbody as the basis for the NPL spectral radiance scale. Metrologia **32**, 431–434 (1996)
10. Sperfeld, P., Raatz, K.-H., Nawo, B., Moller, W., Metzdorf, J.: Spectral irradiance scale based on radiometric black-body temperature measurements. Metrologia **32**, 435–439 (1996)
11. Khlevnoy, B.B., Harrison, N.J., Rogers, L.J., Pollard, D.F., Fox, N.P., Sperfeld, P., Fischer, J., Friedrich, R., Metzdorf, J., Seidel, J., Samoylov, M.L., Stolyarevskaya, R.I., Khromchenko, V.B., Ogarev, S.A., Sapritsky, V.I.: Intercomparison of radiation temperature measurements over the temperature range from 1600 K to 3300 K. Metrologia **40**, 39–44 (2003)

Chapter 2
Radiation Sources in Radiometric Applications

Abstract This chapter deals with basic features of thermal light sources exploited for radiometric applications in the infrared, visible, and near UV spectral range $\lambda > 250$ nm. The calculation techniques of spectral radiant power and spectral photon flux in different units are also considered for the case of tungsten ribbon filament strip lamps. Quartz tungsten–halogen lamps and deuterium gas-discharge light sources are treated herein as radiation sources for the near UV and vacuum UV spectral range. Also principle characteristics of synchrotron radiation sources are discussed in the context of absolute radiation standards and methods of absolute calibration applied to radiation sources and photodetectors based on this type of radiation.

2.1 General

Some present-day light radiation and temperature standards have been considered in the previous chapter. The radiation sources applicable for spectral sensitivity measurements of spectral devices in wide spectral range from the VUV to IR spectral ranges, which can be used in common scientific, nonmetrological, laboratory will be interested first in this chapter. The sources can be subdivided into two classes: incandescent lamps (filament lamps, namely, tungsten ribbon filament strip lamps, see Sect. 1.1) and calibrated quartz tungsten–halogen lamps. It is the latter class of spectral lamps that provides for working standards of radiation spectra. Such lamps are produced and calibrated by various manufacturers.

2.2 Calibrated Sources of Thermal Radiation

Of *light sources* emitted by incandescent media, the black body is the best source of *thermal radiation*, because for the given temperature its surface element emits the most luminous energy. The spectral radiant emittance of

A.M. Pravilov, *Radiometry in Modern Scientific Experiments*,
DOI 10.1007/978-3-7091-0104-9_2, © Springer-Verlag/Wien 2011

nonpolarized radiation $M_e^0(\lambda, T)$ emitted by the black body follows the *Planck's law* [1–3]:

$$M_e^0(\lambda, T) = c_1 \lambda^{-5} [\exp(c_2/\lambda T) - 1]^{-1}, \tag{2.1}$$

where $M_e^0(\lambda, T)$ is expressed in W/m^3; $c_1 = 2\pi hc^2 = (3.7417749 \pm 0.0000022) \times 10^{-16}$ W m^2 is the first radiation constant and $c_2 = hc/k = (1.438769 \pm 0.000012) \times 10^{-2}$ K m is the second radiation constant; c is the light velocity in vacuum; $k = 1.3806505 \times 10^{-23}$ J/K $= 8.617343 \times 10^{-5}$ eV/K is the Boltzmann constant, and h is the Planck's constant. The expression in the *brackets* in (2.1) is the so-called *dimensionless Planck's law*, which can be expressed in terms of spectral radiance $L_e(\lambda)$ [W/(sr m^3)] propagating normal to the surface:

$$L_e^0(\lambda, T) = c_1 \lambda^{-5} [\exp(c_2/\lambda T) - 1]^{-1} \quad \text{W}/(\text{sr m}^2\ \text{m}). \tag{2.2}$$

Light sources like those shown in Fig. 1.1 are very bulk and expensive. Moreover, such a source has too low temperature to be suitable for applications required sufficient emitted irradiance in a short-wave spectral range (see Fig. 2.1).

As mentioned above, the strip lamps and quartz tungsten–halogen lamps are commonly used in scientific laboratories. Brightness and color temperatures of the former (see below) and spectra of the latter can be measured in metrological laboratories. The radiance spectrum of a tungsten ribbon filament strip lamp can be determined with a high precision. Now, features of the lamps of this kind will be discussed in detail.

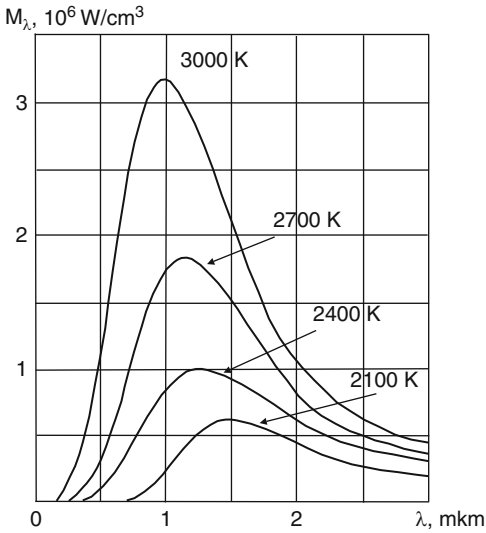

Fig. 2.1 Black body radiation at different temperatures

2.2.1 Planck's Law in Different Units

The measuring system involving *monochromator* and *photodetector* is commonly used for detecting radiation spectra. The *photocurrent* of the photodetector is directly proportional to the photon flux incident on the *photocathode*, but not to the energy flux. In turn, the photon flux is proportional to the *entrance slit* width of the monochromator. The slit width can be expressed in terms of wavelengths. Therefore, the *Planck's curve* should be expressed in suitable spectral units, in wavelengths in this case. Generally, in metrological laboratories, photodetectors are calibrated in energetic units. Finally, sometimes a wavenumber, instead of wavelength, is exploited to calibrate spectral devices. The Planck's law expressed in different units is treated below (see [1–3]).

The spectral radiance, i.e., the energy per unit time, per unit solid angle, per unit surface area, and per unit wavelength interval is expressed to be as follows:

$$L_{\mathrm{e}}^{0}(\lambda, T) = 2\pi hc^2\lambda^{-5}\left[\exp(hc/k\lambda T) - 1\right]^{-1}, \tag{2.3}$$

its physical dimension is W/(sr m^3).

The spectral photon radiance in photonic units, i.e., as the number of photons per unit time, per unit solid angle, per unit surface area, and per unit wavelength interval is given by the formula:

$$L_{hv}^{0}(\lambda, T) = 2\pi c\lambda^{-4}\left[\exp(hc/k\lambda T) - 1\right]^{-1}, \tag{2.4}$$

it is expressed in photon/(s sr m^3).

The energy per unit time, per unit solid angle, per unit surface area, and per unit frequency is as follows:

$$L_{\mathrm{e}}^{0}(v, T) = \frac{2\pi h}{c^2}v^3\left[\exp(hv/kT) - 1\right]^{-1}, \tag{2.5}$$

its physical dimension is W/(sr m^2 Hz).

The photon flux per unit time, per unit solid angle, per unit surface area and per unit frequency is found to be as follows:

$$L_{hv}^{0}(v, T) = \frac{2\pi}{c^2}v^2\left[\exp(hv/kT) - 1\right]^{-1}, \tag{2.6}$$

its unit is photon/(s sr m^2 Hz).

The energy per unit time, per solid angle, per unit surface area, and per unit wavenumber is expressed to be as follows:

$$L_{\mathrm{e}}^{0}(\tilde{v}, T) = 2\pi hc^2\tilde{v}^3\left[\exp(hc\tilde{v}/kT) - 1\right]^{-1}, \tag{2.7}$$

its physical dimension is W/(sr m).

The photon flux per unit time, per solid angle, per unit surface area, and per unit wavenumber is found to be as follows:

$$L_{hv}^{0}(\tilde{v}, T) = 2\pi c\tilde{v}^{2}\left(\mathrm{e}^{hc\tilde{v}/kT} - 1\right)^{-1}, \tag{2.8}$$

it is expressed in photon/(s sr m).

When providing calibration in some *arbitrary* units, the Planck's law should be also expressed in terms of the arbitrary units. It will be noted that the expression in brackets has no physical dimension, whereas the factor with variables λ, v, $\tilde{v}$ has its exponent running from -2 to -5.

2.2.2 Radiation from True Bodies

In fact, thermal radiation is subject to the *Kirchhoff's law* [4], which states that at *thermal equilibrium*, the *absorptivity* (*absorptance*) of a body (or surface) $\alpha(\lambda, T)$ equals its *emissivity* $\varepsilon(\lambda, T)$ for the given wavelength λ and temperature T:

$$\alpha(\lambda, T) = \varepsilon(\lambda, T). \tag{2.9}$$

Here,

- Absorptance is ratio of radiant power absorbed to radiant power incident on the body surface
- Emissivity is ratio of radiant power emitted by emitted area of the body to radiant power emitted by a *black body* area

It follows from (2.9) that:

- With a black body the absorptance is equal to unity for every wavelength and temperature.
- For a given temperature and wavelength, the emissivity of a true luminous body is always less than that of the black body, because the $\varepsilon(\lambda, T) = \alpha(\lambda, T)$ is less than unity for every true luminous body.

In the practically important case, where $\alpha(\lambda, T) = \text{const}$ and $\alpha(\lambda, T) < 1$, the thermal emissivity of such a surface always obeys the condition: $\varepsilon(\lambda, T) \leq 1$. The surfaces having such features are called *gray surface*, in turn, the body is called *gray body*. A metal surface heated to a high temperature can show features of gray body. In the event, where $\alpha(\lambda, T) = f(\lambda)$, the emitting surface is called a *selective radiator*. All radiating surfaces are selective in a wide spectrum range. In the event of a flat radiating surface, i.e., in the absence of multiple reflections, for the given temperature and for every surface material the *absorptance* and *emissivity* can be found experimentally. The obtained data can be applied for every material used in radiator fabrication. In fact, obtained data of absorptance and emissivity of tungsten are most essential (see Table 2.1), because tungsten is commonly used for production of incandescent lamps (Fig. 2.2).

Table 2.1 The emissivity of well-defined tungsten ribbon as a function of wavelength at different temperatures, T varies from 1,800 to 2,800 K [3, 5]

	T (K)					
λ (nm)	1,800	2,000	2,200	2,400	2,600	2,800
230	0.382	0.375	0.368	0.362	0.356	0.348
250	0.442	0.435	0.429	0.424	0.418	0.411
275	0.471	0.466	0.461	0.455	0.450	0.445
300	0.477	0.474	0.471	0.468	0.465	0.456
325	0.477	0.474	0.471	0.468	0.465	0.457
350	0.476	0.473	0.470	0.467	0.464	0.461
375	0.475	0.472	0.469	0.466	0.463	0.463
400	0.473	0.470	0.467	0.464	0.461	0.461
425	0.472	0.468	0.465	0.462	0.458	0.458
450	0.469	0.466	0.462	0.459	0.456	0.454
475	0.466	0.462	0.459	0.455	0.452	0.450
500	0.462	0.459	0.455	0.450	0.447	0.448
525	0.458	0.454	0.450	0.446	0.442	0.446
550	0.454	0.450	0.445	0.441	0.436	0.443
575	0.450	0.445	0.441	0.436	0.431	0.439
600	0.446	0.441	0.436	0.431	0.426	0.434
625	0.443	0.438	0.433	0.428	0.423	0.431
650	0.439	0.434	0.429	0.424	0.419	0.427
656	0.438	0.433	0.428	0.423	0.418	0.426
675	0.435	0.430	0.425	0.420	0.415	0.424
700	0.431	0.426	0.421	0.416	0.411	0.419
725	0.427	0.422	0.417	0.412	0.406	0.415
750	0.422	0.418	0.412	0.407	0.402	0.410
800	0.413	0.408	0.404	0.399	0.394	0.400
850	0.404	0.399	0.394	0.390	0.385	0.391
900	0.394	0.390	0.385	0.381	0.376	0.383
950	0.384	0.380	0.376	0.372	0.368	0.375
1,000	0.375	0.371	0.367	0.364	0.360	0.367
1,100	0.356	0.353	0.350	0.347	0.344	0.352
1,200	0.337	0.336	0.334	0.333	0.331	0.337
1,208	0.322	0.322	0.322	0.322	0.322	0.327
1,300	0;318	0.318	0.319	0.319	0.319	0.325
1,400	0.299	0.301	0.302	0.304	0.305	0.313
1,500	0.283	0.285	0.287	0.290	0.292	0.302
1,600	0.268	0.271	0 2?4	0.277	0.280	0.292
1,700	0 253	0.25?	0.262	0.266	0.270	0.283
1,800	0.239	0.245	0.251	0.256	0.262	0.275
1,900	0.226	0.233	0.240	0.247	0.255	0.267
2,000	0.213	0.222	0.231	0.239	0.248	0.259
2,100	0.202	0.212	0.222	0.232	0.242	0.252
2,200	0.192	0.203	0.214	0.225	0.236	0.245
2,300	0.184	0.195	0.207	0.218	0.229	0.239
2,400	0.177	0.188	0.200	0.212	0.223	0.233

(continued)

Table 2.1 (continued)

	T (K)					
λ (nm)	1,800	2,000	2,200	2,400	2,600	2,800
2,500	0.170	0.182	0.194	0.205	0.217	0.229
2,600	0.164	0.176	0.187	0.199	0.211	0.224
2,700	0.158	0.170	0.182	0.193	0.205	0.219
2,800	0.154	0.165	0.177	0.189	0.200	–
2,900	0.150	0.161	0.172	0.184	0.196	–
3,000	0.146	0.157	0.169	0.180	0.191	–
3,200	0.139	0.150	0.162	0.173	0.184	–
3,400	0.134	0.145	0.156	0.167	0.178	–
3,600	0.129	0.140	0.151	0.162	0.173	–
3,800	0.124	0.135	0.146	0.157	0.168	–
4,000	0.119	0.130	0.141	0.152	0.163	–
4,200	0.115	0.126	0.137	0.148	0.159	–
4,400	0.112	0.123	0.134	0.145	0.155	–
4,600	0.111	0.121	0.131	0.142	0.152	–
4,800	0.109	0.119	0.129	0.139	0.149	–
5,000	0.108	0.117	0.127	0.136	0.146	–

Fig. 2.2 Tungsten ribbon filament strip lamp SIRSH 8.5-200 (MELZ, Russia)

The important point is that the total emission of true bodies involves its own emitted radiation and reflected radiation. In the case of nonflat geometry of radiation source, for example, of spiral shape, then one part of radiation leaves the source after a number of reflections. It is clear that the function $\alpha(\lambda, T)$ determined for a flat surface cannot be applied to that even, a *darkening factor* should be taken into account.

2.2.3 The Brightness and Color Temperatures in Measurements with Strip Lamps

Radiation of heated bodies can be described in terms of the so-called *equivalent temperature*, which is assumed to be the black body temperature. The *brightness temperature* T_b is the temperature at which a black body would have to be to duplicate the observed intensity of the gray body. The *color temperature* T_c of a light source is the temperature of a black body that emits light of comparable hue to that of light source [6, 7]. The brightness and color temperature are most frequently used quantities. It is clear that relationships between the true temperature and equivalent one are dependent on the light source material as well as on its true temperature. Such relationships can be found experimentally that has been done many times. Data of measurements were published in articles and monographs (see Fig. 2.3).

In order to estimate the emission spectrum of a strip lamp it should follow the recommendations given below. For example, the strip lamp calibrated in Russian D.I. Mendeleyev Scientific and Research Institute of Metrology gets the state calibration test certificate from the institute, wherein the dependency of brightness temperature on the lamp current is tabulated at $\lambda = 656$ nm (see Table 2.2).

With choosing a required true temperature, the brightness temperature can be found from Fig. 2.3. Further, a suitable value of the current is calculated from the table attached to the certificate. With required units, see (2.2)–(2.7), and for the given temperature, the blackbody spectrum should be calculated. Finally, the black body intensity should be multiplied by the emissivities of tungsten associated with the given wavelengths (see Table 2.1).

We emphasize that the recommendations above are concerned to strip lamps, whereas the lamps having another shape of their heater element, for example, of spiral shape, will have another emissivity factors. Some special features of calibrating will be discussed in the next chapters of this book. Here, it is worth noting that calibrated strip lamps are lower in cost than that of calibrated quartz tungsten–halogen lamps. The first consideration of using strip lamps at lower temperatures is that they are more long-lived. In other words they should be subject to such expensive procedure as recalibration in a longer period than quartz tungsten–halogen lamps. The author exploited a tungsten ribbon filament lamp several hundreds of hours, which has features similar to those shown in Table 2.2 at temperature 2,700 K (the brightness temperature is equal to 2,152°C). The calibration life as recalibration interval of this lamp class decreases dramatically at high temperatures.

2.2.4 Quartz Tungsten–Halogen Lamps

The maximum accessible temperature of a tungsten lamp depends on the filament evaporation rate. The evaporation causes dusting of the lamp window and

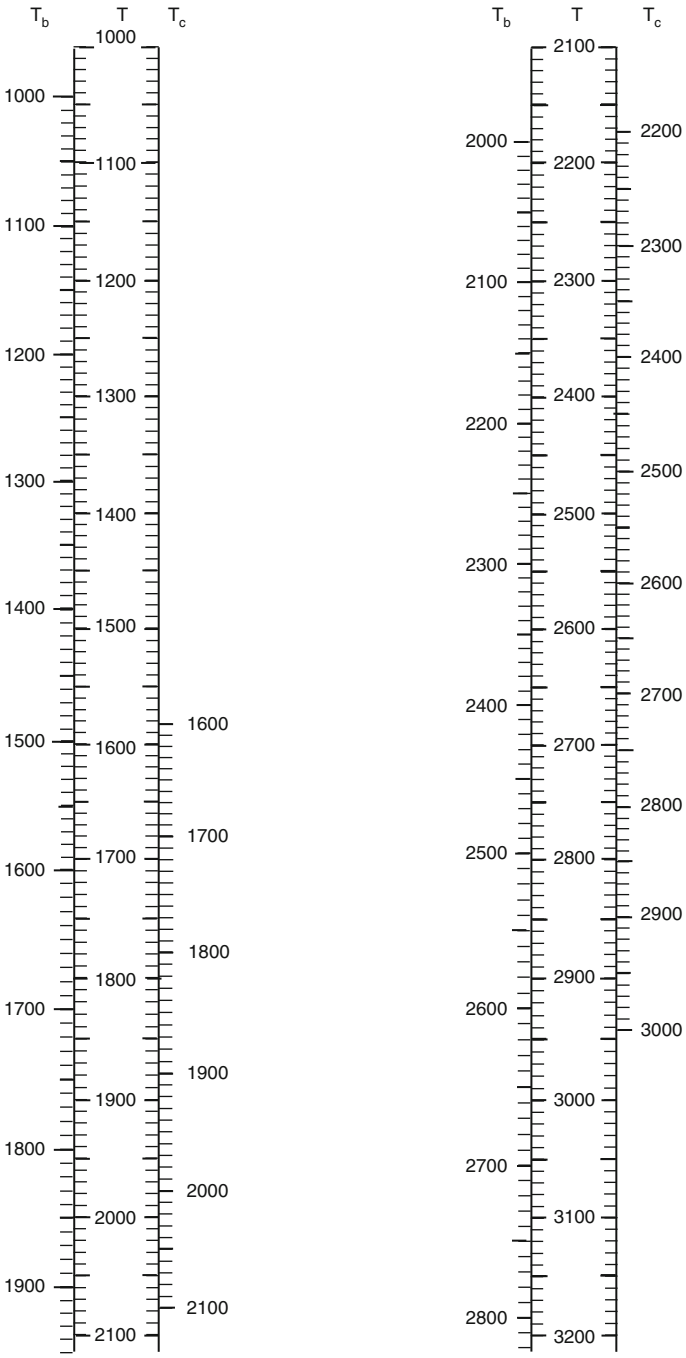

Fig. 2.3 The relationship between the brightness temperature T_b, the true temperature T, and the color temperature T_c in K of a tungsten ribbon lamp [8]

Table 2.2 The brightness temperature as function of the current of a typical SIRSH 8.5-200 tungsten ribbon filament strip lamp

Brightness temperature, t (°C)	1,400	1,500	1,600	1,700	1,800	1,900	2,000	2,100	2,200	2,300
Current (A)	10.76	11.73	12.77	13.88	15.08	16.34	17.68	19.08	20.54	22.04
dI/dt, 10^{-3} A/°C	9.31	10.3	10.76	11.54	12.29	13.01	13.69	14.31	14.84	15.29

Fig. 2.4 The Model 5000-16c 1,000-W FEL lamp [9] (reproduced by permission of Gamma Scientific)

increasing the filament resistance. The addition of halogen such as iodine or bromine to the gas inside the lamp increases the rated life, accessible temperature and light efficiency of the lamp. With high temperature of the lamp bulb, more than 250°C, halogen reacts with atomized tungsten, then resulting product migrate back to the filament, where the very high temperature decomposes it. Bulbs of such lamps are made up of high-quality fused quartz. This results in, among other things, high transmission for the UV radiation. Compared to tungsten strip lamps, the tungsten–halogen lamps (Fig. 2.4) offer the certain advantage due to high temperature. It is because of their high temperature that these lamps make possible to provide calibration up to wavelength 250 nm.

A disadvantage of quartz tungsten–halogen lamps is that there is no way to calculate the emission spectrum, because the lamps have nonstrip shape of their heating element, and there are multiple reflections inside the filament space. Thus for each lamp, the spectrum should be found through measuring, whereas in the case of strip lamps the brightness temperature should only be found. It is of first importance that the lamps call for frequent and expensive recalibrations (in every 50 working hours for the lamps of 200 and 1,000 W). Therefore, when working

within the range $\lambda \geq 320$ nm, the author prefers tungsten ribbon filament strip lamps to tungsten–halogen ones. When tungsten–halogen lamps are preferred to be used, it is worth to purchase two specimens, where one of them should be seldom used as a standard for comparison with those that are frequently used. It has been mentioned in Chap. 1 that this recommendation concerns to every type of measuring devices. The quartz tungsten–halogen lamps are produced and calibrated by various manufacturers.

When operating with the both lamp types in a short-wavelength spectrum range, there is a high level of scattered radiation. It leads to huge distinctions in intensity, in several orders, at wavelength from $\lambda \approx 250$ nm to $\lambda \approx 550$ nm for the lamps with halogen cycle and from $\lambda \approx 300$ nm to $\lambda \approx 550$ nm for the strip lamps. In the case of the lamp shown in Fig. 2.4, the distinction is about 1,000 times. Therein lies the answer to the storing of that why calibration of detecting systems in the short-wavelength ranges should be based on special techniques. The techniques will be discussed in Sects. 5.3 and 5.4.

2.3 Gas-Discharge Radiation Sources for the UV of $\lambda > 190$ nm

In the short-wavelength range $\lambda \leq 250$ nm at temperature $T \leq 2{,}900$ K, the weak intensity of black body radiation renders the use of the black body unsuitable for calibration. Otherwise, it would result in serious errors due to the effect of long-wavelength scattered light. Because of this, so-called gas-discharge lamps are the only radiation sources of well-known emission spectra, which are suitable for calibration in the near UV range. The radiation spectrum of the sources can be found, in one way or another, for example, by means of standards based on synchrotron radiation.

Stability of both the spectrum emission and radiating energy is the required feature of any light source. In the case of the gas-discharge lamps, the stability is dictated by *constancy of gas composition* and transparency of the lamp bulb window. By now a wide variety of different light sources of linear and continuous spectrum in the UV and VUV spectral ranges were designed to be applied, in particular, to photochemical research. However, there are available sources of continuous spectrum, which can be used as working facilities for the spectral sensitivity calibration of detection systems. The absolute intensity from such light sources as high-pressure mercury and xenon lamps is very unstable, due to the bulb transparency decreasing in operation. Generally, this disadvantage is characteristic of all the powerful lamps.

At the present time, the gas-discharged deuterium lamps with pressure of a few torrs are the most-used as working standards for spectrum reproduction in the near UV region (Figs. 2.5 and 2.6). The lamps of this kind are produced by various manufacturers [10–14]. The lamps filled with mixtures of deuterium and inert gases, most often with neon, were previously used extensively. Neon was added to bring down the discharge initiation voltage, because with neon Penning ionization occurs, and the electron–ion recombination cross section of neon is far less than

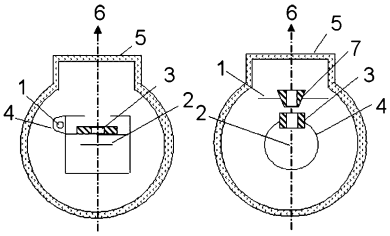

Fig. 2.5 Two representative designs of deuterium lamps in cross sections normal to bulb axis: asymmetric design (the left-hand side); symmetric design (the right-hand side): *1* – cathode, *2* – anode, *3* – discharge pipe, *4* – screen cylinder, *5* – window, *6* – output direction, *7* – anode concentrator [15]

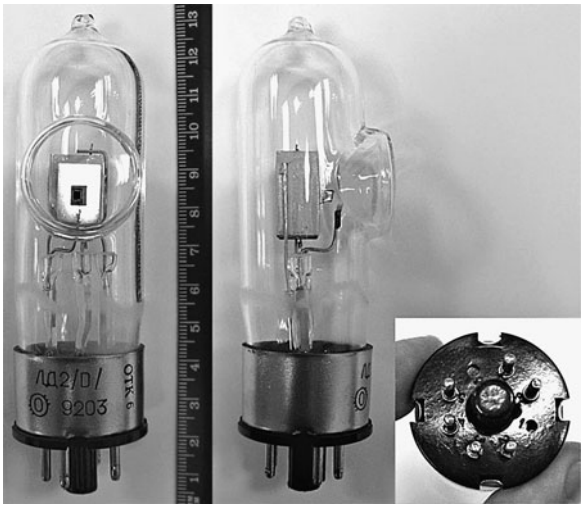

Fig. 2.6 The LD2 (D) deuterium lamp gas-discharge lamp (Russia)

that for hydrogen. Consequently, the concentration of charge particles is higher. Nowadays, deuterium has virtually supplanted hydrogen at all, because of its radiating intensity in the near IR range is 30% greater than that in the event of hydrogen, but in the VUV range it is 10–15% less than that for hydrogen. The operating voltage of such lamps is about 50–80 V, and its current running from 0.3 to 7 A, depending on the lamp power. In his practice, the author tries to avoid extreme operating regimes, which take place at the maximum and minimum permissible value of the lamp current. Operation at a moderate current of the lamp provides more prolonged recalibration period. The discharge initiation voltage of the lamps is found to be between 300 and 500 V, the lamps have falling current–voltage characteristic as of any low pressure discharge process; the lamps are then inoperable without a powerful ballast resistance.

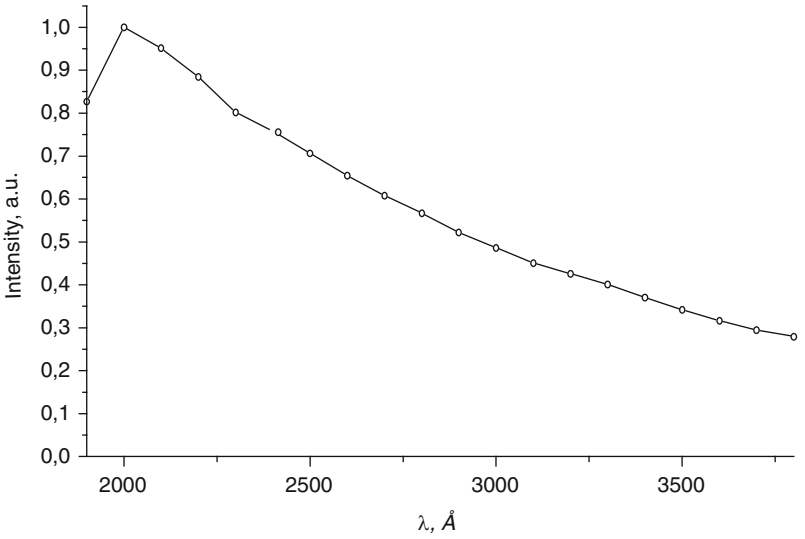

Fig. 2.7 The emission spectrum of the DDS-30 lamp (Russia)

The emission spectrum of the hydrogen and deuterium lamps in the near UV region is a well-known hydrogen continuum $\lambda \geq 380$ nm [16, 17] with the short-wave cutoff due to absorption by the window material (Figs. 2.6 and 2.7). A large body of research has shown the spectrum to be approximately unchanged in a wide range of the lamp current. Hence, if no original transparency of the lamp window loses due to evaporation of the electrodes material and no changes in gas composition occur, one can be sure that the spectrum of the lamp will be unchangeable too. Unfortunately, the lamp windows deteriorate and the gas composition undergoes changes, if for no other reasons than gas emission by internal components of the lamp and decreasing of the deuterium concentration. The lamp intensity decreases and the radiation spectrum changes over time due to several reasons. The internal metal components and coating evaporate, the filament coating material reacts with the window, and the window shadows the lamp output and changes its spectrum due to intense radiation. Therefore, the lamps have need for regular verification, even through the lamps did not used yet. Each lamp, which is scheduled for operation in metrological purposes, should be aged before its calibration procedure, i.e., it should work for 30–80 h in its design mode. It would be a good thing to keep track of the radiation intensity for at least one spectral interval. The lamp will serve for a long time in the event that the observed intensity is virtually unchanged, for example, the relative intensity variations are less than 0.1% for 1 h. Thus this lamp can be calibrated. The calibration life or recalibration interval for deuterium lamps depends on their design, and on external environment. Generally, manufacturers specify 50 operation hours as the calibration life for such lamps. This is not a long period, provided that the preheating period is between 20 and 40 min. In addition, the lamps are assumed to have need for annual recalibration, even though a lamp was not in use.

The anode of the lamp has a small hole, as usual, of diameter 1 mm, which is essentially as the radiation source. Such a design of radiating element of the lamps is generally dictated by that synchrotron radiation is used as a primary standard for calibration. It is assumed synchrotron radiation to be emitted by a point source (see Sect. 2.5). In turn, the small radiating area or "point source" of the lamp is suitable for some applications, and is not well for the other ones. These aspects will be discussed in the next sections in detail.

Ocean Optics [10] and Hamamatsu manufacturer [13] produces xenon lamps of low power 150 W with a quasi-continuous spectrum calibrated in the range 200–800 nm. The recalibration interval of xenon lamps as well as deuterium lamps is assumed to be about 100 h.

2.4 Gas-Discharge Radiation Sources for Vacuum UV of $\lambda > 115$ nm

The operation and basic design of the deuterium lamps used in the VUV range are similar to that have been described in the previous section in detail. The main distinction is the output windows, which usually have plates made up of magnesium fluoride, MgF_2. Second, it is a need to use the vacuum-close joining for the lamp and spectral device [16] (in the so-called vacuum monochromator [17]) (Fig. 2.8).

In the short-wave range, the spectrum of these lamps consists of overlapped lines and bands of atomic and molecular deuterium (Fig. 2.9). Spectra of these lamps were measured many times by using different methods including comparison with synchrotron radiation spectra (see [18–21] and references). Repeatability of the spectra measured in [18] λ = 165–300 нм spectral range are 8–20% depending on wavelength.

The radiation sources of this type are also assumed to be quasi-point sources, since their emitting areas have diameter about 1 mm. Synchrotron radiation is asserted to be a primary standard for these lamps too. It may be assumed that the recalibration interval for the lamps intended in the vacuum UV range is to be less

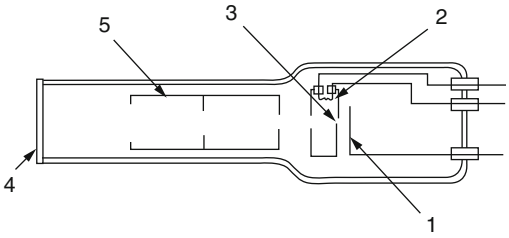

Fig. 2.8 The typical design of deuterium lamps in the vacuum UV range [16]: *1* – anode, *2* – cathode, *3* – emitting area, *4* – MgF_2 window, *5* – antireflection baffles (reproduced by permission of Measurements Science and Technologies, IOP Publishing Ltd)

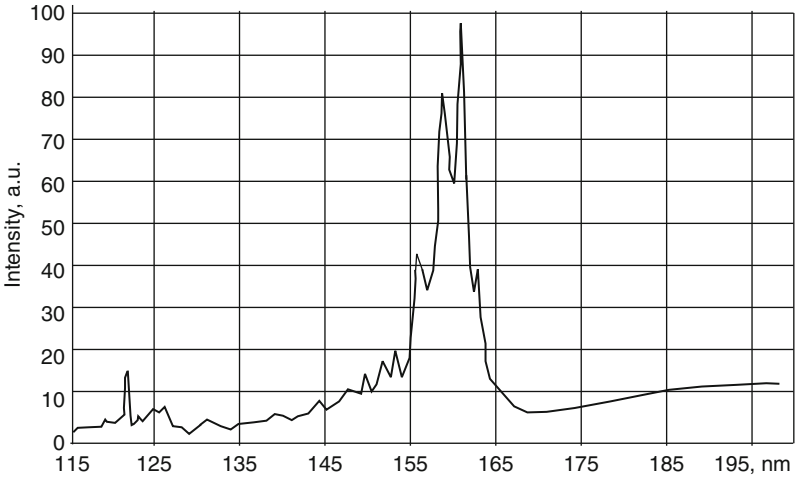

Fig. 2.9 The spectrum of the deuterium lamp of model 632 from McPherson [18] (reproduced by permission of McPherson, Inc.)

than that in the event of the UV range lamps. The first reason is that the so-called F-centers are generated in the fluorite windows, $\lambda \leq 300$ nm, under action of incident radiation of wavelength [19].

2.5 Synchrotron Radiation

Synchrotron radiation (SR) is electromagnetic radiation generated by accelerated charged particle moving near the light velocity through a magnetic field. This may be achieved in the synchrotrons or storage rings. Such artificially produced radiation may range from the IR range to X-rays [20].

Synchrotron radiation is used as an absolute radiation standard, since its characteristics are calculable by the Schwinger equation [21]. In the UV and shorter wavelength, synchrotron radiation emitted from a storage ring has the lowest (about 0.04% [22]) uncertainty in calculable irradiance among all known radiation standards to date. Synchrotron radiation as a primary irradiance standard for a broad spectral range from X-rays to infrared has since been established at several synchrotron facilities around the world in USA, Great Britain, Japan, and Germany (see [22–24] and references).

The characteristics of synchrotron radiation can be accurately determined based on Schwinger's equation, which expresses the radiant power at the wavelength λ, i.e., photon energy emitted from a single relativistic electron with electron energy E deflected in a homogeneous magnetic field of magnetic induction B. The spectral radiant power (see Table 1.1) of synchrotron radiation through an aperture

of size $a \times b$ at distance d, thus, may be calculated and expressed in the general form as follows:

$$\Phi_{\mathrm{SR}}(\lambda, E_{\mathrm{e}}, B, I, \Sigma_y, \Psi, d, a, b), \tag{2.10}$$

where I is the electron beam current, Σ_y is the effective vertical source size, and Ψ is the observer's angle above or below the orbital plane defined by the centre of the aperture. The effective vertical source size is derived from the vertical electron beam size σ_y and beam divergence $\sigma_{y'}$ according to [21]:

$$\Sigma_y = \left(\sigma_y^2 + \mathrm{d}^2\sigma_{y'}^2\right)^{1/2}. \tag{2.11}$$

The spectral radiant power emitted by a relativistic charge e into a solid angle $\mathrm{d}\Omega$ at a wavelength interval of $\mathrm{d}\lambda$ can be written as follows [23, 24]:

$$\frac{\mathrm{d}^2\Phi_{\mathrm{SR}}(\lambda, \Omega)}{\mathrm{d}\lambda \mathrm{d}\Omega} = \frac{27e^2}{32\pi^3\rho^2}\left(\frac{\lambda_{\mathrm{c}}}{\lambda}\right)^4 \gamma^8\left(1+\gamma^2\Psi^2\right)^2\left[K_{2/3}^2(z) + \frac{\gamma^2\Psi^2}{1+\gamma^2\Psi^2}K_{1/3}^2(z)\right], \tag{2.12}$$

$$P_0(\lambda, E, R, \Psi) = \frac{27e^2c}{32\pi^3R^3}\left(\frac{\lambda_{\mathrm{c}}}{\lambda}\right)^4 \gamma^8\left[1+(\gamma\Psi)^2\right]^2 K_{3/2}^2(\xi) + \frac{(\gamma\xi)^2}{1+(\gamma\xi)^2}K_{1/3}^2(\xi), \tag{2.13}$$

where ρ is the radius of curvature of the electron's orbit, $K_{2/3}^2(z)$ and $K_{2/3}^2(z)$ are modified Bessel functions, and λ_{c} is the critical wavelength defined as follows:

$$\lambda_{\mathrm{c}} = 4\pi\rho/3\gamma^3,\ \gamma = E_{\mathrm{e}}/m_{\mathrm{e}}c^2, \tag{2.14}$$

where m_{e} is the rest mass of the electron, and c is the light velocity, $m_{\mathrm{e}}c^2 = 0.511$ MeV. The two modified Bessel functions at the right-hand side of (2.12) represent the contributions from horizontal and vertical polarizations, respectively. At $\Psi = 0$, the term for vertical polarization vanishes, and the radiation is linearly polarized in the horizontal direction. In addition, there are the following definitions:

$$K_{2/3}^2(\xi),\ K_{1/2}^2(\xi) \tag{2.15}$$

are the McDonald functions, and

$$z = \frac{\lambda_{\mathrm{c}}}{2\lambda}\left[1 + (\gamma\Psi)^2\right]^{3/2}. \tag{2.16}$$

Synchrotron radiation propagates within a narrow cone localized close to the tangent to the orbit; the radiation is polarized, its polarization can be calculated. The maximum is positioned at the following wavelength:

$$\lambda_{\max} = 0.42\lambda_{\mathrm{c}}, \tag{2.17}$$

Table 2.3 List of PTB beamlines concerning this book at BESSY II, typical applications and photon energy ranges (see [22])

N in Fig. 2.7	Beamline (application)	Photon energy
3a	Undispersed bending magnet radiation (calibration of energy dispersive detector systems)	6 eV to 50 keV
3b	Normal-incidence spectrometer (source calibration)	3–35 eV

Table 2.4 List of MLS beamlines concerning this book, typical applications and wavelength ranges (see [22])

N in Fig. 2.8	Beamline (application)	Wavelengths	Status
1d	UV/VUV monochromator for undulator radiation	4–400 nm	Operational in 2011
2a operational	White-light bending magnet radiation (use of calculable SR)		Operational
2b	UV/VUV spectrometer (source calibration)	7–400 nm	Operational in 2010
4	UV/VUV monochromator (detector calibration, reflectometry)	40–400 nm	Operational
5	THz beamline	0.6 µm to 8 mm	Operational
6	IR beamline	0.6 µm to 8 mm	Operational

which depends upon the electron energy and the radius of curvature of the electron orbit. For the given parameters of the accelerator or storage unit listed above and electron beam density, absolute intensity of spectral lines and polarization in the given direction can be calculated.

Some metrological facilities of synchrotron radiation laboratories, namely, the Physikalisch-Technische Bundesanstalt (PTB) electron storage ring *BESSY II* and *Metrology Light Source* (MLS) are described in Ref. [22]. At the *BESSY II* and MLS the activities have been extended to a broad range of fundamental and applied photon metrology in the range from the far infrared to hard X-rays, including methods like cryogenic radiometry, reflectometry, and X-ray fluorescence spectroscopy. Some applications of the PTB beamlines concerning this book are given in Tables 2.3 and 2.4.

Calculated spectral radiant power of blackbody, MLS and BESSY II radiation sources are shown in Fig. 2.10.

2.5.1 Calibration of Radiation Sources

Radiation sources are calibrated as secondary standards by comparison with the SR primary standard. For this purpose, the radiation of the sources is spectrally dispersed and detected by means of a movable monochromator–detector system that is alternately exposed under analogous conditions as shown in Fig. 2.11.

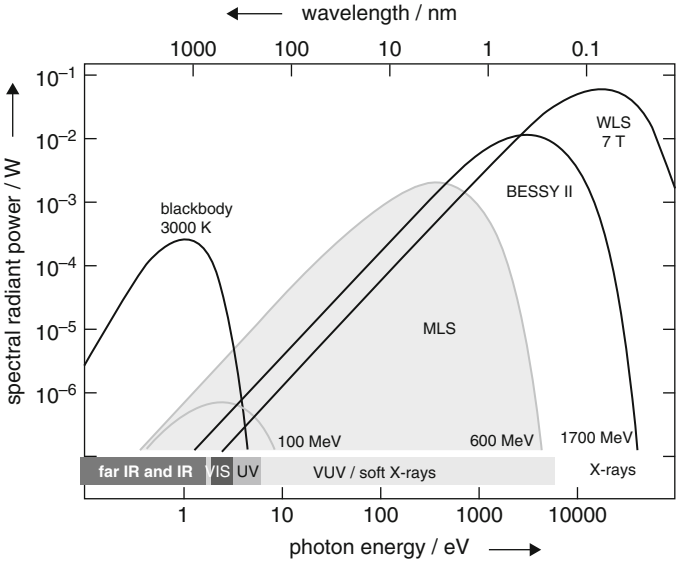

Fig. 2.10 Calculated radiant power of radiation sources into a spectral bandpass of 1% of the photon energy or wavelength and through the aperture of 10 mm radius: blackbody radiator ($T = 3{,}000$ K), MLS (the electron energy 100 and 600 MeV), and BESSY II [the electron energy 1.7 GeV; the bending magnetic field 1.3 and 7 T (WLS)] (see [22] for details) [reproduced by permission of Physica Status Solidi (B)]

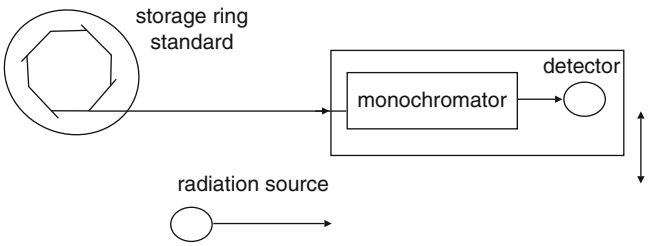

Fig. 2.11 Calibration of radiation sources using the electron storage ring as a primary radiation source standard [22] [reproduced by permission of Physica Status Solidi (B)]

PTB's source calibration capabilities based on calculable SR currently cover the UV and VUV wavelength range from 400 to 40 nm at BESSY II (beamline 3b in Table 2.3) and will be extended down to 7 nm at the MLS (beamline 2b in Table 2.4). The calibration refers to the measurement of spectral radiant intensity $J_e(\lambda)$ and spectral radiance $L_e(\lambda)$ (see Table 1.1) of quasi-point sources with a source area in the order of 1 mm^2.

$$J_e(\lambda) = \Phi_e(\lambda)/\Delta\Omega \text{ and } L_e(\lambda) = \Phi_e(\lambda)/\Delta\Omega\Delta A. \tag{2.18}$$

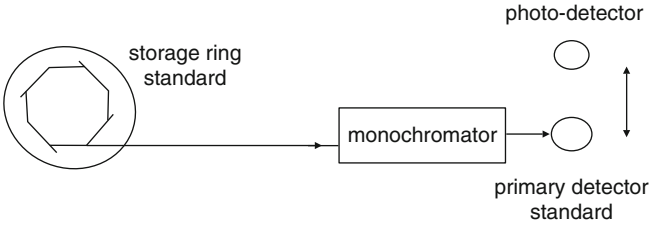

Fig. 2.12 Photodetector calibration by the use of a primary detector standard [22] [reproduced by permission of Physica Status Solidi (B)]

In both cases, the spectral radiant power $\Phi_e(\lambda)$ of the source is obtained by comparing with the calculable SR. The solid acceptance angle $\Delta\Omega$ is defined through an aperture of well-known size and position with respect to the point source. In addition, the accepted part ΔA of the source area is confined and defined by the monochromator entrance aperture which is located in the image plane of the premirror being part of the beamline. In the case of radiant intensity calibrations and SR measurements, the entrance aperture is to be larger than the image of the source.

With deuterium lamps as secondary source standards in the UV and vacuum UV spectral range $\lambda \approx 115$–400 nm, relative calibration standard uncertainties for spectral radiance are as follows: 5, 18, 5, 3.5 and 2.5% in the spectral ranges $\lambda = 115$–120.5, 120.5–122.5, 122.5–165, 165–175 and 175–400 nm, respectively.

2.5.2 Calibration of Photodetectors

In cases where dispersed radiation is required to perform calibrations, the calculability of SR with its broad continuous spectrum cannot be applied. Here, the radiant power of spectrally dispersed SR behind a monochromator is measured in absolute terms by means of a primary detector standard. This allows the output signal of any kind of photodetection system to be calibrated by comparison as shown in Fig. 2.12.

Since the beginning of the 1980s, electrically calibrated substitution radiometers (ESRs) operated at cryogenic temperatures have been used as primary detector standards, initially used for optical radiation only.

These radiometers are thermal detectors based on the equivalence of electrical and radiant heating of a cavity absorber. They are based on the use of a cavity absorber at nearly liquid helium temperature (see [25, 26]).

Problems

1. Based on formulae Sect. 1.2 and formula (2.3), derive the formulae from (2.4) to (2.8).
2. For the given brightness temperature 2,147°C calculate the emission spectrum of a tungsten ribbon filament strip lamp in photon units, in photon/(s sr m^2 nm)

units, at the wavelength interval 5 nm and interval 300–1,000 nm. Estimate the ratio of intensities at $\lambda = 320$ nm and $\lambda = 600$ nm.

3. A radiation source was calibrated in terms of W/(m^2 m sr). Convert the calibration to another units: photon/(s sr m^2 nm).

References

1. Planck's law. http://en.wikipedia.org/wiki/Planck's_law
2. Grum, G., Becherer, R.J.: Radiometry. In: Grum, F. (ed.) Optical Radiation Measurements, A Treatise, vol. 4. Academic, New York (1979)
3. Epshtein, M.I.: Izmereniya Opticheskogo Izlucheniya v Elektronike (Measurements of Optical Radiations in Electronics). Energoatomizdat, Moscow (1990)
4. Kirchhoff's law. http://en.wikipedia.org/wiki/Kirchhoff's_law_of_thermal_radiation
5. De Vos, J.: A new determination of the emissivity of tungsten ribbon. Physica **20**, 690–714 (1954)
6. Brightness temperature. http://en.wikipedia.org/wiki/Brightness_temperature
7. Color temperature. http://en.wikipedia.org/wiki/Color_temperature
8. Rutgers, G.A.W., De Vos, J.C.: Relation between brightness temperature, true temperature and color temperature of tungsten. Luminance of tungsten. Physica **20**, 715–720 (1954)
9. 5000 FEL 1000-watt lamp source. http://www.gamma-sci.com/products/5000FEL.html
10. DH-2000-CAL Deuterium Tungsten Halogen Calibration Standard. http://www.oceanoptics.com/Products/dh2000cal.asp
11. Deuterium lamps. http://www.photron.com.au./.assert/deuterium-lamp.pdf
12. Calibrated source lamp, deuterium. http://search.newport.com/?q=*&x2=sku&q2=63945
13. Calibrated Lamp Light Sources Series L7810_L7820. http://sales.hamamatsu.com/assets/pdf/parts. . ./L7810_L7820_TLSO1054E03.pdf
14. Deuterium lamps. http://sales.hamamatsu.com/en/products/electron-tube-division/light-sources/deuterium-lamps.php&src=hp
15. Shishatskaya, L.P.: Spectrophomometrical deuterium-argon lamp DAS-30. Optiko-Mekhanichwskaya Promyshlennost (USSR) **N5**, 41–43 (1986)
16. Key, P.J., Preston, R.C.: Magnesium fluoride windowed deuterium lamps as radiance transfer standards between 115 and 370 nm. J. Phys. E Sci. Instrum. **13**, 866–870 (1980)
17. Zaidel, A.N., Shreider, E.Ya.: Vakuumnaya Spectroskopiya i ee Primenenie (Vacuum Spectroscopy and Its Application). Nauka, Moscow (1976) (in Russian) [see also Zaidel, A.N., Shreider, E.Ya.: Vacuum Ultraviolet Spectroscopy. Ann Arbor-Humphrey Publishers, Ann Arbor (1970)].
18. Model 632 Deuterium Light Source with Magnesium Fluoride Window for 115 to 380-nm. http://www.mcphersoninc.com/lightsources/model632lightsource.htm
19. Shishatskaya, L.P., Lisitsyn, V.M.: On methods of deleting of radiation-induced coloration of the hydrogen lamp windows. Optiko-Mekhanicheskaya Promyshlennost (USSR) **N8**, 53–55 (1978)
20. Synchrotron radiation. http://en.wikipedia.org/wiki/Synchrotron_radiation
21. Schwinger, J.: On the classical radiation of accelerated electrons. Phys. Rev. **75**, 1912–1925 (1949)
22. Beckhoff, B., Gottwald, A., Klein, R., Krumrey, M., Muller, R., Richter, M., Scholze, F., Thornagel, R., Ulm, G.: A quarter-century of metrology using synchrotron radiation by PTB in Berlin. Review article. Phys. Status Solidi B **246**, 1415–1434 (2009)
23. Jackson, J.D.: Classical Electrodynamics, Chapter 4, 2nd edn. Wiley, New York (1975)

24. Shaw, P.-S., Arp, U., Saunders, R.D., Shin, D.-J., Yoon, H.D., Gibson, C.E., Li, Z., Parr, A.C., Lykke, K.R.: Synchrotron radiation based irradiance calibration from 200 to 400 nm at the synchrotron ultraviolet radiation faculty III. Appl. Opt. **46**, 25–35 (2007)
25. Gentile, T.R., Houston, J.M., Hardis, J.E., Cromer, C.L., Parr, A.C.: National Institute of Standards and Technology high-accuracy cryogenic radiometer. Appl. Opt. **35**, 1056–1068 (1996)
26. Johnson, B.C., Steven, W., Brown, S.-W., Lykke, K.R., Gibson, C.E., Fargio, G., Meister, G., Hooker, S.B., Markham, B., Butler, J.J.: Comparison of cryogenic radiometry and thermal radiometry calibrations at NIST using multichannel filter radiometers. Metrologia **40**, S216–S219 (2003)

Chapter 3
Photodetectors in Radiometric Applications

Abstract Photodetectors are classed here and treated together with their operational features. Various types of thermal detectors are briefly examined. Photoemissive detectors such as vacuum phototubes and photomultipliers are discussed in detail. Then CCD cameras, photodetectors with the internal photoeffect, luminescence quantum counters, and photoionization chambers are briefly discussed. The basic principles and advantages of well-established actinometers as chemical photodetectors are shown here. Much attention is given to gas-phase actinometers operating in the visible, UV, and especially in the vacuum UV spectral range.

3.1 Classification of Photodetectors

Photodetectors as detectors of electromagnetic radiation are conventionally classified to be *physical* and *chemical*, as well as *selective* and *nonselective*. In literature photodetector is commonly meant only as a physical device for detecting radiation. Photodetectors of other types are treated in their own way, among which are detectors, actinometers, and luminophors based on chemical reactions or photoluminescence as a base for radiation–response conversion (see e.g., [1, 2]). Throughout this book, any device, which makes it possible to measure the facilities of electromagnetic radiation listed in Table 1.1, will be called the photodetector. The photodetecting effects of biological nature, such as the eye, skin, and other, will not be discussed in this book. The grading above is rather conventional, if for no other reason than the photodetector making use of a light-induced chemical change is a primary transformer, and the measuring of its photoresponse is usually provided by means of a physical technique. We shall see subsequently, the grading by selectivity is also conventional, because any absolute nonselective photodetectors are not available. Furthermore, the photodetector is often said to be nonselective when its photoresponse is directly proportional to radiometric or photometric quantities, not photonic ones. Nevertheless, such a photodetector is selective with respect to the latter.

A.M. Pravilov, *Radiometry in Modern Scientific Experiments*,
DOI 10.1007/978-3-7091-0104-9_3,

The physical and chemical photodetectors are classified as follows.

In *thermal detectors*, the primary effect is temperature increase caused by absorbed radiation. There are different secondary effects which cause the temperature increase to produce outputs. In *junction* devices, the temperature increase generates a voltage at the junction of two dissimilar materials. *Electrical substitution radiometers* (ESRs), including *cryogenic* ones, have thermal detectors and are based on the electrical substitution principle. The *bulk detectors* are detectors where the essential process occurs in a homogenous material. *In pneumatic photodetectors, so-called Golay detectors,* the increase in black surface leads to boost pressure of gas filling a cell. The black surface is found in one side of the cell, and the other side is a membrane. Membrane deformation can be recorded, for example, by virtue of reflection of light beam from the membrane. *Bolometer and thermistor* are both thermal detectors of radiation. The heating of the device body due to absorption of incident radiation gives rise to a change in electrical resistance. *Pyroelectric detectors* utilize the temperature variations of spontaneous polarization of certain dielectric materials.

Detector based on *photoemissive*, *photoconductive,* or *photovoltaic* effects, all belong to one class of *quantum detectors*, since every detector of the class involves direct quantum interactions between photons and matter. *Photoemissive detectors* are based on the *external photoeffect*, whereas in *photodetectors with internal photoeffect* absorbed photons generate charge carriers. In luminescence quantum counters, absorbed radiation leads to luminescence, intensity of which can be detected, for example, by a *phototubes* or *photomultiplier tubes (PMTs)*. In detector based on the *photoionization,* a so-called *photoionization chamber*, absorption of radiation provides generation of electron–ion pairs. Thus, electrical current formed by the charged particles is measured by virtue of two electrodes. Photochemical effect is used in chemical *actinometers*.

All the detectors listed above are discussed in this chapter. Now we will briefly discuss operational features of photodetectors.

3.2 Operational Features of Photodetectors

3.2.1 Photodetector Responsivity

For the given *input X* and o*utput Y* of a photodetector, its responsivity or sensitivity is specified to be as follows:

$$S = Y/X. \tag{3.1}$$

When X is represented in terms of radiation quantities, e.g., as radiant power of flux Φ_e [W], the term *radiant responsivity* S_e is used. X stands for photometric units, e.g., as luminous flux Φ_v [lm], it is commonly used term *luminous responsivity* S_v.

In the visible range, to estimate the luminous responsivity of a photodetector or photomultiplier, strip lamps are used whose color temperature is $T_c = 2,870$ K (see Sects. 2.1.3 and 3.2.3). The term *photon responsivity* is used for X, provided that this quantity is measured in photonic units, e.g., as photon flux $\Phi_{h\nu}$.

The input can be a monochromatic or polychromatic radiation (see Sect. 1.1). Therefore, in the event of monochromatic radiation the responsivity can be applied for the input within a narrow spectral interval, whereas in the case of polychromatic radiation the responsivity is to be calculated over a wide spectral interval. The responsivity in (3.1) is assumed to be of invariable quantity, which is independent of the input. Thereby the detector is assumed to be linear:

$$S = Y/X = \text{const.} \tag{3.2}$$

The detectors showing constant responsivity are termed *linear*. It is evident that such detectors are more preferable in photometric applications. It is also evident that the linearity property is to be true only within narrow limits of the input. The lower limit is the limiting value of the input, which can be detected by the detector, and which is referred to as *detectivity* (see Sect. 3.2.6). The upper limit is caused by the maximum output. If the output is more than the maximum output, the detector will show nonlinear behavior or be damaged. The sensitivity of a nonlinear detector is subject to the following relationship:

$$S = Y/X = f(X). \tag{3.3}$$

For the given input value X the sensitivity is calculated in the form of derivative:

$$S = \mathrm{d}Y/\mathrm{d}X. \tag{3.4}$$

3.2.2 Spectral Responsivity

The *spectral resposivity* $S(\lambda)$ is the ratio of the output $Y(\lambda)$ to the input $X(\lambda)$, with both quantity depending on the wavelength λ:

$$S(\lambda) = Y(\lambda)/X(\lambda), \tag{3.5}$$

where the spectral input $X(\lambda)$ assumed to be found within infinitesimal wavelength interval $\mathrm{d}\lambda$.

A so-called *spectral responsivity function* is the spectral sensitivity curve against wavelength or wavenumber, or photon energy. Its shape is virtually dependent on the detector type and units taken as the spectral coordinates. For a given spectral respositivity, the relationship between the spectral input and spectral output has an integral form as follows:

$$Y = \int_0^\infty X(\lambda)S(\lambda)\mathrm{d}\lambda, \tag{3.6}$$

where $S(\lambda)$ is the spectral responsivity as a function of wavelength.

3.2.2.1 Thermal Detectors

In the case of black or nonselective thermal detectors, the spectral responsivity function $S_e(\lambda)$, which can be written as follows:

$$S_e(\lambda) = Y(\lambda)/\Phi_e(\lambda) \tag{3.7}$$

remains constant over a certain wavelength interval. Here the quantity $S_e(\lambda)$ is expressed in terms of the following units: V nm/W. For a given value of $S_e(\lambda)$, the relationship between the spectral radiant power $\Phi_e(\lambda)$ and its output takes an integral form:

$$V = \int_0^\infty \Phi_e(\lambda)S_e(\lambda)\mathrm{d}\lambda. \tag{3.8}$$

and the output is the voltage V as an example.

3.2.2.2 Quantum Efficiency

The detector responsivity with respect to photon or quantum input is called the *quantum efficiency*. Usually, quantum efficiency is defined as the ratio of elementary events contributing to the detector output to the number of incident photons. There are two basic types of elementary events, namely, which happen on either electron emission from the photocathode or electron–hole pair generation in the detector body based on the internal photoeffect [1] (see Table 3.1). With photoemissive detectors, the output is the electrical current as the number of photoelectrons per unit time. For the given wavelength λ, the quantum efficiency $\eta(\lambda)$ can be found from the spectral responsivity $S_e(\lambda)$. In a special and important operation mode of photodetector, a so-called *photon-counting mode* of photomultiplier tubes, the spectral responsivity is expressed in terms of the number of detected pulses per one incident photon labeled as "pulse/photon." The spectral output is described here in coordinates: "the number of photoelectrons per unit time or pulses per unit time." Then the spectral flow density is expressed in units: "photon/(c nm)." It is easily shown from the formulae of Sect. 1.1 that the quantum efficiency $\eta(\lambda)$ is to be given as follows:

Table 3.1 Photodetectors

Type	Detector input	Detector output
Physical photodetectors		
Thermal detectors		
Junction detectors (thermocouples, thermopiles)	Radiant power, Φ_e [W]	Voltage, V [V]
Electrical substitution radiometers; cryogenic radiometers	Radiant power, Φ_e [W]	See Sect. 3.3.2
Bulk detectors		
Bolometer, thermistor	Radiant power, Φ_e [W]	See Sect. 3.3.3
Pyroelectric detector	Radiant power, Φ_e [W]	See Sect. 3.3.4
Golay pneumatic detector	Radiant power, Φ_e [W]	See Sect. 3.3.5
Photoemissive detectors		
Vacuum phototube	Spectral photon flux, $\Phi_{hv}(\lambda)$ [photon/(s nm)] or [s^{-1} nm^{-1}]	Current, I [A]
Gas-filled phototubes	Spectral photon flux, $\Phi_{hv}(\lambda)$ [photon/(s nm)] or [s^{-1} m^{-1} nm^{-1}]	Current, I [A]
Photomultiplier	Spectral photon flux, $\Phi_{hv}(\lambda)$ [photon/(s nm)] or [s^{-1} nm^{-1}]	Current, I [A] or number of pulses of single-photon events
Photodetectors with internal photoeffect		
Bulk detectors (photoconductor)	Spectral photon flux, $\Phi_{hv}(\lambda)$ [photon/(s nm)] or [s^{-1} nm^{-1}]	Change in resistor [ohms (Ω)]
Junction photodetectors		
Photocells, photodiodes	Spectral photon flux, $\Phi_{hv}(\lambda)$ [photon/(s nm)] or [s^{-1} nm^{-1}]	Voltage, V [V], current, I [A]
Amplifying photodetectors (phototransistors, photo-field-effect transistors, photothyristors, avalanche photodiodes)	Spectral photon flux, $\Phi_{hv}(\lambda)$, [photon/(s nm)] or [s^{-1} nm^{-1}]	Voltage, V [V], current, I [A]
Luminescence quantum counters		
Luminescence quantum counters	Spectral photon flux, $\Phi_{hv}(\lambda)$ [photon/(s nm)] or [s^{-1} nm^{-1}]	See Sect. 3.6
Photoionization chambers		
Photoionization chambers	Spectral photon flux, $\Phi hv(\lambda)$, [photon/(s nm)] or [s^{-1} nm^{-1}]	Current, I [A]
Chemical photodetectors		
Gas-phase actinometer	Spectral photon flux, $\Phi_{hv}(\lambda)$ [photon/(s nm)] or [s^{-1} nm^{-1}]	See Sect. 3.8.5
Liquid-phase actinometer	Spectral photon flux, $\Phi_{hv}(\lambda)$ [photon/(s nm)] or [s^{-1} nm^{-1}]	See Sect. 3.8.6

$$\eta(\lambda) = \frac{I\ hc}{\Phi_e(\lambda)\ e\ \lambda} = S_e(\lambda)\frac{hc}{e\ \lambda} \tag{3.9}$$

or

$$\eta(\lambda) = 1.2398 \times 10^3 S_e(\lambda)/\lambda, \tag{3.10}$$

where $S_e(\lambda)$ is expressed as A nm/W, λ is expressed in nm, I is the photocurrent in A, and $\Phi_e(\lambda)$ is the flux expressed in W/nm.

3.2.2.3 Spectral Sensitivity of Luminescence Quantum Counters and Chemical Photodetectors

To describe spectral responsibility of luminescence quantum counters and chemical photodetectors, the specific spectral responsivity function $R(\lambda)$ related to luminescence process or chemical process is used. Physical dimension of the quantity $R(\lambda)$ follows from physical dimension of response (see Sects. 3 6 and 3.8).

3.2.3 Total Responsivity

The *total responsivity* is combined from partial contributions, each being arisen from an individual monochromatic emission process. Thus, the total responsivity is expressed in terms of the ratio of the total output to the total input as follows:

$$S = \frac{Y}{X} = \left(\int_0^\infty X(\lambda)S(\lambda)\mathrm{d}\lambda\right) \Big/ \left(\int_0^\infty X(\lambda)\mathrm{d}\lambda\right). \tag{3.11}$$

Let the input of a photodetector be the radiant power Φ_e and its output be the voltage V, then the total responsivity thereof is given by the following integral form:

$$S_e = \frac{V}{\Phi_e} = \left(\int_0^\infty \Phi_e(\lambda)S(\lambda)\mathrm{d}\lambda\right) \Big/ \left(\int_0^\infty \Phi_e(\lambda)\mathrm{d}\lambda\right). \tag{3.12}$$

In the event of phototubes and photomultiplier tubes designed to be exploited in the visible range, wherein luminous flux is right for operation description, luminous responsivity can be calculated to be as follows:

$$S_v = \frac{I}{\Phi_v} = \left(\int_0^\infty \Phi_e(\lambda)S_e(\lambda)\mathrm{d}\lambda\right) \Big/ \left(\int_0^\infty \Phi_e(\lambda)\mathrm{d}\lambda\right), \tag{3.13}$$

where the photocurrent I is expressed in A, the flux Φ_v is expressed in lm. A strip lamp at the color temperature 2,870 K ($T = 2{,}854$ K) is recommended by the International *Electrotechnical Commission, IEEE* for the use of calibrating luminous flux source, a *standard illuminant A*. The lamps of this kind are used as calibrating luminous flux sources. It is the luminous responsibility in A/lm that is specified in technical certificates of the photodetectors designed for the visible range. For nonselective photodetectors, which are designed to operate not only in the visible range, but in the invisible range as well, the total responsivity is known to be unreasonable. Among these are the detectors operating in the UV and vacuum UV ranges or so-called *solar blind* photodetectors.

The input value X may also be represented in terms of spectral function $x(\lambda)$ of the radiation source (in arbitrary units) in the following form:

$$X(\lambda) = X(\lambda_0)x(\lambda), \tag{3.14}$$

where $x(\lambda)$ is the normalized function at the wavelength λ_0, so that $x(\lambda_0) = 1$ and $X(\lambda_0)$ is the input at λ_0.

In the event of the radiant power distribution $\Phi_e(\lambda)$, its value may be also represented in terms of a normalized distribution $\phi_e(\lambda)$ in arbitrary units:

$$\Phi_e(\lambda) = \Phi_e(\lambda_0)\,\phi_e(\lambda), \tag{3.15}$$

where $\Phi_e(\lambda_0)$ is the input value at the wavelength λ_0.

Similarly, the spectral responsivity function can be expressed as a product of the spectral responsivity at the normalized wavelength λ_0, $S(\lambda_0)$ and the spectral responsivity function $s(\lambda)$ in arbitrary units:

$$S(\lambda) = S(\lambda_0)\,s(\lambda). \tag{3.16}$$

3.2.4 Responsivity of Nonlinear Photodetectors

In the preceding paragraphs, all photodetectors were considered to be linear. The responsivity of a nonlinear photodetector is a function of its input. Thereby, input–output characteristics of the nonlinear photodetectors depend upon wavelength (see [1]).

3.2.5 Effects Affecting Responsivity

The most important features of photodetectors affecting responsivity are listed below (see [1]).

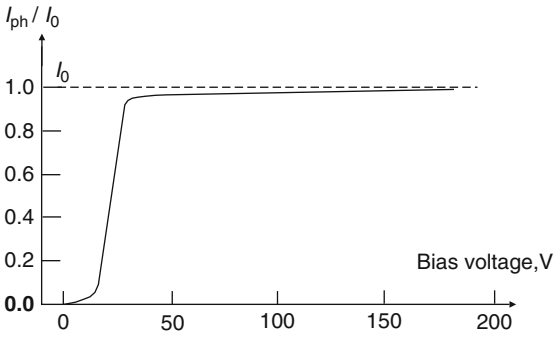

Fig. 3.1 Response of a vacuum phototube at constant irradiation as function of the bias voltage (see [1])

- *Bias effect*. The responsivity of several biased detectors depends on the *bias voltage*. For example, Fig. 3.1 shows the responsivity of a vacuum phototube for a given irradiance as a function of the bias voltage. At low voltage and constant irradiation, the responsivity increases with the voltage, but at high voltage saturation occurs and responsivity becomes independent of the voltage.
- *Temperature effect*. The responsivity can increase or decrease with temperature, and shape of the relative spectral responsivity changing with temperature. Therefore, a photodetector should be calibrated at the temperature, which will be used in measurements. Within a certain temperature range, depending on photodetector type, the variations of responsivity with temperature is reversible. However, if permissible maximum or minimum temperature is exceeded, irreversible *damage* will occur.
- *Nonlinearity*. Linearity property should be treated separately from linearity of the detector electronic environment. The detector may show linear behavior but the electronic environment may make detector–electronic combination to be nonlinear. Thereby, the linearity property should be attributed to the whole radiometric system.
- *Fatigue and aging*. Fatigue is the change of the responsivity with time mostly caused by high input, usually a reduction, for invariable input. Fatigue may be reversible, that is, the responsibility can return to its origin value after input caused the fatigue is removed. Aging is a slow but irreversible reduction of responsivity. This may be accompanied by a change in the relative spectral responsivity function.
- *Polarization effect*. The responsivity of some detectors, for example, silicon photodiodes, is affected by the degree of polarization and azimuth of the incident radiation.
- *Magnetic effect*. Photoemissive detectors are somewhat sensitive to magnetic fields.
- *Nonuniformity*. Some types of photodetectors show considerable nonuniformity across their sensitive area. Thereby, both absolute and relative responsivity can be changed.

Some of the effects listed above will be discussed in the next sections.

3.2.6 Noise and Detectivity

Detectivity is associated with the minimal amount of radiation which can be detected with certainty. The detectivity is specified by the noise inherent in detection. Generally, photocurrent fluctuations are a primary reason of noise generation. Various effects may cause such fluctuations as well as noise. The reader is referred to [1, 3] for further details. The author briefly refers to a so-called *shot noise*, which is very important for detectivity in the case of photomultipliers tubes. The other types of photodetectors are used by the author only for calibration, where fluxes are well above the detectivity level. Shot noise is generated where single events occur either in electron emission from photocathode or in dynodes. Shot noise has statistical nature of twofold origin:

- The number of photons arriving the photocathode per unit time and unit area is subject to fluctuations
- The number of emitted electrons and the kinetic energy of photoelectrons are also subject to fluctuations

A measure of short noise or dark current is expressed in terms of the root mean square of the photocurrent I_s. For the given bandwidth Δf of the measuring equipment in Hz, the value of I_s is calculated as follows:

$$I_s = \sqrt{2e\Delta f I}, \tag{3.17}$$

where e is the electron charge in C, I is the average value of the photocurrent in A, or dark current in this particular case. A distinction needs to be drawn between *signal noise* and *dark current noise*, although both are used to describe operation features of photomultiplier tubes. Signal noise is assigned to signal, and the level of such a noise is a part of the combined quantity called *signal-to-noise ratio*, *S/N* ratio. This quantity describes the minimum uncertainty on measurements of radiation. For example, let the value of *S/N* ratio be found to be as follows:

$$S/N = I/I_s = \sqrt{\frac{I}{2e\Delta f}} = 100, \tag{3.18}$$

and the minimum uncertainty should not be less than 1%. This situation can take place only at very weak photocurrents of the order of 10^{-12} A, at wide bandwidths of the order of 100 Hz, and at a very short counting time of about 0.01 s, for example, as shown in Fig. 3.15 of Ref. [1]. Dark current has a more complicated origin, and it will be discussed in Sect. 3.4.

The next quantity, a so-called *noise equivalent power* (NEP), shows how low level of input X can be detected by the photodetector. On the other hand, the weakest detectable signal is defined by the *S/N* ratio equal to unity. Thereby, for photoemissive detectors, where (3.17) is true, the value of the noise equivalent power is found to be as follows:

$$\mathrm{NEP} = I_\mathrm{d}/S = \sqrt{2eI_\mathrm{d}\Delta f}/S, \tag{3.19}$$

where the detector input is the radiant power Φ_e in W, and S is the responsivity in A/W. Noise equivalent power is often specified as normalized to unit bandwidth of the detection system, the quantity NEP*:

$$\mathrm{NEP}^* = \frac{\mathrm{NEP}}{\Delta f} = \frac{1}{S}\sqrt{\frac{2eI_\mathrm{d}}{\Delta f}}, \tag{3.20}$$

where the physical dimension of this quantity is W $\mathrm{Hz}^{1/2}$.

Noise equivalent power can depend on the radiation spectrum, since responsivity can depend on wavelength. By definition, detectivity D is the smallest amount of radiation, which can be detected by the photodetector. Its value expressed in terms of unit bandwidth of the detection system is easy found to be as follows:

$$D^* = \frac{1}{\mathrm{NEP}^*} = S\sqrt{\frac{\Delta f}{2eI_\mathrm{d}}}, \tag{3.21}$$

where its physical dimension is W^{-1} $\mathrm{Hz}^{1/2}$, provided that the physical dimension of the input quantity is W, as in the event of radiant power.

Since most photodetectors have selective spectral responsivity, the detectivity must be defined as a spectral quantity $D(\lambda)$, or a standard source is defined for which detectivities are quoted [1].

3.2.7 Dynamic Characteristics of Photodetectors

Dynamic characteristics of all photodetectors are specified in terms of following quantities:

- *Response time*. Let us assume that the incidence irradiance varies sharply at a time t_0 from zero level to a level I, generally, the detector output $Y(t)$ than follows an exponential function of time as follows:

$$Y(t) = Y_\infty[1 - \exp(-t/\tau)], \tag{3.22}$$

  where $Y(t)$ begins at t_0, τ is the response time.

- *Rise time*. The time interval t_γ, which takes for the output rising from 0.1 to 0.9 of the final value, is called the rise time.
- *Frequency response*. With modulation of the detector input, the response time affects the frequency with which the output reproduces the time dependency of modulated radiation. For most detectors, the relationship between the peak-to-peak amplitude of the detector output and chopping frequency is given by the equation:

$$A(f) = A(f_0)\sqrt{1 + (2\pi f\tau)^2}, \tag{3.23}$$

where $A(f)$ is the amplitude at frequency f, $A(f_0)$ is the signal amplitude at the reference frequency f_0, and τ is the response time. Usually, the reference frequency f_0 is taken so that the inequality $(2\pi f\tau)^2 \ll 1$ is to be valid. Due to a time lag happened in the dynode system of photomultipliers, several other time-related parameters are necessary for such type of detectors. These parameters will be discussed in Sect. 3.4.

3.3 Thermal Detectors

The responsivity of thermal detector is specified in terms of photoresponse against spectral radiant flux, or in units W/nm. This function is invariable. This is true only when the absorption factor of the detector is invariable quantity too, and the total absorbed radiation is only used for heating the detector. Temperature of the detector can be measured by any way. From the long-wavelength region, a nonselective part of the responsivity is bounded by reduction of the absorption coefficient. Thereby the most feasible materials for browning are niello gold and niello platinum. The absorption coefficient of the former is invariable with an accuracy of 0.5% in the range 250–2,500 nm [1]. From the short-wavelength region, a nonselective part of the responsivity is bounded by photoelectron emission. To extend the spectral range, wherein the absorption coefficient reaches its peak equal to unity, so-called *cavity radiation detectors* are used, where multiple reflection at a black surface provides virtually complete absorption of radiation entering the cavity.

3.3.1 Thermocouples and Thermopiles

A simple radiometric thermocell, a so-called *thermocouple*, consists of two junctions, each being a pair of soldered thin wires, and the wires are made up of different materials. One junction, a measuring junction, is in thermal contact with a small browning area, which is heated by incident radiation. It is desirable to use the area with an evaporated niello gold or electrolytic film of niello platinum. In order to increase sensitivity of a thermocouple, it is essential that equilibrium between absorbed and emitted radiation is reached at temperature at high as possible, this can be provided by reduction of dissipated heat. To do this, thin wires are used and sometimes thermocouples are evacuated, but as this is true, a problem arises if there is spectral transparency of the window.

A so-called *"compensated" thermocouple* has one evident advantage of threshold sensitivity level (Fig. 3.2), wherein the measuring junction is attached to a black

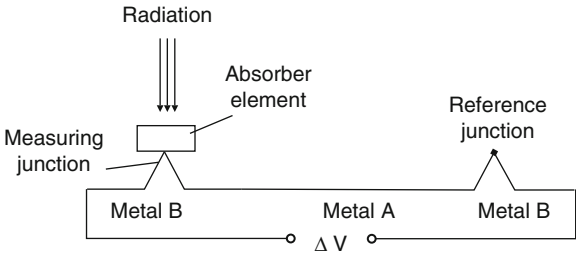

Fig. 3.2 Compensated thermocouple

surface that is exposed to incident radiation. Another junction, a so-called *reference junction*, is mounted in the housing of the measuring junction.

The voltage difference ΔV causing a photocurrent of the thermocouple is directly proportional to the temperature difference between the two junctions as follows:

$$\Delta V = S\Delta T, \tag{3.24}$$

where S is the Seebeck coefficient, its physical dimension is V/K. For various metal pairs the Seebeck coefficient is equal to μV/K; the bismuth–antimony junction has the highest Seebeck coefficient: $S \approx 100$ μV/K (see [1, 5]).

Several thermocouples attached to a black surface can be joined in series to produce a large voltage output. Such a series of thermocouples is called a *thermopile*. Thermopiles are manufactured as vacuum, gas-filled, or air models. Semiconductor materials and thin films are successfully used as junctions. The essential part is the junction between *n*-type and *p*-type semiconductor film. Thermopiles by nature have nonuniformity since they consist of a number of individual thermocouples [1].

Some manufactories, including cited in [1], put on the market thermopile sensors. The author used in his practice the thermopile sensors from OPHIR. Among them is the most sensible sensor of 3A-FS model, which can detect incident radiant power down to 3 μW with an uncertainty of order 10% in the spectral range from 0.19 to 20 μm. This radiant power is equivalent to the photon flow of 6×10^{12} photon per second at wavelength $\lambda = 400$ nm.

3.3.2 *Electrical Substitution and Cryogenic Radiometers*

The operation principle of *electrical substitution radiometers* (*ESRs*) is that the device measures optical radiation by comparison to an equivalent amount of electrical power [1, 6, 7]. This type of radiometers are sometimes referred to as electrically calibrated radiometers or simply as *absolute radiometers*. Figure 3.3 illustrates main design features of electrical substitution radiometer. A cavity, usually designed as having a cone shape, receives incident radiant flux Φ_e. Absorption of radiation causes that the cavity will experience a temperature rise. A thermal

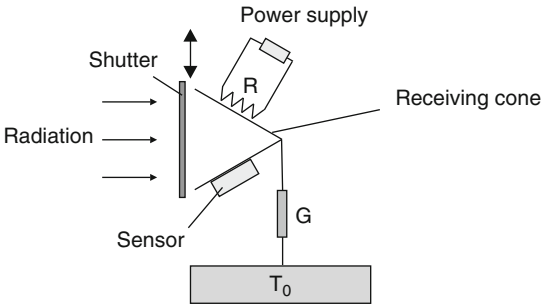

Fig. 3.3 Schematic diagram of essential components of electrical substitution radiometer [6, 7]

conductor provides heat connection between the receiver and a heat sink being at a constant reference temperature T_0. The receiver is coupled to a constant temperature heat sink at a reference temperature T_0 with a thermal conductor of conductance G. For given conductance G of the thermal conductor, with ignoring losses due to radiation, convection and stray thermal conductance, the equilibrium (long time) temperature rise is given by $T - T_0 = \Phi_e/G$. When the shutter is imposed to intercept the light beam, electrical power to the cavity is increased by a sufficient amount to maintain the cavity temperature determined by the temperature sensor system at the shutter open level. Ignoring corrections and losses mentioned earlier, the optical power is given by $\Phi_e = I_h^2 \, R$ where I_h is the increased current applied through the heater of resistance R required to maintain temperature stability.

When utilizing electrical substitution radiometers, it is good practice to carefully characterize the potential loss mechanisms to apply appropriate corrections.

Electrical substitution radiometer technology was worked up by Coblentz at NIST during the early part of 20-th century [8]. Electrical substitution devices were designed and constructed to operate at cryogenic temperatures in order to increase the sensitivity of the devices and to reduce the uncertainties due to radiation and conduction losses. A high accuracy cryogenic radiometer was also developed by Martin and Quinn at the NPI (National Physical Laboratory) in the UK [9, 10]. Several companies are offering commercial versions of absolute cryogenic radiometers. The availability and accuracy of the instruments has resulted in their employment by a number of national standards laboratories to provide the basis of radiometric measurement (see [6, 11, 12]).

Electrical substitution radiometers operating at room temperature have very long response times. Cryogenic electrical substitution radiometers are very expensive. The developing and purchase of the devices may be economically feasible for the institutes and laboratories those specialize in radiometric fields.

3.3.3 Bolometers and Thermistors

Bolometers and *thermistors* consist of narrow strips of a blackened material that has a sufficiently large resistance temperature coefficient. Incident radiation causes a

noticeable temperature increase and subsequent variation in resistance of the material due to absorption of radiation. Material may be either a metal in the case of metal bolometer or semiconductor in the case of thermistor, i.e., thermally sensitive resistor. The relative change of the resistance dR/R and the temperature change dT are related by means of the temperature coefficient α as follows:

$$dR/R = \alpha dT. \tag{3.25}$$

The temperature coefficients of metals used in bolometers are about 0.005 K^{-1}, whereas similar quantity of semiconductor materials are about -0.05 K^{-1} [1, 5]. When connecting to a current supply, such a device, bolometer or thermistor, changes its resistance by an amount ΔR due to absorption of incident radiation. The power supply, in order to maintain the current I, should adjust the applied voltage by an amount $\Delta V = I\Delta R$.

3.3.4 Pyroelectric Detectors

In one type of thermal photodetectors, the so-called *pyroelectric detector*, the operation principle is based on absorption of incident radiation energy by a ferroelectric element. The ferroelectric materials have an internal dipole moment that provides a surface charge distribution. With varying of surface temperature, the surface charge distribution changes too, and they say about exhibition of the pyroelectric effect. The electrical impedance is virtually that of an electrical capacitor. An output signal appears only with temperature changing. Such a detector can be used only with modulated or pulsed radiation. Another restriction is the temperature range, in which the pyroelectric effect exists. Ferroelectics lose their electric polarization when they are heated above the Curie temperature [1, 5].

3.3.5 Golay Pneumatic Detectors

The operating principle of the *Golay pneumatic detectors* is based on the heating of gas inside a small metal cylinder. The cylinder is closed by a blackened metal plate at one end and by a flexible metalized diaphragm at the other. The cylinder is filled with gas and then sealed. The incident radiation heats the gas, which deforms the diaphragm due to expansion. Light from a lamp falling on the diaphragm reflects to a photocell. Motion of the diaphragm changes the output of the phototube.

Small sensitive areas and slow response are disadvantages of this type of thermal detectors. These drawbacks hamper the use of the thermal detectors as verification tools for phototubes and photomultipliers (see Sect. 3.4). Nevertheless, one advantage is that the responsibility is unchanged over the spectral range where the absorption coefficient remains constant. Some types of detectors involving

absorbent materials are used in commercially available thermal detectors. They provide a high absorption coefficient up to 85–95% in their working range.

3.4 Photoemissive Detectors

Nowadays a wide variety of detectors based on external photoeffect are available, which are also referred to as *photoemissive detectors*. While operating of this kind of detectors, photons are absorbed by photosensitive material of the photocathode usually made of a metal or semiconductor. Electrons are emitted from the photocathode surface. There are three major types of photoemissive detectors, namely, *vacuum phototube*, *gas-filled phototube* and *photomultiplier tubes* (*PMTs*). Because of instability of several kinds, gas-filled phototubes are unsuitable for radiometric applications, and this type of photodetectors will not be discussed in this book.

The operational principles and features of photoemissive detectors have been described in a large amount of monographs and books (see [1–4, 13, 14]). Thereby the author will discuss the operational aspects of phototubes and photomultiplier tubes, which may be interested for those, who work with such kind of photodetectors in customary scientific, nonradiometric, laboratories. Nowadays, manufactories advertise for market a wide variety of phototubes and photomultiplier tubes with the *semitransparent* and *opaque* photocathode, all have different spectral characteristics (Fig. 3.4).

As for phototubes and photomultiplier tubes , the *spectral responsivity function* is specified by the photocathode material and window spectral features. The most

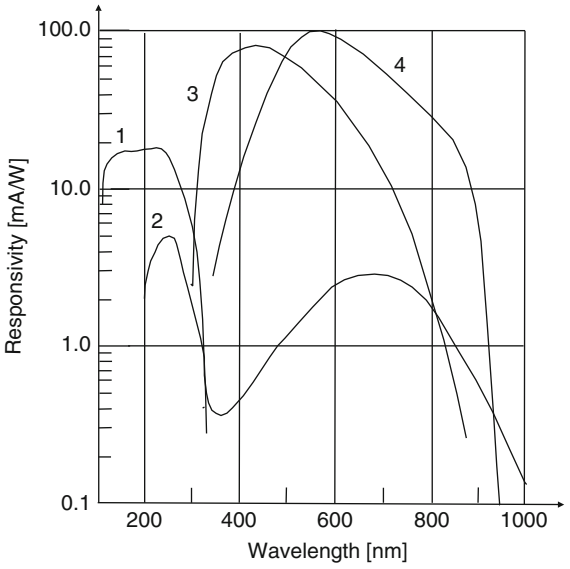

Fig. 3.4 Spectral responsivity functions of some photocathodes. Photocathode material: Cs–Te (*1*), Ag–O–Cs (*2*), Sb–K–Cs (*3*), K–Cs–Sb (*4*) (see [4])

relevant types among them are that having cesium–antimonide photocathodes Sb–Cs, bi-alkaline photocathodes Sb–K–Cs and Sb–Rb–Cs with the long-wavelength cutoff $\lambda_{max} \approx 630$ nm, multialkaline photocathodes Sb–K–Na–Cs with the long-wavelength cutoff $\lambda_{max} \approx 830$ nm, silver–oxygen–cesium photocathodes Ag–O–Cs with the long-wavelength cutoff $\lambda_{max} \approx 1{,}200$ nm. Also among these are so-called solar-blind photocathodes, namely, the photocathodes of cesium telluride CsTe and rubidium telluride RbTe with the long-wavelength cutoff $\lambda_{max} \approx 330$ nm, as well as cesium iodide CsI with the long-wavelength cutoff $\lambda_{max} \approx 250$ nm. For these photodetectors, the minimum spectral responsibility wavelength is defined by absorption of window material. For glass the wavelength is $\lambda_{min} \approx 300$–$360$ nm, for uviol glass $\lambda_{min} \approx 200$ nm, for fused quartz $\lambda_{min} \approx 160$ nm, and for magnesium fluoride, MgF_2, $\lambda_{min} \approx 115$ nm. The long-wavelength cutoff is dictated by the *work function* of the photocathode material. In turn, the work-function in metals is determined by the retaining potential of metal E_w. In semiconductors, this potential consists of two components: the electron affinity E_a, which is true surface potential, and band-gap energy E_g [1, 4]. If $hv \geq E_w$, a photoelectron will be emitted. Therefore, the long-wavelength cutoff is defined from the following equation:

$$\lambda_{max} = hc/E_w = 1{,}239.8/E_w. \tag{3.26}$$

The values of work-functions for various photocathode materials are listed, for example, in books [13, 15]. For a given material of photocathode window, the photocathode current, or photocurrent, is given by the following equation:

$$I(\lambda) = [1 - \rho(\lambda)]\, \eta(\lambda)\, e\, \Phi_{hv}(\lambda), \tag{3.27}$$

where $\rho(\lambda)$ is the spectral reflectivity of the front surface, $\eta(\lambda)$ is the spectral quantum efficiency of photoemission and $\Phi_{hv}(\lambda)$ is the spectral photon flux (see Table 1.1). The maximum spectral quantum efficiency of metallic photocathodes is usually about 0.1%, whereas in semiconductor photoemitters it can be as high as 30%.

The opaque photocathodes are deposited on a thick metallic substrate, and they are generally used in the "*side-on*" or "*side-window*" configuration, although exceptions are possible (see Sect. 3.4). A semitransparent photocathode is vacuum deposited on the inner surface of glass or fused quartz cell, and the photoelectrons are emitted from the opposite cell surface. This type of photocathode is generally used in "head-on" configuration (Fig. 3.5).

A so-called *dark current* of phototube or photomultiplier tube is mainly specified by the photocathode material, as well as the photocathode size. Dark current is subject to the following relationship $I_d \sim T^2 \exp(-E_w/kT)$, which is known as Richardson's formula [16], where E_w is the work function, k is the Boltzman constant, and T is absolute temperature. The work function of photocathode can be evaluated from (3.26) and the value of long wavelength cutoff in the device specification. Dark currents of photomultiplier tubes with silver–oxygen–cesium photocathodes are much more than that of phototubes and photomultiplier tubes

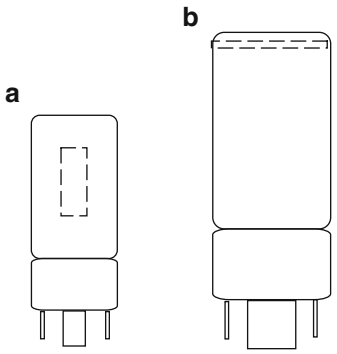

Fig. 3.5 Side-on (**a**) and head-on (**b**) photoemissive detectors

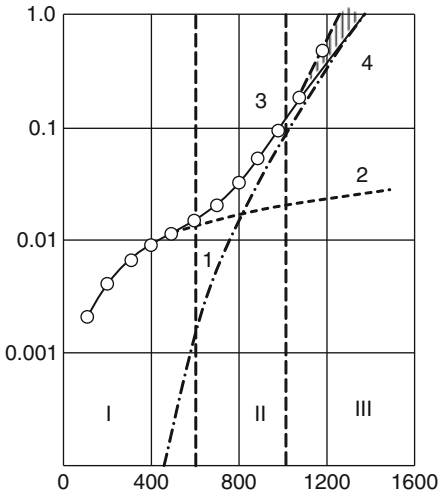

Fig. 3.6 Dark current components against supply voltage for typical photomultiplier [4]; *Y*-coordinate is the dark current, and *X* coordinate is the applied voltage; amplified thermoelectrons emission of the photocathode and dynode system (*1*); the leakage current (*2*); the total dark current (*3*); the unstable operating range (*4*)

with solar blind photocathodes. For phototubes and PMTs operating in the direct current mode under a moderate voltage, leakage currents over the device cell can provide a sufficient contribution to the dark current (Fig. 3.6).

Now we consider what PMTs and photocathode types it worth working with. It is significant that the each type of photodetector should be provided with its own housing and socket. Further, basing on specific character of the investigation task, the researcher should specify the type of photodetector and required spectral features of the detector as well. Researcher can find the most necessary information from Internet sites of the respective manufacturers. For example, the author works in a wide spectral range from the VUV to the near IR spectral range, at $\lambda = 115$–$1{,}200$ nm, mainly under weak light radiation intensities. Thereby phototubes are essentially used for calibration of PMTs. With operating in the direct current mode, photon-counting mode or pulse-analog mode, the author uses PMTs including solar blind photodetectors with semitransparent photocathodes overlapping all spectral ranges, see Table 3.2. This table shows well suited

Table 3.2 The PMT types well suited for operation in the wavelength spectral range 115–1,200 nm

Russian-standard PMT type	Photocathode diameter (mm)	Analogs	Photosensitive materials	Window	*S* number* [1]	Spectral range (nm)
PMT154	10	Hamamatsu R10825	CsI	MgF_2		≈ 115–250
PMT142	10	Hamamatsu R10824	CsTe	MgF_2		≈ 115–400
PMT71	18	Hamamatsu R7459	Cs–Sb	Fused silica	S-21	≈ 160–630
PMT100	20	Hamamatsu R3809-U50	Sb–K–Na–Cs	Fused silica		≈ 160–830
PMT83	25		Ag–O–Cs	Lime glass	S-1	≈ 400–1,200

types of PMTs for operation in the direct current mode and photon-counting mode, as well as in the pulsed analog mode, with the dynamic resolution of several nanoseconds.

* - Spectral responsivity function registered by the *Electronic Industry Association (EIA)*

It is because of the following why these photomultipliers were chosen by the author.

- PMT154 solar blind photomultiplier and similar types from other manufacturers are well suitable for measurements in the vacuum UV, UV spectral ranges against a strong background of scattering visible light.
- PMT142 and similar types from other manufacturers are well suitable for measurements in the vacuum UV and UV spectral range against a weak background of visible scattering light.
- PMT71 and similar types from other manufacturers are well suitable for measurements in the UV spectral range using UV transmitting visible absorbing glass filters. As it is well known, these filters are transparent for radiation in the red spectral range, where the responsibility of PMTs with multialkaline photocathodes (Sb–K–Na–Cs) is sufficient.
- PMT100 with the fused quartz window and similar photomultipliers from other manufacturers, all have high responsivity and overlap a wide spectral range, $\lambda \approx$ 160–830 nm. Generally, when required photoemissive detectors with Cs–Sb and Sb–K–Na–Cs photocathodes, it is appropriate to use detectors with fused quartz windows rather than that with glass windows. The spectral range of the former is wider.
- PMT83 and similar photomultipliers from other manufacturers with Ag–O–Cs photocathodes have low responsibilities and large dark currents. However, the responsibility is greater than that for PMTs with multi-alkaline photocathodes at $\lambda > 800$ nm. If operating in cooled mode, these photodetectors are outstanding ones.

Not long ago, production of the R5509-43 and R5509-73 PMTs with the InP/InGaAsP photocathode and long-wavelength cutoff $\lambda_{max} \approx 1.4$ and 1.7 μm, respectively, are started by Hamamatsu [17]. Responsibility is about that of PMT83, the photocathode is small 3 × 8 mm. It is clear, that such photomultiplier tubes can operate at low temperature.

The spectral responsivity of photoemissive detectors may vary in time. Therefore, it is useful to age them during 2–3 years before calibration. It is noteworthy that spectral responsivity of photoemissive detectors from one manufacturer having identical model designation may considerably differ, up to two times. Besides, considerable nonuniformities occur in head-on as well as side-on phototubes and PMTs (see [1] for details). Thereby, if intending to calibrate a photodetector in arbitrary units, moreover, in absolute units, it is useful to work with a suitable diffusing cavity, provided that the photodetector is required to use under different illuminating environments (see Sect. 4.2.1.1 for details).

3.4.1 Vacuum Phototubes

A vacuum phototube consists of an evacuated envelope containing a photocathode and anode. A vacuum phototube and its basic operating circuit are shown in Fig. 3.7.

The voltage across the resistor $V = I_{pt} R$ is a measure of photocurrent I_{pt}. Generally, two basic groups of phototubes are used as follows.

- Low voltage phototubes with opaque or semitransparent photocathodes, where the applied voltage may range from 50 to 250 V.
- High voltage bi-planar phototubes, where the applied voltage may range from 1 to 5 kV. The phototubes are designed to operate under sub-nanoseconds rise times and peak currents as short pulses of several amperes.

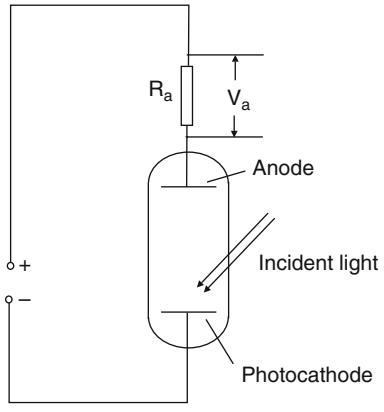

Fig. 3.7 A vacuum phototube circuit

3.4.1.1 Low Voltage Vacuum Phototubes

A typical configuration of low voltage phototube is show in Fig. 3.8.

The opaque photocathode is made of magnesium. The molybdenum anode is mounted at the top of the bulb away from the outlets connecting to the cathode in order to reduce dark currents. The anode contact is the ring-shaped flange at the front end, and the cathode contact is a wire at the rear end of the bulb. The top of the bulb is made of uviol glass ($\lambda_{\min} \approx 200$ nm). Work function of polycrystalline magnesium is $E_w = 3.68$ eV, so that the spectral band of the phototube ranges from 200 to 340 nm [18].

Now we consider factors, which specify principle operating features of phototubes. A typical *current–voltage curve* of a phototube is the curve with current saturation associated with the voltage, when all electrons emitted from the photocathode are collected by the anode or fall on the bulb walls (see Fig. 3.1). Herein secondary emission with yield close to 1 takes place and the secondary electrons are also collected by the anode. Note that under these conditions, a slow arise of photocurrent with applied voltage occurs, approximately 0.2% per 100 V, which is caused by the Schottky's effect [19]. It implies the decreasing of work function of the photocathode material, a value E_w, by value ΔE_w due to applied voltage. The decreasing in work function can be calculated with consideration of the effect of constant external field affecting the potential energy of an electron near the conductor surface. It is found to be proportional to the square root of the field. In addition, it is important that the Schottky effect shifts the photoemission threshold value according to the formula:

$$\Delta\lambda = \lambda^0_{\max} \frac{\Delta E_w}{E^0_w - \Delta E_w}, \tag{3.28}$$

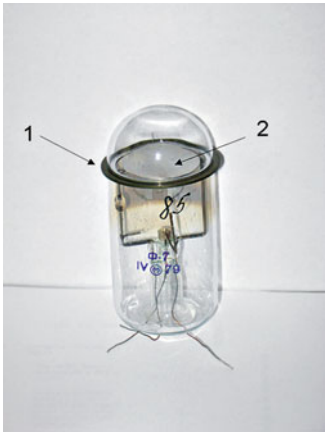

Fig. 3.8 F-7 vacuum phototube (MELZ, Russia)
1 - anode, 2 - photocathode

where λ^0_{max} is the photoemission threshold at zero applied voltage, E^0_w is the work function at zero applied voltage. The effect of responsibility changing is most noticeable in high-current modes. For instance such modes are exploited with pulsing radiation, where the longitudinal resistance of the photocathode–substrate system becomes essential. Under these conditions, the effect can achieve several tens of percentages.

The upper limit of photocathode dynamic range is caused by impact of the volume charge, longitudinal resistance of photocathode, and short-time fatigue of photocathode. Surface charges on the bulb walls can also affect linearity of phototube operation. Short-time fatigue of the photocathode can be negligible at short expositions. With continuous illumination, the upper limit of phototube linearity is usually about 10^{-5}–10^{-4} A, whereas in the pulsed mode, it can get up to tens ampere. Generally, limit modes for phototube operation are listed in its technical certificate. It is clear that if operating near limiting parameters or no limit parameters are specified, the checking up of the linearity property is strongly required for the given experimental parameters such as the applied voltage, pulse duration, spectral range, etc.

Dynamic resolution of phototubes is much better than that of photomultipliers. The time interval between a photoionization event and photoelectron leaving from the photocathode is less than 10^{-12} s, whereas the drift-transit time of the photoelectron is of order of 10^{-10} s. Thereby, with time intervals longer 0.1 ns, the controlling factor determining dynamic resolution is transient in the circuit of the phototube load.

Nonuniformity. Nearly the total amount of photoelectrons emitted from the total photocathode surface can be collected by means of increasing of the applied voltage. It implies that nonuniformity is exclusively caused by nonuniformity of the quantum yield of photoemission, for example, due to difference in the photocathode thickness. The own author's practice shows that such a nonuniformity may get up tens percentages. It is assumed that phototubes with massive photocathode suffer from the nonuniformity in smaller extend. The reason is that the photosensitive layer is essentially thicker. The readers those are more interested of the phototubes features mentioned above can refer to the books and the materials quoted in them [1, 2].

3.4.1.2 High-Voltage Bi-planar Phototubes

For measuring high intensity laser radiation, so-called high-voltage bi-planar phototubes are specially designed. The most important features of these phototubes are their sub-nanoseconds rise times and currents of several amperes. These features are achieved with cellular anode, which is mounted on the inner side of the enter window at several millimeters from an opaque cathode. The readers, those take an interest in more details of characteristics of high-voltage bi-planar phototubes, can refer to the book [1] and references therein.

3.4.2 Photomultiplier Tubes

An another wide class of photoemissive detectors is represented by photomultiplier tubes (PMTs). Photomultiplier as shown in Fig. 3.9 consists of the photocathode, dynode system where the secondary emission effect provides amplification of the photocathode current, and anode, which collects electrons from the last dynode. The anode also produces the output in the form of the anode current.

Design and operating principle of different PMTs are described in numerous books and monographs (e.g., see [1, 2, 4, 13]). Thereby, we will briefly run through these items. The distinctive feature of any PMT is the dynode system. Surfaces of the dynode are covered with special materials provided secondary emission, the effect that they emit under normal operation conditions about 3–10 *secondary* electrons per one incident *primary* electron.

The *dynode efficiency* σ is expressed in terms of the secondary emission coefficient as follows:

$$\sigma = \frac{N_2}{N_1}, \tag{3.29}$$

where N_1 is the number of primary electrons, N_2 is the number of secondary electrons. The value of the secondary emission coefficient is determined by the primary electrons energy, the covered material and its density (CsSb, GaP, GaCs, $CsSb_3$, MgO and BeO are usually used).

An important feature of secondary emission is dependency of the secondary emission coefficient on the primary electrons energy. The author's experience

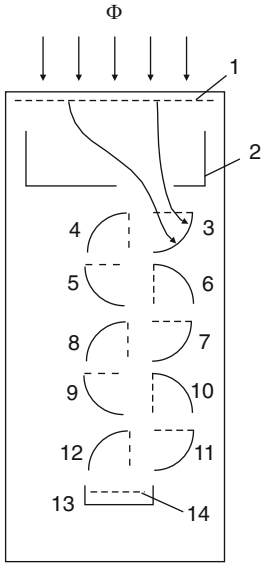

Fig. 3.9 Schematic diagram of PMT. *1* – photocathode; *2* – focusing electrode; *3–13* – dynodes; *14* – anode; Φ is incident light; the *arrowed lines* indicate electron traces [4]

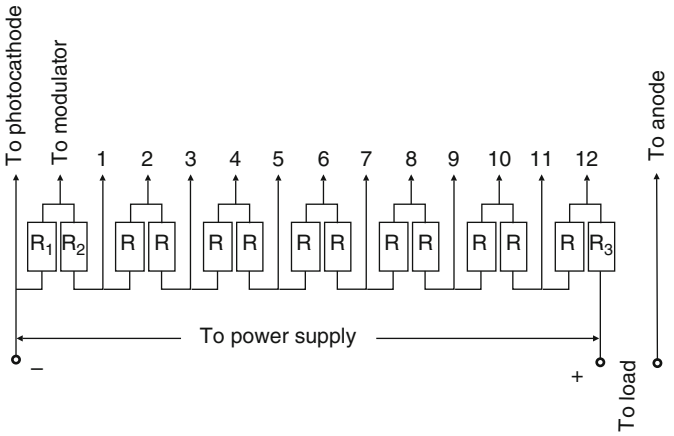

Fig. 3.10 Resistor chain for dynode voltage supply. $R_1 = 0.05R$; $R_2 = 1.5R$; $R_3 = 0.3R$

shows that the acceleration voltage between two adjacent dynodes more than 150 V leads to increased dark current undergoing sharp variations. In this energy range, the value of the secondary emission coefficient varies as follows: $\sigma \leq 10$ (GaP), 6 ($SbCs_3$), 5 (MgO and BeO) [4]. The total gain may get up to $G = 10^7$, depending on the number of dynodes and accelerating voltage. Schematic diagram of voltage divided chain for supplying the dynode stage with accelerating voltage is shown in Fig. 3.10.

3.4.2.1 Performance Characteristics of PMT

Now we will consider photomultiplier tube operation in the analog mode, namely, direct current and pulsed mode, as well as in the single-electron mode, or the so-called photon-counting mode. The photomultiplier tubes working in pulsed mode differ greatly from those intended for working in the photon-counting and direct current modes. The operating features of the two PMT types are also described by different characteristics. These characteristics treat just as PMT as a whole, so also PMTs parts such as photocathode, cathode chamber, dynode system, and anode. The characteristics can be specified as static and dynamic for the PMT under static illumination, as well as under pulse illumination [4].

The *static characteristics* of the PMT photocathode are similar those specified for phototubes.

The static characteristics of the cathode chamber are determined by the photocathode nonuniformity considered above and collection efficiency for photoelectrons emitted from different photocathode areas. The value of collection efficiency is defined as the ratio of the number of photoelectrons emitted from unit area to the number of photoelectrons arrived at the first dynode.

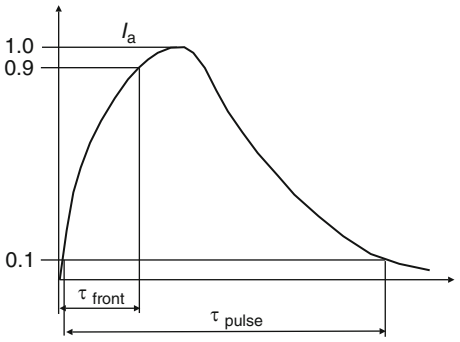

Fig. 3.11 Dynamic characteristics of photomultiplier [4]

The static characteristics of the dynode system, as its electron-optical features and second-emission parameters, are described in terms of the gain for each dynode stage as well as the gain the PMT as a whole.

The static characteristics of the anode determine the maximum anode current at high gains (see below).

One of the important *dynamic characteristics* of the anode unit is that assigned to determine the dynamic resolution in the photon-counting mode, when registration of single photoemission events is required, or the duration and shape of light pulse with operating in the pulse-analog mode.

Among the characteristics are the most important as follows (Fig. 3.11)

- *Rise time for transient response* τ_{front}, as a time interval which takes the anode current on arising from 0.1 to 0.9 of its saturation value after one incident radiation jump.
- *Transient response duration* τ_{pulse} is the dynamic interval during of which the anode current level stays upper 0.1 of its maximum after action of δ-function pulse in incident radiation.
- *Signal transit time* is the dynamic interval between signal entering in the photocathode and signal appearance at the anode.
- *Signal transit time fluctuation.*
- *Time difference in signal transit* from different areas of the photocathode.

It is clear, that the dynamic resolution of a PMT is mostly specified by the duration of its transit response, which is also dependent on all characteristics mentioned above.

For pulsed PMT operating in the analog mode, one of the important parameters is the maximum of its output pulse. For photomultiplier tubes of such type it may get up several amperes. As a whole, photomultiplier tube has the following performance characteristics.

- *Temperature dependence of spectral responsivity*. It is essentially important, because there is a need for cooling the photocathode to provide reduction of the dark current. According to published data [1], for CsSb photocathodes, a sharp decreasing of responsivity is taken place near $\lambda_{\max}$ when temperature decreases,

whereas for multialkaline photocathodes, responsibility may increase near λ_{max}. The author has no any available data relating to PMT with Ag–O–Cs cathodes, which could be used for weak radiation intensity measurements only in the cooling cathode mode. On operating in this mode, the temperature should be kept invariable.

- *Nonuniformity*. As in the case of phototubes, nonuniformity may achieve tens and even hundreds percentages [1].
- *Linearity*. The problem of linearity encountered with measurements by means of PMTs has been discussed [1–4, 13, 14]. Most frequently, nonlinearity appears at high currents, where the electron cloud charge located between the last dynode and the anode screens the electric field between them. The author calls attention to one common error, namely, the PMT output current may get up its saturation value on decreasing the supply voltage *at an invariable incident radiation*. If this is the case the anode current decreases, but the effect mentioned above becomes apparent due to a low voltage between the photocathode and the first dynode. Several ways for linearity testing are available, e.g., see [1]. The author proposes two simple methods, which could be realized easily.

  1. A luminescence spectrum is measured, its intensity grossly varied within a given spectral range and is dependent on the intensity of its excitation. Provide changes of the intensity of excitation and estimate the excitation intensity range, wherein the spectral shape is independent of it. In this event the PMT operates within linear range of its registration system.
  2. The spectrum of an incandescent lamp passed through a long-pass filter is measured with the help of a monochromator at different entrance and exit slit widths. The measured spectrum stays invariable at weak intensities. On increasing the intensity, within the spectral band associated with the maximum intensity, the spectrum falls down. With operating in photon-counting mode, it is possible to find precisely how the counting efficiency depends on illumination (Fig. 3.12).

It is seen that the amplifier used for measuring of the spectrum shown in Fig. 3.12 permits spectra to be measured without distortions at intensity of about 1.5×10^5 s^{-1}. The intensity of value 1.8×10^5 s^{-1} gives to miscounting near 5% at the wavelength 510 nm, and its value of 2.3×10^5 s^{-1} gives to 10% of miscounting at the wavelength 530 nm, and so on.

- *Maximum ratings*. Maximum photocathode current density should not exceed the following values: 5 for Ag–O–Cs photocathodes, 250 for NaKCsSb photocathodes, and 5×10^3 (in nA/cm^2). The photocathode currents should be decreased at low temperatures. The maximum anode current value is specified in the PMT technical certificate. For a given voltage, gain and anode current we may always can determine if the photocathode current lies within the violation limits.
- *Instabilities*. Some types of instabilities have been discussed in the book [1]. Fatigue consisting of reversible drifts is the most troublesome among them.
- *Dark current*. This item has been discussed in the beginning of Sect. 3.4.

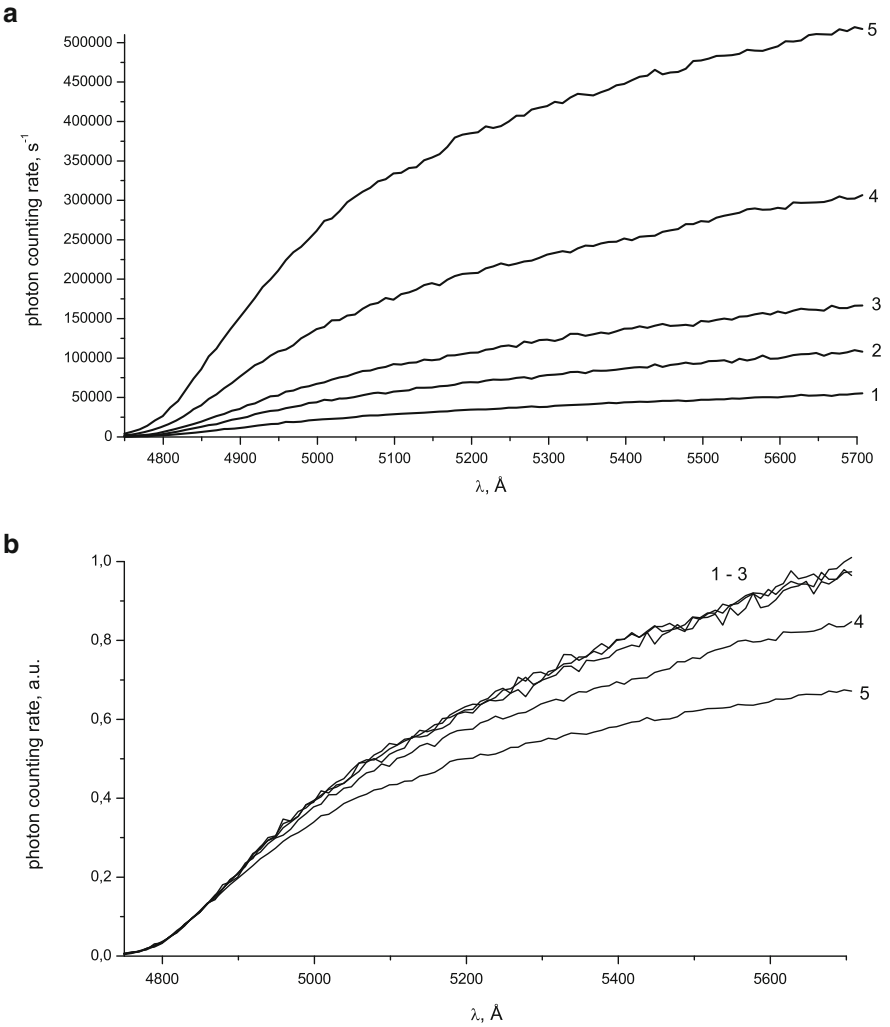

Fig. 3.12 The spectrum of SIRSH8.5-200 lamp radiation passed through the GhS-17 filter and measured in the photon-counting mode at different intensity of incident light; non-normalized (**a**); normalized to the spectral parts with intensity less than 10^5 s^{-1} (b)

- *Cooling and temperature range*. According to [1] *S*-1 photocathodes can be cooled down to −180°C, whereas most of other down to −80°C. The author's experience shows that design of some PMTs does not permit so dipper cooling. Evidently, a possible deformation of PMT parts due to cooling may cause electrical breakdowns, which lead to damage. There are available designs of the cooling housing from different manufactories, e.g., cooling housing for PMTs R5509-43 and R5509-73 [17]. All of them are expensive and sophisticated. A simple and serviceable design for cooling housing was developed by the

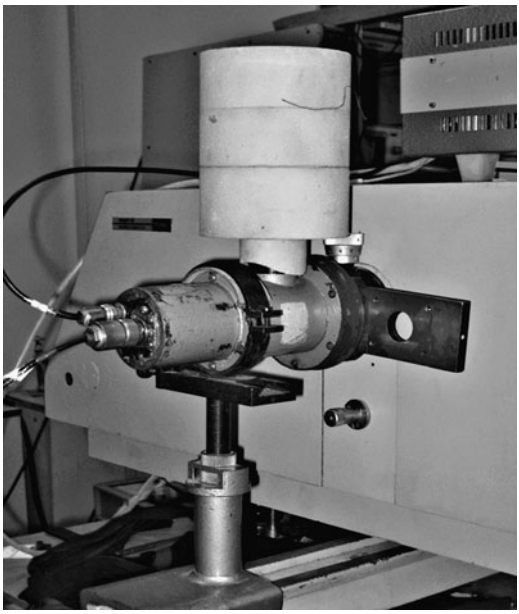

Fig. 3.13 The photo of the PMT cooling housing designed in the author's laboratory

author for PMT71, PMT100, and PMT83. The design provides photocathode cooling down to required temperature with the absence of window weeping (Fig. 3.13).

Cooling of the photocathode and dynodes is provided by means of the heat conductor, material of which is empirically matched to down the dark current to a required level and do not allow damage of the PMT. Radiation passes to the photocathode through two quartz windows, both are pressed out by the Teflon rings. The separation between the windows is 4 mm that does not permit hoar-frost to emerge their inner surfaces. The rear end of PMT is separated by means of the ribbon ring from the housing part, wherein the voltage divider is mounted. Since the photomultipliers of types PMT71, PMT100, and PMT83 all differ in size, as well as in their voltage divider units, there are available different ribbon rings, the foam plastic pipes, which provide low heat-conductivity, the cylindrical cups with radiation entrances, and the semi-circles providing thermal contact between the heat conductor and the cylindrical cup. It was found copper to be the most proper material for the heat conductor for PMT71 and PMT100. Under these conditions, photocathode temperature drops to −65°C, and the dark current downs to 4–6 pulses per second (see below) at the plateau of counting response. Brass is the optimal material for PMT83, that gives the dark current drop to 10–20 pulses per second at –55°C. The photocathode temperature remains the same until nitrogen into the cup boils away. The shutter has a slot to mount optical filters. The housing body is made of "black" steel that provides a magnetic screen to some extent. The design considered above is a low cost, its long-term exploiting shows high service data.

3.4.2.2 PMTs Operation Peculiarities in Different Modes of Operation

Now we consider in more details operational peculiarities of PMTs in the direct current mode, photon-counting regime, and pulse-analog mode.

The direct current mode. Let us discuss PMT specifications shown in Table 3.2, with PMT fabricated by different manufacturers. For example, that characteristics of PMTs from Russian manufactories differ from that specified by Hamamatsu.

In each technical certificate the weight and size of a PMT are listed. Sometimes, herein a temperature range permissible for operation is specified, as well as the base indexing, the typical diagram for voltage divider and limiting operation conditions, such as the maximum current and applied voltage.

For PMTs working in the visible spectral range, PMT83, PMT100, and R2027 from Hamamatsu, the photocathode responsibility is indicated with respect to a standard illuminant A at $T = 2{,}854$ K (see Sect. 3.2.3). For PMT with Ag–O–Cs photocathodes it is approximately two times lower than that for PMT with Sb–K–Na–Cs multialkaline photocathodes. Generally, spectral responsivity of the former is well below than latter (see Fig. 3.4), it becomes greater only at $\lambda > 800$ nm. So negligible difference is caused by that the photoemission threshold for PMT with photocathodes of Ag–O–Cs type is about 1,200 nm and the standard illuminant A has relatively low temperature. At three specimens of PMT154, the photocathode responsivity for the wavelengths 140, 210 and 254.7 nm is specified as follows: 14.2, <0.28, and 0.28 mA/W, respectively. There is no opportunity to compare responsivities of these PMTs without measuring of their relative spectral responsivity functions. The author however found from his own measurements that quantum yields of photoemission at the maximum spectral curves are nearly and of order of 10–20% for PMT with CsI photocathode and with Sb–K–Na–Cs photocathode. These yields vary greatly from one sample to another.

For each PMT type, for a given anode responsivity, the applied voltage is specified as an example 10 A/lm for PMT83; 10, 100, and 1,000 A/lm for PMT100. Alternatively, for the given dynode system gain, e.g., $G = 10^6$ as for PMT154, the applied voltage is also specified. In any case, for a given value of the anode responsibility and responsibility as well, it is easily to calculate the gain. For the value of anode responsibility 1,000 A/lm for PMT100, it is approximately equal to 10^7. It should be noted that Hamamatsu specifies characteristics mentioned above only for one value of applied voltage.

For the same gain, about 10^6, dark currents of PMT100 and PMT154 differ by 1,000 times; these currents are 3×10^{-9} and 3×10^{-12} A, respectively. Dark current of PMT83 are much above then those for PMT100 and PMT154 and they achieve 3×10^{-7} A at 10 A/lm, for comparison, for PMT100, dark current is about 3×10^{-10} A at the same value of luminous responsivity.

In the technical certificate of PMT, instability and luminous equivalent of anode dark current noise sometimes are both specified for given luminous responsivity. For example, with the specimen of PMT100 discussed by the author these quantities are 1.4% and 4×10^{-13} lm/Hz$^{1/2}$ at 100 A/lm. For some types of PMT from Hamamatsu, spectral responsivity functions are specified.

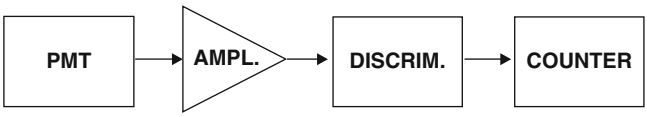

Fig. 3.14 The block diagram of photon-counting circuit. AMPL, DISCRIM, and COUNTER are amplifier, pulse discriminator and pulse counter, respectively

The photon-counting mode. The photon-counting mode of PMT operation is used for registration of very weak luminous fluxes. The operational principle is as follows. A photon achieved the photocathode knocks out a photoelectron, which with a high probability falls on the dynode system. Herein, avalanche-like increase of electrons occurs, which is accompanied by spreading energetic, as well as dynamic, electron distribution. The output current pulse is amplified by a wide-band amplifier. It is desirable to mount the amplifier inside the PMT housing. The output pulses of the amplifier pass to a registration system (Fig. 3.14).

Electrical current produced by a single photon can be evaluated as follows:

$$I = G\eta(\lambda)e/\tau, \tag{3.30}$$

where $\eta(\lambda)$ is quantum yield of photoemission, $e = 1.6 \times 10^{-19}$ is the elementary charge, G is the dynode system gain, τ is the signal transit time. For the photomultipliers listed in Table 3.2, $\eta(\lambda) \approx 0.1$, $\tau \approx 10^{-8}$ s, and for G is taken to be 10^6, we find the current I to be 2×10^{-6} A. With the amplifier input resistance equal to 10^3 Ω, its output pulse voltage achieves 2×10^{-3} V. Hence, in order to generate the output pulse voltage about 2 V, the amplifier gain should be equal to 10^3. If the threshold of action of the registration system (for example, the pulse counter) is equal to 2 V then the generated signal will be counted. In the case of a smaller output pulse, it will not be registered. Therefore, if a photon is associated with a "time broadened pulse," a long time τ, or its "electron response" gets insufficient gain [a small value of G in (3.30)], this response will not pass the pulse discriminator and they say that the photon is discriminated. It is clear that amplitudes of pulses in the PMTs output are determined by the applied voltage, the greater the applied voltage, the greater the pulse amplitude is. In turn, the greater pulse amplitude is, the greater frequency for pulse counting at the same illumination of the photocathode. Typical dependency of the pulse amount counted for a given time interval against the applied voltage is shown in Fig. 3.15.

In the initial stage of the counting response curve, a most part of pulses are discriminated, then, in the plateau, the number of pulses is approximately constant. Further increasing of the applied voltage causes incidental processes such as ionization of residual gases and so on. It makes difficulties for operation under these conditions. The plateau slope is changes from one specimen of PMT to the other. It is need the PMT to be specially picked out for operation in the photon-counting mode. In general, the fact that the PMT type is suitable for operation in such a mode is determined by its design. In particularly, the most suitable type has a

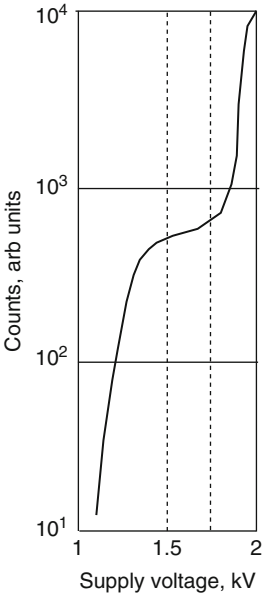

Fig. 3.15 The counting response curve for PMT100 picked for operation in the photon-counting mode [4]

small photocathode, that provides the best photoelectron collection, and a high gain as well. There are available special commercial types of PMT for operation in the photon-counting mode with extended plateaus.

Frequently, the counting response curve of *dark* current pulses is unlike to that formed by photopulses. The former has no plateau. Only a few PMTs with something liked to a plateau on the counting response curve of dark current pulses were encountered by the author during his practice. The reason is that the most contribution to dark current is provided by leakage currents inside the bulb and by electrons emitted from the first and subsequent dynodes, which have a very low energy. Thereby, the signal-to-noise ratio in the photon-counting mode is much greater than that in the direct current mode. The signal-to-noise ratio can be changed by selecting the working point of PMT. Usually, it is necessary to select the best PMTs by performing measurements of counting response curves for a set of PMTs. These curves have to be found as for dark current pulses as well for photopulses. A working point is selected in the initial part of a plateau, wherein the best signal-to-noise ratio is. By the author opinion, a PMT is assumed to be appropriate for working in the photon-counting mode, when a signal increases not more than 10% with the applied voltage increments by 100 V within the plateau. Customary, when working in the photon-counting mode, the author never change the voltage applied to PMT.

Now we consider PMT dynamic resolution in the photon-counting mode or its amplitude–frequency characteristic. It is clear, if the input pulse amplitude occurs above the registration system threshold, this pulse will be counted. Hence, if two single-electron pulses overlap in time interval equal to the time resolution, or when their repetition rate becomes comparable or greater than the bandwidth of PMT

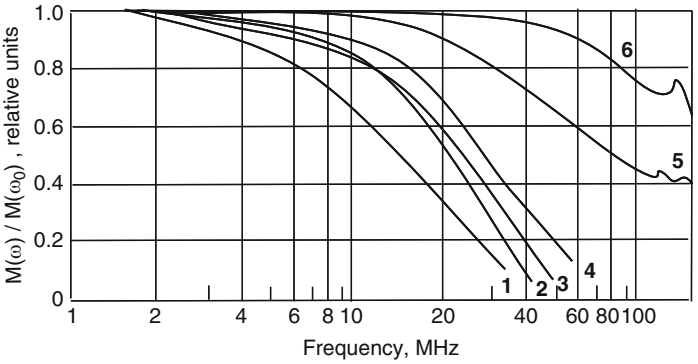

Fig. 3.16 The amplitude–frequency characteristics found for full illuminated photocathode: *1* – PMT52; *2* – PMT58; *3* – PMT51; *4* – PMT28; *5* – PMT36; *6* – PMT87 [4]

together with the registration system, the both pulses will be counted as a *single* pulse. By this is meant that counting response becomes nonlinear. It is also clear that an amplifier with a wide bandwidth is required to increase the dynamic range. Unfortunately, it leads to increasing greatly its own noise. Usually, amplifiers with the bandwidth up to 10–100 MHz are used, which allow to work with counting rates up to 10^6–10^7 pulse per second, and it should be noted that pulses are statistically distributed in time. A PMT with transit time about 10^{-8} s allows itself to pass up to 10^7 pulses per second (Fig. 3.16).

The pulsed-analog mode. This mode is used for kinetic investigation applications, such as dynamic dependencies of luminescence intensities, in particular, for measurements of luminescence decay times, or lifetimes of excited states of the objects under investigation. If these times correspond to the millisecond or microsecond range, any commercial PMT will can be used combined with an oscilloscope or box-car integrator. When working in time range in order of 10^{-8}–10^{-10} s, the problem to select a photodetector and registration system becomes more difficult. The methods developed for measuring in the ranges have been described in numerous monographs, articles, and can be find in Internet (e.g. see [2, 20, 21]). Appropriate apparatus are produced by key manufacturers, such as Hamamatsu [22, 23] and Princeton Instruments [24]. Several methods have been developed, which allow to determine luminescence decay times in the events, when the response time of registration is greater than the decay time determined by the registration system (e.g. see [2, 20]). The author with his colleagues successfully carried out experiments for measuring of luminescence decay time of 4×10^{-9} s by means of laser pulses of half width about 10 ns, PMT100 with the duration of pulsed characteristics of order of 10 ns, and with the help of solutions of a set of kinetic equations describing processes in the system under investigation [25, 26].

At the present time, Hamamatsu produce PMT with rise times and transit times in the 0.11–0.4 and 0.55–4 ns ranges, respectively. In addition, there are produced microchannel plates, MCP, consist of millions of very thin, conductive glass

capillaries, each being of 4–25 μm in diameter. The capillaries are fused together and sliced into a thin plate. Each capillary or channel works as an independent secondary-electron multiplier to form a two-dimensional secondary-electron multiplier, which is sensitive to a wide range of radiation including the UV, vacuum UV, and soft X-ray ranges. The MCP offers many advantages over conventional detectors, compact, light weight, well timing properties due to short length, high gain, excellent pulse height distribution and two-dimensional imaging when used in conjunction with a phosphor screen.

3.4.2.3 Service Conditions Providing PMT Long-Time Operation with a Stable Sensitivity

Prolonged practice allows the author to formulate the following rules.

- Use only selected PMTs, i.e., PMT tested for stability of dark current during several tens hours. Do not use PMTs showing dark current sudden change.
- Never work near maximal applied voltage and anode currents specified in the technical certifications of PMTs. It is desirable to use high-resistance voltage dividers (see Sect. 3.4.2). It provides a lower temperature for the PMT bulb and current-carrying conductors, and, in consequence, decreasing of leakage currents (Fig. 3.6).
- Keep off direct illumination on the PMT photocathode not been alive. After such a photocathode impact, PMT should be at its normal applied voltage during several hours in an absolute dark, until dark current downs to its former level.
- When cooling PMT for decreasing dark currents, do not do it strongly, because the PMT can be damaged (see Sect. 3.4.2.1). Do not cool PMT with the windows from magnesium fluoride.

3.4.3 CCD Cameras

At the present time, it is the most promise the using of so-called intensified CCD cameras combined with long-plane size spectrographs (e.g. see [24, 27]). The operational principle of CCD technology is based on utilization of properties of a small piece of silicon called a charge-coupled device to gather and imprint incident light instead of film. The silicon chip is a solid-state electronic component comprised of light-sensitive cells called photosites. Each photosite is its own pixel – just one tiny cell in the whole body of a photograph that could contain hundreds of thousands of pixels. When incoming light strikes the photosite, the photoelectric effect occurs and creates electrons for as long as exposure occurs. The electrons are then kept "stored" in their individual cells until a computer unloads the array, counts the electrons and reassembles them into the “big picture” [28, 29].

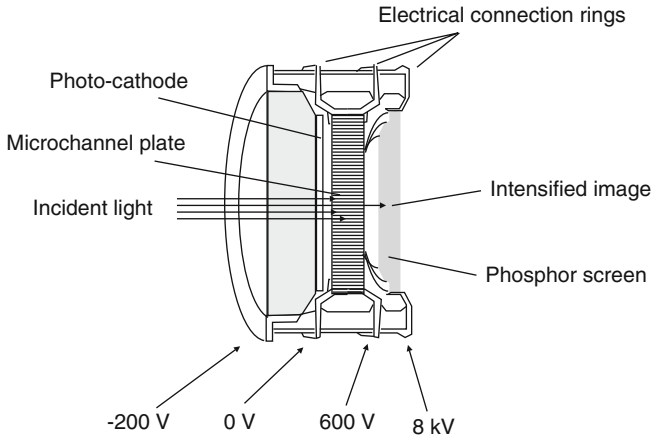

Fig. 3.17 Principle elements of image intensifier

The CCD image sensor includes an image sensing section, which performs photoelectric conversion, and a storage section, which is arranged separate from the image sensing section and temporarily stores charges acquired by the photoelectric conversion. A CCD camera involves a CCD imager IC (integrated circuit) and control circuits typically mounted on a printed wiring assembly. In CCD cameras, either a CCD matrix or one or more CCD lines are located in the focal plane behind the optical system. Charge-coupled device (CCD) camera systems are configured to capture signals according to many different CCD output formats and pixel configurations.

An image intensifier is a vacuum tube device. The intensifier comprises a photocathode input, which is a coating of multialkali or semiconductor layers on the inside of the input window, and a phosphor screen, which is a fluorescing phosphor coating on the inside of the output window. Also included are either simple grid-shaped electrodes (i.e., early intensifier technology) to accelerate electrons through the tube or MCP (Fig. 3.17).

3.5 Photodetectors with the Internal Photoeffect

Now we will discuss photodetectors based on the internal photoeffect, wherein absorbed radiation creates electric charge carriers that remain inside the detector body and either charge its conductivity or generate a voltage. In the bulk detectors (photoconductors or photoresistors) the energy of photons is transferred to conduction electrons if the former is large enough, so conductivity increases. In the junction detectors the electrons and holes are separated in the vicinity of junction of two dissimilar materials.

3.5.1 Photoconductors

There is conductivity change, or internal resistance change, within a photoresistor material under its illumination by the photon flow with the energy, which is higher than the band-gap energy in the case of intrinsic conductivity or than the band width between the levels of electron donors and conducting band in the case of impurity semiconductors. The width of the latter can be only a small, and the photoresistors made up from impurity semiconductors have a low work function, e.g., 0.18 eV at $\lambda_{max} = 6.9$ μm for InSb, very high dark currents at temperatures near the room temperature. A primary advantage of photoresistors is in ability to register IR radiation. Nevertheless, there are available photoresistors, which have a larger work function, e.g., ZnS photoresistor has the work function of value 3.6 eV, $\lambda_{max} = 345$ nm. The general disadvantage of photoresistors restricted their application in metrology is nonlinearity, namely, the photocurrent $I = U/R$ is only roughly linear with intensity. Additionally, responsibility of photoresistors is dependent on temperature, and illumination affects this dependency. Finally, there is a so-called initial state effect, where conductivity is greater, all other factors being equal, providing the photoresistor was kept in dark for a time before its using (see [1, 2]).

3.5.2 Junction Photodetectors

A *photodiode* is a *p–n* junction or PIN structure [30]. A *p–n* junction is formed by joining *p*-type and *n*-type semiconductors together in very close contact. It is the boundary interface where the two regions of the semiconductor meet that refers junction. If they were constructed of two separate pieces this would introduce a grain boundary, so *p–n* junctions are created in a single crystal of semiconductor by doping. For example it may be produced by ion implantation, diffusion of dopants, or by epitaxy (growing a layer of crystal) [31].

A *p–i–n diode* is a diode with a wide, lightly doped "near" intrinsic semiconductor region between a *p*-type semiconductor and an *n*-type semiconductor regions. The *p*-type and *n*-type regions are typically heavily doped because they are used for ohmic contacts [32]. When a photon of sufficient energy strikes the diode, it excites an electron, thereby creating a mobile electron and a positively charged electron hole. If the absorption occurs in the junction's depletion region, or one diffusion length away from it, these carriers are swept from the junction by the built-in field of the depletion region. Thus holes move toward the anode, and electrons toward the cathode, and a photocurrent is produced [1, 2, 30]. A photodiode is capable of converting light into either voltage or current, depending upon the mode of operation [30].

Photovoltaic mode. When used in zero bias or photovoltaic mode, the flow of photocurrent out of the device is restricted and a voltage builds up. The diode becomes

forward biased and dark current begins to flow across the junction in the direction opposite to the photocurrent. This mode is responsible for the photovoltaic effect.

Photoconductive mode. In this mode the diode is often *reverse biased,* dramatically reducing the response time at the expense of increased noise. This increases the width of the depletion layer, which decreases the junction's capacitance resulting in faster response times. The reverse bias induces only a small amount of current (known as saturation or back current) along its direction while the photocurrent remains virtually the same. The photocurrent is linearly proportional to the illuminance.

Avalanche photodiodes have a similar structure to regular photodiodes, but they operate with much higher reverse bias. This allows each *photogenerated* carrier to be multiplied by *avalanche breakdown* (when the voltage is high enough the free electron may move fast enough to knock other electrons free, creating more free-electron–hole pairs, increasing the current. "Fast-moving" holes may also result in more electron-hole pairs being formed. In a fraction of a nanosecond, the whole crystal begins to conduct, resulting in internal gain within the photodiode, which increases the effective *responsivity* of the device).

Phototransistors also consist of a photodiode with internal gain. A phototransistor is in essence nothing more than a bipolar transistor that is encased in a transparent case so that light can reach the *base–collector junction*. The electrons that are generated by photons in the base–collector junction are injected into the base, and this photodiode current is amplified by the transistor's current gain G. Note that while phototransistors have a higher responsivity for light they are not able to detect low levels of light any better than photodiodes. Phototransistors also have slower response times.

The Si ($\lambda \approx$ 190–1,100 nm), Ge ($\lambda \approx$ 400–1,700 nm), InGaAs ($\lambda \approx$ 900–1,700 nm), InAs ($\lambda \approx$ 800–3,700 nm) and PsS ($\lambda \approx$ 1,000–3,500 nm) are commonly used as materials for photodiodes (see [1] and references). The maximum responsivity range of planar diffused silicon photodiodes with quantum yield 0.7–0.9 is extensively used at the wavelength 700–900 nm. Note that spectral sensitivity of a photodiode may alter without use due to aging.

3.6 Luminescence Quantum Counters

It is well known that fast relaxation of molecular excitation energy takes place in condensed phase such as liquids and molecular crystals [33, 34] (see Sect. 3.8.4). In some systems, luminescence occurs from lower vibrational levels of a lower singlet state regardless of what electronic state the molecule absorbed photon passes on. Additionally, with some approximation the spectrum of luminescence and quantum yield of luminescence are both independent upon wavelength of incident light in some wavelength interval. Of course this interval, uncertainty, and conditions of luminophor preparation, the all are required to be determined by somebody in practice. Whereas a user should follow these methods for preparation and using

of the luminophor as that were described in the origin. The luminophor you use, particularly if a molecular crystal with a low vapor tension at the given temperature and nonreactive with substances you study, can be put into a cell or on the external side of the outer PMT window to avoid thereby influence of transparency effect of the window cell. This is especially important when working in the vacuum UV range. It is obvious, it should be provided with filtration for exciting radiation to provide detection by the registration system luminescence generated by the required radiation range. Among a wide range of recommended luminophors suitable for application in the UV and vacuum UV ranges the most approved is sodium salicylate. The author also investigated its characteristics (see Sect. 4.2.2.3). Numerous researches show that a layer of sodium salicylate, for example, applied in alcoholic solution, possesses an invariable luminescence quantum yield with the uncertainty of 10% in the range 10–340 nm (see [35] and references). In particular, we found that the relative luminescence quantum yield remains the same in the limits of 5% at $\lambda = 123.6$ and 147 nm (Pravilov, A.M., Sidorov, I.I., Smirnova, L.G.: unpublished data, 1984) [36, 37]. It was also found that it is possible decreasing the quantum yield in the range $\lambda \leq 160$ nm after several days [35]. Most probably, it is determined by clearness of luminophor and its environment, for instance, if luminophor was polluted by an oil vapor its working characteristics degrade. We note once more that absolute measurements of radiation and quantum yields, especially, in the vacuum UV range are very difficult. The researcher should follow carefully all recommendations and keep up thoroughly with purity of experiments. More details regarding luminophors for the UV and vacuum UV ranges can be found in the monograph [35].

3.7 Photoionization Chambers

Some authors believe that photoionization chambers are almost ideal detectors in the vacuum UV range (e.g., see [38, 39]). It is evidently true with respect to double ionization chambers based on inert gases because their quantum yield is equal to unity above the threshold. Unfortunately, these chambers should be designed in the windowless version, because the ionization potential for xenon is 12.12 eV, that is associated to the wavelength 102.2 nm, whereas the transmission limit for the rather firm material with the shortest wavelength limit such as LiF is about 105 nm [35].

With using a closed ionization chamber, the intensity of radiation passed through the input window is given as follows:

$$\Phi_{h\nu} = \left(\frac{\sigma_0}{\sigma_\mathrm{i}}\right)\left(\frac{I}{e}\right)\left(\frac{1}{1-\exp[-\sigma_0\ N\ l]}\right) \tag{3.31}$$

where σ_0 is the total cross section and σ_i is the cross section of ionization, N is the ionized gas concentration, l is the cell length, wherein collection of ions is provided (Fig. 3.18), $I/e = n$ is the number of pairs of charged carriers, i.e., electrons and ions, generated for this length.

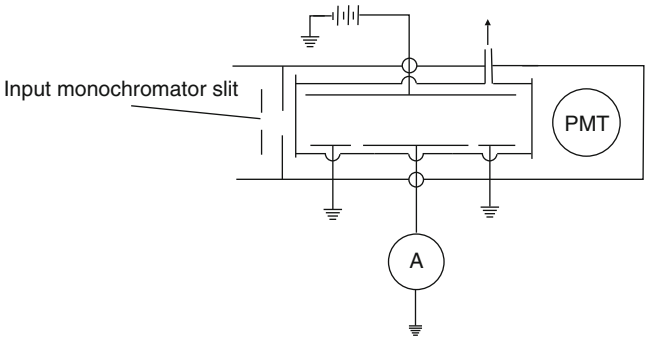

Fig. 3.18 Closed photoionization chamber [35]

Fig. 3.19 Photocurrent versus voltage applied to the ionization chamber electrodes

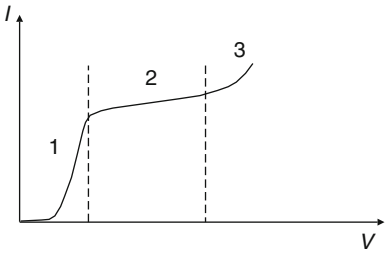

It is clear that the measurement uncertainty is mainly determined by uncertainties of the absolute quantum yield of ionization, total cross section, current value which gives the number of charge carrier pairs, and for opened chamber by the accuracy of N. Figure 3.19 shows a typical current–voltage dependency, where the initial part (1) is associated with an incomplete collection of carriers, the middle part is associated with almost complete collection of carriers, and secondary ionization by accelerated electrons is associated with the third part of the dependency. It is seen that photocurrent in the part 2 of the curve can be measured with an uncertainty, often, of order of 3–10%. All the factors above lead to a large total uncertainty of measuring of $\Phi_{h\nu}$. A method for decreasing such uncertainties was developed in the author's laboratory [37] (see Sect. 4.2.2.2).

It has been mentioned, when working with inert gases, it is lead to use open ionization chambers with differential pumping, having difficulties in determination of N. When working with double ionization chamber filled with a rare gas, the uncertainty of measuring $\Phi_{h\nu}$ can be decreased sufficiently. This allows to avoid estimation of N, provided there is the absence of concentration gradient, i.e., both the input and output opening are rather small (Fig. 3.20, [35]).

Having been measured currents in both parts of the double ionization chamber, the product σN can be estimated according to the formula:

$$\sigma N = \frac{1}{d} \ln \frac{I_1}{I_2}. \tag{3.32}$$

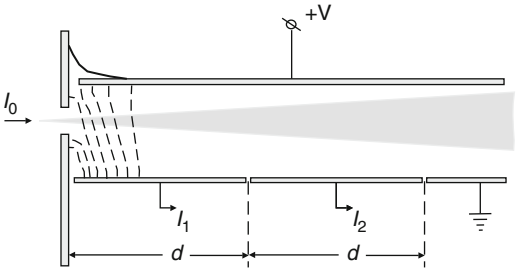

Fig. 3.20 Schematic diagram of double ionization chamber. The *dashed lines* indicate field lines; the potential of the upper plate is equal to that of the input slit [35]

3.8 Chemical Photodetectors

The measurements of photoluminescence intensity as well as photochemical change rate in such effects as photodecay, photoabsorption, photocatalysis and others are frequently suggested as a means for measuring actinic light in absolute units in reactor designed for research of photochemical change rate. Virtually, these chemical techniques have important advantages with respect to physical methods described in previous sections.

With making absolute measurements of radiation intensity, the provision of layout identity is a central problem in the following situations:

- Measuring of intensity assigned for irradiation of an investigated sample in order to find the quantum yield of photoprocess
- Calibrating of registration system assigned for measurements of radiation intensity

Thus, on investigating of photoprocess with gaseous, liquid, or solid sample placed into a cell, minimal errors may be caused by non-identity of illumination layout, all other factors being the same [33, 34, 40, 41]. If you study luminescence, the photodetector should be well-known luminous calibrated photodetector (luminescence quantum counter).

Now we consider photodetectors based on chemical reactions occur under action of incident light. The stable product yield or decreasing of parent product concentration in reaction should be measured. At given conditions, photoprocess stable products do not react with the environment, or the rate of such a reaction is sufficient slow. Techniques of this kind are treated as *actinometry*, and the chemical systems used in actinometry are called (*chemical*) *actinometers*. On investigating photoprocesses in condensed phase, it is best to use liquid-phase or solid-state actinometers, for processes in gas phase, gas-phase actinometers are most suitable. In that event we reduce the uncertainties associated with light reflection on the boundary of two media, and also some other errors. By actinometers are often meant a more wide class of devices for measuring of radiation intensity. According to the "*Glossary of terms used in photochemistry* (*IUPAC Recommendation 1996*)" [42], (see [43], also) an actinometer is a chemical system or a physical device by which the number of photon in a beam absorbed into the defined space of a

chemical reactor can be determined integrally or per time. A *chemical actinometer* or dosimeter is a chemical system (fluid, gas, solid or in a microheteregenous environment) that undergoes a light-induced reaction, at a certain wavelength, λ, for which a quantum yield of the photoprocess utilized in actinometry $\Phi_A(\lambda)$ is accurately known [43]. The subscript *A* denotes the product whereby the actinometer photochemical rate is determined. Further, we denote chemical actinometers just simply actinometers. Owing to the recent progress in the development of physical radiation detectors, these devices furnishes with a direct readout become more and more popular among photochemists for the measurements of radiation intensity. These detectors are often preferred to actinometers for the case of simple irradiation geometries. However, these outstanding properties are inherent in only electrical substitution radiometers (see Sect. 3.3.2). The majority of physical detectors (see Sect. 3.1–3.6) are only secondary standards, which responsivity has to be recalibrated. For example, the sensitivity of thermal detector may decrease with use due to surface damage by high power radiation. The spectral sensitivity of a photodiode may alter without use due to aging. An 18% decrease in sensitivity at 300 nm in 1 year was reported to be a typical value [43]. Visually unnoticeable damage of photodiodes occurs during exposure to high irradiation levels (generally, more than 10 mW/cm^2 for silicon photodiodes in continuous wave experiments) resulting in an irreversible decrease of sensitivity and severe inhomogeneities in the surface (see [43] and references). Spectral sensitivity may be affected by both factors as a high irradiation level as well aging (see Sect. 3.4). In contrast to physical detectors, well-established actinometers lead to accurate absolute radiation intensity measurements, provided that they are employed according to recommended procedures. These actinometers have been proven reproducible and *do not demand recalibration*.

3.8.1 Requirements to Well-Established Actinometers

An established actinometer should meet the following requirements [40, 43].

1. The photochemical system should be simple and well studied. The photoprocesses have to be reproducible under well defined and easily controllable experimental conditions. Quantum yields $\Phi_A(\lambda)$ should be accurately measured in wide spectral range. The wavelength-independent quantum yield is desired. It is also desired that the quantity $\Phi_A(\lambda)$ has not to be determined by competition of the primary and secondary photochemical processes having similar rates, that means the quantum yield *to be determined theoretically and to be an integer number*.
2. Chemical components of an actinometer and its stable products should be thermally and chemically stable to exclude complications due to dark reactions.
3. The measurement method of yields for the photoprocesses should be simple. It is desired the apparatus for the measurements to be not needed for recalibration.

4. It is desirable to use an actinometer display with a high responsivity.
5. The handling of the photochemical system and the evaluation of the photon flux, Φ_{hv} [radiation intensity, I_{hv} (see Table 1.1)] should be simple and straightforward.
6. The actinometric material should be easy to synthesize and purify. Preferably, it should be commercially available.

Among the actinometers proposed in the literature [2, 33, 34, 43], there is only a few part of them, which meet requirements above. More detailed description of the actinometers, limitations, and possible uncertainties for each of them are listed in the following sources [2, 33, 34, 40, 43]. Reading of original literature prior use the actinometer is highly recommended. A great amount of gas-phase actinometers were approved in the author's laboratory. The reader can therefore found below all essential information required for working with them.

3.8.2 Basic Advantages of Actinometers

The basic advantages of actinometers are as follows.

- By choosing the cell diameter, or the input diaphragm, and cell length, as well as concentration of the actinometer material, it is possible to obtain absorption within the special range you require, as well to absorb the light beam of any desired shape and uniformity. An ideal actinometer has no nonuniformity like that inherent most of physical phodetectors.
- If the quantum yield of the photoprocess is independent upon wavelength, the actinometer can be used as a photon counter of a polymonochromatic beam. Here is not a need to measure the radiation spectrum.
- There is no need for taking into account transmission of windows, light reflection from walls of the photodetector and cell used for analysis of the photoprocess. (peculiarities exist with such measurements, they will be discussed in Sect. 4.2.1.4).
- An actinometer is an integrating system and it absorbs a total amount of radiation for exposure time, whether the intensity is invariable or fluctuating.

Some applications of the gas-phase actinometers are described in the next sections of the book. The working range of the actinometer is the spectral range, wherein the quantum yield $\Phi_A(\lambda)$ of the photochemical process is nonzero and well-known. It is clear, that this spectral range should be within the transparency range of the cell entrance window. As with any other kind of metrological operations, when measuring the radiation intensity by means of an actinometer, it should be well known the operating capabilities such as photon energies, pressure and concentrations of actinometer components, temperature and dynamic range in terms of incident radiation intensity limits. At given operating capabilities, the

actinometer is a high-reliability means with a well-known measuring uncertainty of given confidence level.

While measuring the spectral radiation intensity from a *resonance* light source I_{hv} passing through the entrance window, the cell should be irradiated for the time interval t_{ph} . The measured total number of molecules generated as a photolysis reaction product is $[A]V$, where V is the volume of the system with the product concentration of $[A]$, gives the radiation fraction absorbed by the actinometer I_{abs}/I_0. The quantity I_{hv} is calculated to be as follows:

$$I_{hv} = \frac{I_0\,[A]\,V}{I_{\text{abs}}\,\Phi_{\text{A}}\,t_{\text{ph}}}. \tag{3.33}$$

It is seen that the uncertainty in measuring of $I_{hv}(\lambda)$ is mainly determined by the accuracy of I_{abs}/I_0, Φ_{A}, and $[A]$, since V and t_{ph} can be found with a very low uncertainties. When working with the 100% absorption, at the quantum yield equal to even number, then the measuring error is determined only by the uncertainties of $[A]$.

The actinometer sensitivity is mainly dependent on two factors:

1. The sensitivity of the method applied for measuring of the photolysis stable product concentration.
2. The dark decomposition rate of the actinometer (NOCl, HI, HBr, HCl) or the photolysis stable products (O_3).

Photoprocesses in gas-phase and liquid-phase differ dramatically. We briefly discuss some photochemical principles and definitions as that will be used in the following consideration.

3.8.3 Primary and Secondary Photochemical Processes. Quantum Yields of the Gas-Phase Photoprocesses

What does it need to understand as *primary* and *secondary* photolysis processes of molecules? These conceptions in gas-phase photochemistry should be distinguished from that in photochemistry of condensed systems. In addition, terminology of this field of science, at least in gas-phase photochemistry, does not settle yet. Definitions for basic terms are either absent or not implicit. The situation may lead to terminological confusions and mistakes. The author gives a number of definitions that will be used further.

Let us consider the processes taking place with photolysis of a *free molecules* by means of photons of energy hv, provided the photon energy is less than their ionization potentials [41] (Fig. 3.22). Free molecules are taken to mean that the molecules are in conditions patient of free recession of their fragments without a

so-called *cage effect*, i.e., the molecules in gas-phase at not-to-high pressures, less than 10 bars.

$$\mathrm{AB} + h\nu \rightarrow \mathrm{AB}^*(v, J) \rightarrow \mathrm{A}_1 + \mathrm{B}_1 \tag{3.34}$$

$$\rightarrow \mathrm{A}_2 + \mathrm{B}_2 \tag{3.35}$$

$$\rightarrow \mathrm{A}_\mathrm{i} + \mathrm{B}_\mathrm{i} \tag{3.36}$$

$$\rightarrow \mathrm{AB}^{**} + h\nu \tag{3.37}$$

$$\leftrightarrow \mathrm{AB}^{**} \tag{3.38}$$

$$\mathrm{AB}^*(v, J) + \mathrm{M} \rightarrow \mathrm{AB}^{**} + \mathrm{M} + \Delta E_1 \tag{3.39}$$

$$\leftrightarrow \mathrm{AB}^{**} + \mathrm{M} \tag{3.40}$$

$$\rightarrow \mathrm{AB}^{**} + \mathrm{M} + \Delta E_2 (\ \Delta E_2 > \Delta E_1) \tag{3.41}$$

$$\rightarrow \mathrm{AB}^*(v - \Delta v, J - \Delta J) + \mathrm{M} + \Delta E \tag{3.42}$$

$$\rightarrow \mathrm{B}_\mathrm{i} + \mathrm{C}_\mathrm{i} \tag{3.43}$$

$$\rightarrow \text{products} \tag{3.44}$$

$$\mathrm{AB}^*(v - \Delta v, J - \Delta J), \mathrm{AB}^{**} \xrightarrow{(\mathrm{M})} \text{products} \tag{3.45}$$

$$\mathrm{B}^*_\mathrm{k} \rightarrow \mathrm{C}_\mathrm{j} + \mathrm{D}_\mathrm{j} \tag{3.46}$$

$$\mathrm{B}_\mathrm{k} + \mathrm{M} \rightarrow \text{products} \tag{3.47}$$

$$\mathrm{B}^*_\mathrm{k} \rightarrow \mathrm{B}^{**}_\mathrm{k} + h\nu \tag{3.48}$$

$$\mathrm{B}^*_\mathrm{k} + \mathrm{M} \rightarrow \mathrm{B}^{**}_\mathrm{k} + \mathrm{M} \tag{3.49}$$

$$\rightarrow \mathrm{B}^*_\mathrm{k}(v - \Delta v, J - \Delta J) + \mathrm{M} \tag{3.50}$$

where $\mathrm{AB}^*(v, J)$ are rovibronic states of the diatomic or polyatomic molecule resulting after absorption by the molecule AB a photon of energy $h\nu$. AB^{**} are all other rovibonic states including those of the ground state of the molecule, $\mathrm{A_i}$, $\mathrm{B_i}$ are both their fragments.

Photolysis processes are classed as *primary* processes and *secondary* ones.

Primary photolysis processes include photon absorption by the molecule AB and degradation of excited energy for the resultant rovibronic state AB*(v,J), both proceeding *without* another particles M (any medium particle, wall). Among the many primary photolysis processes are as follows:

- Formation AB*(v,J) [reaction (3.34); the period of optical transition 10^{-15} s]
- *Dissociation* (AB*(v,J) lifetime, $\tau_{AB^*} \leq 10^{-12}$ s), predissociation ($\tau_{AB^*} \geq 10^{-13}$ s), diabatic decay of AB*(v,J) bound state or AB*(v,J) unbound state into A, B products, including those in excited states [reactions (3.35 and 3.36)] ($\tau_{AB^*} > 10^{-13}$ s) [41, 44, 45]
- *Luminescence* of AB*(v,J) molecule avoided electronic collisional deactivation or vibrational–rotational (rovibrational) relaxation [$\tau_{AB^*} > 10^{-9}$ s, reaction (3.37)]
- *Spontaneous internal conversion*, a nonadiabatic or *diabatic* transition, into another electronic bound state AB, including *intercombinative* conversion [$\tau_{AB^*} > 10^{-13}$ s, reaction (3.38)].

Photodecay, or *photodecomposition*, of molecule AB – is the primary photolysis process reducing the AB* concentration, [AB*], i.e. photon absorption accompanied by *dissociation, predissociation, diabatic decay* of AB*(v, J) into fragments of the AB molecule.

Secondary photolysis processes are the processes proceeding with collision AB* (v, J) with a particle M and hereupon, as well as the processes proceeding with photodecay products of AB. Secondary photolysis processes include the follows.

- *Collisional deactivation* of AB*(v,J) into other electronic state including the ground state (*electronic deactivation*), it is the process proceeding with a great loss of energy by the AB*(v,J) molecule; this process excludes a possibility to reverse to the AB*(v,J) electronic state [reaction (3.39)] (Fig. 3.21).
- *Collision-induced nonadiabatic transition*, *CINAT* (see [46] and references), into other bound electronic state; this process proceeds with a low loss of the excited energy of AB*(v,J), this process allows a reverse transfer [reaction (3.40)];
- The process similar considered above proceeding with a high loss of energy (ΔE_2); this process allows a reverse transfer only to lower rovibronic levels AB* ($v-\Delta v$,$J-\Delta J$) [reaction (3.41)]
- *Rotational, vibrational*, and *rovibrational relaxation* of AB*(v,J) within the limits of one electronic state [reaction (3.42)]
- *Collision-induced predissociation* or *diabatic decay* of AB*(v,J) into AB fragments, including that coincide in appearance with photodecay products of *AB* (in other words, with primary products of photolysis or primary photoproducts) [reaction (3.43)]
- Reaction involving AB*(v,J) [reaction (3.44)]
- *Decomposition* of AB*($v-\Delta v$,$J-\Delta J$) and AB** states (*spontaneous and collision-induced*) including: dissociation, predissociation, diabatic decay, and luminescence [reaction (3.45)]

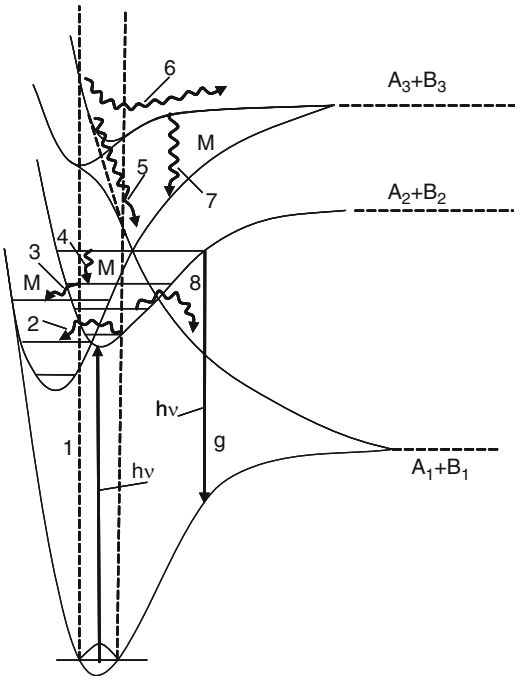

Fig. 3.21 The processes accompanying photon absorption by a free molecule [41] *1* – photon absorption; *2* – nonadiabatic transition into other bound state; *3* – collisional induced nonadiabatic transition into the other bound state at not-too-high loss energy; *4* – rovibrational relaxation within one state; *5* – spontaneous or collisional diabatic decay of a bound state; *6* – dissociation; *7* – collisional electronic deactivation (quenching); *8* – spontaneous predissociation or collision-induced predissociation; *9* – luminescence

– *Spontaneous decay* of one of the photodecay products of AB* – B_k^* into fragments, including that coincide with any of the photodecay products of AB [reaction (3.46)], they also include reaction with photodecay products of AB [reaction (3.43)], luminescence of these products [reaction (3.48)], electronic deactivation [reaction (3.49)], rotational, vibrational and rovibrational relaxation [reaction (3.50)] and so on.

Noyes W.A, Leighton P.A. [47] and, in the wake of them, Okabe [48], all proposed to also include as primaries the processes proceeding with AB*(*v*,*J*) and another particles [reactions from (3.39 to 3.45)]. They also proposed to assume by secondary processes that proceed only with photodecay products of B_i, C_i [reactions from (3.46) to (3.50)]. Methodologically, in the case of gas phase, such a definition is wrong as following. Such a "absolute quantum yield for primary photolysis processes" depends upon of kind and pressure of gases, the ratio of surface area of the reactor to its volume and so on, i.e., it is no any *molecular constant describing for the molecule features*.

The reactions (3.39) to (3.45) are usual mono-, bi-, and trimolecular reactions of excited particles, which are not in thermodynamic equilibrium with environment. These reactions should be described by means of reaction rate constants depending on the AB*, AB** states, rather than by the absolute quantum yield.

In practice, the applying of the primary process definition we used some methodological problems may arise caused by that primary and secondary photolysis products resulting in the reactions from (3.34) to (3.36) and the reaction (3.46),

i.e., in decay processes of AB*(v,J) and spontaneous decay of decay product of AB*(v,J) − B_i, may be the same (they do not coincide in losing energy as well as kinetic one). For example, the ethylene molecule C_2H_4 may be formed in photolysis by two ways: in the reaction (3.51), or in the reaction (3.52, 3.53) as follows:

$$C_2H_5I + h\nu \rightarrow C_2H_5I^* \rightarrow C_2H_4 + HI \tag{3.51}$$

$$\rightarrow C_2H_5{}^{\neq} + I \tag{3.52}$$

$$C_2H_5{}^{\neq} \rightarrow C_2H_4 + H \tag{3.53}$$

where the symbol "$\neq$" denotes rovibrational excitation.

In the case that the reaction (3.53) is dissociation or allowed predissociation ($\tau_{C_2H_5} \leq 10^{-11}$ c), it is possible to determine if the C_2H_4 is the primary or secondary photolysis product by analysis of absolute quantum yield of formation C_2H_4 as function on rate of rovibrational relaxation or pressure of $C_2H_5{}^{\neq}$ radicals acceptor. If this is the case, the process rate of (3.53) should be much less than the process rate of (3.51). If the reaction (3.53) is vastly forbidden predissociation, for analyzing of C_2H_4 formation, it may be very useful to study formation dynamic and angular distribution of C_2H_4 and other products of C_2H_5I photolysis. The processes similar to (3.53) are specific to photolysis of large molecules, however they may also take place with photolysis of triatomic ones.

1. The *absolute quantum yield of the product* of the AB photolysis, $\Phi_{B_i}^{AB}(\lambda)$, (e.g. AB photodecay product of B_i) is the ratio of concentration change of photolysis product *per unit time* (3.54) or *per light pulse interval* (3.55) to the amount of absorbed photons per unit volume, which causes this concentration change:

$$\Phi_{B_i}^{AB}(\lambda) = \frac{d[B_i]/dt}{n_{h\nu}(\lambda)} \tag{3.54}$$

$$\Phi_{B_i}^{AB}(\lambda) = \frac{d[B_i]}{n_{h\nu}^{p}(\lambda)} \tag{3.55}$$

where $n_{h\nu}(\lambda)$, photon/cm^3 s [formula (3.54)], and $n_{h\nu}^{p}(\lambda)$ photon/cm^3 pulse [formula (3.55)] are volumetric density of absorbed radiation. The definition (3.54) is suitable for stationary photolysis, and the definition (3.55) – for pulsed photolysis.

2. *The absolute quantum yield for i-th process of AB molecule photodecay*, $\varphi_i^{AB}(\lambda)$, is the ratio of the concentration change taken with the minus symbol for photolyzed particles of AB due to *i-th* process per unit time [formula (3.56)] or light pulse interval [formula (3.57)] to the absorbed radiation density:

$$\varphi_i^{AB}(\lambda) = -\frac{(d[AB]/dt)_i}{n_{h\nu}(\lambda)}, \tag{3.56}$$

$$\varphi_i^{\mathrm{AB}}(\lambda) = \frac{(\mathrm{d}[\mathrm{AB}])_i}{-n_{hv}^p(\lambda)(\lambda)}. \tag{3.57}$$

It is obvious that for photodecay processes the following is true:

$$\Phi_{\mathrm{A_i}}^{\mathrm{AB}}(\lambda) = \Phi_{\mathrm{B_i}}^{\mathrm{AB}}(\lambda) = \varphi_i^{\mathrm{AB}}(\lambda) \leq 1.$$

3. *The integral absolute quantum yield of photodecay* of *AB*, $\varphi_{\mathrm{AB}}(\lambda)$:

$$\varphi_{\mathrm{AB}}(\lambda) = \sum_i \varphi_i^{\mathrm{AB}}(\lambda). \tag{3.58}$$

Evidently, $\varphi_{\mathrm{AB}}(\lambda) \leq 1$. The quantity $\varphi_{\mathrm{AB}}(\lambda) < 1$, if rates of reactions (3.34)–(3.36) are comparable with those of secondary processes.

4. *The absolute luminescence quantum yield* of AB or photodecay products AB – $\mathrm{B_i}$, $\Phi_{\mathrm{lum}}(\lambda)$, is the ratio of the photon amount emitted by unit volume, which can be calculated to be a quantity per time unit:

$$I_{hv}^{\mathrm{lum}} = \int_{\lambda_1}^{\lambda_2} I_{hv}^{\mathrm{lum}}(\lambda)\mathrm{d}\lambda, \ \mathrm{photon/cm^3 s} \tag{3.59}$$

or to be a quantity per light pulse:

$$N_{hv}^{\mathrm{lum}} = \int_{\lambda_1}^{\lambda_2} N_{hv}^{\mathrm{lum}}(\lambda)\mathrm{d}\lambda, \ \mathrm{photon/cm^3 pulse}, \tag{3.60}$$

to the density of absorbed radiation calculated to be in the following forms respectively:

$$\Phi_{\mathrm{lum}}(\lambda) = I_{hv}^{\mathrm{lum}}(\lambda)/n_{hv}(\lambda) \tag{3.61}$$

and

$$\Phi_{\mathrm{lum}}(\lambda) = N_{hv}^{\mathrm{lum}}(\lambda)/\, n_{hv}^p\,(\lambda), \tag{3.62}$$

where $I_{hv}^{\mathrm{lum}}(\lambda)$ and $N_{hv}^{\mathrm{lum}}(\lambda)$ is the luminescence radiation intensity with limits λ_1, λ_2 expressed in photon/cm^3 s nm and photon/cm^3 pulse nm, respectively.

In general, all the absolute quantum yields are function of wavelength of excited radiation.

The definitions (3.59)–(3.62) differ essentially from that represented in some monographs. Here, by the absolute quantum yield of primary products is meant the yield measured under *monochromatic* radiation within the wavelength interval $\lambda \pm \Delta\lambda$, within of which the quantum yields are independent of wavelength of photolysis radiation, and within unit volume, where $n_{hv}(\lambda) = \mathrm{const}$, compare

with [48]. The remark above is essential with study secondary processes, the rate of which may depend upon the quantities $n_{hv}(\lambda)$, $n_{hv}^{p}(\lambda)$.

5. *The integral absolute quantum yield i-th process of AB molecule photodecay*, φ_i^{AB}, within the absorption band of AB is defined as follows. It is equal to the ratio of the area $\sigma_i^{\mathrm{AB}}(\lambda)$ under the spectral curve of AB partial absorption cross section, which leads to the *i*-th process, to the total area $\sigma_{\mathrm{AB}}(\lambda)$ under spectral curve of AB within the absorption band of AB:

$$\varphi_i^{\mathrm{AB}} = \frac{\int\limits_{\lambda_1}^{\lambda_2} \varphi_i^{\mathrm{AB}}(\lambda)\,\sigma_{\mathrm{AB}}(\lambda)\mathrm{d}\lambda}{\int\limits_{\lambda_1}^{\lambda_2} \sigma_{\mathrm{AB}}(\lambda)\mathrm{d}\lambda} = \frac{\int\limits_{\lambda_1}^{\lambda_2} \sigma_i^{\mathrm{AB}}(\lambda)\mathrm{d}(\lambda)}{\int\limits_{\lambda_1}^{\lambda_2} \sigma_{\mathrm{AB}}(\lambda)\mathrm{d}\lambda}. \tag{3.63}$$

Virtually, this ratio is the ratio of the oscillator strength of the optical transition reducing to *i*-th photodecay channel to the sum of the oscillator strengths of all transitions taking place within the band [41, 48]. Its value is characteristic of the optical transition probability for photodecay of AB into *i*-th channel, this value is very useful in theoretical evaluations.

6. *The integral absolute quantum yield for formation of the product* of AB photodecay $\mathrm{B_i}$, $\Phi_{\mathrm{B_i}}^{\mathrm{AB}}$, is found to be as follows:

$$\Phi_{\mathrm{B_i}}^{\mathrm{AB}} = \frac{\int\limits_{\lambda_1}^{\lambda_2} \Phi_{\mathrm{B_i}}^{\mathrm{AB}}(\lambda)\,\sigma_{AB}(\lambda)d\lambda}{\int\limits_{\lambda_1}^{\lambda_2} \sigma_{\mathrm{AB}}(\lambda)d\lambda} = \frac{\int\limits_{\lambda_1}^{\lambda_2} \sigma_i^{\mathrm{AB}}(\lambda)\mathrm{d}(\lambda)}{\int\limits_{\lambda_1}^{\lambda_2} \sigma_{\mathrm{AB}}(\lambda)\mathrm{d}\lambda}, \tag{3.64}$$

where $\sigma_{\mathrm{AB}}(\lambda)$ is the spectral function of absorption cross section for AB.

7. *The convolution quantum yield of i-th primary photoprocess* within the band λ_j/λ_k, $\varphi_i^{\mathrm{AB,c}}\left(\lambda_j - \lambda_k\right)$, is defined as follows:

$$\varphi_i^{\mathrm{AB,c}}\left(\lambda_j - \lambda_k\right) = \frac{\int\limits_{\lambda_j}^{\lambda_k} \varphi_i^{\mathrm{AB}}(\lambda)\, I_0(\lambda)\{1 - \exp\{\sigma_{\mathrm{AB}}(\lambda)[\mathrm{AB}]l\}\}\mathrm{d}\lambda}{\int\limits_{\lambda_j}^{\lambda_k} I_0\{1 - \exp\{\sigma_{\mathrm{AB}}(\lambda)[\mathrm{AB}]l\}\}\mathrm{d}\lambda}, \tag{3.65}$$

where $I_0(\lambda)$ is the radiation spectrum of light passing into the photochemical cell, l is the cell length.

8. The convolution quantum yield for formation of the $\mathrm{B_i}$ photoproduct, $\Phi_{\mathrm{B_i}}^{\mathrm{AB,c}}\left(\lambda_j - \lambda_k\right)$, is calculated to be as follows:

$$\Phi_{\mathrm{B_i}}^{\mathrm{AB,c}}\left(\lambda_j - \lambda_k\right) = \frac{\int\limits_{\lambda_j}^{\lambda_k} \Phi_{\mathrm{B_i}}^{\mathrm{AB}}(\lambda)\, I_0(\lambda)\{1 - \exp\{\sigma_{\mathrm{AB}}(\lambda)[\mathrm{AB}]l\}\}\mathrm{d}\lambda}{\int\limits_{\lambda_j}^{\lambda_k} I_0\{1 - \exp\{\sigma_{\mathrm{AB}}(\lambda)[\mathrm{AB}]l\}\}\mathrm{d}\lambda} \tag{3.66}$$

In common case, values of the quantities $\varphi_i^{\mathrm{AB,c}}\left(\lambda_j - \lambda_k\right)$, $\Phi_i^{\mathrm{AB,c}}\left(\lambda_j - \lambda_k\right)$ are determined by the mutual position of the curves $I_0(\lambda)$, $\sigma_{\mathrm{AB}}(\lambda)$, $\varphi_i^{\mathrm{AB}}(\lambda)$, the quantities [AB], l. Hence, the convolution quantum yields are dependent on experimental conditions, i.e., are all incommensurable quantities. Nevertheless, you may often encounter articles, where authors deal with photolysis processes of very weak intensities in a wide spectral range, wherein the quantum yields of the photoprocesses have not invariable values.

3.8.4 Photoprocesses in Condensed Phase

Photoprocesses in condensed phase differ dramatically from that in gas phase due to high molecular concentration. For example, in water, where $N \approx (1/18) \times 6 \times 10^{23}$ cm^{-3}, the relaxation rate is to be about $3 \times 10^{-10} N \approx 10^{13}$ s^{-1}. This rate, if possible because of energetic reasons, may be several orders greater than the radiation transitions rate, even than predissociation and dissociation in the case of polyatomic molecules with the number of atoms $N \geq 3$. Thereby, the primary photoprocesses similar reactions (3.35)–(3.37), excluding photon absorption, are unavailable, as a rule, whereas luminescence and molecule decay occur from the states populated in relaxation processes (Figs. 3.22–3.24).

Now we consider advantages and disadvantages of actinometers of different types. Liquid phase actinometers are described in monographs [2, 33, 34] and IUPAC Technical Report [43]. C.A. Parker is the author of a most popular liquid actinometer, a so-called *ferrioxalate actinometer* [43]. Monographs and surveys devoted gas-phase actinometers, including the latest ones, contains a lot of mistakes, and methods are not sufficiently described [2, 34, 43, 48]. The author has been investigated and tested several types of gas-phase actinometers. Taking into account importance of layout factors in measurements, some of them are competitive so far today. Relating others, incorrect information may be encountered sometimes in scientific literature about quantum yields of stable photolysis products. Thereby, these types of gas-phase actinometers will be discussed in sufficient detail. Some method of absolute measurements by means of actinometers will be also discussed in Chap. 4.

3.8.5 Gas-Phase Actinometers

3.8.5.1 The Visible and UV Spectral Range

As noted earlier, the best actinometer, all other factors being equal, has the absolute quantum yield for stable photolysis product $\Phi_{\mathrm{A}}(\lambda)$ equal to an integer in some range of conditions.

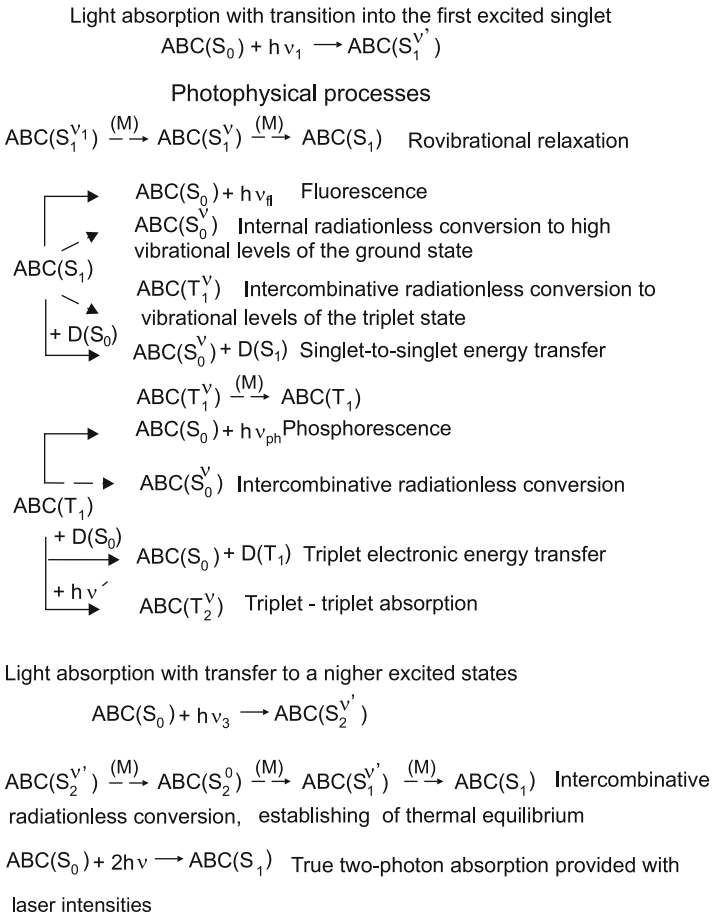

Fig. 3.22 Photophysical processes in polyatomic molecules (see [34])

Nitrosyl chloride, NOCl. One such actinometer is NOCl. Because of low dissociation energy, $D_0 \approx 1.63$ eV, corresponding to $\lambda = 760 \pm 13$ nm

$$\mathrm{NOCl} + h\nu \rightarrow \mathrm{NOCl}^* \rightarrow \mathrm{NO}^{\neq} + \mathrm{Cl}(^2\mathrm{P}_{3/2}), \tag{3.67}$$

(* denotes *rovibronic* excitation), NOCl is the "champion" with respect its spectral working range $\lambda_{wr} \approx 550$–180 nm (see [40, 49, 50] and Table 3.3). High chemical activity of NOCl is the payment for capability to work in the visible spectral range. It matches only with the systems, including such materials as fluoroplastic, glass, stainless steel, quartz, and small amount of kovar needed for molybdenum glass soldering. Copper gaskets should be gilded or silver-plated, aluminum gaskets have not to be used. Nytrosil chloride decomposes on metallic surfaces in dark, with the

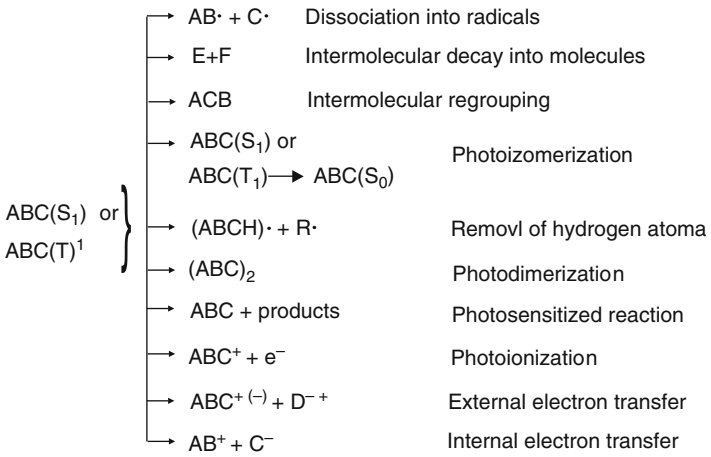

Fig. 3.23 Primary photochemical processes in polyatomic molecules (see [34])

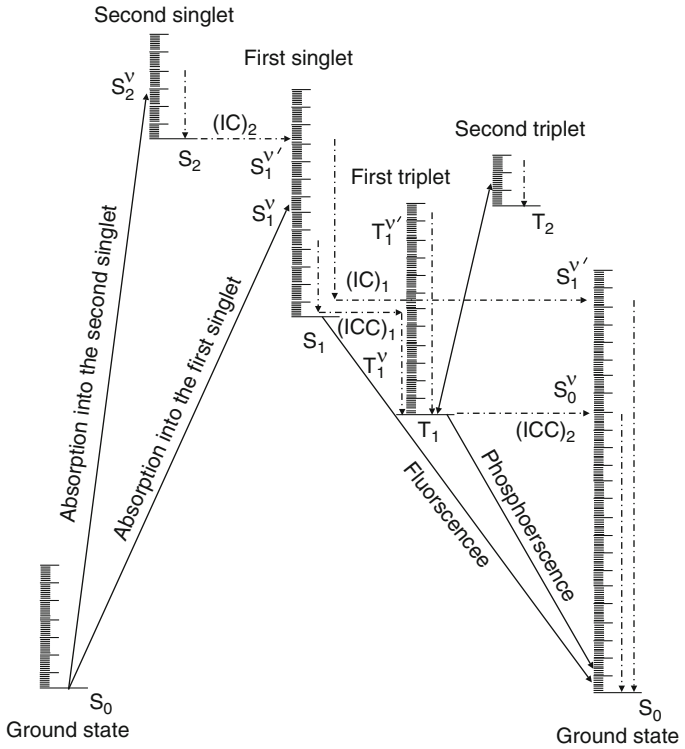

Fig. 3.24 Excited states of a typical organic molecule and physical transfers between them (see [33, 34]). Radiative transitions between states are shown by *solid lines*, nonradiative transitions are shown by *dashed lines*. Here, IC denotes internal conversion, ICC denotes intercombinative conversion, the *dashed vertical lines* show vibrational relaxation within one state. The definitions for yields above are suitable for use in condensed phase

Table 3.3 Gas-phase actinometers and application conditions [40]

Actinometer/photolysis product	$\Phi_A(\lambda)$	p_{act}, torr/T, K	λ (nm)	Refs.	Comments
	2.1 ± 0.1	≈ 90/295	630–356	[51]	Thermopile, addition of N_2 (6 torr) do not change $\Phi_{NO}(\lambda)$
	2.14 ± 0.07	≈ 7.5–100/293	546–409	[52]	Thermopile, addition of N_2 and CO_2 (5 torr) do not change $\Phi_{NO}(\lambda)$
	1.96 ± 0.02	1–120/298	254	[53]	Ferrioxalate actinometer; addition of N_2 (8 torr), CO_2 (4 torr), and Ar (8 torr) do not change $\Phi_{NO}(\lambda)$
	2.0 ± 0.1	2–10/293	248–262	[54]	Diethyl ketone was used as an actinometer (T = 340–430 K), $\Phi_{CO}(\lambda) = 1$ (see the text)
	2.0 ± 0.1	2–10/293	315–230	[49]	Photolysis spectrum was measured by thermopile. Absolute calibration was carried out at λ = 254 nm
NOCl/NO	2.0 ± 0.1	2–10/293	240–155	[50]	Oxygen was used as an actinometer (T = 293 K), $\Phi_{O_3}(\lambda) = 2$ (see the text)
	1.2 ± 0.1	12– 150/436 –678	313	[55]	Thermopile
	1.0 ± 0.1	12–105/383	313; 254	[56]	$\Phi_{hv}(\lambda) = 10^{11}$ photon/s, photolysis time is unknown, thermophile, uraniloxalate, $\Phi_{co}(\lambda)$ is depended on irradiation intensity
CH_3COCH_3/CO	1.0 ± ?	1– ?/394–569	313	[57]	It is assumed that $\Phi_{co}(\lambda) = 1$ (394 K); $\Phi_{co}(\lambda)$ decrease at very high (?) pressure
	1.03 ± 0.05	22– 41/300– 409	313	[58]	Actinometer is unknown
	1.03 ± 0.1	39– 51/329– 393	313	[59]	Acetone was used as an actinometer, T > 379 K, $\Phi_{co}(\lambda) = 1$
	0.98 ± ?	13–24/373– 573	290–320	[60] see [54] and references therein	Photolysis was carried out in all the λ = 290–320 nm spectral range. Description of experimental conditions is incomplete. Acetone was used as an actinometer, T > 448 K, p > 56 torr, $\Phi_{co}(\lambda) = 1$
$C_2H_5COC_2H_5$/CO	1.0 ± 0.02	20/350– 450	254		It was assumed that $\Phi_{co}(\lambda) = 1$ (400 K)
HBr/H_2	0.93 ± 0.04	400/293	208		See the text

(continued)

Table 3.3 (continued)

Actinometer/photolysis product	$\Phi_A(\lambda)$	p_{act}, torr/T, K	λ (nm)	Refs.	Comments
				see [61] and references therein	
HBr/Br_2				[62]	See the text
	1.0 ± 0.05		254	[63]	
$OCCl_2/CO$	1.0 ± ?	?	185	[64]	HBr was used as an actinometer, $\Phi_{H_2}(\lambda) = 1$, p_{HBr} is unknown
$CH_3N_2CH_3/N_2$	1.0 ± ?	?/297– 437	410 - 270	[65]	Data on $\Phi_{N_2}(\lambda)$ are contradictory
	1.0 ± 0.05	6/296– 428	317 – 398	[66]	NO_2 (6 torr) + N_2 (0–10^3 atm)
				Alekseev, A.A., Fedorov, A. V., Pravilov, A.M. (unpublished data)	
	1.0 ± 0.05	1/293	330 – 380		NO_2 (1 Topp) + CO_2 (0 – 10^3 topp) mixture; NOCl was used as the actinometer
	0.90 ±0.15	0.1–1/293	180 – 190	[67]	O_2 was used as the actinometer; the convolution quantum yields
NO_2/N_2	0.85 ± 0.10	0.1–1/293	155–180	[67]	O_2 was used as the actinometer; the convolution quantum yields
O_2/O_3	2.0		193–102.7	[68–75]	See the text
N_2O/N_2				[76–83]	See Table 3.4
	0.97 ± 0.05	0.5– 55/298	147	[84]	N_2O was used as an actinometer, $\Phi_{N_2}(\lambda) = 1.44$
CF_3COCF_3/CO	1.0 ± 0.1	3– 20/293	147	[85]	N_2O was used as an actinometer, $\Phi_{N_2}(\lambda) = 1.41$, O_2 (see the text)
	0.62 ± 0.1	100/293	184.9	[86]	N_2O was used as an actinometer, $\Phi_{N_2}(\lambda) = 1.44$
	0.44 ± 0.01	0.1–100/295–468	184.9	[87]	N_2O was used as an actinometer, $\Phi_{N_2}(\lambda) = 1.44$
	0.46 ± 0.05	20/293	163	[87]	N_2O was used as an actinometer, $\Phi_{N_2}(\lambda) = 1.44$
	0.47 ± 0.06	1–40/293	163	[88]	It was assumed that $\varphi_{C_2H_4}(\lambda) = 1$ (see the text)
	0.37 ± 0.05	5–70/293	147	[87]	N_2O was used as an actinometer, $\Phi_{N_2}(\lambda) = 1.44$
C_2H_4/H_2	0.45 ± ?	30–600/293	147	[89]	It was assumed that $\varphi_{C_2H_4}(\lambda) = 1$ (see the text)

	1.08 ± 0.12	200– 800/293	184.9	[90]	N_2O was used as an actinometer, $\Phi_{N_2}(\lambda) = 1.44$
	0.62 ± 0.06	>10/293	167–160	[78, 91]	Oxygen was used as an actinometer ($T = 293$ K), $\Phi_{O_3}(\lambda) = 2$
	0.5 ± 0.1	>10/293	160–155	[78, 91]	Oxygen was used as an actinometer ($T = 293$ K), $\Phi_{O_3}(\lambda) = 2$
	0.42 ± 0.10	>10/293	155–150	[78]	Oxygen was used as an actinometer ($T = 293$ K), $\Phi_{O_3}(\lambda) = 2$
	0.65 ± 0.10	>10/293	150–143	[78]	Oxygen was used as an actinometer ($T = 293$ K), $\Phi_{O_3}(\lambda) = 2$
	0.65 ± 0.05	5–300/293	147	[78]	Oxygen was used as an actinometer ($T = 293$ K), $\Phi_{O_3}(\lambda) = 2$
	0.75 ± 0.15	21–53/293	147	[92]	Thermopile
	0.47 ± 0.10	>10/293	143–124	[78]	
	0.2–0.85; зависит от длины волны	0.4–4/293	147–120	[93]	Resonance fluorescence of CO
	1.0 ± 0.1	$p_{CO_2} \to 0$	147– 120	[94]	Resonance fluorescence of $O(^3P)$ and CO
CO_2/CO	0.75 ± 0.06	5–300/293	123.6	[78]	Oxygen was used as an actinometer ($T = 293$ K), $\Phi_{O_3}(\lambda) = 2$

? - the data are unknown

decomposition rate accelerating with pressure. Standard practice to work with NOCl is described in [40] and the author's articles, cited in the [49, 50].

What is a reason to realize conditions for that the yield $\Phi_{NO}(\lambda)$ is equal to 2? The reason is that dissociation of NOCl with absolute yield $\varphi_{NOCl}(\lambda)$ equal to 1 at least within the range $\lambda = 630$–180 nm is followed by very rapid processes:

$$NO^{\neq} + NOCl \rightarrow \cdots \rightarrow NO + NOCl \tag{3.68}$$

$$Cl + NOCl \rightarrow NO + Cl_2 \tag{3.69}$$

In parallel with these processes, competing reactions take place.

$$NOCl^* \rightarrow NOCl + hv \tag{3.70}$$

$$NO^{\neq} + NOCl \rightarrow 2NO + Cl \tag{3.71}$$

$$NOCl^* + NOCl \rightarrow \cdots \rightarrow 2NOCl \tag{3.72}$$

$$Cl + Cl + M \rightarrow Cl_2 + M \tag{3.73}$$

$$Cl + NO + M \rightarrow NOCl + M \tag{3.74}$$

$$2NO + Cl_2 \rightarrow 2NOCl \tag{3.75}$$

Rates of these reactions are negligible at least at pressure $p_{NOCl} = 1$–15 torr reasonable intensities, and decomposition rates.

The special convenience of this actinometer type, and some other ones, is that its fusion temperature is much higher than that of the stable photolysis product NO. Thereby, product yield can be determined by simple freezing of the mixture NOCl + NO into the trap of volume much less than V, and then by measuring pressure of nonfreezing products. In this event, the value of [NO] is easy found to be:

$$[NO] = p_{NO}\,(Torr) \times 3.535 \times 10^{16} \times \left(\frac{273}{T}\right) \tag{3.76}$$

where $T = 293$ K is the room temperature. However, there is the interfering factor that NO is dissolved into NOCl at the nitrogen boiling temperature, -196°C, so that this mixture should be frozen by another way, for example, by using liquid oxygen. In addition, absorption coefficient of NOCl in the region $\lambda \geq 250$ nm is not more than 10 cm^{-1} atm^{-1}. It is impossible to provide total absorption of radiation at $p_{NOCl} < 15$ torr. In this case the absorption part should be measured (see Sect. 4.1). Virtually, NOCl allows to measure radiation intensity, provided intensity exceeds 10^{13}–10^{14} photon/s. The short-wave limit for NOCl application is determined by the inequality $\varphi_{NOCl}(\lambda) < 1$ at $\lambda \approx 180$–155 nm (Fig. 3.25).

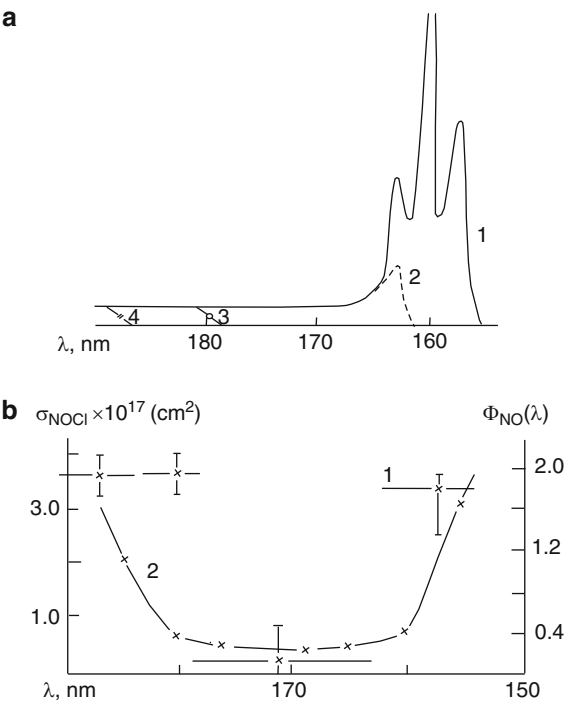

Fig. 3.25 (**a**) Spectral dependences of radiation of hydrogen-discharged lamp, passed through different filters; $p_{NOCl}l = 5$ torr cm. *1* – fused quartz, $d = 3$ mm, *2* – fused quartz + C_3H_8, $p_{C_3H_8}l = 300$ torr cm, *3* – fused quartz + O_2, $p_{O_2}\ l = 200$ torr cm, *4* – fused quartz + C_2H_4, $p_{C_3H_8}l = 200$ torr cm. (**b**) Spectral dependence of convolution quantum yield for NO formation in NOCl photolysis (*1*) [50]. Absorption spectrum of NOCl (*2*) [48]

In Sects. 4.4.2.1 and 4.4.2.2 the method is described for measuring of spectral functions of convolution quantum yields. But here the author notes that photolysis of NOCl is realized through "nondispersed" radiation of hydrogen lamp, radiation is passed through a system involving three quartz windows, each having thickness 1 mm, and gaseous filters (Fig. 3.25a). The filters transform radiation spectrum absorbed by nitrosyl chloride. Thus the convolution quantum yields for NO formation are found. These yields are equal to the absolute quantum yields, provided that the obtained yields are independent of wavelength within the narrow spectral range. Radiation intensity is found by means of the oxygen actinometer considered below.

Generally, the energy of excited molecule is excepted to be higher of adiabatic energy of dissociation, with the absent of luminescence, and the quantum yield of photodecay has to be equal to 1 at any pressures (see, e.g., [43]). The convolution quantum yield of NOCl decomposition is appreciably less than 1 in the $\lambda \approx 160$–180 nm spectral range, i.e., in the spectral range of low absorption coefficient (Fig. 3.25b). Similar effects are also observed in the author's laboratory with photolysis of molecules NO_2, N_2O, CO_2, alkyl iodide, and perfluoralkyl iodide in the vacuum UV spectral range. Feasible reasons of these features are discussed in [41] (see references therein). It was found in the author's laboratory that this effect may have different mechanism. Whatever the mechanism, dissociation of excited states however has to be energetically impossible, that is, any populated state is uncorrelated with dissociation products being lower than the potential energy

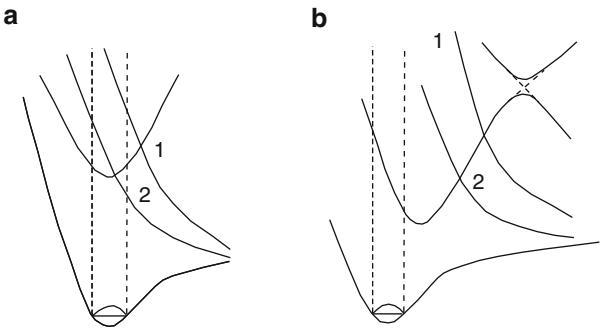

Fig. 3.26 Long-lived states of polyatomic molecules [41]

surface region, populated within the optical transfer (Fig. 3.26a) or in the case of barrier on a dissociation coordinate for decay of this state, and the barrier being due to the nonintersecting rule, see Fig. 3.26b. If this is the case, predissociation may not occur due to energetic reasons (curves 1 in Fig. 3.26a, b) or it may proceed at low rate since it is forbidden (curves 2 in Fig. 3.26a, b).

When luminescence from these molecular states are not observed because the Einstein coefficient is much less than the predissociation rate, or, at high pressures than the rate of collisional deactivation of these states [process (3.41)]. If this is the case, the radiation lifetime may be sufficient more than the value calculated on the base of absorption spectra owing to mixing of states [41].

Acetone, diethylketone. Within the first absorption band, $\lambda = 340$–220 nm, photochemistry for ketones are understood adequately (see [34] and references). Two specimens of this compound class, namely, acetone (CH_3COCH_3) and diethylketone ($C_2H_5COC_2H_5$) are widely used as actinometers. A large body of works on photochemistry for these compounds suggest that basic channels of decay of an excited molecule of R_2CO, R = CH_3, C_2H_5 are as follows [34, 40]:

$$R_2CO + h\nu \rightarrow R_2CO^* \tag{3.77}$$

$$R_2CO^* \rightarrow 2R + CO \tag{3.78}$$

$$\rightarrow RCO^{\#} + R \tag{3.79}$$

The reaction

$$R_2CO^* \rightarrow H + R'COR \text{ or } H_2 + R''COR \tag{3.80}$$

becomes noticeable only at $\lambda < 254$ nm. The radicals R_2CO^* and R_2CO are unstable, and they dissociate either due to high vibrational excitation energy, received during dissociation of R_2CO^*, or due to collisions with R_2CO at temperature T $\geq$ 400 K. The author has data on the function $\Phi_{CO}(\lambda)$ obtained in photolyses reaction of R_2CO under experimental environment, temperature and pressure, only at $\lambda = 313$ and 254 nm. According to these data $\Phi_{CO}(\lambda) = 1.0_{-0.1}$ at $T = 400$–670 K

and $p_{R_2CO} \leq 50$ torr. One can assume that $\Phi_{CO}(\lambda) = 1.0_{-0.1}$ over all spectral range $\lambda = 313 - 254$ nm, provided that the decay rates of different channels for the radicals R_2CO^* and R_2CO do not vary strong within this spectral range. The decay rate for R_2CO^* radical is slow at $\lambda = 313$ nm, one of successful competitive modes of decay is collisional deactivation by diacetyl and O_2 molecules, which may be as admixtures of the original chemical agent. Because of this the use of R_2CO under conditions nonpresented in sources (see Table 3.3) should be done carefully. The same note may refer to uncertainty of measurement of radiation intensity by using these actinometers, which is assumed to be more high than that presented in original works. In any case, the function $\Phi_{CO}(\lambda)$ should be investigated as dependency upon separation efficiency for R_2CO, on photolysis time, and on temperature and pressure at $\lambda \neq 313, 254$ nm. Experimental sensitivity of $\Phi_{CO}(\lambda)$, high uncertainties of $\Phi_{CO}(\lambda)$ presented in sources, and the absent of any data at $\lambda \neq 313, 254$ nm, the all leads to that acetone and diethylketone become not well suitable as actinometers.

Hydrogen bromide, HBr. The authors of monographs [34, 48] and IUPAC Technical report [43] give recommendations about the use of hydrogen bromide as actinometer in the spectral range $\lambda = 180$–250 nm. In fact A – absorption band of this molecule is a continuum, $\lambda \approx 160$–240 nm, and one can concede that the quantum yield of photodecay for HBr molecule is equal to unity within this spectral range [45, 95], $\varphi_{HBr}(\lambda) = 1$:

$$HBr + h\nu \rightarrow H + Br. \tag{3.81}$$

The hydrogen atom reacts with its parent molecule:

$$H + HBr \rightarrow H_2 + Br. \tag{3.82}$$

The rate constant of this reaction is $k_{82} \approx 4 \times 10^{-12}$ cm^3/s at the room temperature, and the absolute quantum yield for H_2 formation is equal to unity, $\Phi_A(\lambda) = 1$. Operation with degrees of decomposition greater than 1% is impermissible because of the rate constant of the following reaction is high, $k_{83} \approx 3 \times 10^{-11}$ cm^3/s [96]:

$$H + Br_2 \rightarrow HBr + Br \tag{3.83}$$

where molecules of Br_2 are formed in recombination of Br atoms

$$2Br \xrightarrow{HBr} Br_2 \tag{3.84}$$

at the room temperature. The authors of the work [62] used molecules of Br_2 as a final product of photolysis reaction of HBr, and concentration was determined by means of radiation absorption at $\lambda = 450$ nm. Any data relating to uncertainty of actinometry are absent. In summary, one can say that the actinometer based on HBr is not well approved yet, HBr shows high chemical activity, its absorption coefficient in the UV spectral range is small.

Hydrogen chloride, HCl, hydrogen iodide, HI. Within *A*-absorption bands, $\lambda \approx 180$–140 nm and 300–180 nm, photochemistry of hydrogen chloride and hydrogen iodine is similar to that for hydrogen bromide (see above). Thus all words said above as to hydrogen bromide molecules relate in full measure to molecules of hydrogen chloride and hydrogen iodine.

Phosgene, $OCCl_2$. Okabe gave recommendation to use phosgene as actinometer in the spectral range $\lambda = 280$–200 nm [48]. The basis of that is the fact $\Phi_{CO}(\lambda) = 1.00 \pm 0.05$ at $\lambda = 254$ and 220 nm. The equality is true providing that the following processes are the only processes [97]:

$$OCCl_2 + h\nu \rightarrow OCCl^{\#} + Cl \tag{3.85}$$

$$OCCl^{\#} \rightarrow CO + Cl. \tag{3.86}$$

The author assumes that data obtained at $\lambda = 254$ nm cannot be extrapolate to full spectral range mentioned above, because of CO formation proceeds in decay process the rotational excited radical of $OCCl^{\#}$. At $\lambda \neq 254$ and 220 nm, it is not inconceivable that the decay rate for OCCl* may be comparable with the rate of their collisional deactivation with successive recombination and reaction with Cl atoms:

$$OCCl^{\#} \xrightarrow{M} OCCl \tag{3.87}$$

$$2COCl \xrightarrow{M} (COCl)_2 \tag{3.88}$$

$$COCl + Cl \rightarrow CO + Cl_2 \tag{3.89}$$

$$\xrightarrow{M} COCl_2 \tag{3.90}$$

In work [64], phosgene was used as actinometer at $\lambda = 185$ nm. One sufficient disadvantage of this compound as actinometer is that it has small value of the absorption coefficient ($k_{COCL_2}(\lambda) \leq 3$ cm^{-1} atm^{-1} at $\lambda \geq 200$ nm) [43].

Azometane, $CH_3 \equiv NCH_3$. Based on photochemical features of azometane in the spectral range $\lambda = 410$–270 nm, Okabe gave recommendation to use this compound as actinometer in this spectral range, assuming that $\Phi_{N_2}(\lambda) = 1$ at $T = 297$–437 K [48]. However, data related to azometane are inconsistent; moreover, the absorption coefficient of azometane in this spectral range is sufficiently low, $\leq$0.4 cm^{-1} atm^{-1} (see [65]).

Nitrogen dioxide, NO_2. Dissociation of NO_2 molecule becomes energy available at $\lambda < 397.7$ nm, whilst this process may be observed at some longer wavelengths due to energy transfer processes. It was discussed over prolonged period if the absolute quantum yield is equal to 1. Data obtained in the late 1980s take off this question (Fig. 3.27).

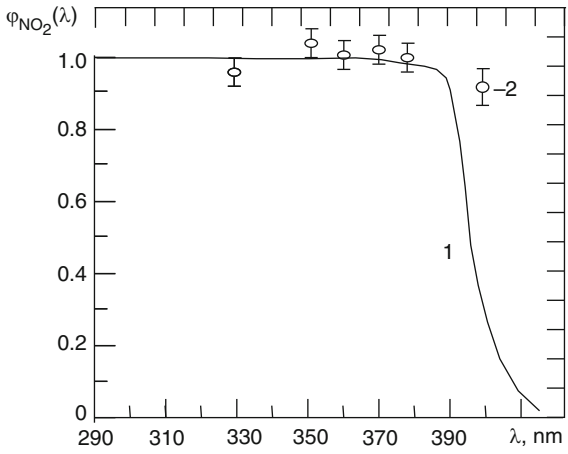

Fig. 3.27 Spectral function of the absolute quantum yield of photodecay NO_2, $T = 293$ K [41]. *1* – according to [66], *2* – according to Alekseev et al. (Alekseev, A.A., Fedorov, A. V., Pravilov, A.M., unpublished data)

It should be noted that primary and secondary processes of NO_2 photolysis are both described at $\lambda = 398$–210 nm, $\Phi_{O_2}^{NO_2} = 1$ as follows:

$$NO_2 + hv \rightarrow NO + O(^3P.^1D) \xrightarrow{NO_2} NO + O(^3P) \tag{3.91}$$

$$O(^3P) + NO_2 \rightarrow NO + O_2 \tag{3.92}$$

As the mixture of NO_2 with the stable photolysis products NO and O_2 is frozen, nitrogen dioxide converts into N_2O_3 molecule, so oxygen becomes the only non-frozen stable photolysis product of NO_2. In dark, NO3 molecule decomposes much slowly than NOCl. However, even with room temperature, NO_2 contains a touch of its dimer N_2O_4, e.g., 0.7% at pressure $p_{NO_2} = 1$ torr. Photochemistry of N_2O_4 is not studied, although it is well known that at least primary dominant process of photolysis is dissociation without decay of NO_2. Absorption spectrum of N_2O_4 was measured only at $\lambda > 185$ nm. Thus it should be very careful when working with NO_2 and always take into account the presence of N_2O_4. In more detail it can become acquainted with this question in my monograph and articles cited herein.

3.8.5.2 The Vacuum UV Spectral Range

Early, the most popular actinometer were the devices based upon dinitrogen oxide N_2O and carbon dioxide CO_2. Even in relatively recent published books and surveys, these actinometers are still advised for work in wide spectral ranges, although it has been shown in the early 80-th of the last century (see [40, 41, 78, 82, 91–93]) that the quantum yield for photodecay of these molecules in some spectral ranges at moderate pressures, about 1 torr, is less than 1. This is because of

Table 3.4 Data of the absolute quantum yield for formation of nonfrozen products of N_2O photolysis [40]

λ (нм)	$\Phi_{N_2}(\lambda)$	Source	Note
123.6; 116.5	1.18 ± 0.09	[76]	Three measurements; O_2 actinometer; conditions of use did not specified
123.6; 116.5	1.34 ± 0.04	[77]	CO_2 actinometer;$\Phi_{CO}(\lambda) = 1^a$, p_{N_2O} = 1–8 torr
123.6	1.04 ± 0.06	[78]	O_2 actinometer; $\Phi_{O_3}(\lambda) = 2$
147	1.40 ± 0.16	[76]	A great dispersion (1.14–1.74). Uncertainty (1.40 ± 0.06)
	1.40 ± 0.02	[79]	calculated wrong. O_2 actinometer; conditions of use
	1.40 ± 0.06	[80]	did not specified; p_{N_2O} = 2 - 660 torr
	1.40 ± 0.11	[81]	CO_2 actinometer; $\Phi_{CO}(\lambda) = 1^b$, p_{N_2O} = 1–760 torr
	0.95 ± 0.06	[78]	CO_2 actinometer; $\Phi_{CO}(\lambda) = 1^b$
			CO_2 actinometer; $\Phi_{CO}(\lambda) = 0.98^6$, p_{N2O} = 1 7 – 5.5 Torr
			O_2 actinometer; $\Phi_{O_3}(\lambda) = 2$
143–123	1.1 ± 0.1	[78]	O_2 actinometer; $\Phi_{O_3}(\lambda) = 2$, convolution quantum yield
150–143	1.10 ± 0.15	[78]	O_2 actinometer; $\Phi_{O_3}(\lambda) = 2$, convolution quantum yield
155–150	1.15 ± 0.15	[78]	O_2 actinometer; $\Phi_{O_3}(\lambda)(\lambda) = 2$, convolution quantum yield
175–155		[82]	See Fig. 3.26 and the text
175–155	1.39 ± 0.08	[82]	O_2 actinometer; NOCl; $\Phi_{O_3}(\lambda) = 2$, $\Phi_{NO}(\lambda) = 2$, convolution quantum yield
213.9	1.51 ± 0.11	[83]	Assuming $\varphi_{N_2O}(\lambda) = 1$, $\Phi_{N_2}(\lambda) = 0$

[a]$\Phi_{CO}(\lambda)$ and, hence $\Phi_{N_2}(\lambda)$, both were set too high 1.33 times (see [78])
[b]$\Phi_{CO}(\lambda)$ and hence $\Phi_{N_2}(\lambda)$ both were set too high 1.47 times (see [78])

photon absorption, formation of a long-lived state also happens, for which the main degradation channel of excitation energy becomes collisional deactivation.

Dinitrogen oxide, N_2O. The authors of works [34, 48] suggested N_2O to be used as actinometer in the spectral range λ = 214–147 nm, although the absolute quantum yield for N_2O formation in photolysis of N_2O was found only at a few wavelengths λ = 123.6, 147, and 213.9 nm (see Table 3.4) by the time of publication of Refs [40, 41].

Unfortunately, the most data in Table 3.4 were obtained with the use of incorrect values of the absolute quantum yield for formation CO in photolysis of CO_2 (see footnotes). In addition, the spectrum within the range λ = 214–147 nm has non-Gaussian shape, but it has a well-defined structure, and the relative probability of different channels for photodecay of N_2O depends upon the photon energy [41, 78] (Fig. 3.28).

It is impossible to interpolate the data obtained at λ = 123.6, 147 and 213.9 into the spectral range noted above. In the short-wavelength range of *A*-absorption band of N_2O, $\lambda \approx$ 240–160 nm, particularly within λ = 175 – 155 nm, optical transitions to bound state occur. Seemingly, these states are $^1\Sigma^-$ or $^3\Pi$. The oscillator strength of the optical transition is $f \leq 10^{-4}$, so, these states are deactivated in collision with N_2O even at $p_{N_2O} \approx 1$ torr. In a longer wavelength range, optical transition into state $^1\Delta$ and/or $^1\Pi$ occur with the probability near 1, which dissociate to $N_2(X^1\Sigma_g^+) + O(^1D)$.

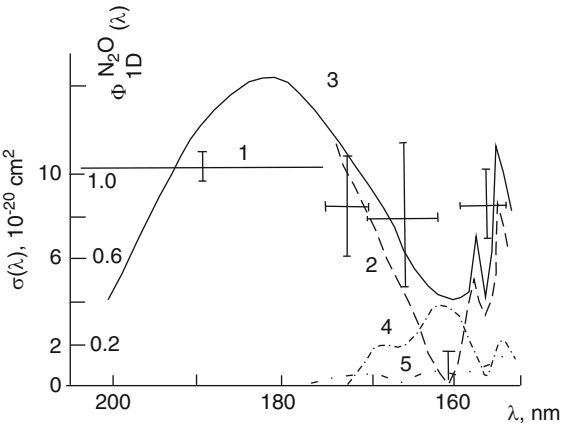

Fig. 3.28 Spectral functions of the convolution quantum yield for photodecay of N_2O into $N_2(X^1\Sigma_g^+) + O(^1D)$ (*1*), the partial cross section of absorption associated with the given process $\sigma^{N_2O}_{O(^1D)}(\lambda)$ (*2*), the total cross section of absorption $\sigma_{N_2O}(\lambda)$ (*3*), the cross section of absorption associated with the transfer into the bounded state (*4*), $\sigma^{N_2O}_{O(^1S)}(\lambda)$ (*5*); $T = 293$ K (*1*) and 273 K (*2–5*) [41, 78]

As N_2O photolysis proceeds in the range, where photodecay of this molecule occurs with the quantum yield remain constant and equal to 1, the photoprocesses are described as follows:

$$N_2O + h\nu \rightarrow N_2 + O(^1D) \tag{3.93}$$

$$O(^1D) + N_2O \rightarrow N_2 + O_2 \tag{3.94}$$

$$\rightarrow 2NO \tag{3.95}$$

When freezing with liquid nitrogen, NO dissolves into N_2O. The quantum yield of nonfrozen stable products of photolysis (N_2 and O_2) is equal to 1.5 ± 0.1, it is determined by the ratio of reaction rate constants k_{94}/k_{95}.

It was found in the 90th of the last century (Fedorov, A.V., Pravilov, A.M., unpublished data). that as photolysis of N_2O took place under pulsed radiation, at energy from 0.1 to some joules per one pulse with microseconds pulses, the quantum yield of nonfrozen stable products of N_2O photolysis is much less than 1, instead of 1–1.4 as with stationary photolysis. The only reasonable explanation may be based on the following mechanism:

$$N_2O + h\nu \rightarrow N_2 + O(^1D)$$

$$O(^1D) + N_2O \leftrightarrow (O\text{---}N_2O)^{\neq}$$

$$N_2 + (O\text{---}N_2O)^{\neq} \rightarrow 2N_2O,$$

with the rate of the last reaction being much greater than that for spontaneous decay of $(O—N_2O)^{\neq}$ complex.

Carbon dioxide, CO_2. A large number of publications was dedicated to photochemistry research of CO_2 in the spectral range $\lambda = 184–123.6$ nm. Table 3.3 shows the most firm data, in the author opinion, on the absolute quantum yields for CO formation in photolysis of CO_2. When a CO_2 molecule absorbs a photon within the *A*-band, $\lambda \approx 175–139$ nm, there occur optical transition to the states dissociating into $CO(X^1\Sigma^+) + O(^1D)$ even at $p_{CO_2} = 300$ torr, and into a long-lived state, $\tau > 1.5 \times 10^{-7}$ s. As $p_{CO_2} \to 0$, the absolute quantum yield of CO_2 photodecay tends to unity, $\varphi_{CO_2}(\lambda) \to 1$, at sufficiently high pressures this value is noticeably less (see Table 3.3, [40, 41, 78, 91–94]). These reasons exclude any use of CO_2 as actinometer.

Hexafluoroacetone, CF_3COCF_3. The authors of works [48, 84, 85] suggest to use of hexafluoroacetone as actinometer at $\lambda = 147$ nm. In the author opinion, the value $\Phi_{CO}(\lambda) = 1$ taken in these works is doubtful, because $\Phi_{N_2}(\lambda) \neq 1.44$ at $\lambda = 147$ nm. The values of the quantum yield above are proved by means of measurements carried out with an O_2 actinometer [85]. However, the author's experience on the actinometer shows that the rate pumping of the mixture $O_2 + O_3$ through the cell in the cited work is rather low, that may lead to underrating the obtained data due to ozone photolysis (see below) as well as reaction of ozone with atomic oxygen and singlet oxygen [40].

Ethylene, C_2H_4. Okabe suggests to use of ethylene as actinometer in the vacuum UV range [48]. When measuring $\Phi_{H_2}(\lambda)$, N_2O was used as actinometer, and there was taken incorrect value of the quantum yield for nitrogen formation in its photolysis.

Oxygen. In the author opinion, oxygen actinometer is the most cheap, precise and effective tool for measurements of radiation intensity in the $\lambda \approx 175–115$ nm, i.e., in the spectral range from the long-wavelength limit of the Shuman–Runge continuum, where the oxygen absorption cross section become large [41, 48] to the LiF transparency limit. It is very important that there is no need to calibrate it. One has to determine the volume of the actinometer system, length of spectrometric cell, where absorption of ozone is measured and time interval t_{ph} [see formula (3.33)].

It has been shown in the 30th of last century that for sufficiently high oxygen pressures and rates of removal of the photolysis products, the absolute quantum yield of ozone formation upon O_2 photolysis in the region of Schumann–Runge continuum is equal to 2. What "high pressures and removal rates" mean and what processes decrease the $\Phi_{O_3}(\lambda)$ were not known (see [34, 40, 41] and references). These problems were solved in [68–71].

In the spectral range 242–102.7 nm, primary and secondary processes of oxygen photolysis can be schematically presented by the following equations:

$$O_2 + h\nu \to O(^3P) + O(^3P, ^1D, ^1S) \xrightarrow{O_2} 2\,O(^3P) \tag{3.96}$$

$$\mathrm{O}(^3P) + \mathrm{O}_2 \xrightarrow{O_2} \mathrm{O}_3 \tag{3.97}$$

$$\mathrm{O}(^3P) + \text{wall} \rightarrow \text{products} \tag{3.98}$$

$$\mathrm{O}_3 + \text{ wall} \rightarrow \text{products} \tag{3.99}$$

$$O_3 + hv \rightarrow O(^3P, ^1D, ^1S) + O_2(X^3\Sigma_g^-, a^1\Delta_g, b^1\Sigma_g^+) \tag{3.100}$$

In order to the absolute quantum yield for ozone formation has to be equal to 2, the following conditions have to be provided:

– The loss rate for oxygen atoms in the reaction of ozone formation has to be much greater than that for the same atoms on the walls:

$$k_{97}[\mathrm{O}_2]^2 >> k_{98}; \tag{3.101}$$

– The density of radiation absorbed in process (3.97), i.e. virtually, the formation rate of ozone has to be much more than the loss rate of ozone:

$$k_{97}\,[O(^3P)] \cdot [O_2] >> k_{99} + n_{hv}^{101} \tag{3.102}$$

These conditions can be easy provided in the event that photon flux is high enough. In practice, the system shown in Fig. 3.29 gives a simplest method for radiation intensity measuring by means of oxygen actinometer. The basic features of the system are as follows. Oxygen photolysis is carried out in a circulating system, where the mixture "oxygen/ozone" is irradiated many times. Why do it is carried out? Ozone pressure can be simple and easily measured by means of ozone absorption on mercury resonance line $\lambda = 253.7$ nm, according to the following formula:

$$p_{\mathrm{O}_3} = \frac{760 \cdot T}{k_{\mathrm{O}_3}(253.7) \cdot l \cdot 273} \ln \frac{I_0^{253.7}}{I_0^{253.7} - I_a^{253.7}}. \tag{3.103}$$

$$[\mathrm{O}_3] = p_{\mathrm{O}_3}\,(\text{Torr}) \times 3.535 \times 10^{16} \times \left(\frac{273}{T}\right) \tag{3.104}$$

where l is length of the spectrometric cell (7); $I_0^{253.7}$ and $I_a^{253.7}$ is the intensity of resonant mercury irradiation at the cell input and the intensity absorbed by the cell, respectively. The absorption coefficient of O_3 is a great value at $\lambda = 253.7$ nm, and it is well known with a uncertainty about 1% (Fedorov, A.V., Pravilov, A.M., unpublished data) [98–101]:

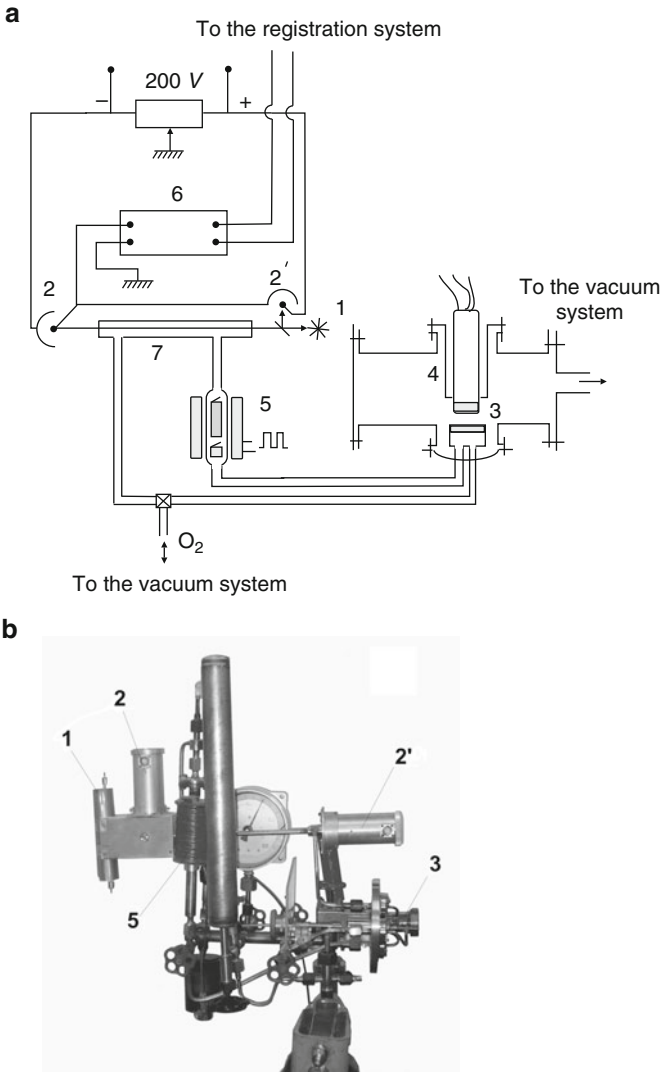

Fig. 3.29 (**a**) Experimental arrangement for measuring photon flux of a lamp by means of oxygen actinometer. The mercury resonance lamp (*1*); solar blind phototubes (*2,2'*); photochemical reactor (*3*); the lamp intensity of which is measured (*4*); the circulation pump (*5*); direct current amplifier (*6*); spectrophotometric cell (*7*). (**b**) Photo of the oxygen actinometer

$$k_{O_3}(253.7\ nm) = 307.2 \pm 3.2\ cm^{-1}\ \text{atm}^{-1}(T = 273\ \text{K}).$$

The ozone concentration can be found by formulae (3.103 and 3.104), and the radiation intensity by the formula (3.33).

The circulating system (Fig. 3.29) has to have a minimal organic pollution on the cell walls. The system has to be pumped out up to high vacuum ($< 10^{-5}$ torr) with

the help of an ion pump or turbo-molecular pump. When either a mercury pump or oil diffusive pump is used, the using of high-effective traps with liquid nitrogen is necessarily essential. Traces of mercury or oil on the walls are the worst enemies for atomic oxygen and ozone. As mercury and copper interacts with atomic oxygen both are oxidized. The recombination efficiency of atomic oxygen $\gamma_{O(^3P)} = 1$ on copper oxide as well as mercury oxide, whereas on the glass surface, quartz surface, or on the stainless steel surface passage by ozone the same quantity is $\gamma_{O(^3P)} = 10^{-5}$–$10^{-4}$. So that, copper gasket is required to be silver-plated or gilded, stainless steel has to be oxidized by using of ozone. Usually, it is provided as follows. The circulating system is filled with oxygen of pressure 1–4 torr, a Tesla generator is switched on, and then the glass branch piece arranged in the pipe (7) and frozen by liquid nitrogen is developed by the Tesla generator (Fig. 3.29).

After accumulating ozone for 1–3 min of operation of the Tesla generator, the glass branch piece has to be unfrozen, precipitated ozone is further pumped through the circulating system. After one to two operational cycles described above, the loss rate for ozone on the system walls will not exceed 10^{13} cm^{-3} min^{-1}. In common case, as the rate of ozone recombination on the walls is sufficient small, providing the pressure and $\gamma_{O(^3P)}$ are both sufficient small too, and the equation $2\lambda_{O(^3P)/}\gamma_{O(^3P)} >> r$ is valid, where $\lambda_{O(^3P)/}$ is the free length for oxygen atoms, r is the cell radius, then this rate can be evaluated by the formula:

$$w_{98} = \frac{1}{4}\gamma_{O(^3P)}\ u_{O(^3P)}\ [O(^3P)]\ \text{cm}^{-2}\ \text{s}^{-1}$$

where $u_{O(^3P)} \approx 7 \times 10^4$ cm/s is the arithmetical mean velocity of atomic oxygen at $T = 293$ K.

The measuring intensity procedure by using the described system is as follows.

1. The system is filled with oxygen, the circulation pump is turned on, the light source is switched on. Then absorption of resonant mercury radiation is measured versus the photolysis exposed time (the range 1 in Fig. 3.30). If the exposure time is not sufficiently long, and the condition (3.101) is valid, then

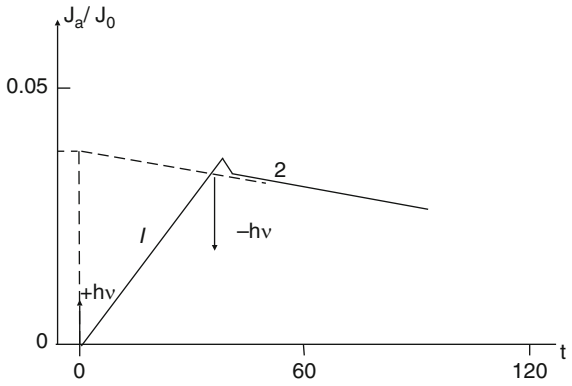

Fig. 3.30 Intensity measurements by oxygen actinometer

concentration will be proportional to the photolysis duration. If the ozone optical layer is small, absorption is also proportional to the photolysis duration. After oxygen irradiation for the time interval t_{ph}, which is usually takes 1–3 min., the light source is switched off, the ozone loss rate is measured (the range 2 in Fig. 3.30). The value of ozone concentration taking into account its losses [reaction (3.99)] is determined by extrapolation the range 2 by straight line to the beginning moment of photolysis. If the obtained correction exceeds 10%, it will need to clean the system once more. When the operation above fails, it will need to check up the pumping block. I am sure that the "firm secrets" listed here were never published so far today, and they are to be enough to complete your work well.

2. Analyze the dependency of the ozone yield versus the circulation rate and pick out this rate so much that ozone left in the photolysis zone will not to decompose with a high rate by the light source.
3. On picking out the operating conditions according items 1, 2, analyze the dependency of the ozone yield versus the oxygen pressure at 100% absorption of measured radiation. It is clear, that with increasing the oxygen pressure, this dependency is to get out a plateau.

The working conditions of the oxygen actinometer include the plateau as in items 2, 3, and the linear range as in item 1.

Note that the oxygen actinometer has a sufficient high sensitivity as compared with another actinometer types, namely, the intensity of 10^{13} photon/s can be measured with an uncertainty of 4–5%, more high intensities are usually measured with an uncertainty of 2–3%. Finally, the advantage of the oxygen actinometer is that the oxygen absorption coefficient is sufficiently high in the range $\lambda \geq 175$ nm, it provides 100% light absorption at the pressure $p_{O_2} \leq 760$ torr and the cell (3) length (Fig. 3.29) of order of 30 cm. Hence, taking into account constancy of the quantum yield for ozone formation in the spectral range 242–102.7 nm, the device can be used for determination of integral radiation intensity from 175 nm to the transparency limit of the cell window. This outstanding feature of oxygen actinometers was used in the author's laboratory many times.

3.8.6 *Liquid-Phase Actinometers*

All sufficient features of liquid-phase actinometers are listed in Table 3.5. Other liquid-phase actinometers are described in the monograph by J. Rabeck [2] and review [43].

Table 3.5 Liquid-phase actinometers [33, 34, 43]

Actinometer	Working spectral range (nm)
Potassium ferrioxalate $K_3Fe(C_2O_4)_3$	509–254
Uranyl oxalate as solution of $UO_2C_2O_4$ in acidic aqueous solution $H_2C_2O_4$	436–208
Reinecke's salt	750–316

Problems

1. *Based on Sect. 1.1, show the quantum efficiency of photoemissive detector to be given by the formula:* $\eta(\lambda) = 1.24\,10^3 S_e(\lambda)/\lambda$, *where the sensitivity function* $S_e(\lambda)$ has physical dimension A/W, and wavelength in nm.
2. *The quantum yield of photocathode emission of PMT is equal to* $\eta_{\mathrm{pc}}(\lambda) = 0.25$ at $\lambda = 400$ nm. Estimate the spectral sensitivity of the photocathode S_e^{pc} and PMT as a whole S_e^{PMT}, assuming the dynode system gain to be $G = 10^6$.
3. *Let us assume that the average PMT current in the direct current mode is measured to be not more than* 10^{-6} *A as recording pulsed radiation of exponential decaying shape at repetition frequency 100 Hz. The lifetime of the light source is* 10^{-6} *s. Estimate maximal PMT current in the pulsed analog mode of operation. Show if PMT operation is permissible under such currents.*

References

1. Budde, W.: Physical detectors of optical radiation. In: Grum, F., Bartleson, C.J. (eds.) Optical Radiation Measurements, A Treatise, vol. 4. Academic, New York (1983)
2. Rabek, J.F.: Experimental Methods in Photochemistry and Photophysics. Wiley, New York (1982)
3. Epshtein, M.I.: Izmereniya Opticheskogo Izlucheniya v Elektronike (Measurements of Optical Radiations in Electronics). Energoatomizdat, Moscow (1990)
4. Anisimova, I.I., Glykhovskoy, B.M.: Photoelectronnye Umnozhiteli (Phomiltipliers). Sovetskoe Radio, Moscow (1974)
5. Higgins, T.W.: Thermal detectors feel the heat of light. Laser Focus World: http://www.optoiq.com/index/photonics-technologies-applications/lfw-current-issue/laser-focus-world/volume-30/issue-11.html
6. Parr, A.C.: A National measurement system for radiometry, photometry and pyrometry based upon absolute detectors. http://physics.nist.gov/Pubs/TN1421/electrical.html
7. Dalta, R.U., Parr, A.C.: Introduction to optical radiometry. In: Parr, A.C., Dalta, R.U., Gardner, J.L. (eds.) Experimental Methods in Physical Science. Optical Radiometry, vol. 41. Elsevier/Academic, New York (2005)
8. Coblentz, W.W.: Various modifications of bismuth-silver thermopiles having a continuous absorbing surface. Bull. Bur. Stand. **11**, 131–187 (1914)
9. Quinn, T.J., Martin, J.E.: A radiometric determination of the Stefan-Boltzmann constant and thermodynamic temperatures between −40 C and +100 C. Phil. Trans. Roy. Soc. Lond. **A316**, 85–189 (1985)
10. Martin, J.E., Fox, N.P., Keys, P.J.: A cryogenic radiometer of absolute radiometric measurements. Metrologia **21**, 147–155 (1985)
11. Beckhoff, B., Gottwald, A., Klein, R., Krumrey, M., Muller, R., Richter, M., Scholze, F., Thornagel, R., Ulm, G.: A quarter-century of metrology using synchrotron radiation by PTB in Berlin. Phys. Status Solidi B **246**, 1415–1434 (2009)
12. Gentile, T.R., Houston, J.M., Hardis, J.E., Cromer, C.L., Parr, A.C.: National Institute of Standards and Technology high-accuracy cryogenic radiometer. Appl. Opt. **35**, 1056–1068 (1996)
13. Sommer, A.H.: Photoemissive Materials: Preparation, Properties, Uses. Wiley, New York (1968)
14. Vetokhin, C.C., Gulakov, I.P., Pertsev, A.N., Reznikov, I.V.: Odnoelektronnye Photopriemniki (One-Electron Photodetectors). Atomizdat, Moscow (1979)

15. Weast, R.C.: CRC Handbook on Chemistry and Physics. CRC Press, Boka Raton (1979–1980)
16. Richardson, O.W.: The Emission of Electricity from Hot Bodies, 2nd edn. Longmans, New York (1921)
17. R5509-43 hotomultiplier tube (Hamamatsu). http://sales.hamamatsu.com/en/products/electron-tube-division/detectors/photomultiplier-tubes.php?src = hp
18. Kaye, G.W., Laby, T.H.: Tables of Physical and Chemical Constants. Longmans, London (1959)
19. Schottky's effect. http://encyclopedia2.thefreedictionary.com/Schottky+effect
20. Demas, J.N.: Excited State Lifetime Measurements. Academic, New York (1983)
21. Fluorescence_lifetime_imaging_microscopy. http://en.wikipedia.org/wiki/Fluorescence_Lifetime_Imaging_Microscopy
22. Photomultiplier tubes (Hamamatsu). http://sales.hamamatsu.com/en/products/electron-tube-division/detectors/photomultiplier-tubes.php?src=hp
23. Picosecond fluorescence lifetime measurement system C1120. http://sales.hamamatsu.com/assets/pdf/hpspdf/e_c11200.pdf
24. Princeton Instruments–PI-MAX 3 ICCD Camera. http://www.princetoninstruments.com/products/imcam/pimax/default.aspx
25. Akopyan, M.E., Lukashov, S.S., Poretsky, S.A., Pravilov, A.M., Torgashkova, A.S.: On mechanism of population of the $I_2(\beta)$ state under photolysis of the $I_2 + SF_6$ mixture. Chem. Phys. Lett. **470**, 191–195 (2009)
26. Akopyan, M.E., Lukashov, S.S., Maslennikova, YuD, Poretsky, S.A., Pravilov, A.M.: Time-resolved studies of decay of the $XeI_2(IP)$ complexes. Chem. Phys. **362**, 27–33 (2009)
27. Princeton Instruments–Acton Series -Spectrographs. http://www.princetoninstruments.com/products/spec/actonseries/
28. CCD Cameras, CCD Imaging Acessories, SBIG Cameas – OPT Telescopes. http://www.optcorp.com/category.aspx?uid=319
29. CCD camera. http://www.electronics-manufacturers.com/products/digital-photography/ccd-camera/
30. Photodiode. http://en.wikipedia.org/wiki/Photodiode
31. p-n junction. http://en.wikipedia.org/wiki/PN_junction
32. PIN diode. http://en.wikipedia.org/wiki/PIN_diode
33. Parker, C.A.: Photoluminescence of Solutions. Elsevier, Amsterdam (1968)
34. Calvert, J.G., Pitts Jr., J.N.: Photochemistry. Wiley, New York (1966)
35. Zaidel, A.N., Shreider, E.Ya.: Vakuumnaya Spectroskopiya i ee Primenenie (Vacuum Spectroscopy and its Application). Nauka, Moscow (1976) [see also Zaidel, A.N., Shreider, E.Ya.: Vacuum Ultraviolet Spectroscopy. Ann Arbor-Humphrey, Ann Arbor (1970)]
36. Zagrubsky, A.A., Pravilov, A.M., Sidorov, I.I., Smirnova, L.G.: The method of calibration of non-selective light detectors. Certificates of Authorship No 1226075, 5 November 1984
37. Pravilov, A.M., Sidorov, I.I., Smirnova, L.G.: The method of measurement of photon flux by using closed photoionization chamber. Certificates of Authorship No 1466448, 16 December 1985
38. Samson, J.A.R., Ederer, D.L.: Photoionization chambers. Vac. Ultraviolet Spectr. **2**, 181–182 (1998)
39. Seib, D.H., Aukerman, L.W.: Photodetectrors for 0.1 to 1 μm spectral region. Adv. Electr. Electron Phys. **34**, 204–209 (1973)
40. Pravilov, A.M.: Gas-phase actinometry for UV and VUV spectral region (review). High Energ. Chem. **21**, 243–255 (1987)
41. Pravilov, A.M.: Fotoprozessy v Molekulyarnykh Gasakh (Photoprocesses in Molecular Gases). Energoatomizdat, Moscow (1992)
42. Braslavsky, S.E., Houk, K.N. (prepared for publication 1st edn), Verhoeven, J.W. (prepared for publication 2nd ed): Glossary of terms used in photochemistry (2nd ed.), IUPAC Organic

Chemistry Division, Commission on Photochemistry. Pure Appl. Chem. **60**, 1055–1106 (1996)
43. Kuhn, H.J., Braslavsky, S.E., Schidt, R.: Chemical actinometry (IUPAC Technical Report. Pure Appl. Chem. **76**, 2105–2146 (2004)
44. Kondratiev, V.N., Nikitin, E.E.: Gas Phase Reactions. Springer, New York (1981)
45. Pravilov, A.M.: Kinetika i Mekhanizmy Gazofazyskh Protsessov (Kinetics and Mechanisms of Gas Phase Processes) (A School Book). St. Petersburg State University, St. Petersburg (2007)
46. Tscherbul, T.V., Buchachenko, A.A., Akopyan, M.E., Poretsky, S.A., Pravilov, A.M., Stephenson, T.A.: Collision-induced non-adiabatic transitions between the ion-pair states of molecular iodine: A challenge for experiment and theory (invited article). Phys. Chem. Chem. Phys. **6**, 3201–3214 (2004)
47. Noyes, W.A., Leighton, P.A.: The Photochemistry of Gases. Dover, New York (1966)
48. Okabe, H.: Photochemistry of Small Molecules. Wiley, New York (1978)
49. Vilesov, F.I., Karpov, L.G., Kozlov, A.S., Pravilov, A.M., Smirnova, L.G.: Nitrosil chloride as a gas phase actinometer for the spectral range 630–230 nm. High Energ. Chem. **12**, 468–469 (1978)
50. Pravilov, A.M., Ryabov, S.E.: Nitrosyl chloride as gas phase actinometer for the 240–180 nm spectral range. High Energ. Chem. **16**, 331–333 (1982)
51. Kistiakowky, G.B.: Photochemical decomposition of nytrosil chloride. J. Amer. Chem. Soc. **52**, 102–108 (1930)
52. Natanson, A.G.: On the mechanism of photochemical decomposition of nytrosil chloride. Acta Physicochim. **XI**, 521–536 (1939)
53. Wayne, N.P.: Photolysis of nytrosil chloride by ultra-violet radiation. Nature **203**, 516–517 (1964)
54. Pravilov, A.M., Karpov, L.G., Smirnova, L.G., Vilesov, F.I.: Reactions of $I(^2P_{1/2})$ + NOCl. I. Quantum yield measurements of $I(^2P_{1/2})$ productions at photolysis of CH_3I and CF_3I and ratio of rates of $I(^2P_{1/2})$ interactions. Khimiya Vysokikh Energ. (High Energ. Chem.) **7**, 335–341 (1973)
55. Leemakers, J.A.: The chain decomposition of diethyl ketones photosentizied by acetone. J. Amer. Chem. Soc. **56**, 1899–1904 (1934)
56. Herr, D.S., Noyes Jr., W.A.: Photochemical studies. XXXI A systematic study of the near ultraviolet photochemical decomposition of acetone. J. Amer. Chem. Soc. **62**, 2053–2059 (1940)
57. Shaw, H., Toby, S.: Photochemistry of gaseous acetone. J. Phys. Chem. **72**, 2337–2343 (1968)
58. Davis Jr., R.: The photochemical decomposition of diethyl ketone. J. Amer. Chem. Soc. **70**, 1868–1869 (1948)
59. Dorfmann, L.M., Sheldon, Z.D.: The mechanism of the photochemical decomposition of diethyl ketone. J. Chem. Phys. **17**, 511–515 (1949)
60. Kutschke, K.O., Wijnen, M.H.J., Steacie, E.W.R.: Mechanism of photolysis of diethyl ketone. J. Amer. Chem. Soc. **74**, 714–718 (1952)
61. Forbes, G.S., Cline, J.E., Bradshaw, D.C.: The photolysis of gaseous hydrogen sulfide. J. Amer. Chem. Soc. **60**, 1431–1436 (1938)
62. Roland, R.P., Bolle, M., Anderson, R.W.: Hydrogen bromide photochemistry: actinometry for determination of absolute power outputs of Xe excimer and other UV/VUV light sources. J. Phys. D Appl. Phys. **31**, 1336–1342 (1998)
63. Okabe, H.: Photodissociation of thiophosgene. J. Chem. Phys. **66**, 2058–2062 (1977)
64. Glicker, S., Okabe, H.: Photochemistry of diacetylene. J. Phys. Chem. **91**, 437–440 (1987)
65. Steacie, E.W.R.: Atomic and Free Radical Reactions. Reinhold, New York (1954)
66. Gaedke, H., Troe, J.: Primary process in the photolysis of NO_2. Ber. Bunsengeselshaft Phys. Chem. **79**, 184–191 (1975)

67. Pravilov, A.M., Shulpyakov, I.O.: Processes of H_2O and NO_2 photodecomposition in the spectral region of $\lambda > 155$ nm. High Energ. Chem. **20**, 31–35 (1986)
68. Vilesov, F.I., Pravilov, A.M.: Photolysis of O_2 and $O_2 + CO_2$ mixtures in the 1925 – 1550 Å spectral range. Khimiya Vysokikh Energ. (High Energ. Chem.) **5**, 401–404 (1970)
69. Pravilov, A.M., Karpov, L.G., Vilesov, F.I., Pravilov, A.M., Karpov, L.G., Vilesov, F.I.: Photochemical processes in the photolysis of O_2 and $O_2 + M$ mixtures, M = He, Ar, Xe, N_2, CO_2. Khimiya Vysokikh Energ. (High Energ. Chem.) **5**, 388–393 (1971)
70. Karpov, L.G., Pravilov, A.M., Vilesov, F.I.: Photochemical equilibrium in the photolysis of O_2 and $O_2 + M$ mixtures in the spectral range $\lambda > 155$ nm with M = He, Ar, Xe, N_2, CO_2. Khimiya Vysokikh Ener. (High Energ. Chem.) **5**, 483–486 (1971)
71. Pravilov, A.M., Vilesov, F.I.: The Photochemical Reactions of Oxygen Atoms in Ground and First Excited States with Simple Molecules. Uspekhi photoniki **2**. Leningrad State University, Leningrad, pp. 41–74 (1971)
72. Washida, N., Mori, Y., Tanaka, I.: Quantum yield of ozone formation from photolysis of oxygen molecule at 1849 and 1931 Å. J. Chem. Phys. **54**, 1119–1122 (1971)
73. Bibinov, N.K., Vinogradov, I.P., Pravilov, A.M.: Spectral dependence of the absolute quantum yield of $O(^1S)$ formation in O_2 photolysis by XeO luminescence method. Opt. Spectr. **53**, 496–499 (1982)
74. Pravilov, A.M., Ryabov, S.E., Shulpyakov, I.O.: On the absolute quantum yield of $O(^1D)$ in photolysis of O_2 in the 176 to 155 nm spectral region. Sov. J. Chem. Phys. **3**, 1029–1034 (1985)
75. Bibinov, N.K., Bolshukhin, D.O., Kokh, D.B., Pravilov, A.M., Vinogradov, I.P., Wiesemann, K.: Absolute calibration of the efficiency of a VUV-monochromator/detector system in the range of 110–450 nm. Meas. Sci. Technol. **8**, 773–781 (1997)
76. Groth, W.E., Schierholtz, H.: The photolysis of nitrous oxide in the far ultraviolet. Planet. Space Sci. **1**, 333–342 (1959)
77. Doering, J.P., Magan, B.H.: Photolysis of nitrous oxide. J. Chem. Phys. **34**, 1617–1620 (1961)
78. Pravilov, A.M., Shulpyakov, I.O.: Photodecomposition of O_2, CO_2, and N_2O in the wavelength region $\lambda = 123.6$–155 nm. High Energ. Chem. **19**, 410–414 (1985)
79. Yang, J.Y., Servedio, F.M.: Photolysis of nitrous oxide at 1470 Å. J. Chem. Phys. **47**, 4817–4819 (1967)
80. Dodge, M.C., Heicklen, J.: The photolysis of N_2O at 1470 Å. Int. J. Chem. Kinet. **3**, 269–282 (1971)
81. Zelikoff, M., Aschenbrandt, L.M.: Vacuum ultraviolet photochemistry, part I. Nitrous oxide at 1470 Å. J. Chem. Phys. **22**, 1680–1684 (1954)
82. Pravilov, A.M., Shulpyakov, I.O.: Photodecay of N_2O at $\lambda > 155$ nm. High Energ. Chem. **19**, 351–354 (1985)
83. Greenberg, R.I., Heicklen, J.: Reaction of $O(^1D)$ with N_2O. Int. J. Chem. Kinet. **2**, 185–189 (1970)
84. Magenheimer, J.J., Timmons, R.B.: Photolysis of hexafluoroacetone at 1470 Å. A convenient vacuum ultraviolet chemical actinometer. J. Chem. Phys. **52**, 2790–2791 (1970)
85. Powell, G.R., Sethi, D.S.: Chemical actinometry at 147.0 nm. Int. J. Chem. Kinet. **10**, 1161–1166 (1978)
86. Borrel, P., Cashmore, P., Platt, A.E.: Photochemical measurements at 1849 Å. Ethylene as an actinometer and method for estimation of extinction coefficient. J. Chem. Soc. A, 3063–3064 (1968)
87. Glasgow, L.C., Potzinger, P.: Ethylene as an actinometer in the wavelength region 147–185 nanometers. J. Phys. Chem. **76**, 138–140 (1972)
88. Hara, H., Tanaka, I.: Photolysis of ethylene at 1643 Å. Bull. Chem. Soc. Jpn. **46**, 3012–3015 (1973)
89. Hara, H., Kodana, K., Tanaka, I.: Photolysis of ethylene at 1470 Å. Bull. Chem. Soc. Jpn. **48**, 711–712 (1975)

90. Krezenski, D.C., Simonaitis, R., Heicklen, J.: The photolysis of CO_2 at 1849 and 2139 Å. Planet. Space Sci. **19**, 1701–1703 (1971)
91. Pravilov, A.M., Shulpyakov, I.O.: Mechanism of photodecomposition of CO_2 in the wavelength region $\lambda = 167–155$ nm. Khimicheskaya Phys. (Sov. J. Chem. Phys.) **3**, 1532–1543 (1984)
92. Inn, E.C.Y.: CO quantum yield in the photolysis of CO2 at λ1470 and λλ1500–1670. J. Geophys. Res. **77**, 1991–1993 (1972)
93. Slanger, T.G., Sharlless, R.L., Black, G.: Photodissociation quantum yields of CO_2 between 1200 and 1500 Å. J. Chem. Phys. **61**, 5022–5027 (1974)
94. Slanger, T.G., Black, G.: CO_2 photolysis revisited. J. Chem. Phys. **68**, 1844–1849 (1978)
95. Nee, J.B., Suto, M., Lee, L.C.: Quantitative spectroscopy study of HBr in the 105–235 nm region. J. Chem. Phys. **85**, 4919–4924 (1986)
96. Kondratiev, V.N.: Rate Constants of Gas Phase Reactions; Reference Book. National Technical Information Service, Springfield (1972)
97. Wijnen, M.H.J.: Photolysis of phosgene in presence of ethylene. J. Amer. Chem. Soc. **83**, 3014–3017 (1961)
98. Inn, E.C.Y., Tanaka, Y.: Absorption coefficient of ozone in the ultraviolet and visible regions. J. Opt. Soc. Amer. **43**, 870–873 (1953)
99. Hearn, A.G.: The absorption coefficients of ozone in the ultraviolet and visible regions of the spectrum. Proc. Phys. Soc. **78**, 932–940 (1961)
100. De More, W.B., Raper, O.F.: Hartley band extinction coefficients of ozone in the gas phase and at liquid nitrogen, carbon monooide and argon. J. Phys. Chem. **68**, 412–416 (1964)
101. Griggs, S.M.: The absorption coefficients of ozone in the ultraviolet and visible regions. J. Chem. Phys. **49**, 857–859 (1968)

Chapter 4
Methods of Absolute Calibration for Photodetectors and Light Sources

Abstract This chapter deals with the techniques of absolute calibration in regard to photodetectors and light sources. Here also are discussed methods of absolute measurements of spectral photon flux for the investigated processes in the range running from the near IR to vacuum UV spectral range, along with absolute calibration techniques by virtue of standard detectors such as thermopiles, photodiodes, and actinometers. These techniques are discussed in regard to application to phototubes, photoionization chambers, and photomultipliers. Some original methods of absolute calibration in the vacuum UV range developed in the author's laboratory are described.

4.1 General

Various types of radiation sources and photodetectors have been discussed in the second and third chapters. With these sources and photodetectors calibrated in absolute units, we can use them for absolute measurements. The light sources and photodetectors calibrated in absolute units in a sufficient wide spectral interval are of primary value for measurements. Such devices have to have well-known spectral responsivity functions expressed in terms of spectral radiance $L_e(\lambda)$, W/(sr m^2 nm), spectral photon radiance $L_{hv}(\lambda)$, photon/(s sr nm) (see Sect. 1.1), and spectral radiant and photon responsivity functions, $S_e(\lambda)$ and $S_{hv}(\lambda)$, respectively (see Sect. 3.2). It is obvious that calibration involves the dependencies $l_e(\lambda)$, $l_{hv}(\lambda)$ and $s_e(\lambda)$, $s_{hv}(\lambda)$ in arbitrary units, which allow the absolute calibration to be estimated at one or several wavelengths. At first we consider absolute calibration methods for photodetectors. The methods may be conditionally divided into two groups. When the methods of the first are applied, the calibration is carried out by a system including a continuous spectrum source or source of linear spectrum, monochromator, and calibrated detector(s) (secondary standard or working measuring facilities). Here the continuous spectrum source or source of linear spectrum and monochromator may be replaced by a resonance light source(s). This method is

A.M. Pravilov, *Radiometry in Modern Scientific Experiments*,
DOI 10.1007/978-3-7091-0104-9_4,

referred the *method of standard detectors* or *comparison method*. When the methods of the second group are preferred to be used, the calibration is based on resonance light sources with well- known intensity distribution over a certain solid angle or *radiating indicatrix*. If the latter is the case, the resonance light source can be replaced by a continuous spectrum source with a filter, with the light source calibrated in absolute units. Such a calibration method is referred the *method of standard sources*.

With the two groups, different ways for absolute calibrations of photodetectors are available. The reader can become familiar with some of the ways in the monograph [1]. The author will pay special attention to the methods used in his practice.

There also exist such tasks, where the photodetector sensitivity is of interest at one or several wavelengths. The calibration of the photodetector can be carried out only at these points, so there is no need for measurements of $s_e(\lambda)$ and $s_{hv}(\lambda)$.

As we have seen in Chap. 3, spectral characteristics of non-selective photodetectors and photodetectors of invariable quantum yield are well known in limited spectral ranges. Among these are thermal photodetectors on the one hand, and luminophors, photoionization chambers on rare gases, and actinometers on the other hand. If this is the case, the spectral transmittance of the actinometer input window is assumed to be well known or the same window can be used as a working measurement facility. In principle, the $s_{hv}(\lambda)$ function of photoionization chambers filled with some molecular gases can be also found by the use of the published spectral dependencies of their partial and total absorption cross-sections. However, the uncertainty for the $s_{hv}(\lambda)$ functions is reasonably high for this type of photodetectors (see Sect. 3.7). The spectral characteristics in arbitrary units of all other photodetector types such as phototubes, photomultiplier tubes, detectors based on internal photoeffect, have to be estimated individually, since these functions may vary from sample to sample.

As a rule, the $s_e(\lambda)$ and $s_{hv}(\lambda)$ functions can be found by the calibration method of standard detector, where the same spectral interval is scanned twice, at first with the use of a device under calibration, and then by means of the other detector, a calibrated detector, with a well-known spectral responsivity function. So, there are two optical schemes, each having its own illumination layout. One scheme involves the detector under calibration, and the other scheme involves the calibrated detector. The compatibility of the illumination layouts of both schemes is a difficulty of the calibration method. Both detectors should have approximately the same dynamic range and nonuniformity that is a further problem. The problems above will be discussed in detail in Chap. 5. Now we assume the $s_e(\lambda)$ and $s_{hv}(\lambda)$ functions to be well known.

The double photoionization chambers filled with rare gases as well as the photoionization chambers filled with some molecular gases with notes mentioned above, all do not need for any absolute calibration (see Sect. 3.7). As for several types of gas-phase actinometers, the cell volume has to be estimated and the manometer to be calibrated providing the yield of photoproducts is measured by the manometer (see Sect. 3.8). The absolute calibrations of phototubes,

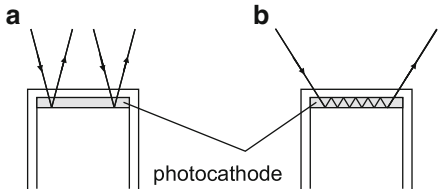

Fig. 4.1 Ray paths with photocathode illumination at angles nearly normal incidence (**a**), and sliding incidence (**b**)

photomultipliers, and photodetectors based on the internal photoeffect have to be carried out individually. Thermal photodetectors, and systems involving a luminophor, which output is to be measured by using of a phototube or PMT, all need only for the absolute calibration at one wavelength within the spectral range of luminophor applicability.

The author would like to specially note that the calibration method and especially calibration layout have to be clearly specified in the working journal. For each experimental setup a separate working journal is suggested to be useful. Such registration rules are available in the author's laboratory.

Figure 4.1 shows why it is important to follow illumination layout identity during calibration. Here phototubes are used for measurements of absolute light flux propagating within different solid angles.

Let us assume that the calibration of a phototube or photomultiplier tube with a semitransparent photocathode is carried out within a relatively small solid angle around the normal to the photocathode surface (Fig. 4.1a). Here two light rays pass through the photocathode sensitive layer: one ray passes directly on the upper photocathode surface, and the other ray reflects from the inner surface of the photocathode. On measuring within a wide solid angle, reflection gives a more sufficient contribution into registered intensity than in the event of near normal light incidence. Sometimes this circumstance is exploited to get a gain in sensitivity of detectors based on external photoeffect. However, here a total reflection prism is to be used for the reduction of reflection at sliding incidence (see Sect. 5.2.5.2 in [1]). It is obvious that you cannot apply the obtained data of calibration, provided that measurements are carrying out at a solid angle different from which has been used in calibration. All the methods of absolute calibration above, each having as advantages as well as disadvantages, will be considered separately. Before studying next sections, look over Sect. 3.1 once more to remember sufficient features of photodetectors.

4.2 Calibration by Means of Standard Detectors

The calibration method of standard detectors, or comparison method, is well available, simple, and it gives quite good results, provided that there are several detectors available as working measuring devices, and the detectors verified at regular time periods. As with measuring the $s_e(\lambda)$ and $s_{hv}(\lambda)$ functions, the main

problem may involve the compatibility of illumination layout of the detector under calibration with that of the calibrated detector. In addition, the questions may arise as to there are the compatibility of their dynamic ranges, the presence of nonuniformity of the detectors, as well nonuniformity across the monochromator beam. Budde notes some other most common sources errors in the instrumentations used for calibration, namely, selectivity of reference thermopile, spectral differences in the two beams of a two-beam system, polarization errors, nonlinearity, and stray radiation [1]. Evidently, the reader will have deeper understanding of specific character of various calibration methods and general problems as long as the author shows some of these methods as they are applied in his laboratory.

4.2.1 The Visible and Near UV Spectral Range

4.2.1.1 Phototube Absolute Calibration by Means of Commercial Thermopile

Radiant power of value 3 μW can be measured with an accuracy of 10% by means of a widely available commercial thermopile (Sect. 3.3.1). At the wavelength 400 nm, this power is associated with the photon flux of 6×10^{12} photon/s. With the quantum yield of the photocathode in order of 0.1, this power leads to the photocurrent of 10^{-7} A. It is quite acceptable value for a phototube, and it can be detected by virtue of a simple direct current amplifier or amplitude–digital converter. Thus, there is not any problem of dynamic bands compatibility. It remains to be seen whether the photocathode and thermopile nonuniformities, a sufficient difference between the area of thermopile and that of the phototube, and the possibility for calibration within a narrow solid angle, all are taken place.

By the author's opinion, a most simple calibration method appeared to be applied in ordinary scientific laboratory may involve the follows. A middle-pressure mercury lamp is the most convenient and available light source [2]. It has intensive spectral lines in a wide spectral range from a near IR to the wavelength 253.7 nm, what is quite sufficient for absolute calibration of any phototube type. A diaphragm is to be fabricated and placed in front of the thermopile so that the light beam does not pass out the boundaries of the sensitive area of the thermopile. The diaphragm has to be placed in the center of the outgoing monochromator beam with approximately uniform intensity distribution over its cross-section (Fig. 4.2). Then a series of alternate measurements is carried out. At first, for example, the output of the thermopile registration system is recorded, whereupon the output of the phototube registration system is recorded, and so on, with both photodetectors illuminated by the light beam passed through this diaphragm. The phototube can be placed behind the diaphragm so that the beam illuminates a working area of the input phototube window. It gives the equality of the intensities of the beams illuminated by the two

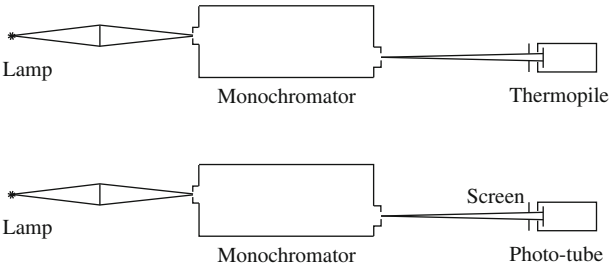

Fig. 4.2 Phototube calibration by a thermopile

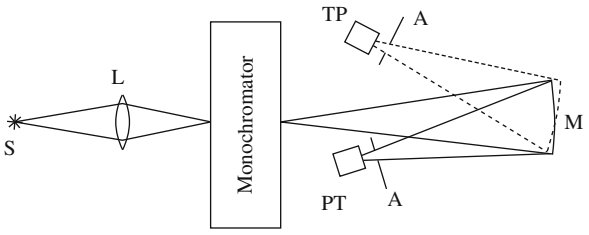

Fig. 4.3 Schematic diagram for absolute calibration of phototube by a thermopile and beam switching. *S* – light source, *L* – lens, *TP* – thermopile, *PT* – phototube, *M* – switching mirror

photodetectors. The phototube sensitivity, S_e^{pt}, over the working area, is calculated to be as follows:

$$S_e^{\mathrm{pt}}(\lambda) = I/\Phi_e(\lambda) \ \ \mathrm{A/W}, \tag{4.1}$$

where I is the phototube photocurrent, $\Phi_e(\lambda)$ is the radiant power of wavelength λ.

When you frequently deal with the phototube calibration, it is useful to use a beam switching system, for example, as shown in Fig. 4.3.

The beam switching device offers successive switching of the light beam between two positions by means of a movable mirror. Two identical apertures A as shown in Fig. 4.3 can illuminate the phototube photocathode as well the sensitive area of the thermopile.

It is well known that the phototube sensitivity depends upon point coordinate on the photocathode surface. When a phototube is utilized, it has to be used for measurements in just the same illumination layout exploited in calibration, i.e., under the same uniform illumination over the photocathode area. Alternatively, the photocathode is needed to be examined if there is a sensitivity dependency versus coordinates. Then obtained data are to be averaged. Nevertheless, there is a smart way suggested by E.D. Miszhenko to overcome this difficulty (E.D. Mischenko, private communication, 1978). This way involves a cylinder made of fused quartz which is mounted on the photodetector. One cylinder face and its walls are polished, whereas its other face is taken the gloss off, or mat. The polished cylinder face is matched with the photocathode (Fig. 4.4).

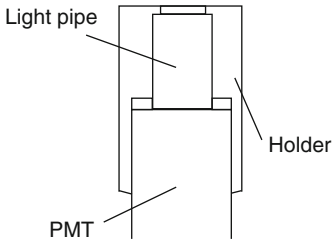

Fig. 4.4 The application of the fused quartz cylinder for calibration and measurements

When the ratio of the cylinder length to its diameter is sufficiently great, a value of 5–10, then regardless of angle of incidence as well as of coordinate of the ray falling on the mat surface, the total photocathode surface will be illuminated uniformly. With this light pipe, there is a loss in sensitivity, about half, but then the problem of nonuniformity of photocathode illumination disappears. It is obvious that measurements of the $S_e^{\mathrm{pt}}(\lambda)$ function and absolute calibration are to be performed for the system including light pipe and phototube. The author uses such light pipes for each photomultiplier assigned for absolute measurements.

4.2.1.2 PMT Absolute Calibration by Thermopile

If you wish to use the direct current mode for your PMT, the problem may originate from high output current corresponding to light intensities, which are confidently registered by the thermopile. Nevertheless, this problem can be solved easily by means of calibrated neutral grid or glass filters. The irradiance weakening by the factor 10–50 times is easily controlled. In order to make the best of PMT in the photon-counting mode, it is a need to perform two-stage calibration procedure. At first, PMT need be calibrated in the direct current mode as described in Sect. 4.2.1.1. Next, the intensity of incident radiation should be reduced down to the level not exceeding linearity limit for registration in the photon-counting mode. For the given level, your PMT has to register confidently incident light in direct current mode with a rate of about $10^4 - 10^5\ \mathrm{s}^{-1}$, what is the same as current of about 10^{-10} A at the PMT gain $G = 10^5$. Thus we carry out a set of measurements in both modes at invariant incident illumination of your PMT. It gives a transfer coefficient between amperes and photons per second: A $\leftrightarrow$ photon/s. Now, for a given wavelength, the absolute quantum yield of the photocathode $\eta(\lambda)$ in terms of pulse/photon can be easily calculated from the obtained data with the help of the formula (3.10). Certainly, it is necessary to remember that the obtained magnitude of the function $\eta(\lambda)$ is dependent on the PMT applied voltage, since it is distorted owing to discrimination of the registration system. Therefore, all measurements planned to be performed by the given PMT, which is calibrated in the photon-counting regime, need be carried out at the voltage corresponding to the working point chosen earlier. In addition, the quantum yield of the PMT photocathode may be changed in the event of its cooling. Commonly, it is better to follow carefully the instructions given for carrying out of absolute measurements.

There also exists the pulsed analog mode in PMT operation, see Sect. 3.4.2.2. However, the author is not aware of works, wherein the PMT absolute calibration is performed in this mode by the method of standard detectors.

4.2.1.3 Absolute Calibration of Phototubes and PMT by Means of Photodiode

The absolute sensitivity of photodiodes in its maximum achieves a value of order of 0.4 A/W that is high somewhat than that of vacuum phototubes. Detectors of this type feature some nonuniformity of their responsivity, however, variations of the responsivity with coordinates are found to be not more than 2–5% [1]. Calibration methods with the use of photodiodes are similar to that with thermopiles. In principle, there are available operations performed in the reverse sequence, namely, calibration of thermocouples and semiconductor photodetectors by means of phototubes and PMTs. However, the author does not encounter with descriptions of such methods in the literature. In the author's laboratory, in common practice, the working facilities as thermopiles, semiconductor photodetectors, and vacuum phototubes are used, all calibrated in metrological laboratories by means of the method of standard sources.

4.2.1.4 Absolute Calibration of Phototubes and PMTs by Means of Actinometers

The responsivities of gas-phase actinometers is found to be not better than $10^{12} - 10^{13}$ photon/s that corresponds to the phototube photocurrent of order of $10^{-8} - 10^{-7}$ A at the quantum yield $\eta(\lambda) = 0.1$. In the event of PMT, this value is associated with the current $10^{-3} - 10^{-2}$ A at the PMT gain $G = 10^5$. It is obvious that PMT calibration cannot be performed by an actinometer in one complete cycle. You can overcome this difficulty to calibrate a phototube and then perform the PMT calibration by means of the phototube. Moreover, from the beginning the voltage divider of the photomultiplier tube is to be shunted so that the PMT will become as a phototube. Then, such a quasi-phototube is calibrated at the applied voltage of order 100–200 V. Now the light intensity is reduced to the level corresponding to the dynamic range of both PMT and quasi-phototube. When the voltage divider shunt is removed, the PMT is calibrated for a required voltage by means of the same PMT operating in the quasi-phototube mode. It is the reader matter of taste as to how treating this situation. As using of an additional phototube, it has to be calibrated and further be exploited as an accepted measuring instrument. However, with replacing the quasi-phototube by PMT, and vice versa, you should keep to the illumination layout identity.

Now we discuss the way for phototube calibration by means of actinometers. The reader apparently remembers two outstanding actinometer features, namely: the absence of nonuniformity, and possibility of any required illumination layout

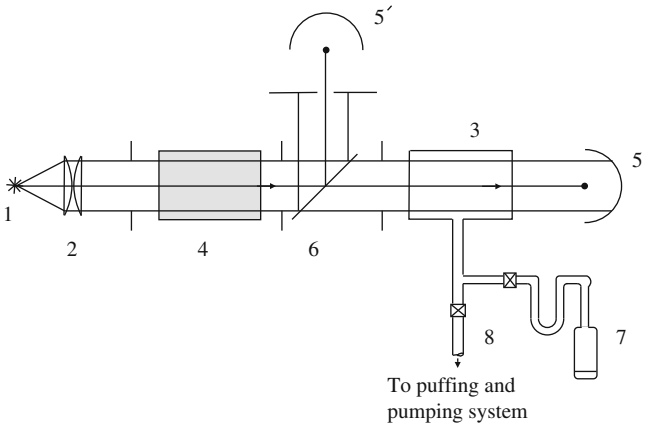

Fig. 4.5 Phototube calibration by the use of the Hg resonance lamp and the NOCl actinometer in the UV spectral range [3]. The middle pressure mercury lamp (*1*); the condenser (*2*); photochemical cell (*3*); the filter transmitting radiation of wavelength $\lambda = 254$ nm (*4*); solar blind F7 phototubes (*5*), (*5′*); the quartz window (*6*); the pressure sensor (*7*); the trap for freezing of NOCl (*8*)

(see Sect. 3.8.2). So an aperture is mounted in front of the input actinometer window to provide layout identity for light beams: one passing through the actinometer and the other incident on the phototube photocathode (see Fig. 4.5). Then the light intensity absorbed by the actinometer is measured, see Sect. 3.8.1, and the radiation fraction absorbed by the actinometer I_{abs}/I_0 is estimated. Now we consider the most difficult situation, where the actinometer absorbs less than 100% of the incident radiation, so that the radiation absorption part needs be measured. Typically, a two-beam optical scheme involving a resonance light source is used for performing such measurements (Fig. 4.5). In the case being considered the absolute calibration of a solar blind phototube is carried out by an actinometer based on NOCl (Sect. 3.8.5.1) at the mercury resonant line $\lambda = 253.7$ nm.

The method for intensity measurements by means of the NOCl actinometer is described in detail in Sect. 3.8.5.1. Before filling up the actinometer cell with NOCl, the photocurrents of the both phototubes are to become equal one to other with the help of the aperture placed in front of the phototube. Thus, the registration system output, e.g., a direct current amplifier, becomes zero. Then you fill the photochemical cell with NOCl and measure the ratio of currents of the two phototubes (5) and (5′). The ratio is found to be the radiation fraction absorbed by the actinometer $I_a^{253.7}/I_0^{253.7}$ [see formula (3.33)].

Note, the radiation fraction reflected from the backside window of the cell estimated to be about 10% passes through the cell once more, further, it is reflected again and so on. At first glance, it seems to be a negligible effect. Nevertheless, under a weak light absorption within the cell, the fraction of absorbed radiation $(I_a/I_0)_t$ can be sufficiently increased with respect to the fraction measured, (I_a/I_0),

Table 4.1 *F* correction factor for different fractions of absorbed light (see [2])

Fraction of absorbed light	Air–quartz–gas boundary			Air–quartz–water boundary		
	577	366	253.7	577	366	253.7
0.05	1.08	1.08	1.09	1.04	1.04	1.04
0.1	1.07	1.08	1.09	1.04	1.04	1.04
0.2	1.06	1.07	1.08	1.03	1.03	1.04
0.3	1.06	1.06	1.07	1.03	1.03	1.03
0.4	1.05	1.05	1.06	1.02	1.02	1.03
0.5	1.04	1.04	1.05	1.02	1.02	1.02
0.6	1.03	1.03	1.04	1.02	1.02	1.02
0.7	1.02	1.02	1.03	1.01	1.01	1.03
0.8	1.01	1.02	1.02	1.01	1.01	1.01
0.9	1.01	1.01	1.01	1.00	1.00	1.00
0.95	1.00	1.00	1.00	1.00	1.00	1.00

up to 10%, due to the effect. These corrections are estimated to be as follows (see Table 4.1 [2]):

$$\left(\frac{I_a}{I_0}\right)_t = \left(1 - \frac{I_\mathrm{a}}{I_0}\right)F, \tag{4.2}$$

$$F = \frac{\left(I_\mathrm{t}^0/I_0\right)^{1/2}\,(1-F)^2}{\left(I_\mathrm{t}^0/I_0\right) - F\left[1 + \frac{\left(I_\mathrm{t}^0/I_0\right)}{(1-F)^2}\left(I_\mathrm{t}/I_0\right)\right]}, \tag{4.3}$$

where I_0 is the intensity of radiation falling on the front side of the input cell widow, I_t^0 the intensity of radiation transmitting through the output window of the empty cell, I_t is the light intensity passing through the actinometer. The dependency of the correction F is determined by dispersion of the window material refraction index n. According to the Fresnel formulae, the fraction of light reflected by two surfaces of the window wall $(1 - \sigma)^2$ depends upon n [4]:

$$\sigma = \left(\frac{n-1}{n+1}\right)^2. \tag{4.4}$$

Having found the radiation intensity passed through the front cell window from formulae (3.33, 3.76) and Table 4.1, you measure the phototube current under the same illumination layout. It gives one calibrated value for the given wavelength. Assuming the absence of absorption, the correction coefficient $(1 - \sigma)^2$ for the cell output window can be found. An alternate procedure involves that a window similar to the cell window has to be placed in front of the phototube before measurements.

These are all the methods used by the author for photodetector calibration in the visible and UV spectral ranges by means of the method of calibrated detectors.

4.2.2 The Vacuum UV Spectral Range

4.2.2.1 Absolute Calibration of Phototubes by Means of Actinometers and Resonance Lamps

Now we consider peculiar features of calibration in the vacuum UV spectral range. Commercial calibrated photodetectors for the vacuum UV spectral range, solar blind phototubes, and PMTs, all are expensive due to high cost of their calibration procedure. Such a procedure is usually carried out with synchrotrons and storage rings or using secondary standards calibrated by means of the former (Sect. 2.5). Thermopiles cannot be exploited in the vacuum UV range without additional calibration (see Sect. 3.3). Thereby, several ingenious methods based on actinometer technique were developed in the author's laboratory to carry out absolute calibration of phototubes and PMTs in the vacuum UV spectral range.

We consider a scheme for absolute calibration with the help of xenon or krypton resonance radiation at the wavelength 147 and 123.6 nm, respectively (Fig. 4.6). It should be noted again that the method being considered is used only for calibration of solar blind photodetectors, because the resonance light sources indented to operate in the vacuum UV spectral range emit a sufficient body of visible radiation.

This calibration method is in many respects similar to that described in Sect. 4.2.1.4. A feature of this method is that all elements of the device have to be placed in a vacuum box. In addition, the oxygen actinometer absorbs 100% of the radiation passing through its input window. In the same manner, having measured the intensity by the actinometer, we perform the phototube photocurrent measurements under the same illumination layout. In the absence of the windows of 100% spectral transmittance in the vacuum UV spectral range, the absorption of the actinometer input window has to be estimated at the resonant wavelength. Elsewise the input window is extracted from the actinometer and placed in front of the phototube during calibration. In the author's laboratory, all cells designed for operation in the vacuum UV spectral range are thereby made as folding. Alkali halide crystals like LiF, MgF_2, all are brittle, therefore the window gaskets are made of teflon, and the window sealing is provided as follows (Fig. 4.7).

Here, the ring 1 is uniformly pressed by bolts, so that it bends the spring 2, pressing up on its outer side. The spring presses the cylinder 3 to the teflon rings 4 by its own inner side. The window 5 is mounted between the teflon rings. This design provides the absence of window cracks, as well as good vacuum sealing of

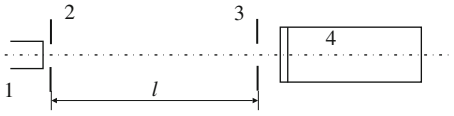

Fig. 4.6 Absolute calibration of solar blind phototube by means of oxygen actinometer and resonance light source. The resonance lamp *1*; the lamp's aperture *2*; the actinometer aperture *3*; the actinometer cell (phototube) *4* [5]

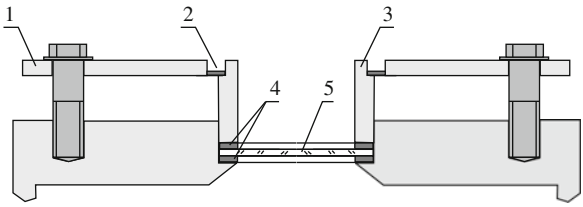

Fig. 4.7 Facilities for vacuum sealing of windows made of alkali halide crystals. The ring *1*; the spring *2*; the cylinder *3*; the teflon gaskets *4*; the window *5*

the window. The teflon rings are spread under pressure, the spring nevertheless provides good sealing even with this factor. The cell can be disassembled, then, it is possible to measure the transmittance spectrum of the window.

However, it is possible to dispense with measurements of the spectral transmittance. There is a method for the recovery of windows made of alkali halide crystals, spectrum of which was changed owing to polymerization of an organic film on the surface or appearance of color centers under the action of the vacuum UV radiation (V.K. Adamchuk, S.I. Fedoseenko, private communication, 1990). We use this technique for many years. Two quartz windows are placed into a muffle furnace, the furnace is then heated up to ≈550°C. The quartz windows are put out the furnace, and the alkali halide crystal window is put on one quartz window, which is covered by the other quartz window. Such a "sandwich" is put again into the furnace, which is switched off. As cooling the furnace down to the room temperature during 2–3 h, the color centers are annealed and the crystal window surfaces are cleaned. Repeated tests showed that the procedure above provide permanency of the spectral transmittance. We apply this method to each purchased crystal window.

Let us return to the absolute calibration procedure for phototubes (Fig. 4.6). Before calibrating the phototube or quasi-phototube, do not remember to mark by any way the coordinates of the diaphragm placed in front of the phototube window. Otherwise the calibration needs be carried out with displacing this diaphragm. Upon completion of the calibration, you can perform the calibration of a photomultiplier tube following the rules described in Sect. 4.2.1.4. Among the spectral lines of resonant xenon and krypton lamps mentioned above there are weak lines of wavelengths $\lambda = 129.55$ and 116.5 nm whose relative intensity is 2 and 25% to the intensity of the principal lines, respectively. One may submit the touch of radiation of wavelength $\lambda = 129.55$ nm in the xenon lamp. As for the radiation touch in the krypton lamp, the contribution of the touch can be taken into account by means of the calibration performed with a special cell of MgF_2 windows, the cell being filled with oxygen.

If the calibration needs be carried out over a large photocathode area of phototube or quasi-phototube, we will not encounter serious problems. However, in the event of a smaller sensitive area, i.e., comparable to the monochromator slit size of about 1×20 mm, the intensity passed through such a small area may occur less than the actinometer threshold. If this is the case, one needs to use one modification of the method of calibrated source (see Sect. 4.3.1).

4.2.2.2 Absolute Calibration of Photoionization Detectors by Means of Actinometers and Resonance Lamps

As we have shown in Sect. 3.7, a closed photoionization chamber using molecular gases is not a most precision instrument. However, the precision of intensity measurements for separate resonance lines may be sufficiently increased by means the method described in [6]. The operating principle of the technique is evident from Fig. 4.8. The electrodes made of a material nonreactive with atomic oxygen and ozone are put into the actinometer cell shown in Fig. 3.29a.

Having filled the system shown in Fig. 3.29a with molecular oxygen, we measure the intensity of the resonance radiation passing through the input aperture and cell window. As the cell is filled with vapors of a matter with the ionization potential less than photon energy corresponding to the resonance radiation, the photocurrent of the photoionization detector can be measured. Such measurements are to be performed for the given electrode configuration and pressure. The para-xylene vapors for the wavelength 147 nm or nitrogen monoxide, NO, for the wavelength 123.6 nm can be utilized for the measurements. The measurements can be performed by a relatively simple electronic scheme involving a direct current power supply of about 100 V and direct current amplifier or amplitude–digital converter. It is unimportant to know well the fraction of absorption light, the quantum yield of photoionization, and the part of charged particles, which are collected by the electrodes. All factors above are of little importance, since the detector has been calibrated for the given parameters. It is precisely these parameters that are required for further operation with this device. The calibration coefficient of the photoionization chamber is as follows:

$$B = \Phi_{hv}/I_{pc} \text{ photon/s A}, \tag{4.5}$$

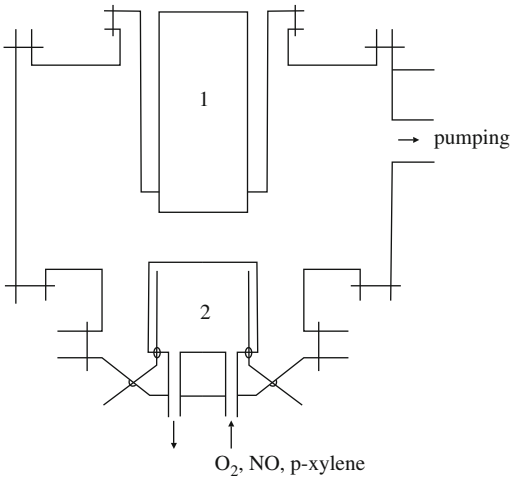

Fig. 4.8 Calibration of the closed photoionization chamber by the oxygen actinometer [6]. The resonance lamp *1*; the actinometer cell *2* (the closed photoionization cell)

where Φ_{hv} is the photon flux passed through the input cell window and measured by the actinometer, I_{pc} is the photocurrent of the photoionization chamber. For the device used by the author, $B = (5–10) \times 10^{20}$ photon/s A according to which matter, the vapors of para-xylene or NO, is used. The uncertainty of B is less than 3%.

What does a gain be given by the method? Photocurrents of value down to 10^{-13} A can be confidently measured that corresponds to the radiation intensity of value 10^6 photon/s. Actually this is true when the product of absorption radiation fraction by the absolute quantum yield of ionization is about 0.5, and the fraction of collected charge particles is about 0.2. Thereby, the sensitivity of your system is increased by seven orders without any loss in accuracy of measurements!

4.2.2.3 Absolute Calibration of Luminophor–PMT System Using Actinometers and Resonance Lamps

The arrangement assigned to absolute measurements of spectral photon flux from the vacuum UV monochromator output is shown in Figs. 3.29a, 4.8, and 4.9 [7]. The setup involves the photochemical cell equipped with sodium salicylate luminophor and PMT.

The cell (6) in Fig. 3.29a includes the electrodes, see Fig. 4.8, so that it can be used as both an actinometer and photoionization chamber. It is of first importance the following features. The aperture shape (5) is chosen so that the luminophor surface (4) illuminated in calibration and measuring of the monochromator output

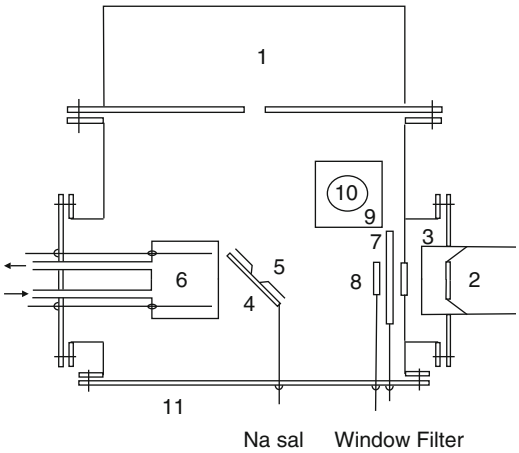

Fig. 4.9 The arrangement for absolute measurements of intensity in the vacuum monochromator output (*the quantometer*) [7]. The vacuum monochromator (*1*); the resonant lamp (*2*); the lock chamber (*3*); the luminescent screen (*4*); the aperture (*5*); the photochemical cell (*6*); the attenuator filter as the MgF_2 window with evaporated aluminum (*7*); the MgF_2 window (*8*); the mirror (*9*); PMT (*10*); the flange with the operation handles "sal. Na," "window," and "filter" (*11*)

flux has to be within the solid angle determined by the aperture of the output. In addition, the plane of the luminophor substrate is to make the angles 45° to the beam axes, one drawing through the lamp 2 and the other drawing through the monochromator. If this is the case, the intensity of the monochromator output beam illuminating the luminophor or the beam passing into the cell (6) has to be equal one to the other. The calibration procedure involves the following steps.

1. With the help of the arrangement shown in Fig. 3.29a and according to improvements considered above, the measurements of intensity radiation passing through the cell input window from xenon and krypton resonance lamps are carried out. The resonance lamp is placed near to the actinometer cell. Calibration of the photoionization chamber is also performed at the wavelengths 147 and 123.6 nm.
2. The luminophor screen (4), filter (7), and the window (8), all are taken off from the light beam trace (Fig. 4.9). Then the cell (6) is filled with para-xylene vapors for using under radiation of the xenon lamp, or NO for using with the krypton lamp. The vapor pressure is to be the same value as used for the photoionization chamber calibration. The photocurrent measurements are carried out at the electrode voltage equal to that used for calibration of the photoionization chamber. Thus the intensity measurements are performed under the layout environment shown in Fig. 4.8.
3. The screen with sodium salicylate (4) is set behind the aperture (5) and the window (8) similar to that used in the cell (6) is then mounted as shown in Fig. 4.9. The PMT photocurrent is measured in the direct current mode. The photocurrent is produced by luminophor luminescence and scattered light from the resonance lamp in the visible and UV spectral ranges. The using of the window (8) allows radiation absorbed by the cell window to be taken into account, i.e., it enables the photon flux passing through the aperture (5) to be estimated with well accuracy.
4. The lock chamber (3) placed between the lamp (2) and output window of the vacuum system is filled with oxygen up to pressure about 200 torr, thus resonance radiation of the lamp is diminished. Thereafter, the PMT photocurrent is measured. The current is caused by radiation of the resonance lamp in the visible and near UV spectral ranges. The photocurrent produced by resonance radiation is calculated to be as difference of the data measured in items 3 and 4.
5. By the given sensitivity of the photoionization detector the quantometer sensitivity in the direct current mode is calculated to be as follows:

$$S_q = I_{PMT}/(I_{pc}/B) \text{ (A s/photon)}, \tag{4.6}$$

where I_{PMT} is the PMT current with due regard for scattered light from the resonance lamp (A).
6. The vacuum UV filter (7) being MgF_2 window with a thin layer of evaporated aluminum is put into the light beam to reduce the photocurrent down to the level, which allows operation in the photon-counting mode. Such a filter design (7)

permits intensity reduction of radiation of the resonance lamp both equally in the visible and VUV spectral range. Thereafter, the transfer coefficient between the direct current mode and photon-counting one is to be found as described in Sect. 4.2.1.2. Finally the sensitivity of the quantometer in the photon-counting mode is estimated.

The story is complete! The quantometer is ready for operation. It provides absolute intensity measurements of radiation falling on its input in the direct current mode and photon-counting mode over the spectral range $\lambda = 340$–10 nm, wherein the quantum yield of luminescence of sodium salicylate remains constant.

Both during calibration and during measurements the angles of incidence are the same. The illuminated areas are equal too. Thus, it is all the same to the registration system whether the incident rays come to the luminophor from the lamp or from the monochromator.

With working of the not-better-sensitive PMT71 the sensitivity of the quantometer used in author's laboratory is estimated to be $S_q = (1.20 \pm 0.06) \times 10^{-5}$ pulse/photon. The sensitivity can be increased in three times via a thicker layer of sodium salicylate. A more effective registration system, and modulation system for the monochromator output, the both appear to be design to subtract automatically of PMT dark pulses. By this way the sensitivity can become in 10–30 higher.

4.3 Calibration by Means of Standard Sources

In principle, both calibration methods, absolute calibration one considered in Sect. 4.2, and the other is treated by this section, are to be quite the same under certain conditions. Having measured the photon flux from a monochromatic source in order to calibrate a photodetector and estimate its responsivity, in fact, you also performed calibration of the source for the given layout. Under the given illumination layout you can use the source for further calibration procedures. However, it would not be bad to perform additional testing of these instruments, i.e., you can carry out verification with other sources and detectors to have a good chance of changing the illumination layout. At first we consider the requirements, which have to be fulfilled by the light source in order to use it as a verification facility. In common use, the light sources used as verification facilities in absolute units are specified by their spectral radiance expressed in W cm^{-2} sr^{-1} nm^{-1} and spectral photon radiance in photon cm^{-2} sr^{-1} nm^{-1} or, in the event of resonance light source, in W cm^{-2} sr^{-1} and photon cm^{-2} sr^{-1} (see Sect. 1.1). In addition, the maximum solid angle and maximum illuminating area are specified. If you intend to prepare your own measuring instrument not being as a point source, at first you will be to determine these limited solid angles and illuminating area, and thereafter you will calibrate the source. Especially, this may be relevant as you work in the spectral range, wherein filament lamps do not operate, e.g., at $\lambda < 250$ nm. Let us consider a simple example of using a resonance lamp.

4.3.1 Photodetector Calibration by Means of Resonance Lamps

So, the resonance lamp you decided to use as a verification facility has to show a stable operation. By this is meant that the lamp has to be aged so that its photon flux becomes virtually independent with time. Potential time dependency is to be investigated and recorded. The lamp current has to be less than a limit value specified in the lamp technical certification. It is also necessary to estimate limits of heater current of the cathode as well as of the lamp current under which the photon flux shows the weakest dependency against current. The resonance xenon lamps of type KsR-2 produced by State Optical Institute (Russia) are relatively well resonance light sources, which are well suitable sources for the purposes being discussed. The photon flux of aged lamps, which have been worked for 4–5 h, decreases in not more than 2% for one worked hour at the discharge current 0.25 A and heater current 5 A. Krypton lamps are much worse than xenon lamps. Having established the normal operation conditions, you need to calibrate the lamp by means of an oxygen actinometer and determine working limits of the lamp. Here the solid angle of emitted radiation and emissive area both have to be estimated, for example, by the arrangement shown in Fig. 4.6. The separation l between the output aperture of the lamp and the input aperture of the actinometer cell is to be much more than the diameter of the output lamp aperture d_l and diameter of the input aperture of the actinometer cell d_a. For the given value of d_a, we find the maximal solid angle $d_a^2/2\pi l^2$, and aperture d_a/l, within of which the radiation intensity is directly proportional to the square of the input actinometer window. We note that such an operation is not valid with respect to the input area of phototube due to nonuniformity of the photocathode sensitivity. Thus, we estimate the maximal solid angle, within of which the photon intensity is proportional to this angle. Thus, the intensity can be estimated for every value of solid angle being less than the maximal value of the solid angle. Then, a similar estimation has to be performed with respect to the lamp diaphragm (2) (Fig. 4.6). You set the maximal working body of the lamp and the maximal opening of the aperture, below of which the intensity gets proportional to the value of the illuminating area. In the limits you set the photon flux is actually proportional to illuminating area and solid angle, within of which radiation spreads. Thereafter you can use the lamp for calibration under the limits you set and currents you chose according with the procedures described in detail in Sect. 4.2.

4.3.2 Photodetector Calibration by Means of Strip Lamps

With a tungsten strip lamp calibrated in absolute units, the lamp can be used for absolute calibration of your photodetector in the spectral range $\lambda > 320$ nm. A setup for the photodetector calibration in absolute units is shown in Fig. 4.10.

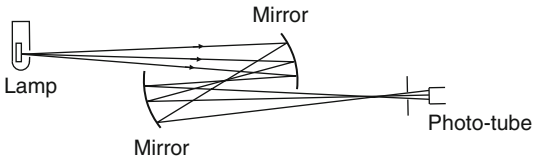

Fig. 4.10 Phototube calibration by means of a strip lamp

Due to thermal conductivity the temperature of the strip lamp decreases from its center to the massive current leads. Thereby a space of the illuminating area has to be certified, wherein the temperature remains constant in some limits. The space area should be used for measurements in absolute and arbitrary units. In the event of a very low uncertainty of calibration, much less than 1%, just this space area has to be focused on a rectangular opening of square a. The opening width is to be equal to the lamp width, and its height is to be equal to the height of the space area. A mirror system of magnification 1:1 focuses the space area onto the rectangle opening. The spectral radiant power receiving by the detector is estimated to be as follows:

$$\Phi_e(\lambda) = L_e(\lambda)\ \tau(\lambda)\ L(\lambda)\left(\frac{Aa}{D^2}\right) \quad [\mathrm{W\ nm^{-1}}], \tag{4.7}$$

where $L_e(\lambda)$ is the spectral radiance in [W cm^{-2} sr^{-1} nm^{-1}] (see Sect. 1.1); $\tau(\lambda)$ is the spectral transmittance of the filter; $L(\lambda)$ is the spectral reflectivity of the mirror system; A is the minimal area of one mirror; D is the distance between the lamp body and the mirror. The aperture A/D^2 needs not be more than the maximal allowable aperture. Evidently, the axes drawing through the centers of the mirrors, diaphragms, and the lamp body should be normal to the plane of the lamp body. The dependency $\tau(\lambda)$ and $L(\lambda)$ have to be well known or well determined in experiments.

The photocurrent of your photodetector I is found to be as follows:

$$I = \int_{\lambda_1}^{\lambda_2} S_e(\lambda)\ \Phi_e(\lambda)\mathrm{d}\lambda = S_e \int_{\lambda_1}^{\lambda_2} s_e(\lambda)\Phi_e(\lambda)\mathrm{d}\lambda, \tag{4.8}$$

where $S_e(\lambda) = s_e(\lambda)S_e$ (A/W) is the spectral sensitivity of the photodetector, λ_1, λ_2 are limit wavelengths of transparency of the used filter. It has been noted that the relative spectral sensitivity $s_e(\lambda)$ has to be determined in additional experiments. During absolute calibration, the calibration coefficient S_e needs be found in terms of the ratio of the photocurrent to the convolution calculated to be the integral form:

$$\int_{\lambda_1}^{\lambda_2} s_e(\lambda)\Phi_e(\lambda)\mathrm{d}\lambda.$$

The task is solved. In metrological laboratories similar methods are used for calibration of photodetectors. Such methods give the least uncertainties, all other factors being equal.

The author described the most important methods for absolute calibration of photodetectors. Virtually, the absolute calibration methods applied to photodetectors and radiation sources are often identical. For example, while providing verification for sensitivity of a calibrated photodetector by a method described in this section, we also verify both the photodetector and light source (see Sect. 1.3).

Now we discuss briefly main techniques for measuring of radiation intensity from light sources not designed for metrological purposes. The measurements of this kind hold a special position, and they will be considered later.

4.4 Absolute Intensity Measurements of Light Sources Used in Experiments

With an accepted detector the intensity of the light source you use in experiments can be measured, providing the source need not be calibrated by its manufacturer. In order to do this, a proper method for absolute calibration or a calibrated detector can be used (see Sects. 4.1–4.3). Such a calibration can be carried out in a required spectral range, under a proper layout environment. With the well-known radiation indicatrix and illuminating area of equal intensity, as well as the functions $\Phi_e(\lambda)$ or $\Phi_{hv}(\lambda)$, you can perform complete calibration of this source (see Sect. 4.3.1).

4.4.1 The Visible and Near UV Spectral Range

The intensity measurement of laser radiation is a simplest procedure. In the continuous mode the radiation is expressed in terms of W or photon/s, in the pulsed mode it is expressed in J/pulse or photon/pulse, and in the pulse-periodic mode it is expressed in terms of J/pulse, photon/pulse, and average power in W or photon/s. Calibration in the latter event involves a calibrated thermopile or a special meter based on thermocouples to estimate the average power or average energy of laser radiation. The author used the laser power meters OPHIR NOVA II, equipped with thermopile, and photodiode sensors, which allow measurements to be carried out in the range 3 μW–12 W. The power meter is a perfect instrument, provided that you follow the operating instructions and work with the accepted instrument.

Rabeck recommended also chemical actinometer for this purpose [8]. The author has no doubts this is possible for every not-high intensity laser in the continuous mode. As for laser operation in the pulsed mode, you have to be sure that there are no secondary processes, which make the quantum yield of the used photoprocess to be reduced. The same is true for actinometry of any other pulsed light sources. One should remember that the radiation spectrum of pulsed lamp depends on time due to temperature variations of plasma.

Absolute calibration of the other continuous light sources, non-laser types, in the visible and near UV spectral ranges can be performed by methods described in Sects. 4.2–4.3. We note once more that the limits of dynamic ranges, nonuniformity of photodetectors, and layout illumination factors should be taken into account. As the output monochromator slit is a light source, it is also possible to perform absolute calibration of the source by any suitable calibrated photodetector.

4.4.2 The Vacuum UV Spectral Range

Point light sources, for example, such as commercial deuterium lamps and deuterium–neon lamps, can be calibrated by synchrotron radiation, as well as by secondary point standards, which have been calibrated by synchrotron radiation. Evidently, these standards should be verified routinely, otherwise the calibration uncertainty becomes unacceptable. These light sources have to be point-like ones, because of that the primary standard is a point source by itself. This is due to the fact that the primary standard is a well remote apparatus to provide biological shielding. Commonly, the calibration of pulsed sources can be carried out only by a thermopile or calibrated phototubes or photodiodes. However, there appears the problem of its spectral sensitivity dependency in the vacuum UV spectral region. As the monochromator output slit is a light source, absolute calibration of $\Phi_e(\lambda)$ can be also performed by a calibrated photodetector suitable due to its dynamic band. One may also use a device similar to that described in detail in Sect. 4.2.2.3.

By the author's opinion, in the vacuum UV spectral range the best way for absolute calibration of laboratory sources of continuous spectra is the method based on oxygen actinometer (see Sects. 4.2 and 4.3). Among these methods are techniques, which may be used for measuring in photon-counting mode to register photon flux from sources of continuous spectrum (see Sect. 3.8.5). Such a technique allows to measure spectra in a wide range, even if the spectra is not been measured even in arbitrary units. This is especially urgent problem in the vacuum UV spectral range, where a relatively strong intensity of monochromatic radiation is realized in the range $\lambda > 110$ only with the use of resonance lamps at several spectral lines: $\lambda = 116.49$ nm (22%) and 123.58 nm (78%), Kr; 121.57 nm, H, L_α; 129.55 nm (2%) and 146.96 nm, Xe [2, 8]. If you need light sources with strong intensity for measurements spectral quantum yields, light sources of non-monochromatic radiation can be utilized (see Sect. 3.8.3.1 and next section).

4.4.2.1 Recording of Spectral Photon Fluxes from Continuous Spectrum Lamps by Using Actinometers

Figures 4.11 and 4.12 illustrate the manner in which the spectral photon flux from a light source of continuous spectrum can be measured by an actinometer and long-pass filter. The spectrum, for example, a hydrogen discharge lamp should be

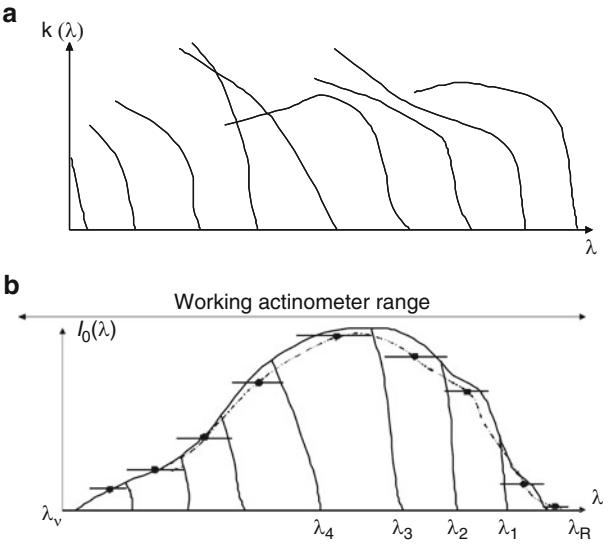

Fig. 4.11 Illustrating absolute measurements of the lamp spectral radiation intensity by using filters. Transparency spectra of the filters (**a**); the lamp spectrum and measured function $I_{hv}(\lambda_i - \lambda_{i+1})$ denoted by horizontal short lines (**b**)

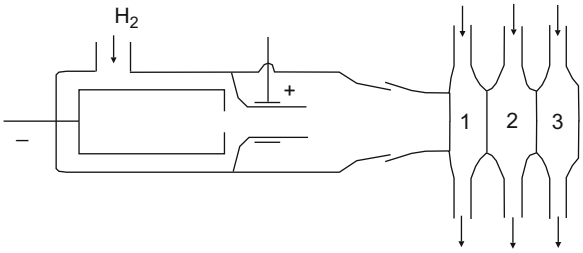

Fig. 4.12 The cell for measurements of spectral functions of convolution quantum yields. *1, 2* are the cells for gas-phase filters; *3* is the photochemical cell

estimated in a wide spectral range. Actinometers with NOCl ($\lambda = 530$–180 nm) or oxygen ($\lambda = 176$–115 nm) should be used as photon-counting detectors, where short-wavelength limit is specified by the transparency of windows made of MgF_2 or LiF, and filters used with sharp absorption edges in long-wave range. Such a filter chosen to be as solid, liquid, or gas-phase is placed in a cell in front of the actinometer window (Fig. 4.11a).

The measuring algorithm is simple as follows:

1. Irradiate the actinometer by radiation passed through the cell windows record its spectral radiation intensity $I_{hv}(\lambda_r - \lambda_v)$, where λ_r is specified by long-wave limits the hydrogen lamp radiation, namely, $\lambda_r \approx 380$ nm, and λ_v specified by transmission of the cell windows made of fused quartz, MgF, or LiF (Fig. 4.12).

2. Set an available filter in front of the actinometer cell, with the filter transmission limit being λ_1 as close as possible to the long-wave limit of radiation in the range $I_{hv}(\lambda_1 - \lambda_v)$. Intensity is found to be equal to $I_{hv}(\lambda_r - \lambda_1) = I_{hv}(\lambda_r - \lambda_v) - I_{hv}(\lambda_1 - \lambda_v)$ in the range λ_r/λ_1 (Fig. 4.11b). The transmission limits can be estimated by wavelengths corresponding to the transparency of value 0.5.
3. Next filter characterized by the transmission limit of $\lambda_2 < \lambda_1$ is set in front of the actinometer cell to estimate the function $I_{hv}(\lambda_1 - \lambda_2)$ and so on.

The emission spectrum estimation follows from the function $I_{hv}(\lambda_i - \lambda_{i+1})$, for example, the horizontal short-lines in Fig. 4.11b. In the event of the lamp spectrum expressed in terms of arbitrary units, calibration through a set of convolutions allows a spectrum in absolute units to be calculated. Usual set of glass filters can be exploited in the near UF and visible spectral range. In the vacuum UV range, unsaturated hydrocarbons such as *cis*-butene-2 (205 nm), ethylene (195 nm), and oxygen (176 nm), as well as saturated hydrocarbons such as butane (162 nm), methane (142 nm) can be used. The numbers in the brackets indicate long-wave limits in nm at the optical path 200 torr cm. Among solid filters are fused quartz (155 nm), sapphire (145 nm), and fluorite (125 nm), for example. In particular, this method was applied to verify the estimation accuracy of the spectral responsivity function for the monochromator/PMT system with the use of different light sources (see Sect. 6.4).

4.4.2.2 Estimation of Spectral Absolute Quantum Yields Without Monochromator

Having estimation of the spectral radiation intensity of the light source, you may make measurements of spectral convolution quantum yields for photoprocesses under study (see Sect. 3.8.3). When the limit wavelength λ_i are close together and the quantum yields depend only slightly on wavelength, then the convolution quantum yields are also close together or coincide.

One version of set-up is shown in Fig. 4.12. The basic element is the triple cell. The first cells offer as gas-phase filters, the third cell contains an actinometer matter or matter under study. Through the procedure described in the previous section the intensity of radiation passed through windows of cell 1, 2 should be estimated in the spectral range $\lambda_i - \lambda_{i+1} - I_{hv}(\lambda_i - \lambda_{i+1})$. On irradiating the matter under study with the same filters the photolysis products are found to be within the range $\lambda_i - \lambda_{i+1} - (\lambda_i - \lambda_{i+1})$, as well as the convolution quantum yields as follows: $\Phi^c(\lambda_i - \lambda_{i+1}) = V[A](\lambda_i - \lambda_{i+1})/I_{hv}(\lambda_i - \lambda_{i+1})$ (see Sect. 3.8.2). Intensity of absorption by the matter under study radiation, $I^a_{hv}(\lambda_i - \lambda_{i+1})$, is assumed to be equal to $I_{hv}(\lambda_i/\lambda_{i+1})$. Sometimes absorption curve dips are likely to occur at some wavelengths within the absorption spectrum; that is absorption of the matter under study does not achieve 100% over all specified spectral range $\lambda_i - \lambda_{i+1}$ for a given optical path within the matter. Actually this is true in the case of absorption spectrum of line or diffuse type. In order to determine exactly the values $I^a_{hv}(\lambda_i - \lambda_{i+1})$ you may make measurements of $I(\lambda_i/\lambda_{i+1})$ twice: at first in usual manner, then with irradiating actinometer

through the filters and the matter under study, with the matter placed into the middle cell. The difference of the data found on the first and second stages of measurements gives the values $I^a_{hv}(\lambda_i - \lambda_{i+1})$.

The technique above was successfully applied in the author's laboratory to investigation of photodecay of molecules NOCl, NO_2, N_2O, H_2O, CO_2, O_2, as well as alkyl iodide and perfluoralkyl iodide in the vacuum UV spectral range (see Figs. 3.25–3.27, Sect. 3.8.5 and references therein).

Problems

1. In addition to the strong lines mentioned above, xenon and krypton lamps have weak spectral lines $\lambda = 129.55$ and 116.5 nm with relative intensities in order of 2 and 25% with respect to the intensity of the principal lines, respectively. One may reconcile with a touch of radiation of wavelength $\lambda = 129.55$ nm in xenon lamp, as for a touch in krypton lamp the contribution can be taken into account by calibration using a special cell with MgF_2 windows filled with oxygen. How does it may be done?
2. Why is the window (8) be needed (Fig. 4.9)?
3. You measured the photocurrent I_{pc} in A for a calibrated photoionization detector of sensitivity $S^{pc}_{hv}(\lambda)$ (Fig. 4.9) and found the radiation intensity $I_{hv}(\lambda)$, photon/s. Then you measured the luminophor/PMT output in the photon-counting mode n, pulse/s. Express the sensitivity of the quantometer $S_q(\lambda)$ in terms of pulse/photon. If the $S_q(\lambda)$ value can depend on wavelength?
4. What is the way for determination of the spectral transparency of the filter you used, $\tau(\lambda)$, as well as the spectral reflection coefficient of the mirror system, $L(\lambda)$?

References

1. Budde, W.: Physical detectors of optical radiation. In: Grum, F., Bartleson, C.J. (eds.) Optical Radiation Measurements, A Treatise, vol. 4. Academic, New York (1983)
2. Calvert, J.G., Pitts Jr., J.N.: Photochemistry. Wiley, New York (1966)
3. Pravilov, A.M., Karpov, L.G., Smirnova, L.G., Vilesov, F.I.: Reactions of $I(^2P_{1/2})$ + NOCl. I. Quantum yield measurements of $I(^2P_{1/2})$ productions at photolysis of CH_3I and CF_3I and ratio of rates of $I(^2P_{1/2})$ interactions. Khimiya Vysokikh Energ. (High Energ. Chem. USSR) **7**, 335–341 (1973)
4. Fresnel equations. http://en.wikipedia.org/wiki/Fresnel_equations
5. Bibinov, N.K., Bolshukhin, D.O., Kokh, D.B., Pravilov, A.M., Vinogradov, I.P., Wiesemann, K.: Absolute calibration of the efficiency of a VUV-monochromator/detector system in the range of 110-450 nm. Meas. Sci. Technol. **8**, 773–781 (1997)
6. Pravilov, A.M., Sidorov, I.I., Smirnova, L.G.: The method of measurement of photon flux by using closed photoionization chamber. Certificates of Authorship No 1466448, 16 Dec 1985
7. Zagrubsky, A.A., Pravilov, A.M., Sidorov, I.I., Smirnova, L.G.: The method of calibration of non-selective light detectors. Certificates of Authorship No. 1226075, 5 Nov 1984
8. Rabek, J.F.: Experimental Methods in Photochemistry and Photophysics. Wiley, Chichester (1982)

Chapter 5
Methods of Calibration of Spectral Instruments in Arbitrary Units

Abstract This chapter deals with calibration methods for system designed to make measurements of radiation spectra of extended, point and narrow cylinder light sources in the near IR, visible, and UV spectral ranges using strip lamps, quartz tungsten–halogen lamps, and deuterium lamps. Calibration techniques are also considered here, which use well-known radiation spectra and calibration methods in the vacuum UV spectral range. The methods using extended hydrogen-discharge lamps in the vacuum UV spectral range are explained here in detail.

5.1 General

Commonly, a spectral instrument is assigned to:

- Serve to measure absorption spectra of the samples under investigation. In this event, there is no necessity to carry out calibration spectral responsivity of the device. Commonly, it is to be graduated by wavelengths.
- Serve as radiation source, along with a light source of linear or continuous spectrum, for excitation of any process being initiated by light absorption in the samples under investigation. A monochromator is usually used for this purpose. Such a device is no virtually different from usual radiation sources. It can be calibrated in arbitrary units by means of suitable photodetectors, which have been calibrated in the relative units. It can be also calibrated absolutely with the help of the methods described in detail in Chap. 4.
- Serve for measuring of spectral photon flux, $\Phi_{hv}(\lambda)$ [spectral radiation intensity, $I_{hv}(\lambda)$], of the objects investigated in terms of functions $\Phi_e(\lambda)$, W/nm, and $\Phi_{hv}(\lambda)$ [$I_{hv}(\lambda)$] photon/(s nm) (see Sect. 1.2). In order to find such kind of spectrum, it is necessary to measure the spectral sensitivity (responsivity) $S_e(\lambda)$ or $S_{hv}(\lambda)$ for a used registration system, for example, the system involving the monochromator, filter, and PMT. There is also a need to find the spectral detector output (spectral photoresponse) (quantity Y, see Sect. 3.2.1), for example, its current, in measuring this spectrum as a function of wavelength. Finally, the true spectral photon

A.M. Pravilov, *Radiometry in Modern Scientific Experiments*,
DOI 10.1007/978-3-7091-0104-9_5,

flux, i.e., the spectral photon flux corrected by this dependency, for example, is calculated using the following formula:

$$\Phi_{hv}(\lambda) = \frac{Y(\lambda)}{S_{hv}(\lambda)}, \tag{5.1}$$

(see Sect. 3.2.2). Seemingly, it would be easier to use a calibrated radiation source with the well-known spectral photon flux $\Phi_{hv}^{et}(\lambda)$, add it to the spectral device, then measure the photoresponse $Y_{et}(\lambda)$, and find the function $S_{hv}(\lambda)$ from (5.2):

$$S_{hv}(\lambda) = \frac{Y_{et}(\lambda)}{\Phi_{hv}^{et}(\lambda)}. \tag{5.2}$$

However, this task is not so simple due to the absence of suitable calibrated sources, difficulties arising with taking into account calibration layout, and forthcoming measurements of the emission spectra, and so on. In this chapter, we will just discuss the ways that admit the functions $S_e(\lambda)$ or $S_{hv}(\lambda)$ to be determined. Sometimes there arises the task of finding the spectral transmittance $F(\lambda)$ of the spectral device. This task will be also discussed. If you need relative spectral sensitivity functions of the registration system $s_e(\lambda)$ or $s_{hv}(\lambda)$, it is sufficient to measure the photoresponse and use spectral photon flux in arbitrary units [$y_{et}(\lambda)$ and $\phi_{hv}^{et}(\lambda)$, respectively].

We begin with the straightforward thing: finding the relative spectral sensitivity functions of the registration system $s_e(\lambda)$ or $s_{hv}(\lambda)$ including monochromator, filter, and photodetector in the near UV, visible, and near IR spectral range. The system of this kind is usually applied for spectral measurement of radiation from extended light sources, i.e., sources having large illuminating areas, radiation of which cannot be focused precisely on the input monochromator slit. For the registration system assigned to measure radiation spectra from point or narrow cylinder light sources, one needs to use a lens (condenser) or a system of mirrors. In the case of a narrow cylinder source, it is better if this lens has a cylindrical shape. All the systems mentioned above have aberrations; additionally, lens (condenser) has chromatic aberration caused by dispersion of the refractive index of the lens material [1–3]. Calibration of such systems is a difficult task, especially in the UV spectral range. Thereby this calibration method will be discussed separately. The author notes once more that the calibration layout has to be similar, if possible, to that assumed to be used on measuring of radiation spectra. We demonstrate with the following example why it has primary importance. Let us assume that a monochromator with a diffraction grating as a system with five reflections arranged by Fastie scheme is used for this purpose [4]. Spectral transparency function of this system $F(\lambda)$, which is the ratio of the output intensity to incident one, is near to zero at $\lambda = 190$ nm. It is mainly caused by decreasing the coating reflectivity of the diffraction grating and mirrors. In the spectral range $\lambda = 200$–300 nm, the

reflection coefficient for aluminum, which varies from 0.8 to 0.95, is critically dependent on the purity of the evaporation aluminum layer as well as evaporation method [3, 5, 6]. It is easy to find that with five reflections, the transparency is found to be proportional to the value $(0.8)^5 = 0.33$. The aluminum reflection coefficient decreases with time, and diffraction gratings are subject to this effect to a great extend [6], especially in the vacuum UV spectral range. In operation, the reflection coefficient of optical surfaces decreases, which is also due to polymerization of organic dirties caused by radiation treatment. If some areas of the mirror or diffraction grating have the reflectivity 0.75 and the other areas have reflectivity 0.7, then the difference in transmission will be about $(0.8/0.70)^5 = 1.95$! It is obvious that the less the reflection coefficient, the greater this effect is. Monochromators have nonuniformity property as some types of photodetectors.

5.2 Sensitivity Calibration Using Calibrated Strip and Quartz Tungsten–Halogen Lamps for Spectrometer/Photodetector Systems

The task of sensitivity calibration in arbitrary units for systems involving spectrometers and photodetectors using calibrated lamps is relatively simple by itself. This is because tungsten ribbon filament strip lamps, as well as quartz tungsten–halogen lamps, are used widely, and they are light sources of well-known radiation spectra in the spectral range running from about 250–300 to 2,600 nm. The methods of working with this type of light sources have been discussed in Sects. 2.1.3 and 2.1.4, and the author notes once more that the strip lamps are preferred to other lamp types, because spectra of them have only a weak dependence on time, and the use of them is much chipper.

Now we consider how the strip lamps are used for calibration of the function $s(\lambda)$. Figure 5.1a shows the scheme of a most precise calibration method. This scheme is similar to that used for absolute calibration of a photodetector by means of a strip lamp (Fig. 4.10) described in Sect. 4.3.2. The distinctions are that, first, a diffuse reflective screen is placed behind the aperture, and the screen with a well-known spectral distribution of the reflection coefficient of diffusion reflection, for example, being made of MgO, $BaSO_4$, or other diffuse reflective materials is used. Second, the input monochromator slit is used instead of the output aperture and phototube. It is convenient to use the slit dismounted from the other monochromator as diaphragm controlling the relative aperture for illuminating the input monochromator slit; the height of this slit can be restricted by a black paper screen, for example. Currently, the author uses the WS-1 Diffuse Reflectance Standard (Ocean Optics) as a diffuse reflective screen [7]. It is made up of a diffuse white plastic that provides a *Lambertian scattering* surface [8]. The WS-1 is mounted inside the anodized aluminum housing. It is hydrophobic, chemically inert, and very stable, even in deep ultraviolet applications. Its reflection coefficient is greater than 98%

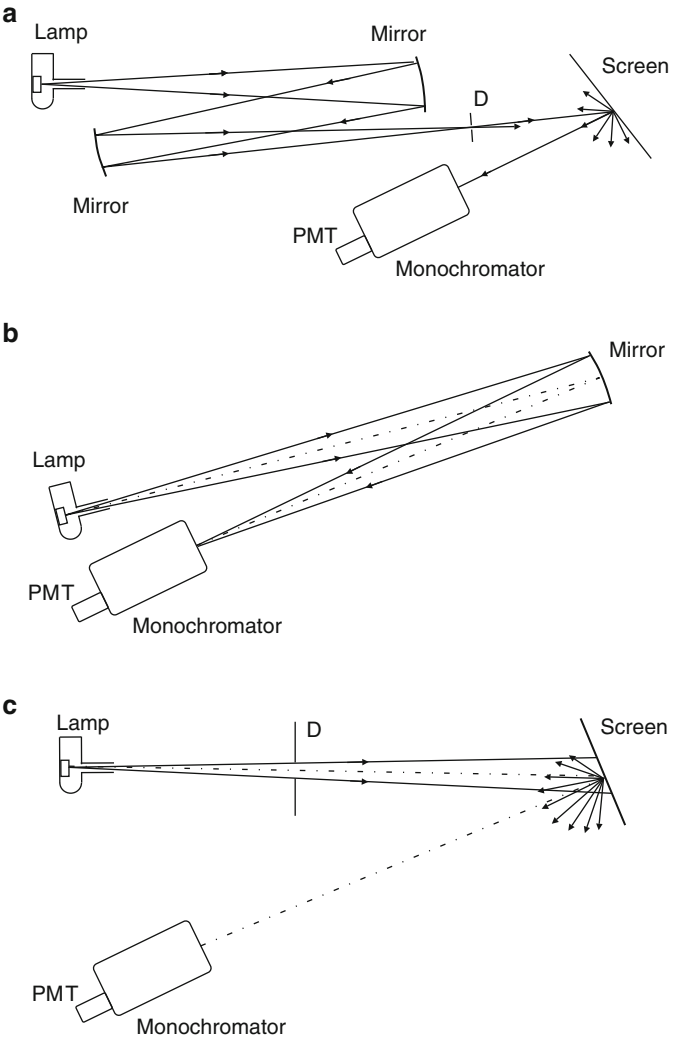

Fig. 5.1 (**a**) Sensitivity calibration of the system including a monochromator, photodetector, concave mirrors, diffuse reflective screen, and filament lamp. (**b**) Sensitivity calibration of the system including a monochromator, photodetector, concave mirror, and strip lamp. (**c**) Sensitivity calibration of the system including a monochromator, photodetector, diffuse reflecting screen, and filament lamp

within 250–1,500 nm and more than 95% within 250–2,200 nm. Unfortunately, the manufacturer did not specify the dependency of the reflection coefficient on wavelength in the spectral range $\lambda \leq 250$, but this dependency can be easily measured as discussed below.

Undoubtedly, the essential advantage of this scheme is that the radiation reaching the diffuse reflective screen is illuminated by the central body of the

illuminating area, having a constant temperature. Besides, you may place rectangular diaphragm with the size just the same as that of the central body between the screen and input monochromator, or may measure the function $s(\lambda)$ just at the solid angle, which will be further exploited. As it has been noted early, this fact is sufficiently important. The potential problems of using this scheme are as follows. Radiation reflected by a mirror is polarized with polarization degree depending on wavelength, and reflection coefficient of a mirror depends on the radiation polarization degree (see Sect. 5.5 for details). The reflection coefficients of the mirrors and screen have to be measured. In the UV and IR spectral range, their values do not equal to unity, and moreover, they depend on wavelengths.

In the absence of any diffuse reflective screen, you may use the scheme shown in Fig. 5.1b. The ratio of the size of the light spot in direction perpendicular to the monochromator entrance slit height to the mirror focal length, f'-number (of illumination), has to be equal to the ratio of the size of the grating in direction perpendicular to the slit height to the monochromator focal length, f number of the monochromator. Radiation reflected by a mirror is also polarized with polarization degree depending on wavelength. Besides, a few part of the input slit of the monochromator is illuminated. Hence, the mirror system and diffraction grating will be also illuminated partially, providing the aperture of the lighter is equal to that of the monochromator. You need to perform several measurements with illumination of different parts of the slit and execute further averaging of the obtained data. The author's opinion is that such a method in not quite good.

In the absence of a mirror, you may use the scheme shown in Fig. 5.1c. The ratio of diameter of the light spot at the screen to distance between it and entrance slit of the monochromator, f'-number, has to be *a little bit* larger than the f number of the monochromator. The reason is that the total surface of the grating is to be illuminated, which enables a sufficient amount of scattered light to be reduced. Under these conditions, the screen may be illuminated by light emitted by the *total* lamp body surface. Thereby, while calculating the radiation spectrum, there is the risk of getting an uncontrolled error. The temperature function of the lamp body against the distance to the lamp center was theoretically analyzed [9]. The measurements of the lamp temperature at the center region of the lamp of SIRSH8.5–200 type as well as its periphery were carried out by M.S. Matveev and O.E. Verkhovskaya (M.S. Matveev, O.E. Verkhovskaya, private communication, 2010). It was found that the temperature may be less or more than that value at the center. The temperature increase at the strip periphery is evidently caused by nonuniformity of its width happened during its flatting process. In any case, the difference between temperature at the center and at the periphery is not more than ± 5 K with respect to the temperature at the center 2,700 K. Obviously, while calculating using the Planck's law, the maximum error may occur in the short-wave spectral range [see Fig. 2.1 and Eq. (2.1)]. The maximal error is found to be about several percents at $\lambda = 320$ nm, which is the minimal wavelength allowable for operation of tungsten strip lamps at $T = 2{,}700$ K. Therefore, this scheme is most suitable for calibration in ordinary scientific laboratory. Remember that radiant flux of these lamps is relatively low in the UV spectral range. Therefore, sufficient errors

may occur due to high level of long-wavelength scattered radiation. The dependency of the output signal on the wavelength caused by the scattered radiation can be easily found. With a sufficient level of scattered light in your experiments, not in calibration, you can also resort to the help of UV filters when carrying out measurements and calibration. In the event of working with a diffraction grating, you should also take into account the second diffraction order, which has to be cut off by a suitable long-pass filter. The main problem, while operating with the diffuse reflecting screen, is the spectrum of light reflected by the screen, a reflection spectrum. Even, according to the literature, the reflection coefficient for a freshly prepared surface is invariable within a certain spectral interval, this coefficient may vary after a time due to dustiness. In addition, the reflection spectrum may depend on purity of the used material. Potential accident intervals are $\lambda \geq 1{,}500$ nm and $\lambda \leq 300$ nm, wherein the diffusive reflection coefficient of screens made of MgO and $BaSO_4$ depends on the wavelength. This is the author's advice to provide re-measuring of these dependencies from time to time. Similarly, the reflection spectrum of the mirrors may be found. While measuring, not on calibration, it is also necessary to take into account thermal radiation of the cell walls as weak radiation spectra in the spectral range $\lambda \geq 2{,}000$ nm.

To provide measurements, to a high accuracy, of the function $s(\lambda)$, spectral functions of photoresponse should be well established. These functions are affected by the long-wavelength scattered lamp radiation in the short-wave range, and by daylight reflected by the diffusive screen and passing into the monochromator. The latter gives an essential contribution in the range of window's glass transparency $\lambda \geq 370$ nm, provided the candlelight is switched off. Having set a proper long-pass filter in front of the photomultiplier, you can measure the spectral photoresponse caused by the scattered lamp radiation in the short-wave range, for example, at $\lambda < 360$ nm. The daylight spectrum is measured with closed iris diaphragm, e.g., the diaphragm can be screened by a black paper. Thus, both photocurrents have to be subtracted from the total current to obtain true lamp radiation reflected from the diffusive screen. During calibration, this procedure should be performed for any registration system. Features of the measurement algorithm are shown by the example of the last time calibration cycle applied by the author to the system involving condenser, monochromator, and photomultiplier in 2010 (see Sect. 5.4.2). It should be remembered that due to the absence of the condenser, lenses, and mirrors, and hence aberrations caused by them, the function $s(\lambda)$ becomes independent of the slit width that facilitates calibration.

5.3 Sensitivity Calibration of Spectrometer/Photodetector Systems in the UV Spectral Range

It is dangerous to use strip lamps with uviol windows in the spectral range $\lambda \leq 320$ nm, where their spectral transmittances differ from unity and the level of scattered light is comparable with that of the lamp. Therefore, hydrogen and

deuterium lamps, as well as lamps filled mixtures of these gases with rare gases are usually used in the 1 £ 320 nm spectral range. Some calibration features are discussed in Sect. 5.2, however, a long-pass filter of transmission cut-off $\lambda \geq 270$ nm should be used to measure the level of scattered light. Operational features of these lamps have been described in detail in Sect. 2.2. The lamps are similar to the point sources and when using them for sensitivity calibration of systems involving a spectrometer and photodetector, it is necessary to set illumination schemes similar to that shown in Fig. 5.1. If you intend to calibrate your device in a wide spectral interval, including the visible range, you should not forget to carry out calibration with overlapped intervals. For example, you use a gas-discharge lamp in the wavelength range 190–380 nm, and a strip lamp in the interval $\lambda \geq 320$ nm. You have also to measure spectra under study with overlapped intervals to fit them.

5.4 Calibration of Lens (Condenser)/Spectrometer/Photodetector System

It is obvious that in the case of small sizes of a light source, there is a need to use a condenser, lens, or mirrors. However, these instruments may have aberrations such as spherical, distortion, astigmatism, and coma. In addition, a lens or condenser has chromatic aberration, where the focal length depends on wavelength due to dispersion of the refractive index.

5.4.1 The Layout Impact on the Spectral Sensitivity Function

Let us consider the system involving a lens, spectrometer, filter, and photodetector. The system is planned for measuring radiation spectra of point or narrow cylinder light sources (O.L. Malinina, A.M. Pravilov, On calibration of lens/spectrometer/detector systems in the UV spectral range, unpublished data, 2002). This work was specially carried out to show the layout impact on the function $s_{hv}(\lambda)$. In other words, here the mutual positions of such optical elements as focused lens, light source, and input monochromator slit may impact on the function $s_{hv}(\lambda)$. The calibration scheme is shown in Fig. 5.2. Radiation from a calibrated source, a strip or gas-discharge lamp, falls on a diffuse reflective screen so that f'-number of input monochromator slit illumination is greater than the monochromator f-number. A screen with an iris diaphragm or slit fulfilling the role of a point light source is placed behind the diffuse reflecting screen. Such a slit or diaphragm is further referred to as *imitator*. A lens is mounted at its double focus length from the light source, and the input monochromator slit is further placed at the double

focus length. This layout provides that the total system magnification is equal to unity. At $|a_1| = |a_2| = 2f$:

$$\frac{1}{a_2} - \frac{1}{a_1} = \frac{1}{f},$$

where f is the focal length of the lens, a_1 is the distance between the object and the lens, a_2 is the distance between the image and lens [10, 11]. In the absence of aberrations, the lens projects the opening of the imitator onto the input slit. As it is clear from the equation of thin lens, a lens width is much less than the focal length of lens, and its focal length depends on the refractive index of the lens material n, as well as on the wavelength due to dispersion of the refractive index [11]:

$$\frac{1}{f} = (n-1)\left(\frac{1}{r_1} - \frac{1}{r_2}\right), \tag{5.3}$$

where r_1 and r_2 are radii of curvature of the lens surfaces. Note that the values of r_1 and r_2 have opposite signs. The data illustrating the dependency of the refractive index against wavelengths are shown in Table 5.1.

For example, the absolute values of radii of both lens surfaces are equal to 8.5 cm. With using the data shown in Table 5.1, it is not difficult to find that the

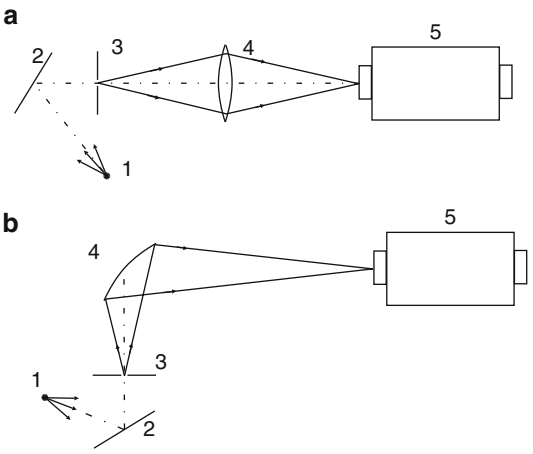

Fig. 5.2 Calibration of the system (**a**) including the light source (*1*), diffuse reflective screen (*2*), slit (*3*), lens (*4*), and monochromator (*5*); and the system (**b**) consists of the light source (*1*), diffusive screen (*2*), slit (*3*), concave mirror (*4*) and monochromator (*5*) (O.L. Malinina, A.M. Pravilov, On calibration of lens/spectrometer/detector systems in the UV spectral range, unpublished data, 2002)

Table 5.1 The refractive index n of fused silica on wavelength in the UV, visible, and IR spectral range [5, 12]

λ (nm)	199.0	214.4	231.3	253.6	280.3	312.5	340.4	365.0	434.1	486.1	589.3
n	1.5515	1.5337	1.5193	1.5056	1.4940	1.4845	1.4786	1.4765	1.4669	1.4631	1.4584
λ (nm)	656.3	766.5	863.0	1,000	1,200	1,500	2,000	2,500			
n	1.4564	1.4539	1.4523	1.4504	1.4480	1.4446	1.4381	1.4298			

values of the focal length are equal to as follows: 7.70, 8.03 and 9.13 cm at $\lambda = 200$, 240 and 440 nm, respectively. If the diaphragm and slit are positioned according to the relation: $|a_1| = |a_2| = 2f$, focal length is numerically equal to 18.26 cm at $\lambda = 440$ nm, then for $\lambda = 200$ nm the image will be positioned 5 cm nearer than with the previous wavelength. Hence, for the given relative aperture equal to 1:3, the diameter of point image in the slit plane is found to be equal to $(18.26 - 13.3)/3 \approx 1.66$ cm! For the slit with a width of 0.1 mm and a sufficient height, the signal is reduced by the factor $(1/4)\pi(1.66/0.01) \approx 130$ due to defocusing.

In order to obtain sufficient output, it is necessary to adjust your system to a spectral range in which spectral photon flux has to be minimal and to minimize the aberrations of other kinds. In order to do this, the imitator, lens, diaphragm, and monochromator slit are to be positioned along one optical axis. As calibration as well as measurements are both have to be carried out at the same experimental layout including identity in mutual positions of such elements as the input minichromator slit, condenser, or lens, and the imitator of light source or the light source itself.

Ignoring this circumstance may introduce dramatic errors. Many works in which luminescence spectra had been measured and used for determination of optical transition dipole moment functions or rate constants of collision-induced nonadiabatic transitions (CINATs) were published in the literature (see, e.g., [13–26] and discussion in them). In some works, the data had been deduced without a correction to the $s_{hv}(\lambda)$ function, and this can be the main reason for great, up to several decades, differences between them and corrected ones (see Figs. 5.3 and 5.4 and [18–23] and discussion in them).

In some other works, the $s_{hv}(\lambda)$ had been measured but methods of their determination were not described (see, e.g., [13–16]). One of the most complicated problems in the determination of $s_{hv}(\lambda)$ is the conservation of the identity of the

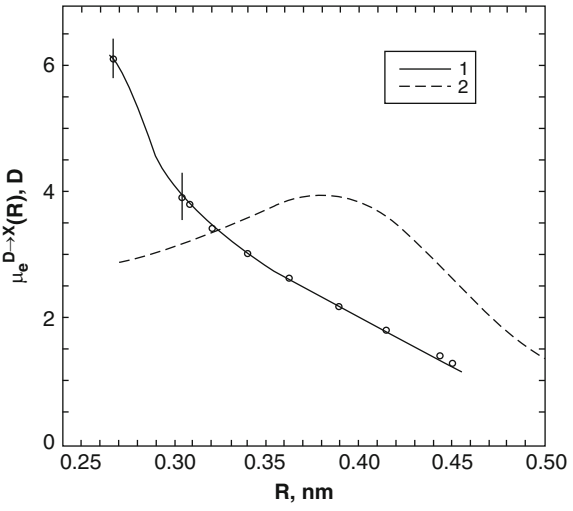

Fig. 5.3 The dependence of the $I_2(D\,0_u^+ - X\,0_g^+)$ electronic transition dipole moment function on internuclear distance. *Points and curve 1*: derived from spectra simulation [18]; *curve 2* is the $\mu_e^{D-X}(R)$ function from [24]

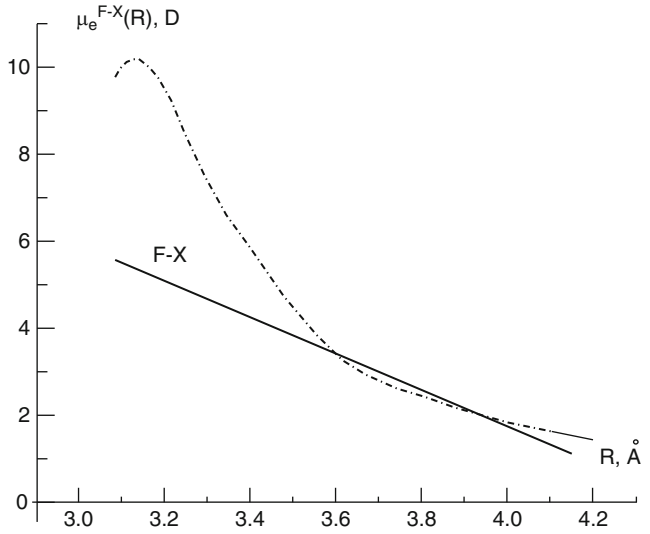

Fig. 5.4 The dependence of the $I_2(F\,0_u^+ - X\,0_g^+)$ electronic transition dipole moment function on internuclear distance. *Points and curve 1*: derived from spectra simulation [25]; *curve 2* is the $\mu_e^{F-X}(R)$ function from [15]

layout during calibration of the spectral instrument and its application. A difference in the layout can distort results of spectral measurements.

The transition dipole moments at some values of internuclear distances (Figs. 5.3 and 5.4) differ by the factor 2, i.e., radiation intensities differ by the factor 4 (see [18, 25, 26] and references).

In order to check how refraction index affects the spectral sensitivity in the schemes discussed above, first, the $s_{hv}(\lambda)$ function was found in the system including a lens, monochromator, and PMT at $|a_1| = -|a_2| = 16.0$ and 18.3 cm, which corresponds to the unit magnification for $\lambda \approx 220$ nm and $\lambda \approx 440$ nm, respectively. Second, similar measurements were carried out for the system including the concave mirror, monochromator, and PMT (Fig. 5.2).

A calibrated deuterium–neon lamp DNU-170 combined with calibrated $BaSO_4$ screen served as referenced standard $\phi_{hv}^{et}(\lambda)$ (see Sects. 5.1 and 5.2). The screen provided uniform, diffuse illumination of an iris. Diameter of the iris, $d = 0.7$ mm, was equal to entrance and exit slit width of the $f = 1/3$, 2.4 nm/mm monochromator MDR-12 performed at the Fastie scheme (see Sect. 5.1) and equipped with a cooled PMT100 photomultiplier tube ($\lambda = 160$–730 nm, see Sect. 3.4) operating in photon-counting mode. An image of the iris was focused on the entrance slit of the monochromator by means of $f' = 1/3$, $R_1 = -R_2 = 8.5 \pm 0.2$ cm lens (Fig. 5.2a) or $f' = 1/3$, $R = 9 \pm 0.5$ cm aluminum-coated concave mirror (Fig. 5.2b) to provide a unit magnification in both cases as it has been described above. The $s_{hv}(\lambda)$ functions were calculated according to formula (5.2). All the measurements were made in the 180–380 nm spectral range with 2.0 nm step. The red limit of the

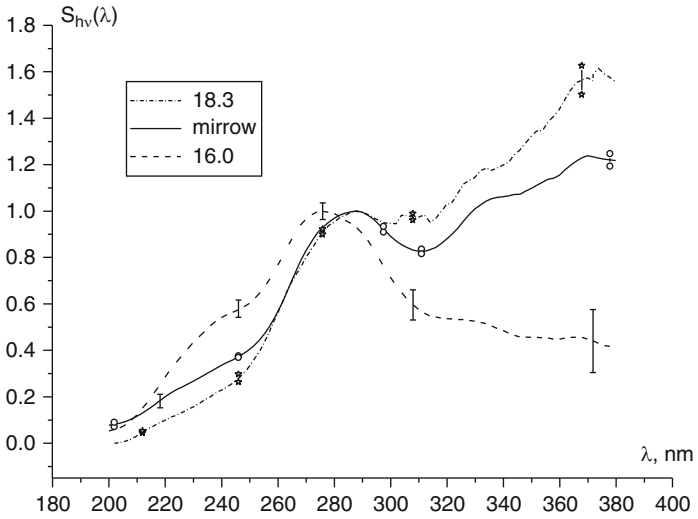

Fig. 5.5 The $s_{hv}(\lambda)$ functions corresponding to the lens placed at $-a_1 = a_2 = 16.0$ cm, $-a_1 = a_2 = 18.3$ cm according to Fig. 5.2a, and to the concave mirror according to Fig. 5.2a. *Error bars* correspond to the light signal averaged on five scans (O.L. Malinina, A.M. Pravilov, On calibration of lens/spectrometer/detector systems in the UV spectral range, unpublished data, 2002)

range was chosen due to appearance of the lamp second-order light at $\lambda > 380$ nm. The signal in the 180–190 nm range where $\phi_{hv}^{et}(\lambda) = 0$ was used for determination of the signal corresponding to sum of dark current plus scattered light. It was subtracted from the total signal.

Three $s_{hv}(\lambda)$ curves corresponding to the lens placed at $-a_1 = a_2 = 2f$ ($\lambda = 220$ nm) $= 16.0 \pm 0.2$ cm, $-a_1 = a_2 = 2f$ ($\lambda = 440$ nm) $= 18.3 \pm 0.2$ cm (see Fig. 5.2a) and the concave mirror (see Fig. 5.2b) are shown in Fig. 5.5.

It is seen that $s_{hv}(\lambda)$ tends to zero at $\lambda \to 190$ nm because of decrease in reflectivity of the monochromator mirrors and grating and five refractions from these elements (see Sect. 5.1). Nevertheless, these functions differ from each other. In the scheme with lens, the shape of $s_{hv}(\lambda)$ functions is caused by quartz refraction index. In the case of concave mirror, the $s_{hv}(\lambda)$ function is mainly formed by the response of the monochromator/PMT system. In order to demonstrate the difference between the $s_{hv}(\lambda)$ functions, a number of function rations are calculated as shown in Fig. 5.6.

Comparing data from the Fig. 5.6, we see that the lens position at $-a_1 = a_2 = 2f$ ($\lambda = 440$ nm) $= 18.3$ cm gives a more suitable sensitivity function in the $\lambda = 280$–380 nm spectral range than that at $-a_1 = a_2 = 2f$ ($\lambda = 220$ nm) $= 16$ cm. However, in this event zero sensitivity is found to be at $\lambda \approx 210$ nm. The values of sensitivity in the long-wavelength region are worse than that in the short-wave region at $-a_1 = a_2 = 2f$ ($\lambda = 220$ nm) $= 16$ cm. More uniform values of sensitivity are found with the concave mirror. The s_{16}/s_{mir} ratio is found to be maximum at $\lambda \approx 230$ nm.

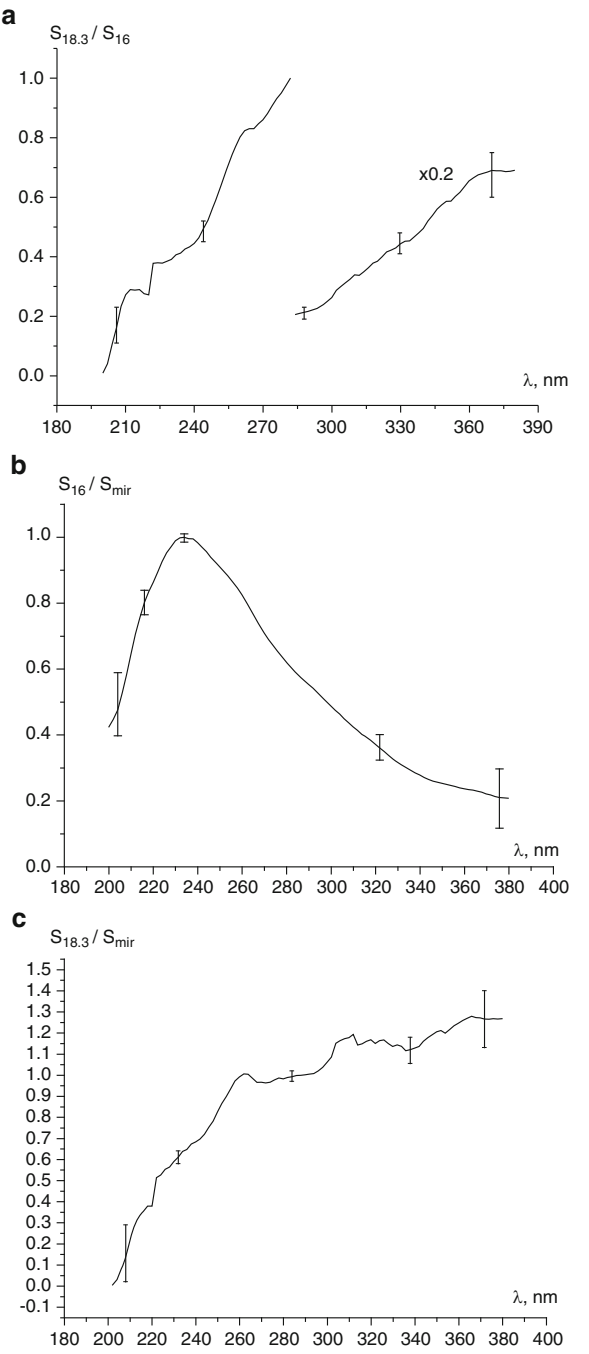

Fig. 5.6 (**a**) The $s_{hv}(\lambda)$ function ratios found with the lens placed at $-a_1 = a_2 = 18.3$ cm and $-a_1 = a_2 = 16$ cm as $s_{18.3}$ and s_{16}, respectively (O.L. Malinina, A.M. Pravilov, On calibration of lens/spectrometer/detector systems in the UV spectral range, unpublished data, 2002). (**b**) The $s_{hv}(\lambda)$ function rations found with the lens placed at $-a_1 = a_2 = 16$ cm and mirror placed at 9 cm as s_{16} and s_{mir}, respectively (O.L. Malinina, A.M. Pravilov, On calibration of lens/spectrometer/detector systems in the UV spectral range, unpublished data, 2002). (**c**) The $s_{hv}(\lambda)$ function rations found with the lens placed at $-a_1 = a_2 = 18.3$ cm and mirror positioned at 9 cm as $s_{18.3}$ and s_{mir}, respectively, (O.L. Malinina, A.M. Pravilov, On calibration of lens/spectrometer/detector systems in the UV spectral range, unpublished data, 2002)

Data in Fig. 5.6a–c show the influence of lens position on the sensitivity function. With a system without calibration, or when any element in a calibrated system such as light source, lens, or monochromator changes its position, the spectra will be distorted. In the spectral range $\lambda < 300$ nm, shapes of spectra, for instance, like $I_2(D\,0_u^+ - X\,0_g^+)$ or $I_2(F\,0_u^+ - X\,0_g^+)$ in Figs. 5.3 and 5.4, are mainly caused by the fact that a noncalibrated system is used. Most errors occur when a noncalibrated system is used in measurements of spectral intensity ratios under investigation of CINATs from the $I_2\,(E\,0_g^+)$ and $I_2\,(f\,0_g^+)$ states (luminescence in the $\lambda_{lum} \approx 300$–$450$ nm spectral ranges) to the $I_2\,(D\,0_u^+)$ or $I_2\,(F\,0_u^+)$ (luminescence in the $\lambda_{lum} \approx 220$–$330$ nm spectral ranges). Large errors may also happen when calibration is carried out under conditions of different layouts. Differences between obtained data and true ones can be as high as several times or several decades [20, 21]. In the case of measurements of luminescence spectra in a wide range of wavelengths 200–400 nm, it is useful to use concave mirror(s).

5.4.2 *Scheme and Algorithm of Calibration of Condenser/Spectrometer/Photodetector System*

Currently the scheme shown in Fig. 5.7 is used for calibration in the author's laboratory [26, 27].

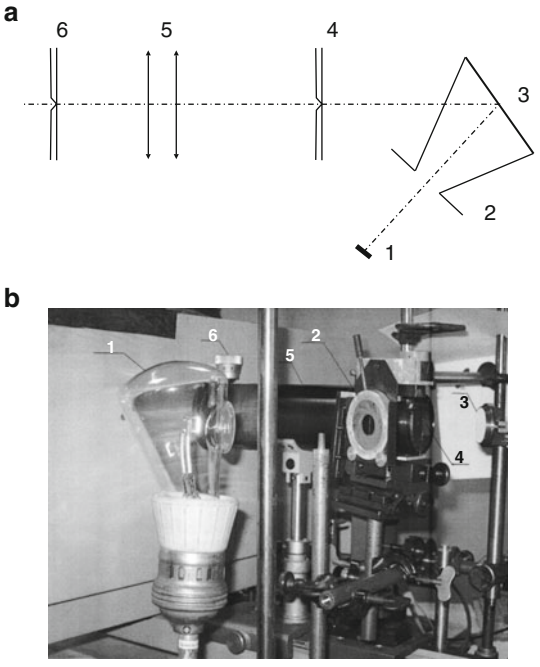

Fig. 5.7 (**a**) Setup for calibration of the system including a condenser, monochromator, and detector. Calibrated strip lamp (SIRSH8.5-200) or deuterium lamp (DDS-30) (*1*), iris diaphragm (*2*), diffuse reflecting screen (*3*), slit (*4*), condenser (*5*), entrance slit of monochromator (*6*) [26, 27]. (**b**) Photo of the setup schematically shown in Fig. 5.7a

The diameter of the iris diaphragm is chosen so that radiation from the lamps falls only on the reflective surface of WS-1. The plane of WS-1 screen is placed at the angle 45° to the axis drawing through the centers of WS-1, the slit (4), condenser, and the input slit of the monochromator. This provides that for the given values of the reflective surface diameter of $d_{\text{WS-1}}$ and the distance between the surface center and the slit center l, the ratio $d_{\text{WS}-1}/(l\sqrt{2})$ of the light beam diameter in the plane normal to the optical axis to the value of the distance l (f' number) is equal to the f-number of the monochromator, value 1/2.5 in the considered case. The slit (4) is the imitator of a point or narrow cylinder light source, more precisely, it models a very narrow slit. Its width may vary from 0 to 5 mm, and height may be changed by means of a black-paper mask of rectangular shape. It is of primary importance that all geometrical features of your experiment intended for measuring radiation spectra are to be defined with a high accuracy. The imitator center has to be accurately positioned. The distance between the center and the input opening of the condenser has to be the same as the distance between the object under study and the condenser opening. In the author's laboratory, the object is often caustics of focused laser beams used for excitation of molecule luminescence (see, e.g., [19–27]). It is obvious that the imitator (4) has to be mounted on an adjusting unit, which permits to vary the parameters mentioned above. Generally, we provide required dimensions with the accuracy of ±0.5 mm that approximately equal to the uncertainty of caustics positions.

Calibration should be carried out with diffraction gratings which you plan to use in the maximal spectral range, wherein the photomultiplier tubes and grating still operate well. Remember that the second diffraction order may affect your measurements, and proper long-pass filters are to be applied to cut off radiation of the second-order diffraction.

It is clear that the $s_{hv}(\lambda)$ function has to be dependent on the imitator size as well as the size of the monochromator slits. This is completely sustained by the data below. The system including the condenser, monochromator of type MDR2, and PMT100 photomultiplier with the condenser focused at $\lambda \approx 375$ nm was calibrated within the spectral interval $\lambda = 200$–630 nm by means of the calibrated strip SIRSH8.5-200 and deuterium DDS-30 lamps.

For the given imitator size and slit widths of your monochromator, it is appropriate to carry out one calibration cycle for the registration system, for example, by means of a strip lamp at first, and then using the deuterium lamp, or vice versa. Carry out calibration several photomultiplier tubes, one after the other, each being chosen by its signal to noise ratio and stability (see Sect.3.4.2.3).

Let us consider the case of calibration, where a strip lamp is used in the beginning. The calibration algorithm is as follows.

1. Set one combination of the imitator size and slit width.
2. In order to find the level of scattered light, perform measurements of spectral function for photoresponse against wavelength using the long-pass filter in the range $\lambda > 355$ nm (Fig. 5.8). Author used the filter of type "BS8."

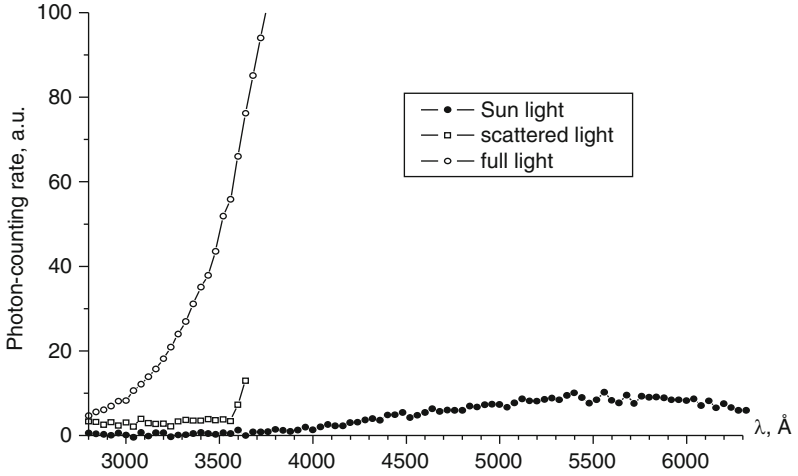

Fig. 5.8 Spectral functions of photoresponses in calibration of the registered system shown in Fig. 5.7 using the grating of 1,200 grooves per mm and PMT100 (N 4285). Temperature of the SIRSH 8.5-200 lamp is $T = 2{,}700$ K, the width of the imitator slit is 0.2 mm, its height is 6 mm. The condenser is adjusted to form a maximal signal at $\lambda \approx 375$ nm

3. Remove the long-pass filter, close the iris diaphragm in such a way that light from the lamp cannot fall on WS-1 screen. Measure the spectral function for photoresponse under daylight.
4. Open the iris diaphragm, then measure the spectral function of photoresponse caused by lamp light reflected from the diffused screen.
5. After subtracting the photoresponses found in 2nd and 3rd items from the photoresponse found in 4th item, a new spectral function is formed. Divide this spectral function by the spectrum of the used strip lamp at the temperature determined according to the procedure described in Sect. 2.1.3. Thus, you find the $s_{hv}(\lambda)$ function in the spectral range $\lambda \geq 320$ nm (Fig. 5.9). It is clear that it cannot provide calibration of the system in the range $\lambda \geq 640$ nm without the long-pass filter cutting off the second diffraction order of the diffraction grating.
6. Perform measurements according to items from 2 to 5, with other sizes of both the imitator and monochromator slits as well as with other available photomultipliers, e.g., PMT designed for operation in the near IR spectral range (Sect. 3.4). You may use other diffraction grids, for example, with the period 600 or 300 lines per mm.
7. Perform measurements according to items from 2 to 5 with the help of the deuterium lamp in the spectral range $\lambda = 190$–380 nm at the parameters similar to that applied in the case of the strip lamp, the same imitator size and monochromator slits and the same PMT type. There is no necessity to provide measurements of photoresponse for daylight, and the light scattered from the lamp of DDS-30 type should be detected with shorter wavelength cut-off filters, for example, in the range $\lambda > 270$ nm. The long-pass filter of BS3 type is used in the author's laboratory in this case.

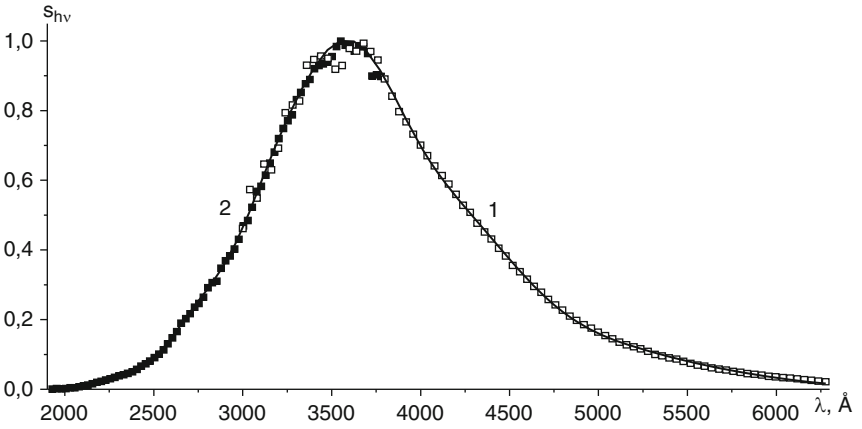

Fig. 5.9 The function $s_{hv}(\lambda)$ of the monochromator of MDR-2 type with the grating of 1,200 grooves per mm and PMT100 (N 4285); the function was found by the use of the calibrated strip SIRSH8.5-200 (*1*) and deuterium DDS-30 (*2*) lamps. The imitator slit of width 0.2 mm and height 6 mm and the slits of the monochromator of width 0.25 mm were used

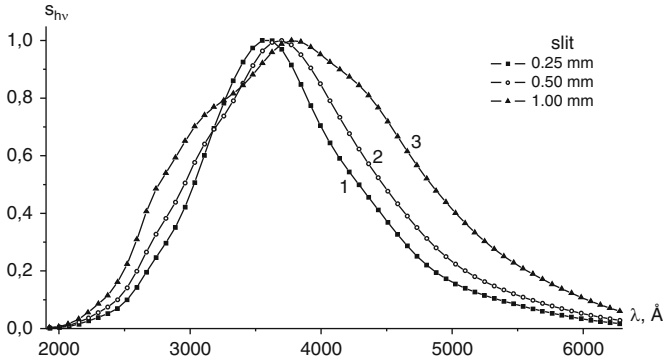

Fig. 5.10 The function $s_{hv}(\lambda)$ of the monochromator of MDR-2 type with the grating of 1,200 grooves per mm and PMT100 (N 4285); the function was found using the calibrated strip SIRSH8.5-200 and deuterium DDS-30 lamps. The imitator slit of width 0.2 mm and height 6 mm was used; the slits of the monochromator of width 0.25 mm (*1*), 0.5 mm (*2*), and 1.0 mm (*3*) were used

The functions $s_{hv}(\lambda)$ found after using the strip and deuterium lamps have to be joined in their overlapping spectral range $\lambda = 320$–380 nm by virtue of averaging over all the ranges (Fig. 5.9).

With narrow imitator slit, the shape of $s_{hv}(\lambda)$ function depends critically on the widths of slits of the monochromator, as well as on the height of the imitator slit (Fig. 5.10). By increasing the monochromator slit width, the maximum of $s_{hv}(\lambda)$ slightly shifts toward the long-wave range, with the function half-width being wider. This effect is caused by the lesser impact of defocusing of the imitator

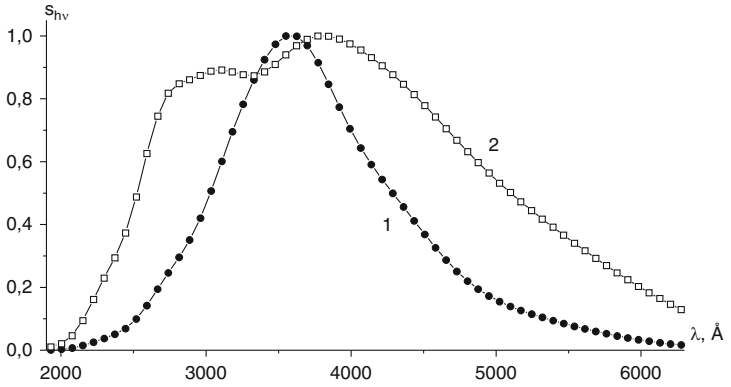

Fig. 5.11 The function $s_{hv}(\lambda)$ of the monochromator of MDR-2 type with the grating of 1,200 grooves per mm and PMT100 (N 4285); the function was found using the calibrated strip SIRSH8.5-200 and deuterium DDS-30 lamps. The imitator slit of width 0.2 mm and height 6 mm (*1*), and width 5 mm and height 18 mm (*2*) were used

image on the input monochromator slit. After increasing the imitator height up to 18 mm, the $s_{hv}(\lambda)$ function shifts toward the long-wavelength range, and sensitivity is slightly down in the spectral range $\lambda < 300$ nm. In the case of a wide imitator (Fig. 5.11), $s_{hv}(\lambda)$ depends weakly on the monochromator slit widths.

A further difficulty is the measuring of spectral reflectivity function for the diffuse reflective WS-1 screen in the spectral range $\lambda < 250$ nm, wherein this screen is not specified by its manufacturer. Such measurements were carried out by the authors in two ways as follows [26, 27].

1. The imitator and WS-1 screen are removed so that the input slit is illuminated directly by the DDS-30 lamp. Due to nonuniformity of the monochromator, and small parts of the grid surface and mirror surface are illuminated in this scheme, it is necessary to carry out a set of measurements. While measuring this spectral function, the DDS-30 lamp has to be slightly moved in the vertical and horizontal directions around the optical axis passing through the centers of the input and output slits of the monochromator. In order to determine WS-1 spectral reflectivity, the spectral function estimated as in items 2–5 (see above) has to be divided by the averaged spectral function. Measurements show that spectral reflectivity function obtained in such a way depends on illumination layout, whereas the function averaged by several measurements becomes invariable with uncertainty a few percentages in the range $\lambda = 200$–380 nm (Fig. 5.12).
2. Irradiation of the input monochromator slit is provided by the DDS-30 lamp through a small opening, about 5 mm, of the iris diaphragm placed in the front of the imitator on the optical axis passing through the centers of the input and output slits of the monochromator (Fig. 5.13a). Then the diffusive screen is mounted instead of the lamp. The screen is illuminated by the DDS-30 lamp (Fig. 5.13b).

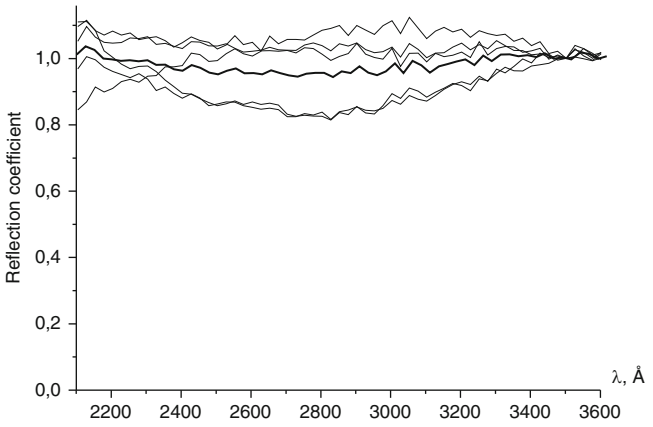

Fig. 5.12 Spectral reflectivity function of the diffuse reflecting screen of WS-1 type found with direct irradiation of the input monochromator slit by the deuterium lamp of DDS-30 type at different position of the lamp with respect to optical axis, which is drown through centers of the input and output monochromator slit (the first method). The *bold line* indicates averaged function

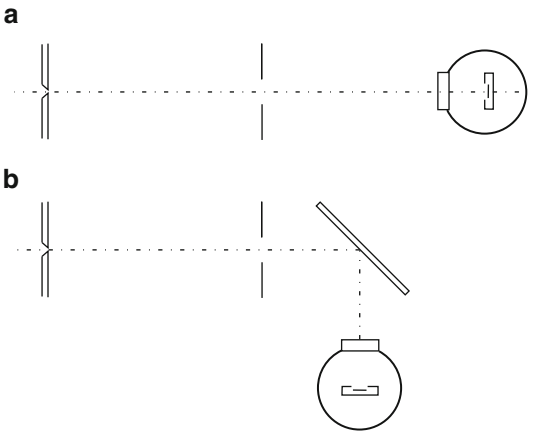

Fig. 5.13 Measurements of the spectral function of spectral reflectivity function of WS-1 diffuse reflecting screen (the second method); measurements by direct irradiation of the input monochromator slit (**a**), measurements with the diffuse reflecting screen in the same illumination layout (**b**)

Such a layout gives illumination of identical areas of the diffraction grating and monochromator mirrors in both series of measurements. It is assumed, however, that the reflectivity of the WS-1 screen is independent of coordinates of the illuminated area, and this fact is guaranteed by the screen manufacturer [7]. The spectral reflectivity functions obtained by the methods discussed in the items 1 and 2 are found to be near identical (Fig. 5.14).

Upon completion of the calibration, the cell designed for photoprocesses research can be mounted. It is important that the center of the zone, where luminescence assumed to be taken place, has to be located exactly in the imitator center position. While setting the cell, the mutual position of the light source, condenser, and monochromator should not be changed. What is a way to achieve it?

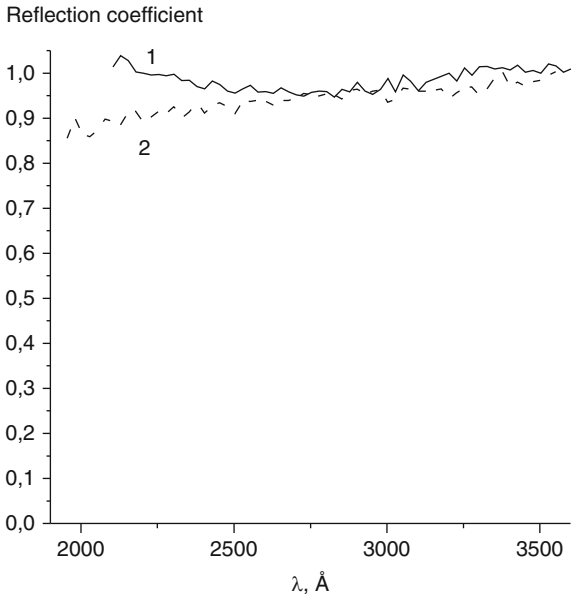

Fig. 5.14 The spectral reflectivity functions of the WS-1 screen found by the first method (*1*) and second method (*2*)

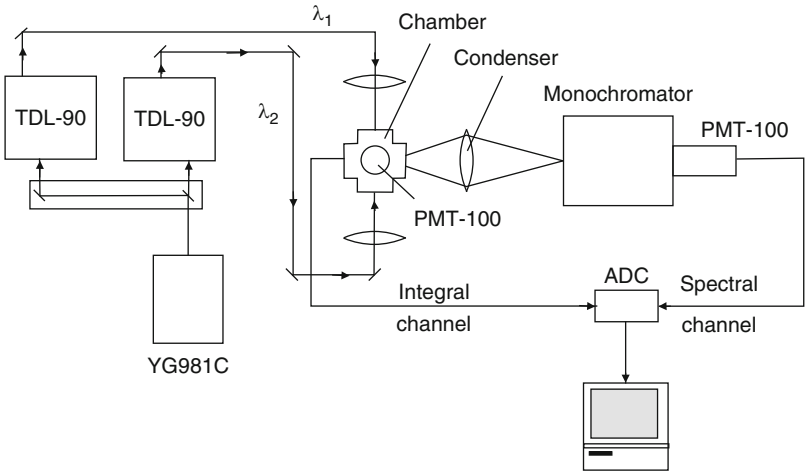

Fig. 5.15 Setup in the author's laboratory for recording photoprocesses using stepwise and multiphoton two- and three-color, 1 + 1, 1 + 2, 1 + 1 + 1 laser excitation [26, 27] (reproduced with permission from American Institute of Physics)

Figure 5.15 shows the setup for studying photoprocesses in the author's laboratory by virtue of stepwise and multiphoton two- and three-color laser excitation (1 + 1, 1 + 2 and 1 + 1 + 1). Figure 5.16 shows the photo of the setup. Among the photoprocesses, one is shown as follows:

$$I_2(E0_g^+,\ v_E,\ J_E) \xleftarrow{\lambda_2} I_2(B0_u^+, v_B, J_B) \xleftarrow{\lambda_1} \mathrm{I}_2(X0_g^+, v_X, J_X).$$

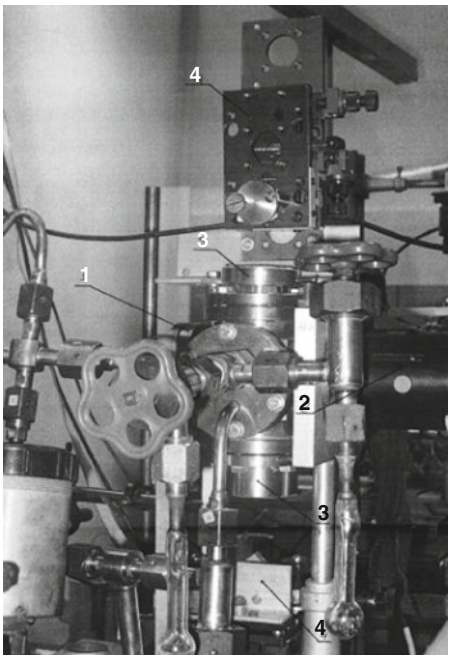

Fig. 5.16 The photo of the setup schematically shown in Fig. 5.15: the chamber (*1*), the condenser (*2*), the target (*3*), the adjustment blocks with the total reflection prisms (*4*)

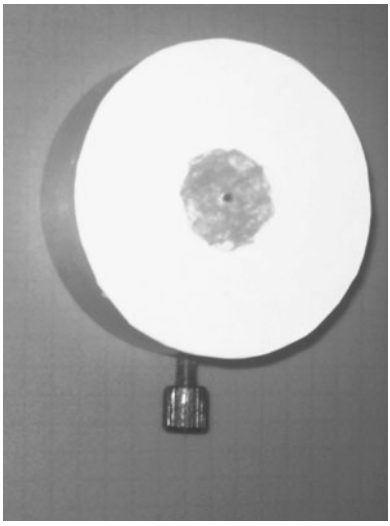

Fig. 5.17 The photo of the target for adjustment of laser beams

For adjustment of the laser beams, the target consisting of a ring was mounted on the flanges of the windows, through which laser rays pass into the cell. On the ring a paper is glued with a centered hole of diameter about 1 mm (Fig. 5.17). A space around this hole is painted by a red highlighter. So for each of emission type, an

illuminated ring space around the hole can be visualized. Namely, in the case of UV radiation, it may be done by the blue luminescence of a paper, whereas in the case of IR radiation it may be realized by the white paint.

If laser radiation has to be focused on the cell center, it is necessary to measure the distance between the center of the focusing lenses and caustic, a point, where the laser beam is focused. Then these lenses are to be positioned at the same distance from the cell center. At first, the laser beam is focused roughly by means of adjusting systems of the laser rays, but in so doing the laser beam center approximately coincidences with the center of the input hole. Furthermore, adjustment is carried out using the adjustment blocks (4) in Fig. 5.16.

If the latter is the case, for a given light beam, the beam is to be passed exactly through the output opening, as this opening is the input opening for the other beam. With precise adjustment, the visualization of UV and IR radiation is also used near the input window. The other laser beams are to be adjusted in such a way. Such adjustment allows the caustic position to be set with a precision of ± 2 mm in the vertical direction, which is provided due to a large slit height. In the other directions, the precision is found to be about 0.5 mm.

Caustic deviations from the optical axis drawn through the caustic, condenser, input, and output monochromator slits are critical. Small shifts of the axis drawn through the centers of the condenser from the optical are also critical. Owing to this the testing procedure is necessary to verify if the condenser axis coincides with this optical axis. The smallest deviation of the condenser axis results in sufficient decreasing of the registered signal in the UV spectral range, especially at $\lambda \leq 250$ nm, where dispersion of the quartz refractive index is large. During calibration and measurements in a wide spectral range including UV spectral range, adjustment of the condenser with respect to the caustic and imitator is to be carried out *at the same wavelength in the UV range*, because of the largest value of the refractive index of quartz.

In the author's laboratory, such adjustment is performed at $\lambda \approx 260$ nm. When wide spot laser beams are exploited, rough adjustment is just enough, although the author prefers to carry out a more precise adjustment in any case.

5.5 Sensitivity Calibration of Spectrometer/Photodetector Systems in the VUV Spectral Range

Sensitivity calibration in the vacuum UV spectral range is more difficult than considered in the previous sections. The major problem is the absence or high cost for stable and effective measuring tools such as light sources with proper aperture and emitting area, as well as mirrors. The author never met works, where diffuse reflecting screens were used for calibration any spectrometer/photodetector system in the vacuum UV spectral range.

In this spectral range, synchrotron radiation is the primary spectral standard, and any secondary standard is calibrated with respect to this radiation source; they are very expensive. In turn, working measuring facilities are calibrated by means of the secondary standards (see Sect. 2.5). Uncertainty, which appears in the calibration of the secondary standards by the primary ones, is about 5, 18, 5, 3.5, and 2% in the spectral ranges 115–120.5, 120.5–122.5, 122.5–165, 167–175, and 175–400 nm, respectively (see Sect. 2.5). So-called polarization factors are the major reason for this. These factors will be discussed just below. It has been noted that all the lamps act as "point sources" that hampers the correct calibration procedure for spectrometer/photodetector equipments in a noticeable large solid angle (see Sect. 4.4.2). It should be also remembered that spectral devices have nonuniformity, which becomes sufficient in the vacuum UV spectral range, where reflectivity of diffraction gratings is much less than unity (see Sect. 5.1). Commonly, owing to insignificant reflectivity of metals in the vacuum UV range, vacuum monochromators are based on the use of spherical concave or toroidal gratings, which provide effective dispersion of incident radiation by reflection only [6]. Because of nonuniformity, you need to carry out calibration under the solid angle, which will be exploited in further operation. In the case that such a point light source is available, and you decide to apply it for calibration, then scheme shown in Fig. 5.1b should be used. Here the most serious difficulty is the estimation of the reflectivity spectral function for the concave mirror, taking into consideration that the polarization factors and nonuniformity take place. Using such point sources, the calibration uncertainty may achieve tens percentages [28, 29]. Additionally, other methods and other radiation sources can be applied for calibration. Let us discuss these methods briefly.

5.5.1 Extended Hydrogen (Deuterium) Lamp

In the short-wave range $\lambda < 165$ nm, radiation spectrum of hydrogen lamps, as well as deuterium point-like lamps, consists of overlapped spectral bands and lines of molecular and atomic hydrogen or deuterium (see Fig. 2.8). It was measured repetitively by means of numerous methods, including double monochromator method, and by comparison with synchrotron radiation. In the range $\lambda = 165$–300 nm, repeatability of the radiation spectra is 8–20% that depends on the wavelength (see Sect. 2.3). In direct current mode, the spectrum depends only slightly on pressure at 2–4 torr, at least in the range $\lambda = 165$–380 nm. If the lamp current is maintained invariable with a high precision, the spectrum will remain constant [30, 31]. Reflectivity of metallic surfaces is small in the vacuum UV spectral range; thus diffraction gratings have sufficient nonuniformity [6, 32]. Because of this, its calibration should be carried out over all reflected surfaces, i.e., f'-number has to be equal to the f-number of the monochromator. By virtue of the fact that large errors occur when operating with a point-like source in the scheme shown in Fig. 5.1b (see above), the use of an extended hydrogen-discharge lamp is more preferable. Such lamps of diameter 60–80 mm for illuminating body

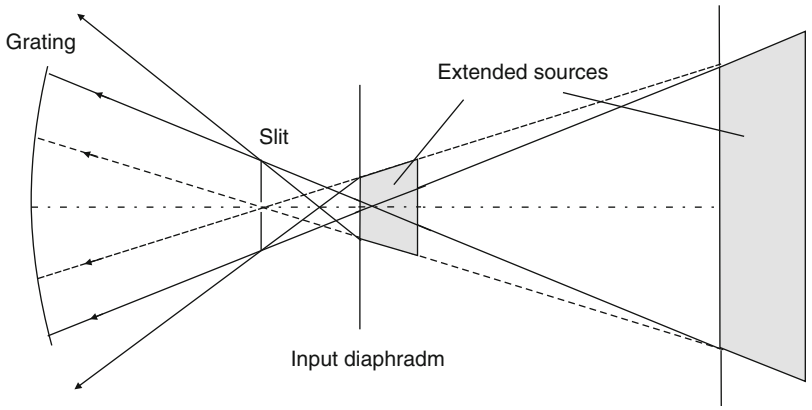

Fig. 5.18 Illumination of the monochromator grating by the extended light source in two cases: one is calibration, the source is at near position to the grating, and second is measuring of emission spectra, the source is at distant position to the grating. The *dotted lines* indicates light rays propagation in the direction normal to the slit extension, and *solid lines* show light propagation in the direction along the slit [34] (reproduced with permission from Measurements Science and Technologies, IOP Publishing Ltd)

are described in [33]. The lamps are to be calibrated any way. Thus, when the area of the calibrating light source differs from that of the light source, spectrum of which you wish to find, it is necessary to use an extended calibrating source.

This situation is illustrated in Fig. 5.18 for the event when the calibrated source area is less than that of the studied light source. We assume these sources to be at different distances from the monochromator slit, so that they have the same value of f'-number (see [34]). We also assume that f'-number to be less than f-number of the monochromator. It is important that calibration has to be carried out at the same value of f'-number. It is seen from Fig. 5.18 that in the direction *perpendicular* to the extension of the slit (*dotted lines*) the geometry of the grating illumination is the same for constant f' number in calibration procedure and measurements of the spectra of the light source under study. In the direction parallel to the input monochromator slit (solid lines), illumination of the grating depends on the distance between the entrance slit and light source, as well as the slit height, provided that f'-number has the same value. The closer the light source is to the slit, larger is the angle of the light beam falling on the monochromator. For distant position of the source under study, the bundle cannot illuminate the full grating (full lines). However, the rays from the source at closer position enters the monochromator under such a large angle that part of the light does not hit the grating *despite the fact that* f'*-number* $<$ *f-number*. For constant f'-number, this effect is the larger the longer is the slit and the larger is the ratio of the slit height to the dimensions of the light source.

Intensity distributions on the grating surface in the calibration procedure at close (a) position and in measurements of emission spectra of a extended light source at

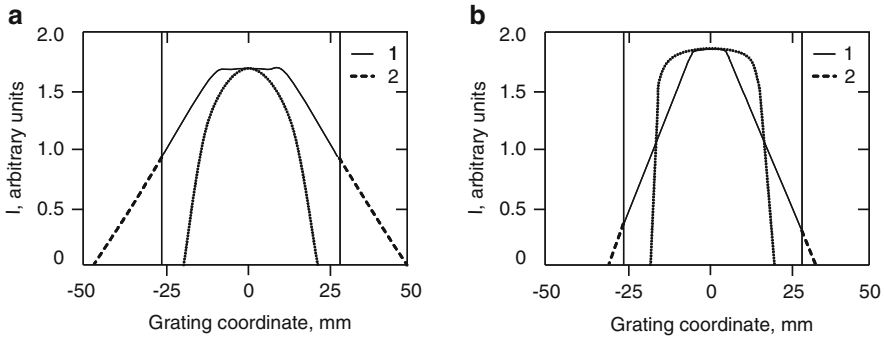

Fig. 5.19 The curves calculated to model the intensity distribution over the grating surface in the two cases of illumination illustrated in Fig. 5.18: (**a**) illumination by the near light source, (**b**) illumination by the distant light source. Here the distribution shown by *dotted lines* in (**a**) and (**b**) demonstrate intensity distributions in the directions along the slit (*1*) and normal to the slit extension (*2*) [34] (reproduced with permission from Measurements Science and Technologies, IOP Publishing Ltd)

distant (b) position are shown in Fig. 5.19. The illumination in the direction perpendicular (dotted line) and along the slit orientation (full line) is shown [34].

Figure 5.19a, b illustrates the data obtained by numerical calculation of the effect for calibration at $f' = 1/11.2$ [34]. The data were found for the case of homogeneous spatial intensity distribution for illuminating surfaces of both light sources. The solid line indicates the intensity distribution over the grating surface in the direction parallel to the slit. The dotted curves show the intensity distribution over the grating surface in the direction perpendicular to the extension of the slit. The data were obtained at $f' = 1$ cm/11.2 cm $= 1/11.2$ for the case of calibration and at $f' = 3.2$ cm/35.8 cm $= 1/11.2$ for the case of measurements. The monochromator features are as follows: Jobin-Yvon AS50 type, the focal length 500 mm, entrance aperture $f = 1/8.5$, slit height 12 mm, aluminum-coated grating 1,200 grooves per mm, radius of curvature 500 mm. The monochromator is equipped with a solar-blind photomultiplier of PMT142 (see Sect. 3.4) with the window of diameter 8 mm.

It is seen that there is distinction between grating illumination for the two directions mentioned above. In the direction parallel to the slit, part of the light do not hit the grating, especially in the case of calibration, though the aperture of the monochromator, $f = 1/8.5$, is larger than that achieved on calibration and measurement, $f' = 1/11.2$. It is obvious that systematic uncertainty cannot be found for the case of unknown or not uniform spatial distribution of the intensity. Uncertainty is greater the greater is the f'/f ratio, as well as the values of f' number and f number. It is also seen that there is distinction between illumination layout in the direction normal to the slit orientation in the case of calibration and measurements. This is because light sizes are comparable with the distance between the sources and slit. However, in all cases light from the source fully illuminates the diffraction grating. Here, astigmatism of the monochromator has to be taken into account [34].

The data show that both calibration and measurements are to be carried out under identical values of f'-number, as well as at the same distance from the light source to the entrance slit. In the case, when the tested object has large sizes, the light source assumed to be used for calibration has to have about the same sizes. The impact of the size factors on measurements of absolute spectral radiation intensity with the help of monochromator will be discussed in Sect. 6.4.

5.5.2 *Collapsible Extended Hydrogen-Discharge Lamp*

A lamp design was proposed by the author (unpublished data, 1997), wherein calibration methods were also discussed, and these combined factors allow characteristics below to be achieved. These methods for calibration of extended lamps and spectrometer/monochromator systems in arbitrary and absolute units guarantee uncertainties less than that ensured by virtue of light sources calibrated against synchrotron radiation. Schematically, collapsible extended discharge lamp is shown in Fig. 5.20.

The principle features of the lamp design are specified as follows:

- The frame is made up of stainless steel, and its internal construction is fabricated with high precision.
- The diameters of the exit diaphragm and emission zone are large, about 50 mm. This fact guarantees layout identity between calibration and measurements in a wide f'-number range.

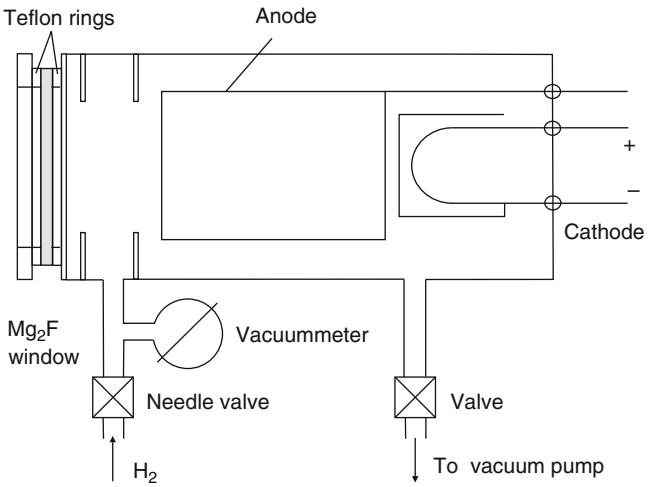

Fig. 5.20 Arrangement of collapsible extended hydrogen discharge lamp (A.M. Pravilov, unpublished data, 1997)

– Flow of pure hydrogen from a hydrogen cylinder or electrolytic cell is exploited here.
– MF_2 window is designed and fabricated as removable (see Sect. 4.2.2.1).
– The lamp design can be fabricated as windowed, as well as windowless.

In the case of widowed design, the window is to be vacuum sealed by Teflon rings and can be easily removed for cleaning or measuring transparence spectra (see Sect. 4.2.2.1). In the case of windowless design, a differential pumping unit should be used.

The design offers the following advantages:

– Stability of gas composition and pressure of the lamp
– The possibility for measuring the transparency spectrum of its window, and the possibility for restoring the window to its original transparency after cleaning (see Sect. 4.2.2.1)
– Stability of spectral photon flux. It is easily found the hydrogen pressure and current limits, wherein the spectrum is independent of these parameters, and intensity is independent of the pressure and be approximately proportional to the current. Therefore, only for a few lamps absolute calibration should be carried out, and all the others do not need calibration
– Possibility of the use of the lamp of windowless design for calibration in 78–380 nm spectral range. Range is wider than the operating range of windowed lamps, which involves $\lambda = 115$–380 nm

Before applying any monochromator for calibration of the extended lamp, the monochromator has to be calibrated by virtue of a scheme similar to that shown in Fig. 5.1b. Calibration methods will be discussed below (see also [34]).

5.5.3 *Branching Ratio Methods*

The branching ratio method is based on the use of relative intensities of optical transitions from *single* atomic or molecular level to the lower ones, and the transition intensity preliminary measured or calculated. Sometimes, the methods in which several upper levels are used are also called as branching ones. In this event, relative population of these levels should be well known, and ranges of excitation conditions related to these levels at invariable emission spectra have also to be found. In the author opinion methodologically these methods should be named *calibration methods by virtue of well-known spectra* (see Sect. 5.6). Uncertainty is defined in the main by the uncertainty of branching ratio coefficients. In other words, it depends on the Einstein's coefficients for these transitions, and the uncertainty of relative populations of vibronic levels and decomposition of luminescence spectra onto partial ones, provided that transitions from several levels took place and bands or lines associated with them are not resolved.

In the 1970s and earlier atomic transitions in the visible range and vacuum UV range were commonly used as standard, the so-called atomic branching ratio

Table 5.2 The molecular transitions exploited in the branching ratio methods

Molecule	Transition	Spectral range (Å)
H_2	H_2 Lyman bands, $B^1\Sigma^+_u, v_B = 3 \rightarrow X^1\Sigma^+_g, v_X = 0$–13	1,100–1,650
H_2	H_2 Werner bands, $C^1\Pi_u, v_C = 0$–7 $\rightarrow X^1\Sigma^+_g, v_X = 0$–13	1,000–1,345
N_2	N_2 LBH[a] bands, $a^1\Pi_g, v_a = 0$–6 $\rightarrow X^1\Sigma^+_g, v_X = 0$–13	1,275–1,850
CO	CO fourth positive group, $A^1\Pi, v_A = 0$–5 $\rightarrow X^1\Sigma^+, v_X = 0$–9	1,400–1,850
N0	NO γ bands, $A^2\Sigma^+, v_A = 0$–3 $\rightarrow X^2\Pi, v_X = 0$–7	1,900–3,000
NO^+	NO^+ Baer–Mischer bands, $A^1\Pi, v_A = 0$–3 $\rightarrow X^1\Sigma^+, v_X = 0$–5	1,300–1,620

[a]Lyman–Birge–Hopfield

methods (see [6, 35] and references). Works dealing with the atomic branching methods are published, e.g., see [36]. Authors estimate the method uncertainties to be about 40–50% [6].

Calibration methods based on relationships between intensities of optical transitions in molecular spectra became more precision methods (see [6, 37, 38] and references). The most well-accepted molecular systems that used the branching ratio method in the UV and vacuum UV spectral ranges are shown in Table 5.2.

The transitions shown in Table 5.2 are observable on photoexcitation of molecules in H_2 Lyman bands, NO γ-bands, and NO^+ Baer–Mischer bands, and on excitation by electron impact for all systems, and on recombination accompanied by radiation in N_2 LBH[a] bands and NO γ bands [39, 40].

A true branching ratio method is the method utilizing H_2 Lyman bands on photoexcitation of $H_2(B^1\Sigma^+_u, v_B = 3)$ by resonance argon radiation, $\lambda = 1{,}066.66$ Å, since in this case the optical transition occurs from the single vibronic level. All other events relate to population of several vibronic levels. The relative concentrations of the levels are to be found in experiment, by this it is meant that the vacuum monochromator has to be calibrated by an another method, for example, double monochromator method, or by means of one or a few molecular systems shown in Table 5.2. On using any one of branching ratio method modifications, there is a need to comply with the regulations for luminescence excitation cited in original articles. Unfortunately, these systems each evinces luminescence for comparatively narrow spectral range, and calibration uncertainty within each spectral range may be as great as several tens of percentages.

5.5.4 Double Monochromator Methods

In the event of one source and two vacuum monochromators, there is a possibility to measure the output spectrum of one of the monochromators, and it is desirable to use a nonselective source with respect to photon energies, for example, a proper luminophor. Furthermore, having set the output slit of the first monochromator as the input slit of the second monochromator, or having mounted these slits one behind the other, or having reflected the output beam of the first monochromator by

a mirror onto the input slit of the second monochromator you measure the input spectra of this monochromator by the same photodetector. For the given first spectrum outgoing from the first monochromator and second spectrum from the second monochromator, the function $s_{hv}(\lambda)$ has to be found. It is not necessary to provide direct measurements for this function to obtain the transmittance spectrum of the monochromator. It is a need only to measure the spectral efficiency of the diffraction grating [6, 41, 42]. The most difficulty is that radiation reflected by the grating is polarized, with polarization degree having a high value and dependent on the wavelength [6]. The reflectivity of the diffraction grating of the second monochromator therefore depends on polarization of radiation from the first monochromator, i.e., it depends on their mutual orientation. Thus, at least the output spectrum from the second monochromator has to be measured at two mutual positions of the monochromators: one is with the two parallel slits, and the other is with the two crossed slits. Even so, differences between calibration results obtained by the double monochromator methods and other methods are rather large, as much as two times [43]. This method therefore is a very expensive, inconvenient, and inaccurate. In calibration of vacuum monochromators, it is necessary to apply as much methods as possible. If this is the case the uncertainty will go down to an acceptable value. As described in [34], three methods of calibration in arbitrary units were carried out in the vacuum UV spectral range, including a method with an extended discharge hydrogen lamp, whereas in the range 110–450 nm the number of methods arose to six.

5.6 Sensitivity Calibration of Spectrometer/Photodetector Systems by Means of Well-Known Spectra

The author has already called special attention to identify the problem of layouts in calibration and measurement procedures, as well as the necessity of measurements of reflectivity of mirrors, diffuse reflecting screens, and so on. Difficulty is that the spectrum you need to measure may be distorted by numerous reflections from a surface. These problems can be overcome, provided that you use a calibrated light source, whose layout is just the same you used in measurements of the studied spectrum. It is obvious that the spectrum of the calibrated source has to be well known with a low uncertainty. It is useful to verify calibration by several methods. In the case of investigation of spectra:

- Of the gas-phase luminescence by the optical–optical double resonance (OODR), there is a need to provide identical environment for measurements of the spectrum you used for calibration and of the investigated spectra [13–16, 18–27]
- Of the gas-phase luminescence under the action of resonance radiation of a light source or light source/monochromator combination, it is necessary to set the calibrated object into your cell and provide the same optical density as for the investigated object

– Of a liquid or solid sample, it is necessary to use a calibrated liquid- or solid-state luminophor of the same size
– Of chemiluminescence in the gas phase, it is necessary to pass flow of reagents of the calibrated chemiluminescence system through just the same reactor

In the author's laboratory, luminescence spectra of ion-pair state of iodine molecule produced by OODR method were measured many times. Many of these spectra can be used for calibration of registration systems. Advantage of this method is that after optical population of selected rovibronic level of the $I_2(E\,0_g^+)$ ion-pair state, for example,

$$I_2\,(E\,0_g^+, v_E, J_E \xleftarrow{\lambda_2} B\,0_u^+, v_B, J_B \xleftarrow{\lambda_1} X\,0_g^+, v_X, J_X),$$

other ion-pair states of the first tier (Fig. 5.21) are populated in CINATs

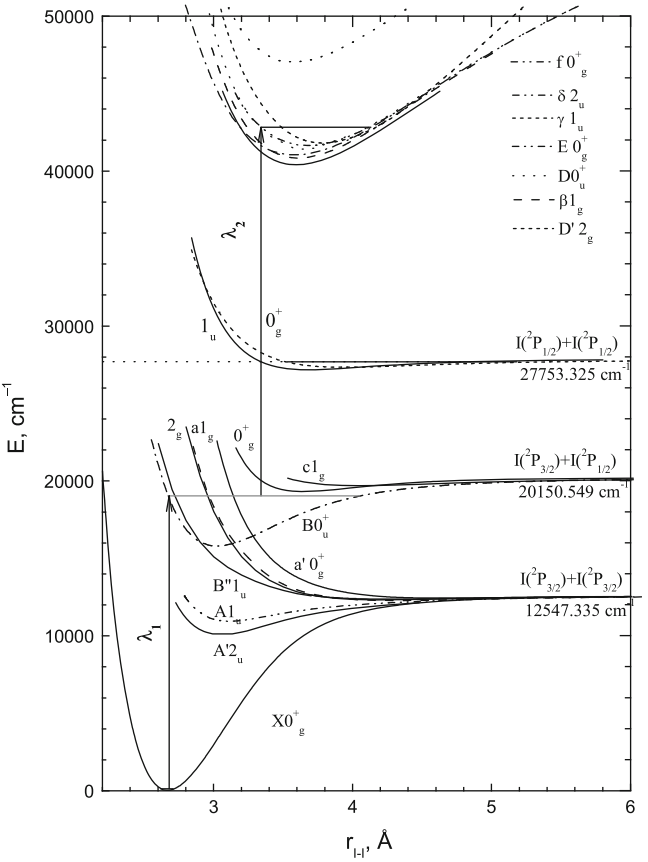

Fig. 5.21 Potential energy curves of some iodine valence and first-tier ion-pair states (see [24, 42] and references therein)

$$\mathrm{I}_2\,(E, v_E, J_E \xrightarrow{M} D\,0_u^+, v_D, J_D),$$

$$\mathrm{I}_2\,(E, v_E, J_E \xrightarrow{M} D'\,2_g, v_{D'}, J_{D'}),$$

$$\mathrm{I}_2\,(E, v_E, J_E \xrightarrow{M} \beta\,1_g, v_\beta, J_\beta),$$

$$\mathrm{I}_2\,(E, v_E, J_E \xrightarrow{M} \gamma\,1_u, v_\gamma, J_\gamma),$$

$$\mathrm{I}_2\,(E, v_E, J_E \xrightarrow{M} \delta\,2_u, v_\delta, J_\delta).$$

Therefore, one can observe luminescence spectra in a wide spectral range, $\lambda_{\mathrm{lum}} \approx$ 220–500 nm, from the optically and collisionally populated states:

$$\mathrm{I}_2(E, v_E, J_E \rightarrow B, v_B, J_B) + h\nu,$$

$$\mathrm{I}_2(D, v_D, J_D \rightarrow X, v_X, J_X) + h\nu,$$

$$\mathrm{I}_2\,(D, v_D, J_D \rightarrow a'\,0_g^+, v_{a'}, J_{a'}) + h\nu,$$

$$\mathrm{I}_2(D', v_{D'}, J_{D'} \rightarrow A'2_u, v_{A'}, J_{A'}) + h\nu,$$

$$\mathrm{I}_2(\beta, v_\beta, J_\beta \rightarrow A1_u, v_A, J_A) + h\nu,$$

$$\mathrm{I}_2(\gamma 1_u, v_\gamma, J_\gamma \rightarrow a1_g, c1_g, c'1_g; v, J) + h\nu,$$

$$\mathrm{I}_2(\delta 2_u, v_\delta, J_\delta \rightarrow (1)2_g, (2)2_g; v_{2g}, J_{2g}) + h\nu.$$

Some of these spectra are available on the author's scientific group site http://photonics.phys.spbu.ru/pravilov/ru/index.php. Now the author will show the calibration method using well-known spectra for calibration of the system involving chemiluminescence reactor, spectrometer, and photodetector described in [44]. Calibration was carried out within a wide spectral range, 210–1,150 nm, by means of chemiluminescence processes in three systems: O + N + M, N + N + M, and O + NO + M (N≡N(^{4}S)), O≡O(^{3}P), NO≡NO($X^2\Pi$), where M = N_2.

Previous studies of NO afterglow kinetics and mechanism:

$$\mathrm{N} + \mathrm{O} \xrightarrow{(\mathrm{M})} \mathrm{NO}(A, 0) \rightarrow \mathrm{NO}(X, v'' = 0 - 6) + h\nu, \tag{5.4}$$

$$\mathrm{N} + \mathrm{O} \xrightarrow{(\mathrm{M})} \mathrm{NO}(B, v' = 0 - 4) \rightarrow \mathrm{NO}(X, v'' = 0 - 16) + h\nu, \tag{5.5}$$

$$\mathrm{N} + \mathrm{O} \rightarrow \mathrm{NO}(C, 0) \rightarrow \mathrm{NO}(X, v'' = 0 - 6) + h\nu, \tag{5.6}$$

have shown that populations of NO(A, $v_{\mathrm{A}} = 0$ and B, $v_{\mathrm{B}} =$ 0–4) levels are nearly proportional to the pressure of M = N_2 in the range $p_{N_2} =$ 3–8 torr, whereas population of NO(C,0) level is independent of this pressure [40, 45, 46]

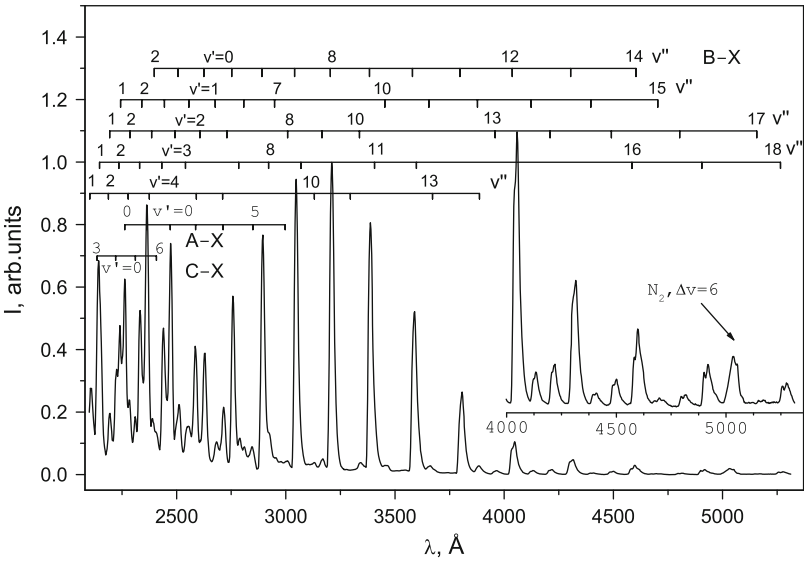

Fig. 5.22 Spectrum of the NO afterglow measured in pure N_2 environments, $p_{N_2} = 3.4$ torr; full width of half maximum, FWHM = 1 nm. Insert: the same spectrum in the 400–535 nm region. The assignments of the β-, γ-, and δ-bands are shown (see [40, 44] and references therein)

(A.A. Matveev, A.M. Pravilov, A.F. Vilesov, unpublished data, 1989). Here NO $(A, B, C, X) \equiv NO(A^2\Sigma^+, B^2\Pi, C^2\Pi, X^2\Pi)$. The γ-, β-, and δ-bands [reactions (5.4), (5.5) and (5.6), respectively] emit in the wavelength range $\lambda \approx 225$–302, 200–530 and 191–242 nm (Fig. 5.22). The spectral radiation intensity (spectral photon flux) of the reactions (5.4 and 5.5) is greater than that of reaction (5.6) at $p_{N_2} > 0.2$ torr.

Therefore, spectra of NO afterglow at $\lambda > 242$ nm mainly consist of the NO $(A,0) \rightarrow X, v'' = 2$–6 and $B, v' = 0$–$4 \rightarrow X, v''$ progressions. The relative intensities of the N + O chemiluminescence spectrum bands, $I_{5.4}(\lambda) + I_{5.5}(\lambda) + I_{5.6}(\lambda)$, $\lambda = 191$–530 nm, are independent of the N_2 pressure until nitrogen pressure remains within several percentages.

Nitrogen afterglow is caused by the following optical transitions [40, 47–49]:

$$N + N \xrightarrow{(M)} N_2(B, v' = 0 - 12) \rightarrow N_2(A, v'') + hv \tag{5.7}$$

$$N + N \xrightarrow{(M)} N_2(B', v' = 3 - 9) \rightarrow N_2(B, v'') + hv. \tag{5.8}$$

These transitions occur from vibronic levels of $N_2(B^3\Pi_g, B'^3\Sigma^-_u; v)$ as the first positive and nitrogen Y-band, respectively, $\lambda = 478$–2,531 nm, Fig. 5.23.

The relative populations of these levels are nearly independent of the pressure of N_2 at $M = N_2$ owing to fast collision-induced relaxation of the upper states. Therefore, the relative intensities of the chemiluminescence spectra of (5.7) and (5.8) reactions are to be nearly independent of p_{N_2} in pure N_2 and at $p_{N_2} > 3$ torr.

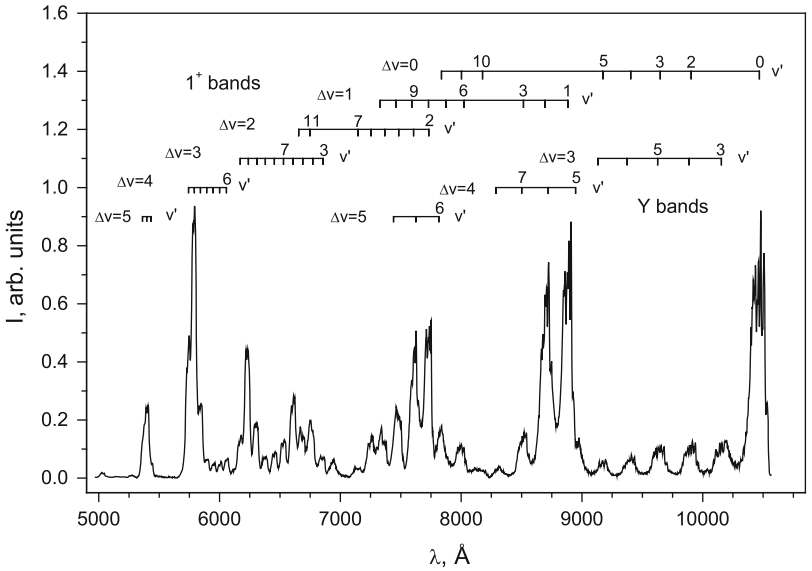

Fig. 5.23 Spectrum of the N_2 afterglow measured in pure N_2 environments, $p_{N_2} = 3.4$ torr; FWHM = 1 nm. The assignments of the 1+ and Y-bands are shown (see [40, 44, 47, 48] and references therein)

The 190–2,531 nm spectral range is covered by the chemiluminescence bands of O + N and N + N. In the $p_{N_2} = 3$–8 torr pressure range, the relative intensities of the most bands are to be independent of the pressure.

It is well known that special efforts are needed to eliminate oxygen atoms from the products of N_2 discharge. There is always an impurity of molecular oxygen in molecular nitrogen, and atomic oxygen is produced either directly in discharge or in the following reaction:

$$N + NO \rightarrow N + O \tag{5.9}$$

(nitrogen monoxide is produced in microwave discharge). As pure molecular nitrogen passes through the microwave discharge, afterglow spectra of NO and N_2 become observable. In order to increase the intensity of NO afterglow, a weak flow of NO may be introduced to provide partial titration of N atoms, reaction (5.9) [46]. In order to obtain the chemiluminescence spectra of O + N and N + N inside the N_2 environment with a low uncertainty, the nitrogen pressure has to be kept invariable which decreases the dependency of $I_{5.4}(\lambda) + I_{5.5}(\lambda) + I_{5.6}(\lambda) + I_{5.7}(\lambda) + I_{5.8}(\lambda)$ on the pressure of N_2. The use of a total intensity registration channel for normalization of the spectra diminishes the influence of changes of the N and O atomic concentrations on the spectra [44]. The NO and N_2 afterglow spectra can be used for $s_{hv}(\lambda)$ calibration of an optical system in the spectral ranges at $\lambda \leq 530$ nm and $\lambda \geq 500$ nm, respectively. The true spectral radiation intensity, $I_{hv}^{et}(\lambda)$ (spectral

photon flux) of emission spectra in arbitrary units as corrected by the $s_{hv}(\lambda)$ function are calculated as follows:

$$I^{et}_{hv}(\lambda) = I^{u}_{hv}(\lambda)/s_{hv}(\lambda). \tag{5.10}$$

Here, $I^{u}_{hv}(\lambda)$ is uncorrected spectral radiation intensity. The $s_{hv}(\lambda)$ curves are fairly smoothed. Its value therefore can be calculated in a narrow wavelength interval $\lambda_i - \lambda_{i+1}$ as the ratio of the total intensity of the uncorrected spectrum to that of the true spectrum. The intensity within a narrow band or a wide interval can then be used as a total intensity within the interval:

$$s_{hv}(\lambda) = I^{u}_{hv}(\lambda_i - \lambda_{i+1})/I^{et}_{hv}(\lambda_i - \lambda_{i+1}). \tag{5.11}$$

The values of $I^{et}_{hv}(\lambda_i - \lambda_{i+1})$ function can be found from the spectra obtained in [44], where λ is the wavelength of the band maximum. In the range $\lambda \geq 400$ nm, calibration can also be carried out with the help of chemiluminescence spectra of O + NO, so-called *air afterglow* spectrum. To provide extra examination of the air afterglow spectrum obtained early [50–54], this spectrum was measured with N_2/O_2/He/NO mixture in the proportion 3.4 + 0.04 + 0.07 + 0.001 torr (Fig. 5.24). It is independent of the nitrogen pressure, in the range $p_{N_2} = 1$–8 torr, and flow velocity of interval 190–1,800 cm^{-3} with the accuracy of about 2%. In the work [44] it was shown that the chemiluminescence spectrum of O + NO is identical to that found for pure N_2. The accuracy of intensity measurements is better than 2% in $\lambda = 400$–1,050 nm range and 2–3% in 1,050–1,150 nm spectral range. The

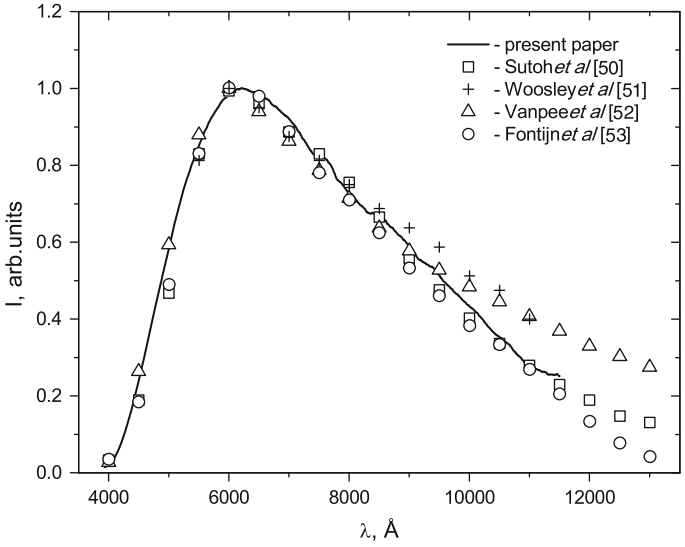

Fig. 5.24 The air afterglow spectra measured at the N_2/O_2/He/NO (2.84 + 0.04 + 0.07 + 0.001 torr) mixture compared with the data from [50–53] (see [44, 54])

spectrum obtained is in close agreement with that of measured in [54]. The discrepancies of the spectra measured in this work and some other ones are most for $\lambda < 550$ and $\lambda > 850$ nm [50–53]. The experimental setup and procedures of spectral measurements are described in detail in [44] (see references therein, also). Here, it should be noted that only that uncertainties of spectral measurements are 2% in the 320–1,150 nm spectral range and 12–8–5–2% in the 210–260–290–320 nm ranges.

Any spectra are advised to apply as standards on condition that:

- These spectra are measured with low uncertainties under conditions of a weak dependency on partial pressures of components, potential impurities, and so on
- These spectra are tested by several independent methods to verify if any errors of measurements occur
- The range of conditions corresponds to the given uncertainties of measurements
- The applied method is proved by means of other monochromators and photodetectors

After proving the applied method, the data obtained in calibration procedure are to be compared with that measured by the standard methods described in Sects. 5.2 and 5.3. Furthermore, it is necessary to set limits on spectral resolution, reagent and N_2 concentrations, potential impurities under which this method and the standard methods give the same calibration data within the given limits of measurement uncertainties. Why should this method be verified? Regarding the spectral resolution, spectral bands get overlapping as the resolution downs. Thus, when the function $I^{et}_{h\nu}(\lambda_i - \lambda_{i+1})$ is calculated from spectra measured with a high resolution and the function $I^{u}_{h\nu}(\lambda_i - \lambda_{i+1})$ is obtained under a low resolution, then the function $s_{h\nu}(\lambda)$ can be calculated as distorted. As for pressure, it is still a question about system behavior beyond the bounds of the applied pressure. With impurities of O_2 and NO, they are more undesirable to reactions (5.4)–(5.8). These impurities may occur in discharge products of N_2 together with a small amount of O_2. The matter is that these molecules make excited states of NO and N_2 be deactivated, with rate constants for deactivation dependent on the vibrational quantum numbers of levels of these states. The exact values of the rate constant are unknown. In order to unsure oneself against troubles, it may be assumed the deactivation rate constant to be equal to the gas-kinetic one, $k_{gk} \approx 3 \times 10^{-10}$ cm^3/s, and the deactivation rate is not to be more than 1% of spontaneous decay rate for the states equal to the inversely proportional value of the radiation lifetime τ, the Stern–Volmer law, as follows:

$$3 \times 10^{-10}[\mathrm{X}] < 0.01\ \tau,$$

where X = NO, O_2, and $\tau_{\mathrm{NO}(A,B,C;v)} \leq 3 \times 10^{-6}$ s, $\tau_{\mathrm{N_2}(B,B';v)} \leq 3 \times 10^{-5}$ s are radiation lifetimes of these excited states. Having found the functions of dipole transition moments against the internuclear distances of N–O and N–N in reactions (5.4)–(5.8) and compared them with literature data (e.g., Fig. 5.22), the author [44] confirmed validity of the obtained data for the function $I^{et}_{h\nu}(\lambda_i - \lambda_{i+1})$.

5.6.1 Test of the Calibration Method

To examine the method and understand whether the determined $s_{hv}(\lambda)$ curve depends on spectral resolution, the authors of [44] measured the O + N and N + N chemiluminescence spectra by means of another monochromator equipped with *other* PMTs, determined the $s_{hv}(\lambda)$ curves obtained as ratios of the measured *uncorrected* intensities of the bands to the true ones (see Appendix B), and compared these curves with those measured here by the standard way [see formula (5.11)]. The measurements were carried out at $\lambda = 210$–370 and 330–530 nm (FWHM = 0.4 and 1 nm), 700–900 nm (FWHM = 1, 2, and 3 nm), and 600–1,050 nm (FWHM = 1 and 2 nm) ranges. One part of the data is shown in Fig. 5.25 at FWHM = 1 nm. It is seen that the $s_{hv}(\lambda)$ curves obtained by the usual procedure and this method are in excellent agreement. Uncertainty of the $s_{hv}(\lambda)$ function obtained by our method increases as FWHM is more than 2 nm at $\lambda \geq 270$ nm, and 1 nm in $\lambda < 270$ nm ranges, increases due to that the overlapping of neighbor bands (Fig. 5.26).

Thus, pressure and resolution are limited, and the described method is assumed to be efficient within these limits.

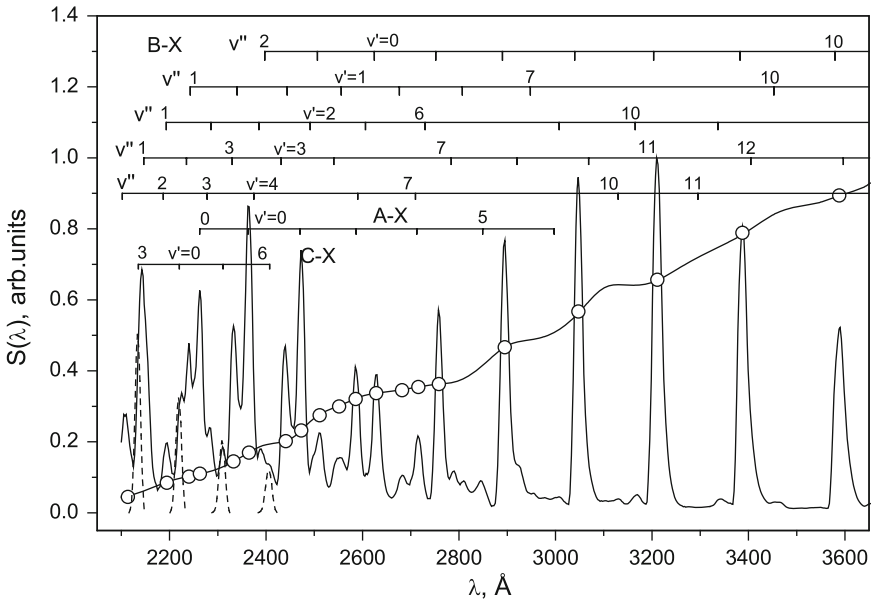

Fig. 5.25 The $s_{hv}(\lambda)$ calibration curves measured by means of the standard methods considered in the Sect. 5.3 for the system including monochromator and PMT71 (*solid lines*) and using the method under discussion (*open circles*). Simulation of the NO(C,0-X,v'') bands illustrating their relative intensities at $p_{N_2} = 3.4$ torr (*broken lines*) (see [44])

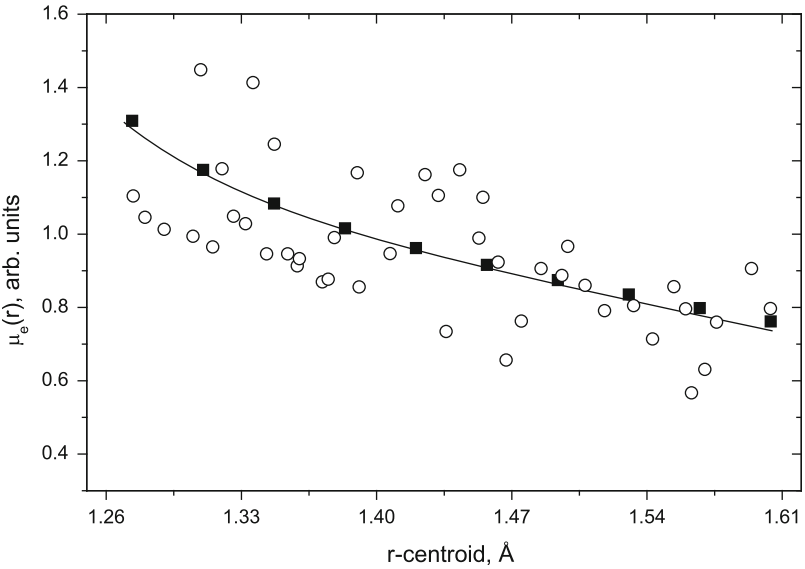

Fig. 5.26 The dependence of the dipole moment of the NO($B^2\Pi$–$X^2\Pi$) transition on the r-centroids. Experimental values of the dipole moment and their best fit shown by *open circles* and *solid line*, respectively (see [44]). The *solid squares* show the best fit of the dipole moment presented in [55]

Recommendations. To calibrate spectrometer/detector system using the O + N, N + N and O + NO chemiluminescence spectra described in this section and [44], one has to measure them in pure N_2 environment in 3–8 torr pressure interval, providing $\lambda = 242$–$1{,}050$ nm, and at $p_{N_2} = 3.4 \pm 0.3$ torr, providing $\lambda = 210$–242 nm. Besides, FWHM has to be better than 1 nm in $\lambda = 210$–285 nm and 2 nm in $\lambda = 285$–$1{,}150$ nm ranges, respectively.

It should not be forgotten that there is strong deactivation of NO(A,B,C;v) and N_2(B,B';v) vibronic levels by NO and O_2 molecules competing with radiative decay of these states, and rate constants of these processes depend on the level numbers (see, e.g., [56–58] and references therein). Besides, there are NO Ogawa bands in the near IR region (see Fig. 4 in [44]), and they can distort N_2 afterglow spectrum. Therefore, one has to be careful with NO and O_2 impurities in N_2. Their upper limit can be estimated from inequality

$$3 \times 10^{-10}[\mathrm{X}] < 0.01\,\tau^{-1}$$

(X = NO, O_2, and $\tau_{\mathrm{NO}(A,B,C;v)} \leq 3 \times 10^{-6}$ s, $\tau_{\mathrm{N_2}(B,B';v)} \leq 3 \times 10^{-5}$ s are the NO(A,B,C;v) and N_2(B,B';v) radiative lifetimes) i.e., [NO] or/and $[O_2] < 10^{12}$ cm^{-3} in $\lambda = 530$–$1{,}050$ nm and $<10^{13}$ cm^{-3} in $\lambda = 210$–530 nm.

The author's opinion is that this method is very promising for the calibrations of Fourier-transform spectrometers.

5.7 Calibration of Spectral Transmittance of Spectral Device

This task is virtually similar in its principle steps to calibration of spectrometer/photodetector system. You should only calibrate your photodetector in relative or absolute units.

Problems

1. The spectral photoresponse is affected by the lamp long-wavelength radiation scattered in monochromator (the short-wavelength range) and by daylight passing into the monochromator. How can you take that into account to provide measurements of the function $s(\lambda)$ with low uncertainty?
2. You use the scheme of monochromator/photodetector shown in Fig. 5.1c, wherein total unfocused light from the strip lamp is used for sensitivity calibration of the registration system. The temperature function of the strip is given against distance from its center. What is the manner you need to estimate the calibration error?
3. What a filter, or filters, have to be applied for calibration of the system including diffraction grating monochromator in the range of wavelengths 190–600 nm?
4. What a filter, or filters, have to be applied for calibration of the system including diffraction grating monochromator by means of a strip lamp in the 400–1,300 nm spectral range?
5. A light source you plan to use has a small size. A condenser or mirror should be applied. Why?
6. The radii of curvature of lens surfaces are equal to 10 cm, $|r_1| = |r_2| = 10$ cm. The lens of focal length f is made from fused quartz. For the given wavelength $\lambda = 440$ nm, you set a diaphragm and input slit at the distance $|a_1| = |a_2| = 2f$ from the lens with magnification 1:1. Calculate the distance between the input slit and the image of your light source at $\lambda = 240$ nm.
7. You carried out calibration of a spectrometer/photodetector system, where the photodetector was calibrated in absolute or arbitrary units. What is the way for calculating the spectrometer transmittance function?

References

1. Optical aberration. http://en.wikipedia.org/wiki/Optical_aberration
2. Chromatic aberration. http://en.wikipedia.org/wiki/Chromatic_aberration
3. Rabek, J.F.: Experimental Methods in Photochemistry and Photophysics. Wiley, Chichester (1982)
4. Golovlev, N.L., Chistyakov, V.A., Shevchenko, VYa: SHIFT-2 infrared spectrocomparator. Meas. Tech. **37**, 1377–1380 (1994)
5. Kaye, G.W., Laby, T.H.: Tables of Physical and Chemical Constants. Longmans Green, London (1959)

6. Zaidel, A.N., Shreider, E.Ya.: Vakuumnaya Spectroskopiya i ee Primenenie (Vacuum Spectroscopy and Its Application). Nauka, Moscow (1976) (in Russian) [see also Zaidel, A.N., Shreider, E.Ya.: Vacuum Ultraviolet Spectroscopy. Humphrey, Ann Arbor (1970)]
7. WS-1 diffuse reflectance standard. http://www.oceanoptics.com/Products/ws1diffrefstan.asp
8. Lambertian_reflectance. http://en.wikipedia.org/wiki/Lambertian_reflectance
9. Gibson, C.E., Ma, C.K., Hartmann, J.: Decreasing dependence of the calibration of the tungsten strip lamp on the temperature of the lamp base with increasing filament length. Metrologia **42**, 383–388 (2005)
10. Feynman, R.P., Leighton, R.B., Sands, M.: The Feynman Lectures on Physics, vol. 1. Addison-Wesley, London (1963)
11. Thin lens_equation. http://en.wikipedia.org/wiki/Lens_(optics)#Thin_lens_equation
12. Sosman, R.B.: The Properties of Silica. Chemical Catalog, New York (1927)
13. Lawley, K., Jewsbury, P., Ridley, T., Langridge-Smith, P., Donovan, R.J.: Einstein A-coefficients and transition dipole moments for some ion-pair to valence transitions in I_2. Mol. Phys. **75**, 811–828 (1992)
14. Holmes, A.J., Lawley, K., Ridley, T., Donovan, R.J., Langridge-Smith, P.R.R.: Optical-optical double resonance (OODR) studies of the halogen ion-pair states. Part 2. The $f(0_g^+) \rightarrow B(0_u^+)$ transition dipole moment function in I_2. J. Chem. Soc. Faraday Trans. **87**, 15–18 (1991)
15. Jewsbury, P.J., Lawley, K.P., Ridley, T., Donovan, R.J.: Optical-optical double resonance studies of the halogen ion-pair states. Part 3. The $F(0_u^+) \rightarrow X(0_g^+)$ transition dipole moment function in I_2. J. Chem. Soc. Faraday Trans. **88**, 1599–1603 (1992)
16. Wilson, P.J., Ridley, T., Lawley, K.P., Donovan, R.J.: Double resonance nozzle cooled spectroscopy (DRINCS) of the $E(^3P_2)$, $f(^3P_0)$ and $f'(^1D_2)$ 0_g^+ ion-pair states of I_2. Chem. Phys. **182**, 325 (1994)
17. Bibinov, N.K., Davydov, V.G., Fateev, A.A., Kokh, D.B., Lugovoj, E.V., Ottinger, Ch, Pravilov, A.M.: The transition dipole moment function of the chlorine $E0^+_g$ - $B0^+_u$ system. J. Chem. Phys. **109**, 10864–10872 (1998)
18. Akopyan, M.E., Bibinov, N.K., Kokh, D.B., Pravilov, A.M., Stepanov, M.B.: The iodine $E0^+_g$ - $B0^+_u$ and $D0^+_u$ - $X0^+_g$ transition dipole moment functions. Chem. Phys. **242**, 253–261 (1999)
19. Bibinov, N.K., Fateev, A.A., Kokh, D.B., Lugovoj, E.V., Pravilov, A.M.: Optical transitions from the chlorine $0^+_u(^3P_2)$ state. Chem. Phys. **254**, 89–98 (2000)
20. Akopyan, M.E., Bibinov, N.K., Kokh, D.B., Pravilov, A.M., Sharova, O.L., Stepanov, M.B.: The approach-induced $I_2(EO_g^+ \xrightarrow{M} DO_u^+)$ transitions, M = He, Ar, I_2, N_2, CF_4. Chem. Phys. **287**, 399–410 (2003)
21. Bibinov, N.K., Malinina, O.L., Pravilov, A.M., Stepanov, M.B., Zakharova, A.A.: The approach-induced and collision-induced $I_2(EO_g^+ \xrightarrow{I_2,(X)} DO_u^+)$ transitions from low, v_E = 8–23 vibronic levels of the $I_2(E)$ state. Chem. Phys. **277**, 179–189 (2002)
22. Akopyan, M.E., Pravilov, A.M., Stepanov, M.B., Zakharova, A.A.: The collision-induced $I_2(E0_g^+ M \longleftrightarrow D0_u^+)$ transition, M = He, Ar, N_2, CF_4. Chem. Phys. **263**, 459–470 (2001)
23. Tscherbul, T.V., Buchachenko, A.A., Akopyan, M.E., Poretsky, S.A., Pravilov, A.M., Stephenson, T.A.: Collision-induced non-adiabatic transitions between the ion-pair states of molecular iodine: a challenge for experiment and theory. Phys. Chem. Chem. Phys. **6**, 3201–3214 (2004)
24. Tellinghuisen, J.: The $D(0_u^+)$ state of I_2: analysis by quantum simulation of bound-free D – X fluorescence. Can. J. Phys. **62**, 1933–1940 (1984)
25. Akopyan, M.E., Novikova, IYu, Poretsky, S.A., Pravilov, A.M., Smolin, A.G., Fedorova, T. V.: Dipole moment functions for electronic transitions from ion-pair states of the second tier of molecular iodine. Opt. Spec. **99**, 36–42 (2005)
26. Akopyan, M.E., Baturo, V.V., Lukashov, S.S., Poretsky, S.A., Pravilov, A.M.: Dipole moment functions of the iodine D'2g–A'2_u and $D0_u^+ - a'\,0_g^+$ transitions (submitted to J. Phys. B: Atom. Mol. Opt. Phys.)
27. Akopyan, M.E., Khadikova, E.I., Lukashov, S.S., Poretsky, S.A., Pravilov, A.M., Buchachenko, A.A., Suleimanov, Yu.V.: Dynamics and mechanism of the non-adiabatic

transitions from the ungerade $I_2\,(D\,0_u^+)$state induced by collisions with rare gas atoms. J. Chem. Phys. **133**, 244304-1-10 (2010)
28. Carraro, L., Cortiana, M., Puiatti, M.E., Sattin, F., Scarin, P., Valisa, M.: Absolute calibration of a Czerny-Turner spectrometer in the range 1200–7000 Å. Rev. Sci. Instrum. **66**, 613–615 (1995)
29. Zaidel, A.N., Shreider, E.Ya: Vacuum Ultraviolet Spectroscopy. Humphrey, Ann Arbor (1970)
30. Vilesov, F.I., Akopyan, M.E., Kleymenov, V.I.: Improvement of electrical and radiation parameters of hydrogen lamps working at high voltage. Pribory i Tekhnika Eksperimenta (USSR) (Instr. Exp. Tech.) **6**, 150–153 (1963)
31. Model 632 Deuterium Light Source with Magnesium Fluoride Window for 115 to 380-nm. http://www.mcphersoninc.com/lightsources/model632lightsource.htm
32. Samsom, J.A.R.: Efficiency of aluminized gratings in the spectral range 555 to 1600 Å. J. Opt. Soc. Amer. **52**, 525–528 (1962)
33. Shishatskaya, L.P., Yakovlev, S.A., Volkova, G.A.: VUV lamps with a large emitting surface. J. Opt. Technol. **65**, 1025–1028 (1998)
34. Bibinov, N.K., Bolshukhin, D.O., Kokh, D.B., Pravilov, A.M., Vinogradov, I.P., Wiesemann, K.: Absolute calibration of the efficiency of a VUV-monochromator/detector system in the range of 110–450 nm. Meas. Sci. Technol. **8**, 773–781 (1997)
35. Boldt, G.: Absolute intensity calibration methods in the vacuum UV region. Ultraviolet Stellar spectra and related ground-based observations. In: Hounziau, L., Butler H.E. (ed.) Proceedings from IAU Symposium No. 36, Lunteren, Netherlands (1968)
36. Daltrini, A.M., Machida, M.: Modified branching ratio methods for absolute intensity calibration in VUV spectroscopy. IEEE Trans. Plasma Sci. **33**, 1961–1967 (2005)
37. Mumma, M.J.: Molecular branching-ratio method for intensity calibration of optical system in the vacuum ultraviolet. J. Opt. Soc. Amer. **62**, 1459–1466 (1972)
38. Ando, K., Okazaki, K., Mori, K.: Intensity calibration of normal incidence monochromator by the double monochromator method. Jpn. J. Appl. Phys. **18**, 1833–1837 (1979)
39. Golde, M.F., Trush, B.A.: Vacuum ultraviolet emission by active nitrogen. I. The formation and removal of $N_2(a_1\Pi_g)$. Proc. Roy. Soc. **A330**, 79–85 (1972)
40. Pravilov, A.M.: Fotoprozessy v Molekulyarnykh Gasakh (Photoprocesses in Molecular Gases). Energoatomizdat, Moscow (1992)
41. Michels, D.J., Mikes, T.L., Hunter, W.R.: Optical grating evaluator: a device for detailed measurements of diffraction grating efficiencies in the vacuum ultraviolet. Appl. Opt. **13**, 1223–1229 (1974)
42. Reevs, E.M., Parkinson, W.H.: Efficiencies of gold and platinum grating in the vacuum ultraviolet. J. Opt. Soc. Amer. **53**, 941–945 (1963)
43. Adjello, J.M., Shemansky, D., Kwok, T.L., Yung, Y.L.: Studies of extreme-ultraviolet emission from Rydberg series of H_2 by electron impact. Phys. Rev. **A29**, 636–653 (1984)
44. Fateev, A.A., Fink, E.H., Pravilov, A.M.: Simple method of spectrometer/detector sensitivity calibrations in the 210–1150 nm range. Meas. Sci. Technol. **10**, 182–189 (1999)
45. Kenner, R.D., Ogryzlo, E.A.: Chemiluminescence in gas phase reactions. In: Burr, J.G. (ed.) Chemi- and Bioluminescence, pp. 45–185. Dekker, New York (1985)
46. Matveev, A.A., Pravilov, A.M., Vilesov, A.F.: Anomalously large isotope effect in the chemiluminescence from $N(^4S)$ + $O(^3P)$ recombination Chem. Phys. Lett. **217**, 582–588 (1994)
47. Vilesov, A.F., Pravilov, A.M., Sidorov, I.I., Smirnova, L.G.: Spectral distribution of the radiative recombination rate constant of the nitrogen atoms first positive band system. Sov. J. Chem. Phys. **2**, 2284–2296 (1985)
48. Bystrov, D.S., Vilesov, A.F., Pravilov, A.M., Smirnova, L.G.: Chemiluminescence kinetics in first positive and Y systems of N_2 during recombination of $N(^4S)$ nitrogen atoms. Sov. J. Chem. Phys. **6**, 2306–2325 (1990)

49. Vilesov, A.F., Pravilov, A.M., Smirnova, L.G.: Temperature dependence of chemiluminescence in the first positive and Y-systems of N_2 induced by recombination of $N(^4S)$ atoms. Sov. J. Chem. Phys. **6**, 2797–2810 (1990)
50. Sutoh, M., Morioka, Y., Nakamura, M.: Absolute rate constant for the chemiluminescent reaction of atomic oxygen with nitric oxide. J. Chem. Phys. **72**, 20–24 (1980)
51. Woolsey, G.A., Lee, D.H., Slafer, W.D.: Measurement of the rate constant for NO-O chemiluminescence using a calibrated piston source of light. J. Chem. Phys. **67**, 1220–1224 (1977)
52. Vanpee, M., Hill, R.D., Kineyko, W.R.: Absolute rate constant measurement for the radiative combination of atomic oxygen with nitric oxide. AIAA J. **9**, 135–138 (1971)
53. Fontijn, A., Meyer, C.B., Schiff, H.I.: Absolute quantum yield measurements of the NO-O reaction and its use as a standart for chemiluminescent reactions. J. Chem. Phys. **40**, 64–70 (1964)
54. Pravilov, A.M., Smirnova, L.G.: The spectral distributions chemiluminescence rate constant in the $O(^3P)$ + CO (+M) and $O(^3P)$ + NO (+He) reactions. Kinet. Catal. **19**, 902–908 (1978)
55. Luque, J., Crosley, D.R.: Electronic transition moment for the $B^2\Pi$-$X^2\Pi$ system of NO. J. Quant. Spectrosc. Radiat. Transfer **53**, 189–200 (1995)
56. Greenblatt, G.D., Ravishankara, A.R.: Collisional quenching of NO(A, v' = 0) by various gases. Chem. Phys. Lett. **136**, 501–503 (1987)
57. Rotem, A., Rosenwaks, S.: Laser induced fluorescence studies of molecular nitrogen. Opt. Eng. **22**, 564–570 (1983)
58. Piper, L.G., Cowles, L.M., Rawlins, W.T.: State-to-state exitation of $NO(A^2\Sigma^+$, v' = 0,1,2) by $N_2(A^3\Sigma_u^+)$ v' = 0,1,2). J. Chem. Phys. **86**, 3369–3378 (1986)

Chapter 6
Absolute Measurements of Spectral Radiation Intensity of Processes Under Study

Abstract The chapter discusses some methods of absolute measurements of spectral radiation intensity of investigated photoprocesses, providing the photoprocess spectra have been well known in arbitrary units. The methods of absolute measurements are also considered in the events, where the radiation indicator function is a well-known, and the task of the radiation fraction falling on the photocathode has the exact solution as with a point light source, uniform illuminating sphere, and infinite illuminating plane. Several techniques of absolute calibration are discussed with respect to registration systems through such photoprocesses as the Rayleigh scattering and photoluminescence, provided that the calibrated photoprocesses as well as the photoprocesses under study illuminate as a uniform illuminating cylinder. Finally, the methods of absolute calibration are treated with respect to spectrometer/photodetector systems in the events, where any absolute calibration methods cannot be applied to the photodetector.

6.1 General

When studying photoprocesses, among of which are photoluminescence, chemiluminescence, plasma radiation, and so on, we are faced with the problem of finding spectral radiation intensities of these processes. Physically, the radiation of any photoprocess is emitted by an illuminating volume inside the light source under study, with the radiation propagating within a particular solid angle. Since the light source is commonly an extended illuminating body, the measuring procedure of the intensity per unit volume in absolute units is assumed to involve the following stages:

- Measurements of the spectrum of the light source under study in arbitrary units
- Estimation of the radiation indicator function
- Calculation of the radiation fraction falling on the sensitive area of the photodetector

A.M. Pravilov, *Radiometry in Modern Scientific Experiments*,
DOI 10.1007/978-3-7091-0104-9_6,

– Estimation of the intensity within the required solid angle and spectral range as described in Sect. 4.3.2
– Calibration of the intensity in absolute units

Further, for the given geometry of the light source, particularly, point, sphere, or plane, it is a need to calculate the spectral radiation intensity from the solid angle 4π. In the case of the light source as illuminating cylinder, the method described in Sect. 6.3 can be applied. The spectra in arbitrary units are measured by the methods discussed in Chap. 5. In order to go from spectral radiation intensity over *given spectral range* to the spectral distribution over *all wavelength range* we should follow recommendations considered in Sect. 4.3.2.

Now we consider the question of how geometrical factors can be taken into consideration during calibration and measurements. Assuming a simple event patient of an analytical solution, or a more difficult event, where possible, the absolute calibration should be performed by individual photodetector. In principle, to make absolute measurements of intensity you can use the system involving spectrometer and photodetector identical to that for measurements of the spectrum in arbitrary units. This problem being a more difficult is considered in Sect. 6.4. Now we discuss these methods.

6.2 Absolute Intensity Measurements from Point Source, Illuminating Sphere, and Illuminating Plane

6.2.1 Point Source and Uniform Illuminating Sphere

There are two simplest events of irradiation, a point source and uniform illuminating sphere, both have well-known radiation indicator functions. With point source, the photoresponse, e.g., the photodetector photocurrent, is expressed as follows:

$$I = \frac{A}{4\pi R^2} \int_{\lambda_1}^{\lambda_2} S_{hv}(\lambda)\Phi_{hv}(\lambda)\mathrm{d}\lambda, \tag{6.1}$$

where A is the square of the input opening of the photodetector, R is the distance between the photodetector and illuminating point, $\Phi_{hv}(\lambda)$ is the spectral photon flux within the solid angle 4π. The fraction of the radiation falling on the photocathode is equal to the ratio of the photocathode area A to the sphere radius R: $A/4\pi R^2$. The calculation algorithm for the spectral photon flux is identical to that described in Chap. 4, see (4.8), except that the function $S_{hv}(\lambda)$ is well known, $S_{hv}(\lambda) = S_{hv}(\lambda_0)s_{hv}(\lambda)$. Here the quantity Φ_{hv} is estimated by the virtue of the measured photoresponse as follows:

$$\Phi_{hv} = \frac{I \times 4\pi R^2}{AS_{hv}(\lambda_0)\int_{\lambda_1}^{\lambda_2} s_{hv}(\lambda)\Phi_{hv}(\lambda)}, \tag{6.2}$$

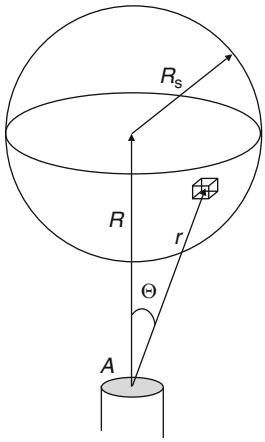

Fig. 6.1 Illustrating measurements of intensity from the uniform illuminating sphere

and the spectral photon flux $\Phi_{hv}(\lambda)$ of the photoprocess under study as follows:

$$\Phi_{hv}(\lambda) = \Phi_{hv}(\lambda_0)\phi_{hv}(\lambda), \tag{6.3}$$

where $\phi_{hv}(\lambda)$ is the spectral radiation intensity of the photoprocess, expressed in arbitrary units. The uniform illuminating sphere produces the photoresponse as being from one illuminating point whose spectral photon flux is equal to that of the sphere: $\Phi_{hv}(\lambda) = 4\pi R_s^3 \varphi_{hv}(\lambda)$, provided that the inequality $\sqrt{A} \ll R_s$ is valid, where $\varphi_{hv}(\lambda)$ is the volumetric spectral radiation intensity, R_s is the sphere radius, Fig. 6.1 [1] (Fateev, A.A., Pravilov, A.M., unpublished data, 2000).

6.2.2 Uniform Illuminating Plane

Assuming the uniform illuminating plane to be infinite, the spectral photon irradiance $E_{hv}(\lambda)$ expressed in terms of photon/(s m^2 nm) is equal to the spectral photon emittance $M_{hv}(\lambda)$ (see Sect. 1.1 and [1]). The spectral photon flux is therefore equal to $\Phi_{hv}(\lambda) = M_{hv}(\lambda)A$ [photon/(s nm)], where A is the photocathode area.

6.3 Absolute Calibration of Registration Systems by Means of Well-Known Photoprocesses

With thinking of any photoprocess such as photoluminescence, chemiluminescence, or Rayleigh scattering to be treated well, implying that the process is tested by different methods with a given uncertainty, you may apply it for absolute calibration of your registration system. You also have to follow the same layout for the calibration to occur. It is meant that your photodetector may not be

calibrated in absolute units separately, and its indicator function may not be calculated. Now we illustrate it by two examples.

6.3.1 Calibration by Means of Rayleigh Scattering

With studying photolysis in the gas phase, a most precise calibration method, by the author opinion, is using the Rayleigh scattering calibration, i.e., calibration by means of scattering by gas density fluctuations. This method has the following advantages:

- The Rayleigh scattering is treated theoretically well
- The Rayleigh scattering cross-sections were measured repeatedly

In particular cases of nitrogen and argon, the cross-sections are measured to better than 1%. The cross-sections found by an experimental approach are perfectly compatible with that calculated theoretically. The cross-sections of greatest practical utility are the cross-sections for the total solid angle of value 4π. Further, starting from the obtained data of the calibration, the intensity of scattering radiation will need to be estimated within this angle. The scattering of laser radiation, which is usually linear polarized, gives a more handy way of calibration, with the laser radiation wavelength adjusted within the spectral range scheduled for specifying the radiation under investigation. As usual, the scattering radiation under study is non-polarized, so that the fraction of the radiation detected within the solid angle $\Delta\Omega$ needs to be recalculated under the conditions shown in Fig. 6.2. For the given angle φ between the polarization plane of incident radiation and the propagation direction and the angle Θ between the direction of observation and the propagation direction, the intensity of scattering radiation has to be estimated within the solid angle $\Delta\Omega$ around the direction of observation $\vec{r}$.

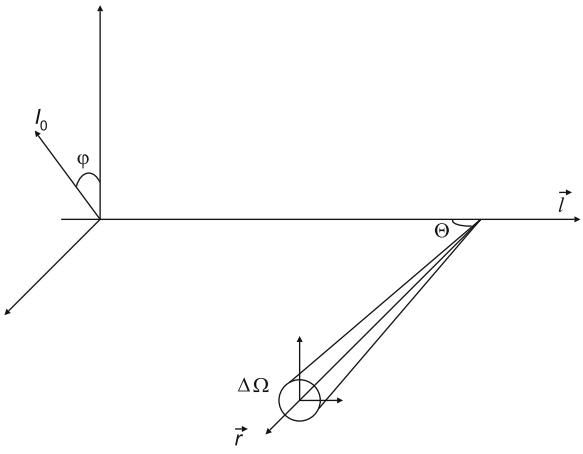

Fig. 6.2 Illustrating the method of calibration using Rayleigh scattering of the linear polarized laser radiation

Now we consider the basic features affecting the cross-section of Rayleigh scattering on:

- Spherically symmetric species, among of which are atoms of rare gases of K_h point symmetry group and molecules of regular tetrahedron symmetry as T_d point symmetry group, for instance, CH_4
- Diatomic molecules

By the author opinion, argon and nitrogen are both more suitable for calibration, because the Rayleigh scattering on these molecules is studied well, and these gases are available as pure at a low price.

6.3.1.1 The Rayleigh Scattering Cross-Sections for Spherically Symmetric Species

Within the total solid angle 4π the Rayleigh scattering cross-section of a spherically symmetric scatterer $\sigma_{ss}(\tilde{\nu})$ is given by the following integral form:

$$\sigma_{ss}(\tilde{\nu}) = \int_0^{2\pi} d\varphi \int_0^{\pi} \sin\Theta d\Theta = \frac{24\pi^3\tilde{\nu}^4}{N^2}\left(\frac{n^2-1}{n^2+1}\right), \tag{6.4}$$

where N is the density of molecules in cm^{-3}; $\tilde{\nu}$ is the wavenumber of incident radiation in cm^{-1}; n is the refractive index of the matter [2, 3]. Specifically, the (6.5) allows the argon refractive index to be calculated at the temperature $T = 15°C$ and pressure 760 torr in the spectral range $\lambda = 303$–$2{,}000$ nm [3, 4]:

$$(n-1)\times 10^{-8} = 6{,}432.135 + \frac{286.06021\times 10^{12}}{14.4\times 10^{-9} - \tilde{\nu}^2}. \tag{6.5}$$

With the second harmonic of the Nd laser, for the given $\lambda = 532.25$ нм and $p_{Ar} = 760$ torr, we find from (6.5) the value $(n-1) = 268\times 10^{-6}$ that allows the cross-section is calculated to be equal to $\sigma_{Ar} = 4.56\times 10^{-27}$ cm^2 [3]. With standard lasers, the Rayleigh scattering signal consists of the so-called Cabannes line associated with elastic scattering [3].

6.3.1.2 The Rayleigh Scattering Cross-Section of Diatomic Molecules

In the case of diatomic molecules the Rayleigh scattering spectrum consists of three lines, namely: the Cabannes line, rotational Raman lines, and vibrational Raman lines. For N_2 molecules, the rotational Raman spectrum lies within the range about ± 50 cm^{-1}, whereas the two vibrational lines are as far as 2,331 cm^{-1} [2]. The vibrational Raman lines are so small, typically 0.1%, that its contribution can usually be neglected. In the total solid angle 4π, a diatomic molecule is specified by the scattering cross-section given by the following expression:

$$\sigma(\tilde{\nu}) = \int_0^{2\pi} \mathrm{d}\varphi \int_0^{\pi} \sin\Theta \mathrm{d}\Theta = \frac{24\pi^3\tilde{\nu}^4}{N^2}\left(\frac{n^2-1}{n^2+1}\right)F_{\mathrm{k}}(\tilde{\nu}), \tag{6.6}$$

where, as above, N is the density of molecules in cm^{-3}; $\tilde{\nu}$ is the wavenumber of incident radiation in cm^{-1}; n is the refractive index of the matter; $F_k(\tilde{\nu})$ is the King correction factor [2, 3]. This factor is specified by the depolarization ratio ρ_n, which is defined to be the ratio of horizontally polarized intensity to the vertically polarized intensity of scattered light: $\rho_n = I_{\parallel}/I_{\perp}$. The latter assumes the polarized light to be scattered at 90° to the $\vec{l}$-axis in Fig. 6.2 as the propagation direction of the incident natural light. The depolarization ratio ρ_n depends on the molecule polarizability α and anisotropy γ as follows:

$$\rho_n = \frac{6\gamma^2}{45\alpha^2 + 7\gamma^2}. \tag{6.7}$$

For example, all spherically symmetric molecules have $\rho_n = 0$, because of $\gamma = 0$. The polarization ratio of diatomic molecules is about several hundredths, it slightly depends on wavelength. For linear and symmetric top molecules the King correction factors are expressed as follows:

$$F_{\mathrm{k}}(\tilde{\nu}) = \frac{6+3\rho_n(\tilde{\nu})}{6-7\rho_n(\tilde{\nu})} = \frac{6+6\rho_p(\tilde{\nu})}{6-4\rho_p(\tilde{\nu})}. \tag{6.8}$$

In the particular case of nitrogen the correction factor takes the following form [4]:

$$F_{\mathrm{k}}(\tilde{\nu}) = 1.034 + 3.17 \times 10^{-12}\tilde{\nu}. \tag{6.9}$$

For example, $F_{\mathrm{k}}(\tilde{\nu}) = 1.034$–$1.043$ and $\rho_n(\tilde{\nu}) = 0.0199-0.0250$ within the spectral range $\lambda = 1{,}000$–200 nm. Now, for the given temperature 15°C and pressure 760 torr the nitrogen refractive in the spectral range $\lambda = 468$–$2{,}058$ and 254–468 nm is calculated to be as follows [3]:

$$(n-1)\times 10^{-8} = 6{,}498.2 + \frac{307.43305 \times 10^{12}}{14.4 \times 10^9 - \tilde{\nu}^2}, \quad 4{,}860\ \mathrm{cm}^{-1} < \tilde{\nu} < 21{,}360\ \mathrm{cm}^{-1}, \tag{6.10}$$

$$(n-1)\times 10^{-8} = 5{,}677.4 + \frac{318.81874 \times 10^{12}}{14.4 \times 10^9 - \tilde{\nu}^2}, \quad 21{,}360\ \mathrm{cm}^{-1} < \tilde{\nu} < 39{,}370\ \mathrm{cm}^{-1}. \tag{6.11}$$

With the second harmonic of the Nd laser, for the given $\lambda = 532.25$ nm and $p_{\mathrm{Ar}} = 760$ torr, we find the value $(n-1) = 268 \times 10^{-6}$ and $F_{\mathrm{k}}(\tilde{\nu}) = 1.035$ that allows the cross-section is calculated to be equal to $\sigma_{\mathrm{N_2}} = 5.30 \times 10^{-27}\ \mathrm{cm}^2$ [3, 5].

In the case of *natural* incident light, accordingto Fig. 6.2 the cross-section is found to be as follows:

$$\sigma(\tilde{\nu},\ \Theta = 90^\circ) = \sigma_\perp(\tilde{\nu},\ \Theta = 90^\circ)[1 + \rho_n(\tilde{\nu})]\left(\frac{6}{6 - 7\rho_n(\tilde{\nu})}\right), \tag{6.12}$$

where $\sigma_\perp(\Theta = 90^\circ)$ is the differential cross-section of the $I_\perp$ component at the angle $\Theta = 90^\circ$. In the context of such a model, the integral cross-section within the total solid angle is found to be as follows:

$$\sigma_\mathrm{r}(\tilde{\nu}) = 4\pi\sigma_\perp(\tilde{\nu},\ \Theta = 90^\circ)(1 + \rho_n)\left(\frac{6}{6 - 7\rho_n}\right). \tag{6.13}$$

For the given spectral range $\lambda = 500$–700 nm, this quantity takes the form $\sigma_\mathrm{r} = 4\pi\sigma_\perp(\Theta = 90^\circ)$ in the case of argon, and in the same spectral range the following form $\sigma_\mathrm{r} = 4\pi\sigma_\perp(\Theta = 90^\circ) \times 1.044$ in the case of nitrogen. It was shown in [6] that the cross-section expressed in terms of the correction factor also takes the following integral form:

$$\sigma(\tilde{\nu}) = \int_0^{2\pi} \mathrm{d}\phi \int_0^{\pi} \sin\Theta \mathrm{d}\Theta = \left(\frac{16\pi}{3}\right)\sigma_\perp(\Theta = 90^\circ)F_\mathrm{k}(\tilde{\nu}). \tag{6.14}$$

It follows from (6.13) and (6.14) that the following approximation is true:

$$\sigma_\mathrm{r}(\tilde{\nu}) = \left(\frac{3}{4}\right)\sigma(\tilde{\nu})[1 + \rho_n(\tilde{\nu})]\left(\frac{6}{6 - 7\rho_n(\tilde{\nu})}\right)\left(\frac{1}{F_\mathrm{k}(\tilde{\nu})}\right) \approx \left(\frac{3}{4}\right)\sigma(\tilde{\nu}). \tag{6.15}$$

Even with an approximate estimation given by the formula, the uncertainty is less than 1% in the case of nitrogen, whereas for argon this formula gives the exact value.

6.3.1.3 Calibration Using Rayleigh Scattering from Linear Polarized Laser Beam

The differential cross-section of Rayleigh scattering can be estimated by formulae listed in Table 1 of the review [3] according to the experimental layout shown in Fig. 6.2. The application of the formulae assumes the solid angle $\Delta\Omega$, within of which the signal is detected, to be sufficiently small, about 10^{-3}. Then the formulae take the following forms:

$$\frac{\partial^\varphi \sigma_v}{\partial\Omega} = \left(\frac{3\sigma}{8\pi}\right)\left(\frac{1}{2 + \rho_n}\right)\left[\rho_n + (2 - 2\rho_n)\cos^2\varphi\right] \tag{6.16}$$

$$\frac{\partial^n \sigma_n}{\partial\Omega} = \left(\frac{3\sigma}{8\pi}\right)\left(\frac{1}{2 + \rho_n}\right)[2 - (1 - \rho_n)] \tag{6.17}$$

for linear polarized, $\partial^{\varphi}\sigma_v/\partial\Omega$, and non-polarized, $\partial^{n}\sigma_n/\partial\Omega$, radiation. Assuming the polarization ratio to be equal to zero $\rho_n = 0$ for rare gases, the formulae may be simplified. There exists the angle φ, which allows the cross-section of linear polarized light to be equal to the cross-section of non-polarized radiation:

$$\frac{\partial^{\varphi}\sigma_v}{\partial\Omega} = \frac{\partial^{n}\sigma_n}{\partial\Omega}. \tag{6.18}$$

For spherically symmetrical molecules this angle is found to be equal to 45°. In the case of nitrogen, this equality is valid with uncertainty not more than 1%.

Thus, when calibrating by Rayleigh scattering with linear polarized laser beam, the polarization plane should make the angle 45° to the vertical direction, and the photodetector placed in the horizontal plane as shown in Fig. 6.2. Under these conditions the scattered intensity within a small solid angle in the direction of observation is the same as the intensity of non-polarized radiation.

The intensity of Rayleigh scattering is proportional to the gas concentration M, i.e., the Rayleigh scattering photon flux from the unit volume is to be equal to

$$\Phi_{hv}^{\mathrm{R}} = \Phi_{hv}\,\sigma_{\mathrm{r}}(\lambda_0)M, \tag{6.19}$$

where Φ_{hv} is the laser photon flux in photon/s; $\sigma_{\mathrm{r}}(\lambda_0)$ is the Rayleigh scattering cross-section at the laser generation wavelength λ_0. For the given gas concentration M, the photocurrent I_{r} produced by the Rayleigh scattering within a small solid angle $\Delta\Omega$ is to be equal as follows [2, 6, 7]:

$$I_{\mathrm{R}} = \Delta\Omega V_{\mathrm{eff}} S(\lambda_0)\Phi_{hv}\sigma_r(\lambda_0)M, \tag{6.20}$$

where V_{eff} is the volume irradiating the photocathode; $S(\lambda_0)$ is the spectral responsivity at λ_0. The illuminating volume is here the uniform, infinite illuminating cylinder of diameter equal to that of the laser beam. We note the PMT spectral responsivity to be expressed as follows: $S(\lambda) = s(\lambda)S(\lambda_0)$ with $s(\lambda)$ being well known, see Sects. 3.2.2 and 3.2.3. Having measured the photocurrent for a given concentration M ($[M]$) or for the photocurrent function on $[M]$, we can determine the following product:

$$\Delta\Omega V_{\mathrm{eff}} S(\lambda_0) = \frac{I_{\mathrm{R}}}{\Phi_{hv}\sigma_{\mathrm{r}}(\lambda_0)M} = \frac{I_{\mathrm{R}}}{\Phi_{hv}^{\mathrm{R}}} \tag{6.21}$$

which will be exploited further to determine the intensity of the photoprocess under study.

6.3.2 *Calibration by Means of Photoluminescence*

There exist experimental situation, where the Rayleigh calibration cannot be applied to the registration system by reasons listed below:

– The absence of a powerful resonant light source or the lack of a photodetector in the spectral range you plan to use for investigation, for example, in the vacuum UV spectral range
– A great spectral interval between the spectral ranges, within of which photoexcitation should be performed and luminescence should be observed

If this is the case, the calibration can be carried out through a well-studied photoluminescence. By way of example let us consider a registration system calibration on luminescence of $O(^1S)$ atoms in the visible light of wavelength $\lambda_{lum} = 557.7$ nm under photolysis of N_2O produced by a hydrogen lamp. The lamp illuminates in the vacuum UV range with $\lambda_{ph} \approx 150$–170 nm [8]. This range is associated to the formation threshold of $O(^1S)$ atoms and transmission cutoff of fused quartz [9, 10]. A simple set of the following reactions can describe the photolysis processes of N_2O dealing with the problem under consideration:

$$N_2O + h\nu \rightarrow N_2 + O(^1S), \tag{6.22}$$

$$O(^1S) \rightarrow O(^1D) + h\nu_{lum}, \tag{6.23}$$

$$O(^1S) \xrightarrow{N_2O} O(^3P). \tag{6.24}$$

The formation rate, radiation lifetime, $\tau_{O(^1S)}$, and deactivation rate constant k_{24} of $O(^1S)$ atoms, all are needed for the calibration to be carried out. Deactivation of $O(^1S)$ is caused by collisions with N_2O molecules. The $O(^1S)$ atoms production rate is calculated to be as follows:

$$w_{O(^1S)} = \int_{150\text{ nm}}^{170\text{ nm}} \Phi_{h\nu}(\lambda)\ \sigma_{N_2O}(\lambda)\ \ \Phi_{O(^1S)}^{N_2O}(\lambda)\mathrm{d}\lambda, \tag{6.25}$$

where $\Phi_{h\nu}(\lambda)$ is the hydrogen lamp spectral radiation intensity. Under conditions of N_2O photolysis in the spectral range 100–170 nm both the absorption cross-sections of N_2O molecule and quantum yields for $O(^1S)$ formation, $\Phi_{O(^1S)}^{N_2O}$, are measured reasonably well (see [9, 10] and references). The radiation lifetime of $O(^1S)$ as well as the deactivation rate constant of $O(^1S)$ under collisions with N_2O molecule are also well known: $1/\tau_{O(^1S)} = 1.18 \pm 0.2\ s^{-1}$, $k_{24} = 1.6 \times 10^{-11}\ cm^3/s$ [9, 11, 12]. The steady-state concentration of $O(^1S)$ is given by the equation

$$[O(^1S)] = \frac{w_{O(^1S)}}{1/\tau_{O(^1S)} + k_{23}[N_2O]}. \tag{6.26}$$

In turn, the intensity of atomic radiation in the total solid angle 4π from unit volume is given by the following formula:

$$\Phi_{O(^1S)} = \frac{1}{\tau_{O(^1S)}}\left[O(^1S)\right] = \left(\frac{1}{\tau_{O(^1S)}}\right)\left(\frac{w_{1S}}{1/\tau_{O(^1S)} + k_{23}[N_2O]}\right). \tag{6.27}$$

The product $\Delta\Omega\, V_{\text{eff}}\, S(557.7\text{ nm})$ therefore takes the form

$$\Delta\Omega\, V_{\text{eff}}\, S(557.7\text{ nm}) = \frac{I}{\Phi_{\text{O}(^1\text{S})}}. \tag{6.28}$$

6.3.3 *Absolute Measurements of Spectral Radiation Intensity of the Uniform Illuminating Cylinder*

When studying radiation excited by laser beam or by any other well collimated light beam you deal with the radiation similar to that emitted by uniform illuminating cylinder. The radiation under study is within a thin optical layer, for example, when chemiluminescence is observed from a flowing reactor.

In order to apply calibration techniques for registration systems described in Sects. 6.3.1 and 6.3.2 the distance R between the cylinder axis and photodetector receiving area A should be much larger than the cylinder radius as well as the size of the receiving area $\sqrt{A}$. If this is the case, the photoresponse is calculated to be as follows:

$$I = \Phi_{h\nu}\, \Delta\Omega\, V_{\text{eff}}\, S(\lambda_0) \int_{\lambda_2}^{\lambda_2} s_{h\nu}(\lambda)\, \Phi_{h\nu}(\lambda)\text{d}\lambda. \tag{6.29}$$

The product $\Phi_{h\nu}(\lambda) = \Phi_{h\nu}(\lambda_0)\, \phi_{h\nu}(\lambda)$ allows the spectral photon flux of a cylinder unit volume to be estimated. This product can be found during calibration, see (6.21) and (6.28). The calibration techniques described in Sects. 6.3.1 and 6.3.2 and the methods of absolute intensity measurements of photoprocesses were applied for studying recombination with radiation of atoms $\text{I}(^2\text{P}_{1/2})$ + $\text{I}(^2\text{P}_{3/2})$ [7], of atoms $\text{I}(^2\text{P}_{1/2})$ with perfluoroalkyl radicals [13], and of atoms $\text{O}(^1\text{D})$ with atoms Xe, Kr [8, 14] and molecules CO, N_2 [14, 15]. In the case described in [13], the calibration was carried out through the Rayleigh scattering technique on He–Ne laser radiation; and in the case mentioned in [14, 15], the calibration was produced through luminescence of $\text{O}(^1\text{S})$ atoms.

6.4 Absolute Calibration of Spectrometer/Photodetector Systems

If for some reason the methods mentioned in Sects. 6.1–6.3 cannot be applied and it is a need to measure spectral radiation intensity of the photoprocess in absolute units then calibration of the spectrometer/photodetector system has to be performed in order to make absolute measurements of the intensity of the photoprocess under study. Both the calibration and measurements are to be carried out at the same

illumination layout. Author should note that this technique is far from simple, accurate, and correct method with respect to systematic errors, especially in the vacuum UV spectral range. In order to calibrate a system in absolute units the following steps are to be executed:

1. Calibrate the system in arbitrary units in the spectral range and within the solid angle which are planned to be further used
2. Provide with a light source, or light sources, calibrated in absolute units in the spectral range and within the solid angle mentioned in the item 1
3. Perform the absolute calibration of the system using the light source mentioned in the item 2 and photodetector calibrated in absolute units
4. Check the calibration against the other calibration techniques you are available
5. Calculate corrections, when the occasion requires, related to possible distinctions between the calibration layout and measurements layout

The algorithm listed above was applied for absolute calibration of the system involving monochromator and detector in wide spectral range including vacuum UV, $\lambda = 110$–450 nm [16]. Let us consider the ways of solution of these questions.

1. The calibration algorithm on the item 1 was detailed in Sects. 5.2, 5.3 and 5.5. On calibrating in the visible and near UV spectral range, the strip lamp SI8-200u manufactured in MELZ (Russia) and calibrated in Russian D.I. Mendeleev Scientific and Research Institute of Metrology ($\lambda \geq 320$ nm) were used. Also the quartz tungsten–halogen lamp with sapphire window of type 550A (Optronics Laboratory, USA) calibrated absolutely against a NBS standard ($\lambda = 250$–450 nm) was used. A white screen of pressed dispersed $BaSO_4$ was used as diffuse reflecting standard. In the vacuum spectral range were used the following secondary standards:
   - The DC window-less hydrogen-discharge lamp at H_2 pressures 0.2–0.5 torr. The spectrum of hydrogen lamp was measured with a resolution of FWHM = 0.4 nm by the double monochromator method. The uncertainties of measurement were less than 20 and 5% in the range $\lambda = 110$–170 nm and 170–250 nm, respectively, as it is maintained in [17] (see Sect. 5.5.4)
   - The hydrogen Lyman and Werner bands excited by monoenergetic electrons (see Table 5.2)
   - The nitrogen LBH bands excited by the monoenergetic electrons or within the nitrogen plasma (see Table 5.2)

2, 3. In the case of extended light source, to avoid uncontrolled systematic errors, the absolute calibration should be performed through a source, which gives the input aperture illumination at least in the same manner as for measuring. It is best to provide with the size of calibrated light source larger than the size of the source under investigation (see Sects. 5.5.1 and 5.5.2). Such a source is not to be calibrated in metrological laboratories, hence it has to be done on your own as described in Sect. 4.4. The light source may emit as resonant radiation as well as continuous spectrum radiation. The absolute

calibration needs to be carried out with assuming the indicator function of calibrated radiation is equivalent to that of the source under study. The latter is taken place in the case of uniform illuminating sources. Otherwise, these functions have to be estimated; this is a challenging task, especially in the vacuum UV range.

Due to small sizes, the illumination of the monochromator grating produced by the strip lamps or quartz tungsten–halogen lamps during measurements is different from the illumination realized in these experiments [16]. Therefore, the spectral line $\lambda = 364.13$ nm from the Kr discharge lamp was calibrated against the radiation of tungsten–halogen lamps with using of the interference filter at $\lambda = 364 \pm 2$ nm. In the vacuum UV spectral range the spectral line $\lambda = 147$ nm of the Xe resonance lamp of type KsR-2 was calibrated through the oxygen actinometer as described in Sects. 3.8.5.2 and 4.2.2.1. The parameters of the Xe resonance lamp such as the required output diameter $d_l = 10$ mm, f'-number of illumination $f' = 1/11.2$, were all found as described in Sect. 4.3.1. These lamps were utilized for absolute calibration of the monochromator/PMT142 system with the layout shown in Fig. 5.18. The ratio of the distance from the light source to the entrance slit to the illuminating surface diameter remained the same in making measurements with the Xe lamp and carrying out the experiments. The opening of the rectangular diaphragm 1.55×10 mm equal to the entrance monochromator slit was mounted on the PMT142 window. The photomultiplier operated in the quasi-phototube mode (see Sect. 4.2.2). The distance between the lamps' and PMT's diaphragms was 11.2 cm. There were made three measurements, each involving the turning of the rectangle diaphragm by 45°, to smooth a potential effect from the photocathode spatial non-uniformity.

4. A light source of continuous spectrum, actinometer, and a set of long-pass filters, each having a sharp-edge transparency function, were needed for the sensitivity calibration to be tested. The method described in Sect. 4.4.2.1 was applied, where the vacuum UV light sources mentioned in the item 1, CaF_2, BaF_2, and fused quartz filters were used. Due to modifying the used light source, the achieved accuracy was further improved.
5. We have noted in Sect. 5.5.1 that the illumination of grating in calibration differed fairly from that in measurements (see Fig. 5.19). After absolute calibration of the monochromator/PMT142 system, the systematic error was found to be $\left(\Phi_{h\nu}^{\text{meas}} - \Phi_{h\nu}^{\text{cal}}\right)/\Phi_{h\nu}^{\text{cal}} = -0.15$, whereas the systematic error of output light flux was found to be equal to $\left(\Phi_{h\nu}^{\text{meas}} - \Phi_{h\nu}^{\text{cal}}\right)/\Phi_{h\nu}^{\text{cal}} = +0.24$. Both errors were caused by astigmatism and the difference in illumination layout mentioned above.

Calibration in arbitrary units. In the visible and UV spectral range the calibration in arbitrary units had uncertainties changed as 7, 3, 6 and 10% against running of the spectral range as follows: 200–250, 250–350, 350–400 and 450 nm.

The spectral sensitivity functions found in the vacuum UV range by different techniques are shown in Fig. 6.3.

There is a good agreement of the curves measured by means of the Lyman, Werner (curve 2) with LBH systems (curve 3). The curve 1 differs fairly from the other curves in the region $\lambda \leq 150$ nm. A set of measurements was made to identify trustworthy curves among these curves as mentioned in the item 4. It was found the curves 2 and 3 to be much better than the curve 1. Further, the curves 2 and 3 were fitted in the vacuum UV range of wavelength from 130 to 170 mm, whereas the curves 1 and 3 were fitted in the range 165–210 nm. The uncertainties of the relative curve were found to be 18, 14 and 7% in the ranges 110–120, 120–140 and 140–200 nm, respectively.

Absolute calibration. The relative spectral sensitivity curves determined in the range 200–450 nm and 110–250 nm were matched onto their overlapping intervals. Then these functions were calibrated absolutely at $\lambda = 364 \pm 2$ and 147 nm according to the technique described above. The spectral responsivity curve $S_{hv}(\lambda)$ expressed in terms of absolute units is shown in Fig. 6.4.

The monochromator/PMT142 system was calibrated absolutely at two wavelengths, one lay in the UV and the other lay in the vacuum UV range. In the UV range the uncertainty of the calibration was equal to 8% that was mainly dependent on the current measurements noise in some series of the two-step calibrations. The mean-square deviation of the calibration at 147 nm was about 8%. The results of the calibration in the UV and the vacuum UV range agreed well. Thus, on fixing the relative curve at one point allowed to compare at the other point.

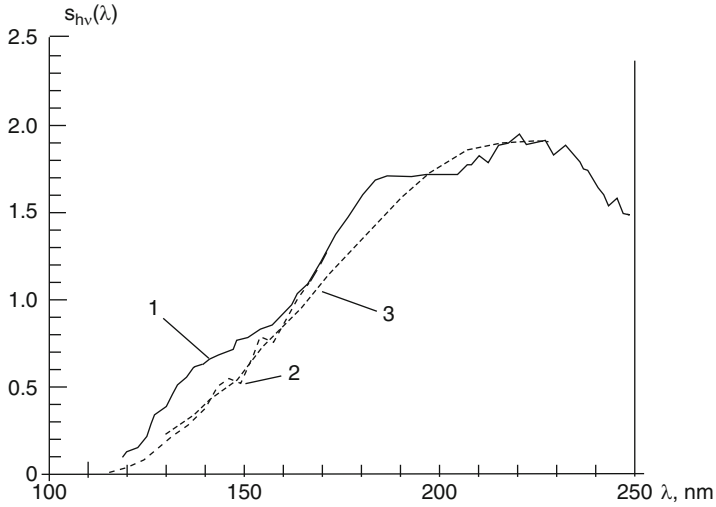

Fig. 6.3 Relative spectral sensitivity functions measured by means of the hydrogen DC lamp (1); by the H_2 Lyman and Werner bands excited by an electron beam (2), and by the N_2 LBH systems (3) (see [16])

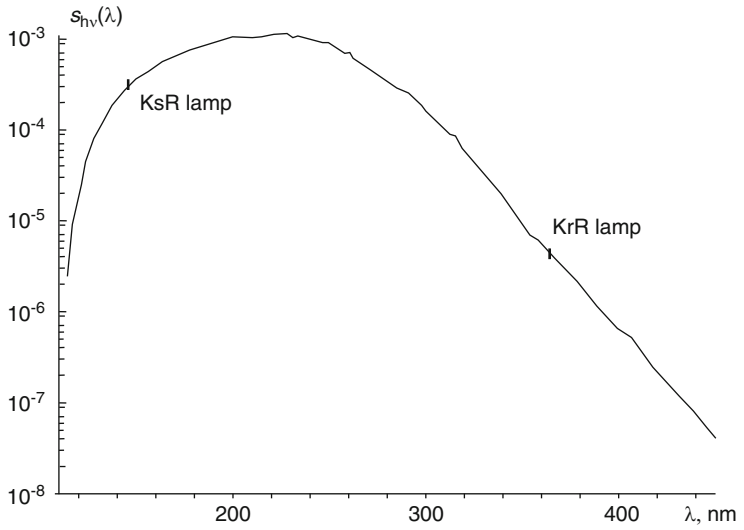

Fig. 6.4 The absolute spectral responsivity curve $S_{hv}(\lambda)$ of the Jobin-Yvon AS50 VUV-monochromator equipped with PMT142 photomultiplier tube (see [16])

The results were in a good agreement within the uncertainty of 8%, which is better than the precision of the relative and absolute measurements. This may be regarded as additional confirmation of a reasonably high accuracy of the relative and absolute calibrations.

The comparison of point-like sources and extended sources exploited for calibration shows the following. The both source types used for calibration of spectrometer/detector systems give systematic errors caused by the distinction in illumination layouts: one is used for calibration and the other one is used for applications. The extended light sources are therefore preferable as standards when the application deals with extended light sources. However, the accuracy and reproducibility of the used standards and procedures must be considered too.

It is seen that the absolute calibration makes experiments more difficult, and it can involve potential systematic errors. So apply, where possible, other techniques for measurements.

Problems

On recording the luminescence signal from O(^{1}S), estimate the quantity $\Delta\Omega\, V_{\text{eff}}\, S$, providing the pressure of N_2O is 0.1 torr, the radiation intensity of resonant line $\lambda = 147$ from a Xe-lamp is found to be $\Phi_{hv}(\lambda) = 10^{14}$ photon/s, and the recorded signal is equal to $n = 7 \times 10^3$ pulses/s. The absorption cross-section of N_2O is equal to σ_{N_2O} ($\lambda = 147$ nm) $= 6 \times 10^{-18}$, the quantum yield for O(^{1}S) formation is equal to $\Phi^{N_2O}_{O(^1S)}(\lambda) = 0.4$ at $\lambda = 147$ nm.

References

1. Pravilov, A.M., Smirnova, L.G., Sumbaev, I.O.: Spectral distribution of rate constant of chemiluminescence in reaction of O(^{3}P) + CO (+He) → CO_2 (+He) + hν. ZH. FIZ. KHIM. (USSR) **52**, 1863–1866 (1978); Eng. transl.: Rus. J. Phys. Chem. **52**, 902–908 (1978)
2. Miles, R.B., Lempert, W.R., Forkey, J.N.: Laser Rayleygh scattering. Meas. Sci. Technol. **13**, R33–R51 (2001)
3. Sneep, M., Ubachs, W.: Direct measurement of the Rayleigh scattering cross section in various gases. J. Quant. Spectrosc. Rad. Transf. **92**, 293–310 (2005)
4. Peck, E.R., Khanna, B.N.: Dispersion of argon. J. Opt. Soc. Amer. **54**, 1362–1364 (1964)
5. Bates, R.D.: Rayleigh scattering by air. Planet. Space Sci. **32**, 785–790 (1984)
6. Zaidel, A.N., Shreider, EYa: Vakuumnaya Spectroskopiya i ee Primenenie (Vacuum Spectroscopy and Its Application). Nauka, Moscow (1976) (in Russian)
7. Egorov, S.M., Pravilov, A.M., Skorokhodov, V.A.: The very fast chemiluminescence reaction $I(^2P_{1/2}) + I(^2P_{3/2}) \xrightarrow{M} I_2(B0_u^+, v') \rightarrow I_2(X0_g^+, v'') + hv$. Chem. Phys. **165**, 371–383 (1992)
8. Pravilov, A.M., Sidorov, I.I., Skorokhodov, V.A.: Mechanism and kinetics of photorecombination of O(^{1}D) with Xe (Engl. transl.). Sov. J. Chem. Phys. **3**, 793–807 (1985)
9. Bibinov, N.K., Vilesov, F.I., Vinogradov, I.P., Mikheev, L.D., Pravilov, A.M.: Determination of spectral dependences of the absolute quantum yields of O(^{1}S) formation by the method of observation of XeO luminescence. I. CO_2 and N_2O photolysis (Eng. transl.). Sov. J. Quant. Electron. **9**, 838–844 (1979)
10. Pravilov, A.M.: Fotoprotsessy v Molekulyarnykh Gasakh (Photoprocesses in Molecular Gases). Energoatomizdat, Moscow (1992)
11. Nicolaides, C., Sinanoglu, O., Westhaus, P.: Theory of atomic structure including electron correlation: IV. Method for forbidden-transition probabilities with results for [0I], [OII], [OIII], [NI}, [NII], and [CI]. Phys. Rev. **A4**, 1400–1410 (1971)
12. Donovan, R.J., Husain, D.: Recent advances in the chemistry of electronically excited atoms. Chem. Rev. **70**, 489–516 (1970)
13. Egorov, S.M., Pravilov, A.M., Skorokhodov, V.A.: Recombination of perfluoroalkyl radicals with the I($5p^5$ $^2P_{1/2}$) and I($5p^5$ $^2P_{3/2}$) atoms accompanied by radiation. Chem. Phys. **173**, 467–477 (1993)
14. Pravilov, A.M., Sidorov, I.I., Skorokhodov, V.A.: Population and decay of the KrO and N_2O excited states in collisions of atoms O(^{1}D) with Kr and N_2. Sov. J. Chem. Phys. **5**, 1–9 (1989)
15. Pravilov, A.M., Protopopov, S.V., Sidorov, I.I., Skorokhodov, V.A.: Photorecombination of O(^{1}D) with CO. Sov. J. Chem. Phys. **3**, 2010–2033 (1985)
16. Bibinov, N.K., Bolshukhin, D.O., Kokh, D.B., Pravilov, A.M., Vinogradov, I.P., Wiesemann, K.: Absolute calibration of the efficiency of a VUV-monochromator/detector system in the range of 110–450 nm. Meas. Sci. Technol. **8**, 773–781 (1997)
17. Zaidel, A.N., Shreider, EYa: Vacuum Ultraviolet Spectroscopy. Ann Arbor-Humphrey, London (1970)

Solutions to the Problems

Chapter 2

1. To verify the formulae (2.4)–(2.8), we check in the physical dimension of the formulae. The expressions in *brackets* have no physical dimensions.

2. The brightness temperature 2,147°C corresponds to the color temperature $T_b = 2{,}420$ K and true temperature $T = 2{,}700$ K. We calculate the radiation spectrum of black body using the formula (2.4) in terms of wavelength in nm at $T = 2{,}700$ K, and the obtained data are multiplied by quantities $\varepsilon(\lambda,T)$ found from extrapolation to required wavelengths and temperature $T = 2{,}700$ K through the values listed in Table 2.1. Finally, the required ratio is found to be $L_{hv}(320,T)/L_{hv}(600,T) = 6 \times 10^{-3}$.

3. $L_{hv}(\lambda) = \left(\frac{hc}{\lambda}\right) L_e(\lambda) = \left(\frac{2 \times 10^{-16}}{\lambda}\right) L_e(\lambda)$ photon/(s sr m^2 nm).

Chapter 3

1. The sensitivity of photoemissive detector is given by the formula:

$$S_e(\lambda) = \frac{I}{\Phi_e(\lambda)} = \frac{n_e\, e\, \lambda}{hc\, N_{hv}(\lambda)} \quad \text{A/W}$$

where hc/λ is the photon energy, N_{hv} is the photon number, $I = n_e\, e$ is the photocurrent, and $e = 1.602 \times 10^{-19}$ C is the elementary charge. The quantum efficiency is given by the formula:

$$\eta(\lambda) = \frac{n_e}{N_{hv}(\lambda)} = S_e(\lambda)\left(\frac{hc}{e\lambda}\right).$$

Substituting numerical values of h, c, e in the formula above, we get the desired formula, provided wavelength is expressed in nm.

2. The spectral sensitivity of the photocathode is equal to 80.6 mA/W.

3. At the repetition frequency of 100 Hz, current associated with one pulse is found to be 10^{-8} A or about 10^{11} electrons per pulse. Such an electron flow passes

A.M. Pravilov, *Radiometry in Modern Scientific Experiments*,
DOI 10.1007/978-3-7091-0104-9, © Springer-Verlag/Wien 2011

to the PMT anode during the time interval 10^{-6} s. It is meant that the maximal current is not less than 10^{17} electrons per second or 10^{-2} A which is well permissible for operation in the analog mode.

Chapter 4

1. The oxygen cross section is equal to 5×10^{-19} and 2×10^{-20} cm^2 at $\lambda = 123.6$ and 116.5 nm, respectively, i.e., it differs about 25 times. When using the oxygen filter of optical pass $[O_2] \times l = 7 \times 10^{18}$ molecules/cm^2 ($p_{O_2} l \approx$ 200 topp cm), radiation of wavelength $\lambda = 123.6$ nm is weaken 30 times and $\lambda = 116.5$ nm is weaken by 13%.

2.1. The window 8 is identical to that in the cell 6, i.e., both have identical transmission spectra. Inserting the window 8 you introduce the absorption correction caused by the window 6 as measuring intensity from resonant lamps by the actinometer, as well as while performing calibration of the ionized chamber.

2.2. $S_q(\lambda) = n/\Phi_{h\nu}(\lambda)$. The sensitivity should be independent of wavelength.

3. The input monochromator slit is put at the point of converging of the light beam reflected from the second mirror (Fig. 4.10). The function of the system photoresponse $I_1(\lambda)$ against wavelength is measured. Then you make measurements with the setup shown in Fig. 5.1c, where the spectral function of the diffusive screen reflectivity is well known. Also the input apertures of light beams in both measuring sets assumed to be equal. Having the photoresponse in the second set $I_2(\lambda)$ as proved by the reflectivity of the diffusive screen, you can estimate the quantity $L(\lambda) = I_1(\lambda)/I_2(\lambda)$.

Chapter 5

1. To find the level of scattered light, you make measurements of spectral function for photoresponse against wavelength using proper long-pass filters. To find spectral function for photoresponse, you should close output window of the lamp or iris diaphragm (see Sects. 5.2, 5.3, and 5.4.2).

2. You should determine the emission spectrum of the strip lamp for the brightness temperature corresponding to one strip edge as described in Sect. 2.1.3. As the brightness temperature at the strip center is equal to $T_b = 2{,}147^\circ$C or 2,420 K and the true temperature is $T = 2{,}700$ K, the brightness temperature of the strip edge is decreased by 5°C with the error not more than 2%.

3. While calibrating using the deuterium lamp which is calibrated in the range $\lambda = 190$–380 nm, you may not use any filter, because lamp radiation is negligible and the second diffraction order becomes noticeable at $\lambda \geq 380$ nm. Strip lamp emission of temperature $T = 2{,}700$ K is distinctly measured at $\lambda \geq 300$ nm. Hence, the strip lamp allows to calibrate your system without any filter up to the wavelength $\lambda = 600$ nm.

4. In the range $\lambda = 400$–600 nm, you calibrate the system without any filter. Further, using long-pass filter of transmission in $\lambda > 550$ nm you calibrate the system in the range $\lambda \approx 550$–1,000 nm, and using the filter of transmission in $\lambda > 950$ nm you calibrate the system in the range $\lambda \approx 950$–1,300 nm.

5. Without a condenser or mirror, in any case the input aperture f'-number is less than the monochromator f-number. Even if the deuterium lamp is placed right up to the monochromator input slit, f'-number will not be greater than 1:15, because the light spot diameter is about 1 mm, whereas the distance between the spot and input window of the lamp is about 15 mm. Thus, you need to perform a large number of measurements shifting the lamp slightly from left to right and from top to bottom, with further averaging of the obtained data (see Fig. 5.12).

6. At $\lambda = 440$ nm, the refractive index of quartz glass is $n = 1.47725$ (see Table 5.1), and the focal length of your lens is $f = 10.47$ cm ($|a_1| = |a_2| = 20.95$ cm). At $\lambda = 240$ nm, $n = 1.5139$, $|a_1| = |a_2| = 19.46$ cm. The distance between the input slit and the image of your light source at $\lambda = 240$ nm is 20.95 – 19.46 = 1.49 cm.

7. The spectral sensitivity function of a spectrometer/photodetector system is $S_{hv}(\lambda) = F(\lambda)\, S_{hv}^{\mathrm{pd}}(\lambda)$, where $S_{hv}^{\mathrm{pd}}(\lambda)$ is the spectral sensitivity function of the photodetector. The $F(\lambda)$ is equal to $F(\lambda) = S_{hv}(\lambda)/S_{hv}^{\mathrm{pd}}(\lambda)$.

Chapter 6

The intensity of radiation from atoms $O(^1S)$ in the solid angle 4π emitted by a unit volume is given as follows:

$$I_{O(^1S)} = \left(\frac{1}{\tau_{O(^1S)}}\right)[O(^1S)] = \left(\frac{1}{\tau_{O(^1S)}}\right)\left(\frac{w_{1S}}{1/\tau_{O(^1S)} + k_{23}[N_2O]}\right).$$

Since $w_{1S} = \Phi_{hv}(\lambda) \cdot \sigma_{N_2O}(\lambda) \cdot \Phi_{N_2O}^{O(^1S)}(\lambda)[N_2O] = 8 \times 10^{11}\ \mathrm{cm}^{-3}\,\mathrm{s}^{-1}$, the product $\Delta\Omega\, V_{\mathrm{eff}}\, S(557.7\ \mathrm{nm})$ is calculated to be equal to:

$$\Delta\Omega\, V_{\mathrm{eff}}\, S\ (557.7\ \mathrm{nm}) = \frac{n}{I_{O(^1S)}} = \frac{7 \times 10^3}{1.8 \times 10^7} = 3.9 \times 10^{-4}$$

Appendix A

Treatment of Data Measured Directly

By making measurements we obtain numerical values of a desired quantity. Measurements are classified as direct measurements and as indirect measurements. Direct measurement is performed by a tool or device, which gives the measured quantity directly. While making indirect measurements, values of some quantity are measured in direct measurements, and then the other quantity is calculated to be composed from the obtained values. The treatment procedure of data obtained through direct measurements is outlined below. More detailed discussion of treatment of data obtained in direct measurements, as well as indirect measurements, can be found in [1, 2].

Measurement errors can be subdivided into three groups as *systematic errors*, *random* or *statistical errors (uncertainties)*, and *rough errors* or *overshoots*. Systematic errors occur due to many reasons, and the experimenter should persevere in trying to find the error source and estimate the magnitude of them. Typical sources of systematic errors are as follows:

- Disadvantages of measuring tools such as nonlinearity, zero drift, and errors of calibration
- Changes in experimental conditions and environment
- Other errors, including experimentalist's mistakes

Rough errors are caused by experimenter's mistakes and failures of measuring devices. Errors of this kind can be clearly recognized through statistical analysis of experimental data (e.g., see [2]). Statistical errors will be exclusively discussed below.

We assume a quantity x to be measured in one series of n successive measurements as one sample of length n:

$$x_1, x_2, x_3, \ldots, x_n. \tag{A.1}$$

The arithmetic mean is believed as the best estimation of the true value $\bar{x}_0$:

$$\bar{x}_n = \sum_1^n \frac{x_i}{n}. \tag{A.2}$$

A root mean square value of uncertainty should be ascribed to the arithmetic mean according to the expression:

$$\sigma_x = \frac{1}{n}\sqrt{\sum_{i=1}^{n}(x_i - \bar{x}_n)^2}. \tag{A.3}$$

The measurement result is written as follows:

$$x = \bar{x}_n \pm \sigma_x. \tag{A.4}$$

With making large quantity of measurements the estimation in the form (A.3) is chosen in such a way to get the estimated uncertainty less than σ_x in 2/3 times, and in 1/3 times to get the estimated uncertainty more than σ_x. The uncertainty defined with estimation reliability 2/3 is named the root mean square deviation or standard deviation σ. The square of the root mean square deviation is referred as the dispersion σ^2.

In most cases, measured values, each having statistical nature, are subject to Gaussian distribution or normal distribution. Let $\Delta x = x - \bar{x}_0$ be the deviation of the quantity x from the true value $\bar{x}_0$, the Gaussian distribution $f(x)$ takes the following form:

$$f(x) = \frac{1}{\sigma\sqrt{2\pi}} \exp\left[-\frac{(\Delta x)^2}{2\sigma^2}\right]. \tag{A.5}$$

The value x is proved to be within the interval $\pm 2\sigma$ in 95 cases among 100, in other words the probability of this event, sometimes they say about confidence level of the event, is equal to 0.95. According to the definition of the root mean square deviation above, the value x is expected to be within the interval $\pm\sigma$ with the probability 2/3 (Fig. A.1).

In the author's opinion, in most cases, it is not necessary to make measurements with the confidence level more than $P = 0.95$. The Gaussian distribution shows a limited situation, which could take place as the number of measured values n tends to infinity. In practice, the formula (A.3) or the formula:

$$\sigma'_x = \sqrt{\frac{\sum_{i=1}^{n}(x_i - \bar{x}_n)^2}{n(n-1)}} \tag{A.6}$$

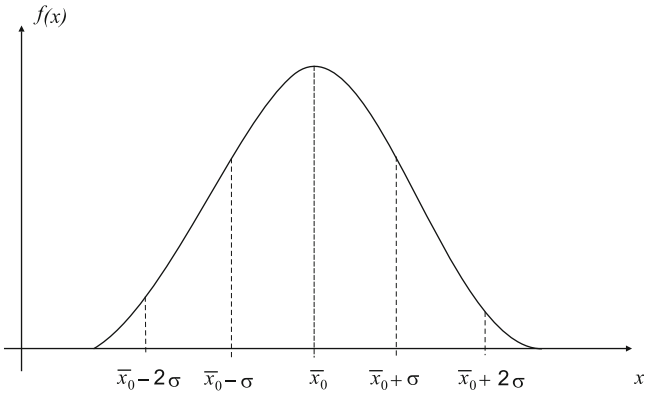

Fig. A.1 The Gaussian distribution. The square bounding the curve $f(x)$ between the points $\bar{x}_0 - \sigma$, $\bar{x}_0 + \sigma$ gives the probability, $P = 0.68$, for x within the limits of the standard deviation σ; the square bounding the curve $f(x)$ between the points $\bar{x}_0 - 2\sigma$, $\bar{x}_0 + 2\sigma$ gives the probability, $P = 0.95$, for x within the limits of the two standard deviation 2σ

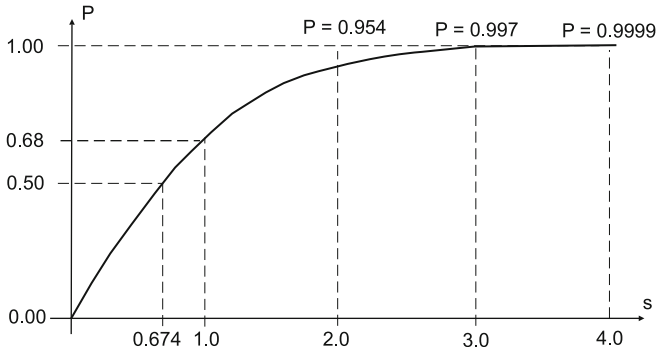

Fig. A.2 The probability P of the event that x lays in the limits of s standard deviations from the mean value $\bar{x}_0$

is used for estimation of the root mean square error. In both cases (A.3) and (A.6), the estimated error decreases with increasing the number n (Fig. A.2):

$$\sigma_x \sim \frac{1}{\sqrt{n}}, \quad \sigma'_x \sim \frac{1}{\sqrt{n}}. \tag{A.7}$$

In order to estimate errors for a not great n, the Student's t-distribution is applied to a series of measured values [3, 4]. The Student's distribution is transformed to the Gaussian distribution when n tends to infinity. The so-called Student's coefficient t, which is dependent on n and P, is used to estimate the error (Fig. A.3), for example, as follows:

$$\sigma''_x = \sigma'_x t \tag{A.8}$$

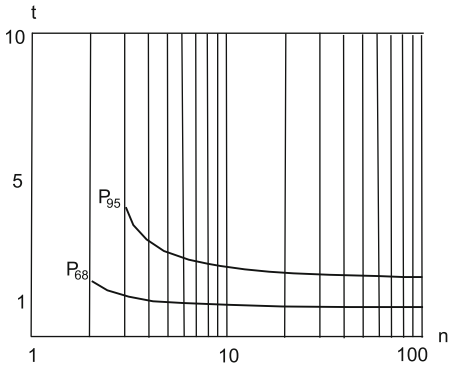

Fig. A.3 The function of the Student's coefficient t against the number of measured values n for the probabilities $P = 0.68$ and $P = 0.95$

Note that the value of estimated error σ_x'' should be compared with the systematic error or the uncertainty of the measuring facility, provided the latter has been estimated. Having the value of estimated σ_x'' less than 30% of the facility uncertainty and systematic error, there is no necessity to enlarge the sample length n. Some techniques for overshoots recognizing and estimation of uncertainties of indirect measurements are discussed, for example, in [2].

References

1. Kunze, H.-J.: Physikalische Messmethoden. Eine Einfuhrung in Prinzipen Klassischer und Moderner Verfahren. B.G. Teubner, Stuttgart (1986)
2. Taylor, J.R.: An Introduction to Error Analysis. University Science Book, Mill Valley (1982)
3. Student, B.: The probable error of a mean. Biometrika **6**, 1–25 (1908)
4. Student's t-distribution. http://en.wikipedia.org/wiki/Student's_t-distribution

Appendix B

Tables B.1 and B.2 show the true total band intensities of the NO and N_2 afterglow spectra measured in pure N_2 environments under the conditions: $p_{N_2} = 3.4$ torr, FWHM = 1 nm (see Sect. 5.6).

Table B.1 The true total band intensities of the NO afterglow spectra measured in pure N_2 environments, $p_{N_2} = 3.4$ torr, FWHM = 1 nm[a] (reproduced with permission from Measurements Science and Technologies, IOP Publishing Ltd)

Limit wavelengths, $\lambda_i - \lambda_{i+1}$ (nm)	Limit wavenumbers, $v_i - v_{i+1}$ (cm^{-1})	Intensity[b] (a.u.)
212.50–217.50	47,058.82–45,977.01	0.705
217.50–220.70	45,977.01–45,310.38	0.163
220.90–223.00	45,269.35–44,843.05	0.205
223.00–224.80	44,843.05–44,483.99	0.278
224.80–227.70	44,483.99–43,917.44	0.450
231.70–234.70	43,159.26–42,607.58	0.399
234.70–238.20	42,607.58–41,981.53	0.705
242.30–245.50	41,271.15–40,733.20	0.383
245.60–248.90	40,716.61–40,176.78	0.553
249.00–253.00	40,160.64–39,525.69	0.250
253.00–256.70	39,525.69–38,955.98	0.182
256.70–260.40	38,955.98–38,402.46	0.356
261.00–265.90	38,314.18–37,608.12	0.363
266.00–269.60	37,593.99–37,091.99	0.109
269.60–273.60	37,091.99–36,549.71	0.198
274.00–278.00	36,496.35–35,971.22	0.455
287.20–291.70	34,818.94–34,281.80	0.650
302.70–309.00	33,036.01–32,362.46	0.856
318.90–325.50	31,357.79–30,721.97	1.000
336.70–344.00	29,700.03–29,069.77	0.861
356.30–363.90	28,066.24–27,480.08	0.612
378.00–386.00	26,455.03–25,906.74	0.322
386.20–393.80	25,893.32–25,393.60	0.043

(continued)

Table B.1 (continued)

Limit wavelengths, $\lambda_i - \lambda_{i+1}$ (nm)	Limit wavenumbers, $\nu_i - \nu_{i+1}$ (cm^{-1})	Intensity[b] (a.u.)
393.80–401.50	25,393.60–24,906.60	0.020
402.00–410.00	24,875.62–24,390.24	0.139
410.70–418.70	24,348.67–23,883.45	0.020
419.00–427.00	23,866.35–23,419.20	0.024
428.00–437.50	23,364.49–22,857.14	0.075
446.70–455.00	22,386.39–21,978.02	0.018
456.20–466.00	21,920.21–21,459.23	0.050
477.70–488.00	20,933.64–20,491.80	0.010
488.00–498.10	20,491.80–20,076.29	0.031
523.70–531.30	19,094.90–18,821.76	0.018

[a]Data for relative intensities of the bands are available at $p_{N_2} = 3$–8 torr, $\lambda = 242$–1,050 nm, and $p_{N_2} = 3.4 \pm 0.3$ torr, $\lambda = 210$–242 nm. FWHM has to be better than 1 nm at $\lambda = 210$–285 nm and 2 nm at $\lambda = 285$–1,150 nm intervals

[b]Uncertainties of the data are as follows: 12–8–5–2% in the 210–260–290–1,150 nm range

Table B.2 The true total band intensities of the N_2 afterglow spectra measured in pure N_2 environments, $p_{N_2} = 3.4$ torr, FWHM = 1 nm[a] (reproduced with permission from Measurements Science and Technologies, IOP Publishing Ltd)

Limit wavelengths, $\lambda_i - \lambda_{i+1}$ (nm)	Limit wavenumbers, $\nu_i - \nu_{i+1}$ (cm^{-1})	Intensity[b] (a.u.)
497.47–510.00	20,101.71–19,607.84	0.010
531.75–546.74	18,805.83–18,290.23	0.159
568.00–576.00	17,605.63–17,361.11	0.190
576.00–582.41	17,361.11–17,170.04	0.420
582.41–588.00	17,170.04–17,006.80	0.103
588.00–592.58	17,006.80–16,875.36	0.025
592.58–597.71	16,875.36–16,730.52	0.020
597.71–603.17	16,730.52–16,579.07	0.022
603.17–609.40	16,579.07–16,409.58	0.029
609.40–619.25	16,409.58–16,148.57	0.071
619.25–626.80	16,148.57–15,954.05	0.229
626.80–634.10	15,954.05–15,770.38	0.098
634.10–641.53	15,770.38–15,587.74	0.041
641.53–648.83	15,587.74–15,412.36	0.046
648.83–656.50	15,412.36–15,232.29	0.072
656.50–664.78	15,232.29–15,042.57	0.155
664.78–671.56	15,042.57–14,890.70	0.093
671.56–680.86	14,890.70–14,687.31	0.122
680.86–688.83	14,687.31–14,517.37	0.044
688.83–704.99	14,517.37–14,184.60	0.045
707.21–718.28	14,140.07–13,922.15	0.026
718.28–729.35	13,922.15–13,710.84	0.099
729.35–740.42	13,710.84–13,505.85	0.126
740.42–753.48	13,505.85–13,271.75	0.187

(continued)

Table B.2 (continued)

Limit wavelengths, $\lambda_i - \lambda_{i+1}$ (nm)	Limit wavenumbers, $\nu_i - \nu_{i+1}$ (cm^{-1})	Intensity[b] (a.u.)
753.48–767.13	13,271.75–13,035.60	0.351
767.13–778.02	13,035.60–12,853.14	0.375
778.02–792.03	12,853.14–12,625.78	0.149
792.03–806.34	12,625.78–12,401.72	0.105
841.99–858.68	11,876.63–11,645.78	0.145
858.68–879.31	11,645.78–11,372.55	0.690
879.31–895.51	11,372.55–11,166.82	0.737
908.63–927.71	11,005.58–10,779.23	0.061
927.71–950.79	10,779.23–10,517.57	0.083
950.79–977.56	10,517.57–10,229.55	0.139
977.56–1,001.87	10,229.55–9,981.34	0.142
1,001.87–1,028.65	9,981.34–9,721.48	0.186
1,028.65–1,056.43	9,721.48–9,465.84	1.000

[a]Data of relative intensities of the bands are available at FWHM better than 2 nm and $p_{N_2} = 3$–8 torr

[b]Uncertainty of the data is better than 2%

Index